UNIVERSITÉ DE GRENOBLE

THÈSE

Pour obtenir le grade de

DOCTEUR DE L'UNIVERSITÉ DE GRENOBLE

Spécialité : **NanoPhysique**

Arrêté ministériel : 7 août 2006

Présentée par

Chi VÕ VĂN

Thèse dirigée par **Johann CORAUX** et **Olivier FRUCHART**

préparée au sein de l'**Institut Néel (CNRS/UJF UPR 2940)**
dans **l'École Doctorale de Physique de Grenoble**

Epitaxial graphene on metal for new magnetic nanometric systems

Thèse soutenue publiquement le **19 Mars 2013**,
devant le jury composé de :

Mr. Matthieu JAMET
Directeur de recherche, Institut Nanociences et Cryogénie/CEA-Grenoble, Président
Mr. Stefano RUSPONI
Profeseur, Ecole Polytechnique Fédérale de Lausanne, Rapporteur
Mr. Eric BEAUREPAIRE
Directeur de recherche, Physique et Chimie des Matériaux de Strasbourg, Rapporteur
Mr. Rodolfo MIRANDA
Professeur, Universidad Atónoma de Madrid, Examinateur
Mr. Abdelmadjid ANANE
Maître de conférence, Unité Mixte de Physique CNRS/Thales-Palaiseau, Examinateur
Mr. Olivier FRUCHART
Directeur de recherche, Institut Néel/CNRS&UJF-Grenoble, Co-Directeur de thèse
Mr. Johann CORAUX
Directeur de rechercher, Institut Néel/CNRS&UJF-Grenoble, Directeur de thèse

Université Joseph Fourier / Université Pierre Mendès France /
Université Stendhal / Université de Savoie / Grenoble INP

Remerciements

Dank u! Thank you! Merci! Grazie! ¡Gracias! Cảm ơn!

I have about 50 months of research work comprising my engineering internship and my PhD in the group of Micro- NanoMagnetism, Departement Nanosicences, Néel Institute. Il would like to thank Alain Fontaine and Alain Schuhl, directors of the Néel Institute/CNRS & UJF, Roland Herino, ex-director and again Alian Fontaine who got a transfer as present director of the Nanosciences Fondation which support the finance during my PhD. I'm thankful the additional support from the People Committee of the Đà Nẵng City who also offered me an expected job just after finishing my PhD.

I'm grateful the administrative teams who amicably and throughly occupied the administrative formalities of my finance and a lot of my missions, notably Joël Cibert and Hervé Courtois - directors, Véronique Fauvel, Sabine Gadal and Marielle Lardato at the Nanosciences Departement; Marie-Anne Carré, Stéphanie Monfront, Maud Dayez and Fériel Kouiten at the Nanosciences Fondation; Sandrine Ferrari at the Ecole Doctorale de Physique de Grenoble. I express my gratitude to Nguyễn Bá Thanh, President of People's Council of Đà Nẵng City.

I'm thankful "Micro and NanoMagnetism" and "Hybrid Systems at low dimension" groups, I keep in my mind the agreeable memory of both scientific and non-scientific activities with the members of groups. In particular, Nora Demsey, Dominique Givord, Jan Vogel, Nicolas Rougemaille, Laurent Ranno, Stefania Pizzini and the other permanents of our big group assisted me in the measurements and discussed with me their ideas in discussion mixing with their humor. My colleagues, Georgeta Cuita, Sandrine Da-col, Aleš Hrabec, Antoine Reserbat-Plantey, Luiz-Fernando Zanini, Zahid Ishaque, André Dias, Shakti Singh, Rajasekhar Medapalli, Nguyễn Văn Đại, Nguyễn Ngọc Việt shared with me our offices, coffee breaks times and had lunch together, Zoukaa Kassir-Bodon, Amina Kimouche and Fabien Jean supported each other with me in the graphene investigations. I have learned so much form you not only in science but also in your cultures, I sincerely wish the success in carriers and in life up to each one's expectation, especially reserved for the PhD students of the groups.

Foremost in the judgement of my PhD thesis, I have the honor of showing my deep gratitude to the members of the jury commission, the examiners Rodolfo Miranda, Abdelmadjid Anane and Matthieu Jamet, the rapporteurs Stefano Rusponi and Eric Beaurepaire who accepted the invitation to evaluate my works and to read attentively my thesis. Thank you for your time and your schedule for my PhD defense!

My supervisors, Johann Coraux and Olivier Fruchart, gave me the excellent opportunity to come to France and to integrate onto the research environment of Néel Institut for this nice period. They had created and maintained the best working conditions for me with continuous supports since my internship until the end of my PhD. Along with their greatly pedagogic tutorship, their kind personal attitudes encouraged me on my work and on my life in Grenoble, and certainly, their enthusiasms and kindliness will be a reliable source of inspiration for my carriers whatever I do and wherever I am in the future. Thank also for your time to listen my personal confidences and plan and help me to challenge my personal difficulties. I would think that one of the most lucks of my life is working with you as your PhD student. Je vous remercie du fond de mon esprit, je suis reconnaissant envers vous, à jamais!

At the Néel Institute, I appreciate the technical supports of Valérie Guisset and Philippe David who are responsible for the "laser room", the essential experimental setup of my studies. I relied on them to resolve many serious issues of the systems, always with their smiles. They was all the time available as soon as possible when the technical problems had happened. I also

thank to Luc Ortega, responsible for the x-ray diffraction equipment and Nedjma Bendiab with her help in Raman spectroscope. Thank you all for your sense of responsibility!

I express my gratitude to groups and laboratories from Grenoble, Paris, Köln (Germany), Berkeley (California, USA) who contributed to the works through many collaborations: The CEA, thanks to Pascale Bayle-Guillemaud and Violaine Salvador of INAC/SP2M/LEMMA for their HRTEM implementation, Mairbeck Chshiev and Hong-Xin Yang of SPINTEC for their ab initio calculations. The Univesity of Köln, I had nice occasions to manipulate with Professor Thomas Michely who is scholarly in science and humorous during stressful experiences at the ESRF, and Carsten Busse who was very patient and lucid in the repeated malfunctions of our experiences. I would amicably thank their practised students Stefan Schumacher, Sven Runte and Felix Huttmann from whom I learned a lot of experimental skills. The ESRF, I had ten or so interesting weekly sessions on different beamlines at the European Synchrotron, there are impressive chances for me to manipulate ceaselessly, sometimes at night and weekend, at an international research environment. I express my gratitude to Nick N. Brookes and Violetta Sessi of the ID08, Jörg Zegenhagen and Blanka Detlefs at the ID32, Gilles Renaud, Nils Blanc and Tao Zhou at the BM32. Thanks to Violetta for confiding with me about the working environment at the ESRF, Jörg for his level-headed attitude during hard manipulation, Gilles and Nils for driving me home after over-late experiences at around 3 am, Tao for exchanging with me views on our future orientation. Above all, I have great times to work together the kindly and less-sleep experts in XMCD, XWS and GISXAS world-class unique instruments. The SOLEIL Synchrotron, I'm thankful to Philippe Ohresser who joined with us in three XMCD beamtimes including one at his beamline DEIMOS. He has a good sense of responsibility not only during the experiences but also in the discussion afterward. In addition, he nicely assisted me to evaluate the XMCD data with sum rules calculations. The NCEM, I'm grateful to Andreas Schmid and Alpha T. N'Diaye, their SPLEEM contribution and discussion are greatly important for the studies.

During the whole periods of a student far from home, I luckily get the continuous and, sometimes, silent supports of lots of friends in Việt Nam, in France and other places. As I have an occasion to name them, I thank, Quốc Huy, Công Thành, Quốc Bảo, Công Pháp, Đức Tùng, Minh Châu, Nhật Minh, Nhất Hải, Phương Quỳnh, Mạnh Hưng, Thuý Hiền, Văn Giang, Damien, Cléopold, Ngọc Duy, Duy Thao, Đạt Sơn, Văn Lượng, Xuân Quy, Thế Phương, Trọng Sơn, Thanh Trà, Văn Quốc, Văn Vĩ, Chí Bửu, Thanh Trung, Đức Dưỡng, Anh Vũ, Hạ Thi, Xuân Hoà, Quang Nhật, Kim Trâm, Linda, Thị Thuý, Trâm Hiền, Kiều Giang, Quỳnh Phương, Thanh Thu, Tấn Luận, Ái Diệp, Phúc Thành, Thu Thảo, Thu Hồng, Thu Trang, Thu Trang, Hạnh Trang, Phương Trà... Either with the same point of view or not, but you always give the right encouragement. Especially, I express my gratitude to Thu Nhi and Hải Vân as sisterliness for her encouraging and to Thanh Quang, my fatherlike friend who gives me the helpful advices and orients me for my carriers in future as my expectation. Thank you all very much!

Deeply from my heart, I acknowledge the motivative and speechless supports from my parents, my young sister and my young brothers in Đà Nẵng and my grand family in Quảng Nam, Việt Nam. Thanks you for steadily speeding me up, for such long time since I was born!

Thương yêu dành tặng Ba Má và các Em!

Résumé

Graphène est un candidat pour la préparation de dispositifs spintroniques de nouvelle génération tirant partie de sa grande longueur de diffusion de spin et de la grande mobilité de ses porteurs de charge. En interagissant avec matériau ferromagnétique, il pourrait en outre devenir un élément actif, comme le suggèrent des études récentes par physique des surfaces, qui mettent en évidence un moment magnétique de quelques fractions de magnéton de Bohr dans le graphène en contact avec du fer, et une séparation en spin des bandes électroniques du graphène, d'environ 10 meV, par un effet Rashba au contact d'un élément de grand numéro atomique (l'or). La façon dont le graphène peut influencer les propriétés, par exemple magnétiques, des matériaux qui y sont contactés, reste peu étudiée. Les systèmes hybrides de haute qualité, constitués de graphène en contact avec des couches minces magnétiques ou des plots de taille nanométrique, sont des terrains de jeu pour explorer les deux aspects, la manipulation des propriétés du graphène par son interaction avec d'autres espèces, et vice versa. Dans le graphène contacté à des couches magnétiques ultra-minces par exemple, de forts effets d'interface pourraient être exploités pour contrôler l'aimantation du matériau magnétique. L'auto-organisation quasi-parfaite récemment découverte pour des plots nanométriques sur graphène, pourrait permettre d'explorer les interactions magnétiques, potentiellement transmises par le graphène, entre plots.

Trois systèmes hybrides de haute qualité, intégrant du graphène préparé par dépôt chimique en phase vapeur sur le surface (111) de l'iridium, ont été développés sous ultra-haut vide (UHV) : des films ultra-minces de cobalt déposés sur graphène, et intercalés à température modérée entre graphène et son substrat, ainsi que des plots nanométriques riches-Co et -Fe, organisés avec une période de 2.5 nm sur le moiré entre graphène et Ir(111). Auparavant, des films de 10 nm d'Ir(111), monocristallins, déposés sur saphir, ont été développés. Ces films ont été par la suite utilisés comme substrats en remplacement de monocristaux massifs d'Ir(111). Ces nouveaux substrats ont ouvert la voie à des caractérisations multi-techniques ex situ, peu utilisées jusqu'alors pour étudier les systèmes graphène/métaux préparés sous UHV.

Au moyen d'une combinaison de techniques de surface in situ et de sondes ex situ, les propriétés structurales, vibrationnelles, électroniques et magnétiques des trois nouveaux systèmes hybrides ont été caractérisées et confrontées à des calculs ab initio. Un certain nombre de propriétés remarquables ont été mises en évidence. L'interface entre graphene et cobalt implique de fortes interactions C-Co qui conduisent à une forte anisotropie magnétique d'interface, capable de pousser l'aimantation hors de la surface d'un film ultra-mince en dépit de la forte anisotropie de forme dans ces films. Cet effet est optimum dans les systèmes obtenus par intercalation entre graphène et iridium, qui sont par ailleurs naturellement protégés des pollutions de l'air. Les plots nanométriques, au contraire, semblent peu interagit avec le graphène. Des plots comprenant environ 30 atomes restent superparamagnétiques à 10 K, n'ont pas d'anisotropie magnétique, et leur aimantation est difficile à saturer, même sous 5 T. D'autre part, la taille des domaines magnétiques semble dépasser celle d'un plot unique, ce qui pourrait être le signe d'interactions magnétiques entre plots.

Mots-clés: graphène, moiré, auto-organisation, plots, intercalation, couche mince, anisotropie magnétique perpendiculaire.

Abstract

Graphene is a candidate for next generation spintronics devices exploiting its long spin transport length and high carrier mobility. Besides, when put in interaction with a ferromagnet, it may become an active building block, as suggested by recent surface science studies revealing few tenth of a Bohr magneton magnetic moments held by carbon atoms in graphene on iron, and a Rashba spin-orbit splitting reaching about 10 meV in graphene on a high atomic number element such as gold. The extent to which graphene may influence the properties, e.g. magnetic ones, of the materials contacted to it was barely addressed thus far. High quality hybrid systems composed of graphene in contact with magnetic thin layers or nanoclusters are playgrounds for exploring both aspects, the manipulation of the properties of graphene by interaction with other species, and vice versa. In graphene contacted to ultra-thin ferromagnetic layers for instance, strong graphene/ferromagnet interface effects could be employed in the view of manipulating the magnetization in the ferromagnet. The recently discovered close-to-perfect self-organization of nanoclusters on graphene, provides a way to probe magnetic interaction between clusters, possibly mediated by graphene.

Three high quality hybrid systems relying on graphene prepared by chemical vapor deposition on the (111) surface of iridium have been developed under ultra-high vacuum (UHV): cobalt ultra-thin and flat films deposited on top of graphene, and intercalated at moderate temperature between graphene and its substrate, and self-organized cobalt- and iron-rich nanoclusters on the 2.5 nm-periodicity moiré between graphene and Ir(111). Prior to these systems, 10 nm-thick Ir(111) single-crystal thin films on sapphire were developed: they were latter employed as a substrate replacing bulk Ir(111) single-crystals usually employed. This new substrate opens the route to multi-technique characterizations, especially ex situ ones which were little employed thus far for studying graphene/metal systems prepared under UHV.

Using a combination of in situ surface science techniques (scanning tunneling microscopy, x-ray magnetic circular dichroism, spin-polarized low-energy electron microscopy, auger electron spectroscopy, reflection high-energy electron diffraction) and ex situ probes (x-ray diffraction, transmission electron microscopy, Raman spectroscopy, MOKE magnetometry) the structural, vibrational, electronic, and magnetic properties of the three new graphene hybrid systems were characterized and confronted to first-principle calculations. Several striking features were unveiled. The interface between graphene and cobalt involves strong C-Co interactions which are responsible for a large interface magnetic anisotropy, capable of driving the magnetization out-of-the plane of the surface of an ultra-thin film in spite of the strong shape anisotropy in such films. The effect is maximized in the system obtained by intercalation between graphene and iridium, which comes naturally air-protected. Nanoclusters, on the contrary, seem to weakly interact with graphene. Small ones, comprising ca. 30 atoms each, remain super paramagnetic at 10 K, have no magnetic anisotropy, and it turns out difficult, even with 5 T fields to saturate their magnetization. Besides, the magnetic domains size seem to exceed the size of a single cluster, possibly pointing to magnetic interactions between clusters.

Keywords: graphene, moiré, self-organization, clusters, thin film, intercalation, perpendicular magnetic anisotropy.

Contents

Introduction

The electronic structure of graphene, an atomic two-dimensional crystal of honeycomb structure, has been predicted about half a century ago. Graphene has now been synthesized, observed and investigated experimentally. It waited for such a long period until the technology of experimental instruments allowing us to detect its peculiar properties, for instance, transport properties based on its massless Dirac fermions. In addition, graphene is known as a material with the best mechanic property, and high quality in electrical and thermal conductivity. Nowadays, graphene is considered as a material with high potential thanks to these characterizations, both for fundamental physics and promising applications. Therefore, graphene more and more attracts attention for enhancing its properties, and also has triggered commercial activity for realizing its applications. Graphene has been predicted to take niche applications in replacement of of silicon in future technology. With such high interest, graphene was the focus of the 2010 Nobel's prize in Physics.

One year before the Nobel's prize was honoured to the graphene's producers and investigators, A. Geims and K. S. Novoselov, the study of graphene-based systems reported in this PhD thesis had started. Hence, in the context of increasing interest in many fields of research, graphene is considered as interesting materials for new research and applications in magnetism and spintronics. For instance, graphene is attractive in spintronics thank to its electric-field-controlled conductivity, its expected long spin lifetime and its two-dimensional nature.

The potential huge surface-area ratio of sp^2-hybridized carbon has long been acknowledged to be a valuable feature for taking benefit of large interface effects in hybrid systems. Rechargeable batteries provide a telling example, from traditional graphite-based ones [1] to advanced graphene—titanium oxide hybrid systems combining the high conductivity of graphene and the Li-insertion/extraction the high capacity of TiO_2 nanoparticles [2]. So far, most graphene-based hybrids have been developed using chemical routes. This holds strong applicative potential and has already yielded a wealth of multifunctional systems [3]. These systems involve graphene randomly structured at the nanoscale thanks to top-down preparation method.

The term hybrid was also employed for a new class of materials, composed of high-quality graphene, in contact with materials with intrinsically different physical properties. In such systems, the intrinsic properties of purely single-layer graphene can be exploited or manipulated. Superconductivity was, for instance, induced in graphene by proximity with Sn dots [4], and graphene was made semiconductor by aryl groups grafting [5]. Graphene—metal hybrid systems are also investigated for spintronics. Net magnetic moments in carbon, of 0.05 to 0.1 μ_B and 0.25 μ_B, were, for instance, estimated in Ni- and in Fe-contacted graphene, respectively [6, 7]. This holds promise for spin-polarized electrons flowing in carbon channels. Spin-splitting of graphene bands at the Fermi level was, however, not found in graphene contacted with transition-metal ferromagnets [8]. Only in graphene in contact with high-atomic mass metals could such a splitting of 10 meV be observed [9]. Magnetic tunnel junctions based on graphene sandwiched

between two ferromagnets are another filed of application of graphene hybrid systems, having such desirable characteristics as low resistance-area product and high magneto-resistance [10].

The properties of the ferromagnetic metal may also be noticeably modified by the graphene/ ferromagnet interface. A noticeable effort is focused at theory level on understanding the magnetic properties and role of graphene in hybrid systems with the presence of transition metals like Fe, Co, or Ni. For example, the graphene-mediated exchange interaction between adatoms or impurities each holding a net magnetic moment has been explored and unconventional scaling with distance has been anticipated [11]. Also, magnetic anisotropies as high as required for room-temperature magnetic storage have been predicted for Co dimers [12]. So far, experimentalists investigated simpler systems, most prominently the interface between a ferromagnetic layer and graphene. These are indispensable for basic information on proximity-induced magnetic moments in carbon or the graphene/Co magnetic anisotropy. We investigated hybrid system consisting of graphene in contact with magnetic nanostructures, either nanoclusters and ultrathin films of Co.

Among the many preparation procedures of graphene, we employe the chemical vapour deposition of graphene on metal. We focus on Ir thin films and single crystal. With this method, we can easily control the quality of graphene by manipulating experimental condition during the growth, such as precursor pressure of surface temperature. The graphene quality is a key for the further growth of metal. For instance, whereas the intercalation mechanism is effective with the graphene with high density of defect, the self-organization of cluster need the perfect moiré pattern of graphene of high quality on metal. The metal is deposited by either pulsed-laser deposition forming extremely flat films down to only one atomic layer, or molecular beam epitaxy forming the clusters on graphene.

Numerous available *in situ* and *ex situ* characterization techniques allowed us to understand the structure as well as the magnetism of our systems. For instance, magneto-optical Kerr effect as *ex situ* technique allowed us to characterize the magnetic properties at room temperature. We used x-ray magnetic circular dichroism (XMCD), a powerful magnetic technique using synchrotron sources, which is sensitive to nanostructures and provides quantitative information about spin and orbital moments. We also performed spin-polarization low energy electron microscopy (SPLEEM) which is suitable for studying the magnetic behaviour of surfaces. The XMCD and SPLEEM were conducted in collaboration with expert users.

The main aspects of the PhD thesis have been: (i) develop a new procedure of graphene growth on thin Ir(111); investigate the properties of three systems based on epitaxial graphene on Ir(111); (ii) Au-capped Co ultrathin films on graphene, (iii) graphene-capped Co ultra-thin films, and studied their structural and magnetic properties and (iv) assemblies of equally sized Fe, Co, or Ni clusters comprising 10–10^3 atoms, which are well adapted to the study of the size-dependent magnetic properties.

The first system consists of chemical vapour graphene on a thin film of Ir(111). The Ir single crystal films were prepared on pieces of sapphire wafers. Then, graphene was prepared by chemical vapour deposition. Structural characterizations were conducted with the help of *in situ* scanning tunnelling microscopy and reflection of high energy electron diffraction, as well as with *ex situ* high resolution transmission electron microscopy, x-ray diffraction and Raman spectroscopy. We obtained a single crystalline Ir(111) surface for the film's thickness of 8–10 nm. The surface quality is as high as that of single crystals, i.e., suitable for the growth of high-quality graphene. Together with *in situ* characterization, Raman spectra reveal on a monolayer of μm-scale graphene. Our results provide a versatile procedure for large area fabrication of high-quality graphene.

The second system consists of Co thin films grown on graphene/Ir(111) by pulsed laser deposition. We found that pulsed-laser deposition, unlike metal evaporation, yields smooth epitaxial Co thin films, which are characterized by extended, atomically flat terraces. Using ex situ focused magnetic-optical Kerr effect microscopy and magnetometry, and extraordinary Hall effect measurements, we probed the magnetic properties of the Au-capped Co thin films at room temperature. These display perpendicular magnetic anisotropy in the thickness range of 0.65–1.30 nm. Spin-polarized first-principles calculations suggest that the origin of perpendicular magnetization is the hybridization between Co and C orbitals at the Co/graphene interface. X-ray magnetic circular dichrosim revealed the possibility of the intercalation of the thin film underneath graphene or diffusion of carbon atoms into the Cobalt films because graphene may be damaged by the high energy of pulsed-laser species. The low coercive field, of the order of a few mT is consistent with the fact that magnetization reversal proceeds by the nucleation of a few reversed domains at defects of the film. Perpendicular magnetic anisotropy, epitaxy and ultra-small thickness bring new perspectives on graphene based spintronic direction, band matching between electrodes and graphene, and interface phenomena such as the Rashba effect.

The third system consists of ultra-thin Co films between graphene and the Ir substrate. The thin films were grown beforehand by molecular beam evaporattion, and then intercalated between the graphene layer and Ir substrate via an annealing step at mild temperature, at which the smooth Co layer is obtained underneath graphene without dewetting nor diffusion within the Ir substrate. Together with scanning tunnelling microscopy, Raman spectroscopy, Auger spectroscopy, the structural and magnetic properties were mainly characterized by spin-polarized low energy electron microscopy technique. In this system, the graphene/Co interface clearly exhibits the perpendicular magnetic anisotropy thanks again to the hybridization between Co and C and the strain of the Co atomic layers. The system displayer PMA up to 13 monolayers of Co, i.e., 2.6 nm, much higher than many other systems.

The fourth system consists of clusters self-organized on epitaxial graphene, e.g., on Ir(111) using a graphene moiré as template. Following previous studies, the magnetic clusters are effectively self-organized via a seeding deposition on the graphene/metal moiré template. Surprisingly, in contradiction with previous prediction, the ordered clusters shown no magnetic anisotropy. The analysis of the superparamagnetic magnetization curves hint at non-linear arrangement of magnetic moment inside clusters and interaction between neighbouring clusters. Possible graphene damage during the characterization are reported due to the soft x-ray exposure.

The thesis is organized in two parts. I start by providing a background for the work, and present experimental methods (Part I) and then report our results and discussion during my PhD (Part II). A significant number of works are performed in collaboration with various groups at Institut Néel—France, Universität zu Köln—Germany, the European Synchrotron Radiation Facility (ESRF)—France, le Synchrotron SOLEIL—France, le Commissariat à l'énergie atomique et aux énergies alternatives (CEA)—France and the Lawrence Berkeley National Laboratory—USA.

Part I

BACKGROUND and METHODS

1

Graphene and epitaxial graphene in the view of nanomagnetism

Contents

This chapter introduces the different ingredients which will be manipulated in this thesis. I will first present from a rather general perspective the material "graphene" and its unique properties, emphasizing those which will be of special relevance latter in this manuscript but also highlighting some which made him so quickly a material of prime importance in nowadays condensed matter Physics. Special attention will be paid to graphene preparation on metal surfaces and to the possible interplay of graphene with magnetic moments. An extended discussion about low dimensional magnetism will then allow shedding light on the objectives of the present work: developing and exploring novel ferromagnet-graphene systems.

1.1 From the discovery of graphene to the 2010 Nobel prize in Physics

Carbon has undoubtedly been playing a central role in life of Earth, and has been accompanying in a significant part human civilizations. This low atomic number element, with $Z = 6$, has a $1s^2 2s^2 2p^2$ ground state electronic configuration. It comprises four valence electrons and follows the octet rule when forming four bonds with other atoms. The hybridization theory predicts various bond geometric configurations depending on the number of neighbor atoms with which it forms bonds. Carbon can adopt sp, sp^2, and sp^3 hybridizations, in which the $2s$ orbitals hybridize with one, two, or three of $2p$ orbitals ($2p_x$, $2p_y$, $2p_z$). In a sp hybridization the C atoms are included in linear fragments in which C forms a triple bond with one C and a single one with another C atome, like is the case in alkynes. In a sp^2 hybridization C atoms are in trigonal planar geometry, for instance forming one double bond with one C atom and a single one with another C atom in an alcene. In a sp^3 hybridization C atoms are in a tetragonal geometry, forming only single bonds with other atoms. The bond energies increase from single to triple bonds while their length decrease in this sequence [13].

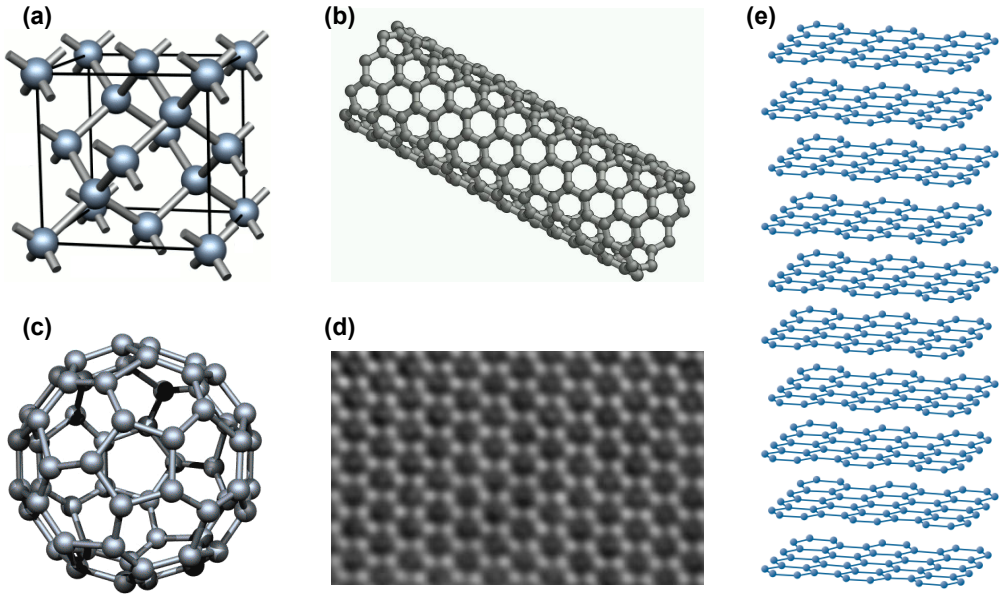

Figure 1.1: Popular carbon allotropes: (a) 3D diamond crystal, (b) 1D carbon nanotubes (c) 0D fullerene, (d) HRTEM of 2D graphene [14] (d) 2D graphite, stacking of numerous graphene layers [15].

Carbon exists in nature under many forms, with different hybridizations, degrees of crystallinity, and dimensions. A very precious form is its three-dimensional (3D), sp^3-hybridized, fully crystalline one, diamond [figure 1.1(a)]. Graphite, the sp^2 crystalline 3D form [figure 1.1(e) is the thermodynamically stable one at ambiant conditions, and has been employed by humans since antiques, for instance in painting decoration of pottery from from 4^{th} millennium B.C [16], or mixed with clay for our familiar handy pencils from the 17^{th} century. More recently, low-dimensional forms have attracted considerable attention for both fundamental and applied research prospects. Zero-dimensional (0D) buckminster C_{60} fullerenes [figure 1.1(c)] were discov-

ered in 1985 by Kroto et al. [17] and their promising applications in materials science, electronics and nanotechnology where highlighted by the 1996 Nobel Price in Chemistry. The discovery of one-dimensional (1D) carbon nanotubes [figure 1.1(b)] is usually associated to Iijima et al. in 1991 [18], and thought this contribution is a central one, it is interesting to note that Radushkevich and Lukyanovich had published the first images of this form of C 40 years before [19]. Probably to an even larger extent than the fullerenes, carbon nanotubes have been considered in a broad range of applications. The most recently isolated form of carbon probably is graphene [20], which was given this name by Boehm in 1962 [21]. Pioneering experiments on these two-dimensional (2D) form of carbon, which can be seen as the mother of all other sp^2 hybridized crystalline forms (graphite, fullerenes, nanotubes, see figure 1.1(b–e)), were awarded what is probably one of the most controversial Nobel Prices in Physics, in 2010, to Andre Geim and Konstantin Novoselov.

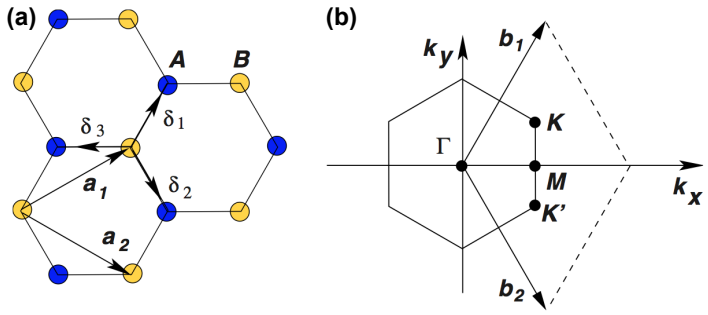

Figure 1.2: (a) Honeycomb lattice structure of graphene, made out of two triangular sub-lattices: $\mathbf{a}_1$ and $\mathbf{a}_2$ are unit vectors of the triangular Bravais lattice and δ_1, δ_2 and δ_3 connect nearest-neighbour carbon atoms, separated by a distance $a = 0.142$ nm. (b) Corresponding first Brillouin zone. The Dirac cones are located at the K and K' points [22].

The atomic structure of graphene consists of two triangular carbon sublattices, named A and B in figure 1.2(a) and in the following of this manuscript, shifted by 0.142 nm (the C-C nearest neighbor distance) 30° off the highest symmetry direction of, *e.g.* the A sub-lattice. The reciprocal lattice is characterized by hexagonal Brillouin zones, the borders of the first one being sketched in figure 1.2(b).

Along with graphene, other 2D materials, for instance $Bi_2Sr_2CaCu_2O_x$, $NbSe_2$, BN, MoS_2 [24], Bi_2Te_3 [25], silicene (silicon atoms arranged in a honeycomb lattice) [26, 27], have also been reported. In the last two years they have attracted increasing importance, with the motivation that unique properties usually emerge in ultimately thin materials. For instance, molybdenum disulfide is a an indirect bandgap semiconductor in the bulk becoming a direct bandgap one when thinned down to a single layer [figure 1.3] [23].

In the following of this section, I will discuss the unique electronic properties of graphene, which have stimulated considerable effort worldwide since 2004. I will then briefly review the methods for preparing graphene, with of focus on those methods producing high quality samples. Finally, I will give an overview on some promising application based on the unusual properties of graphene.

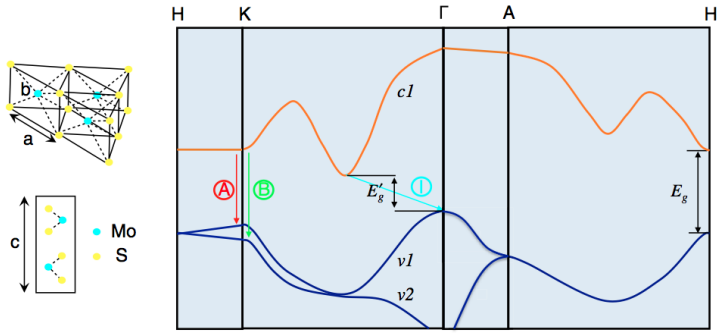

Figure 1.3: An example of 2D material: Lattice structure of MoS_2 in both the in- and out-of-plane directions and simplified band structure of bulk MoS_2, showing the lowest conduction band $c1$ and the highest split valence bands $v1$ and $v2$. A and B are the direct-gap transitions, and I is the indirect-gap transition. E'_g is the indirect gap for the bulk, and E_g is the direct gap for the monolayer [23].

1.1.1 Electrons and holes mimicking chiral massless Dirac fermions in graphene

Historically, graphene's electronic properties have been calculated as a step towards the calculation of the more complex, 3D, band structure of graphite. This was done using a tight-binding method in 1947 [28], i.e., well before any experimental observation could corroborate the result. In his calculation, Wallace considered excluded the three valence electrons involved in the formation of the C—C bonds and considered the remaining electron, occupying the $2p_z$ orbital, involved in electronic conduction in the system. He then considered an electronic wave-function being a linear combination of two electronic waves, one living in the A C sublattice, the other in the B sublattice. Neglecting the overlap of the $2p_z$ orbital centered on different atoms, and considering only interactions between nearest neighbors in the lattice, he derived a dispersion energy (E)—wave-vector (k) relationship which can be approximated to

$$E = \hbar k v_{\mathrm{F}} \tag{1.1}$$

in an E range of ± 0.5 eV about the point where the valence and conduction bands touch, the so-call Dirac point.

The low-energy electronic band structure of graphene is thus conical, with two inverted cones (one for the valence band, the other for the conduction band) meeting right at the Fermi level, accounting for the fact that graphene is half-filled with conduction electrons (each C atom brings one conduction electron). This happens at the six corners of the Brillouin zone, at the inequivalent, i.e., so-called K and K' points [figure 1.4]. The peculiar conical dispersion, together with the construction of the electronic wave-function in the base of the A and B sub-lattices, is often made explicit by re-writing the Hamiltonian of the system with the help of Pauli matrices ($\boldsymbol{\sigma} = (\sigma_{\mathrm{x}}, \sigma_{\mathrm{y}})$), in the form [29, 30, 31]:

$$\hat{H} = -\mathrm{i}\hbar v_{\mathrm{F}} \sigma \cdot \boldsymbol{\nabla} \tag{1.2}$$

, and the same holds for holes. This is characteristic of Dirac fermions, interconnected to holes, which would have a spin described by σ and a linear energy—momentum relationship, i.e., massless, with a velocity v_{F}. As noticed before σ does not refer to an actual spin, but rather to a pseudospin, describing the components of the electronic wave-function on each of the A and

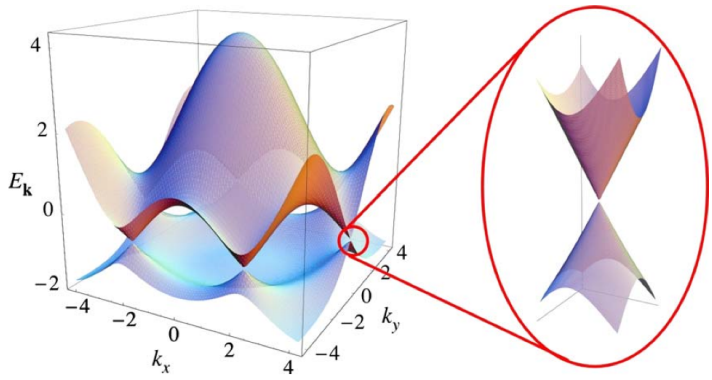

Figure 1.4: Electronic bands obtained from the tight-binding model with nearest-neighbour hopping. The valence band touches the conduction band at the two inequivalent Brillouin zone conners K and K'. For undoped graphene, the Fermi energy lies precisely at the contact points, and the band dispersion in the vicinity of these points is conical. Inset: Dirac cone at K point [22].

B sublattices. The pseudospin is often accounted for under the notion of chirality, formally the projection of the pseudospin along the direction of motion. The value of v_{F} is ca. 300 times smaller than the speed of light. Overall, electrons and holes in graphene mimik massless chiral Dirac fermions. This has stimulated the proposition of condensed matter experiments addressing phenomena previously only accessible in high energy particle accelerators where Dirac fermions are more commonly encountered. For instance, Klein tunneling, i.e. the total transparency of an energy barrier to chiral massless Dirac fermions impinging it in normal incidence was proposed to become accessible in graphene devices (while inaccessible in high energy Physics experiments) [32], and was actually observed soon after [33, 34].

The investigation of the unique electronic properties of graphene started with magneto-transport experiments [36, 37, 38]. In these experiments graphene samples are flown by an electric current and their resistance perpendicular and parallel to the current were measured as a function of a back-gate potential, under a magnetic field B [figure 1.5(a)]. Large potential gradients are found around the edges of the samples and around charged impurities. There, due to the presence of the magnetic field, electrons follow cycloid trajectories along equipotential lines, in a semi-classical picture. Their energy is quantified and they form a quantum states, which is delocalized along the edges of the samples and localized around charged impurities, named integer quantum Hall state (IQHS, see lecture note of Goerbig in [39] for a pedagogical review). The IQHS consists in a series of maxima in the electronic density of states (DOS) which are known as Landau levels and vanish at vanishing magnetic field. These Landau levels can be populated either by increasing the charge density (by increasing the back-gate voltage) at fixed magnetic field, or at a fixed charge density, by increasing the number of accessible levels, i.e., by increasing the magnetic field. Using simple dimensional analysis arguments, the cyclotron frequency in graphene is defined as the ratio between the Fermi velocity and magnetic length, $l_B = \sqrt{\hbar/(eB)}$, $\omega_{\mathrm{C}} = \sqrt{2}v_{\mathrm{F}}/l_B$. This allows to qualitatively understand the conclusion, obtained in a rigorous quantum electrodynamics approach [31, 40], that the spacing between Landau levels scales like $\sqrt{B}$, while in a usual two-dimensional electron gas (2DEG) the scaling law is B [22]. The measurement of a $\sqrt{B}$ sequence of Landau levels and the occurrence of a

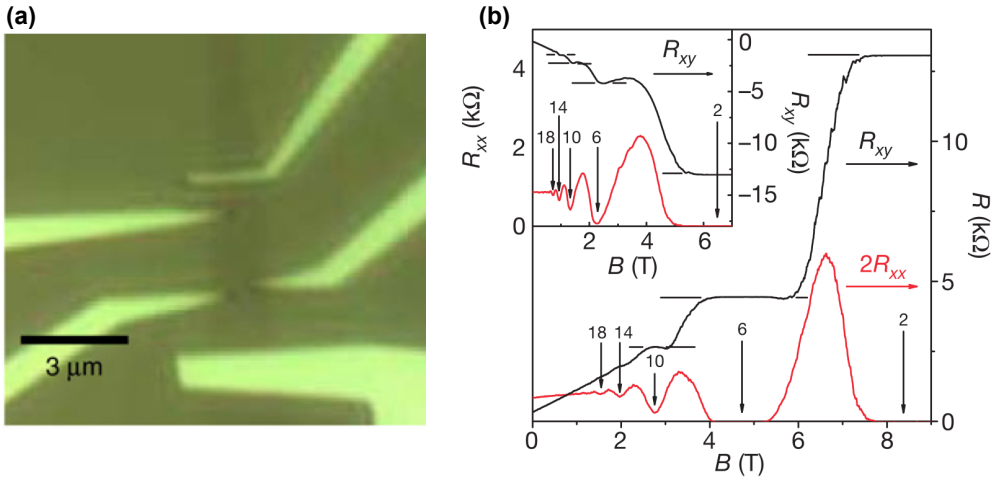

Figure 1.5: (a) Optical microscope image of naturally Hall bar shaped graphene devices. (b) Quantized magnetoresistance (red) and Hall resistance measured in the device in (a) at $T = 30$ mK and $V_g = 15$ V. The vertical arrows and the numbers of them indicate the values of B and the corresponding filling factor v of the quantum Hall states. The horizontal lines correspond to h/e^2v values. The QHE in the electron gas is shown by at least two quantized plateaux in R_{xy}, with vanishing R_{xx} in the corresponding magnetic field regime. The inset shows the QHE for a hole gas at $V_g = -4$ V, measured at 1.6 K. The quantized plateau for filling factor $v = 2$ is well defined, and the second and third plateaux with $v = 6$ and $v = 10$ are also resolved [35].

zero-energy level [36, 37, 38] provided the first evidence of electrons behaving like massless chiral Dirac fermions. The corresponding IQHS is often referred to anomalous or relativistic.

A remarkable feature of the IQHS in graphene is that it survives at temperatures well above those needed in other 2DEG, up to room temperature. This is consistent with the very high values of the cylcotron frequency in graphene, which writes very differently than in other systems. For instance, for a 10 T magnetic field, the cyclotron energy is of the order of 1000 K in graphene and of 10 K in other typical 2DEG [22]. Besides, in ultra-clean graphene samples, i.e., suspended graphene [41] or graphene on graphite [42], the contribution of charge impurities is so marginal, and the broadening of the Landau levels which the localized states around these defects so small, that IQHS have been observed in graphene with fields as low as a few 10 mT. For these reasons graphene is being considered has a possible system for metrology, which would allow to define the resistance quantum h/e^2 with unprecedented accuracy [43].

1.1.2 Graphene preparation

The preparation of graphene by mechanical exfoliation of graphite made graphene preparation accessible to every laboratory. The infatuation about graphene then stimulated both the development of new methods and the improvement of approaches which had been discovered long ago. There used to exist a tradeoff between high quality large area samples and production cost, which guided the choice of the preparation method with the view of applications and fundamental research. Here I briefly describe a few preparation routes: mechanical exfoliation, epitaxial growth on SiC and metals, and a popular chemical approach, the reduction of graphene oxide. Graphene preparation on metals will be reviewed in Section 1.4 of this Chapter.

Table 1.1: Comparison between graphene preparation methods in charge density mobility μ (cm^2 V^{-1} s^{-1}) at charge density n (cm^{-2}), size of single crystal grain d (μm), quality of graphene and the cost of in mass production. The value of epitaxial graphene on SiC given in C surface. Parameters updated in 01/2013.

Method	Sources	μ	n	d	Quality	Cost
Exfoliation	HOPG	10^6 [41]	$< 2 \times 10^{10}$	> 1000	high	high
Epitaxy/SiC	3C, 6H—SiC	2.7×10^4 [38]	few 10^{12}	50	medium	medium
CVD/metals	hydrocarbon	5×10^4 [44]	$< 5 \times 10^{11}$	2000 [45]	high	low
Reduction of GO	HOPG	39 [46]	n-doped	~ 100 [47]	low	low

Starting from ca. 2000, a number of research groups worldwide was aiming at isolating graphene from the peeling off graphite [48, 49]. In 2004, a surprisingly simple method was reported, consisting in repeatedly exfoliating smaller and smaller graphite crystals with commercial scotch tape, and eventually stamping the exfoliated graphite onto a piece of oxidized silicon wafer. Luckily, a simple optical interference effect between the silicon surface and the graphene flakes on top of the 300 nm-thick silicon oxide makes it possible to identify graphene single layer with the naked eye (and an optical microscope as well, thus) [20]. The method has been applied to other crystals [24]. Using this technique, graphene single crystal flakes of a few hundreds of micrometers can be obtained routinely. These high quality graphene samples come directly on a proper substrate, for instance for building up graphene-based transistors whose back-gate is the doped silicon wafer and which is contacted with electrodes on top by standard nanofabrication techniques. The quality of graphene prepared using this method is high, which can be quantified by the measure of the electrons' mobility μ and of their residual charge carrier density n. Highest quality samples can be obtained by suspending graphene and annealing it by flowing a current through it, yielding $\mu = 10^6$ $cm^2V^{-1}s^{-1}$ at $n < 2 \times 10^{10}$ cm^{-2} measured typically at room temperature (table 1.1). In such sample the purity is such that a very fragile quantum states, the fractional quantum Hall state, can be explored [50, 51]. As an alternative to the suspension of graphene, which poses severe constraints in terms of further nanofabrication and limits the extend to which the back-gate, and thus the charge carrier density, can be tuned, graphene has been deposited on substrates trapping much less charged impurities than SiO_2, few layer h-BN [52].

Epitaxial growth of graphene on silicon carbide under ultra-high vacuum (UHV) was reported decades ago [53, 54] and has been a parallel preparation route to exfoliation of graphite since 2004 [55]. The graphitization of SiC(0001) and $(000\bar{1})$ occurs at high temperature, typically above 1300 K, through the sublimation of Si. The process is rather complex, involving various surface reconstructions as the temperature increases [54, 56]. On SiC(0001), the first graphene layer is strongly coupled to SiC, and does not have typical electronic band structure of graphene [57]. It is usually called the before layer, and only the second layer exhibits similar properties as those of exfoliated graphene. The epitaxy between the various graphene planes and the SiC substrate is rather well-defined on this surface termination of SiC and the number of graphene layers is readily controlled. Under Ar, Si, or C atmospheres, the temperature at which graphene forms is increased (these atmospheres are thought to hinder the evaporation of Si), and high quality graphene can be obtained [58, 59, 60, 61, 62, 63, 64]. The mobility of such graphene is rather high, ca. 1000 cm^2 V^{-1} s^{-1} for a 10^{13} cm^{-2} residual charge carrier mobility at room

temperature. The anomalous IQHS has been studied in these samples [65, 66]. On the opposite face of SiC, controlling the number of graphene layers and orientation between layers is more difficult [54, 67]. The structure of the graphene layer forming at the interface with SiC($000\bar{1}$) is only partially known [68]. Single-layer high quality graphene can however be prepared on 4C–SiC($000\bar{1}$), which exhibits 15000 $cm^2V^{-1}s^{-1}$ for a 10^{12} cm^{-2} residual charge carrier mobility [69].

The growth of thick graphite layers on metals during high temperature treatments, Kish graphite, is a well-known by-product of steal making processes. The preparation of multilayer (and possibly, also of single-layer) graphene on metals has been explored from the 1960's, using solid carbon [70] and gaseous hydrocarbon [71] sources decomposed at the hot surface of various transition metals. Depending on the carbon solubility in the metal and propension of the metal to form carbides, various graphene growth processes can occur, which we will discuss latter in this chapter. In the literature however, graphene growth on metals is usually referred to under the generic name of chemical vapor deposition (CVD). Until 2008, most developments about CVD of graphene were conducted under UHV environments, where ultra-high quality could be obtained [72, 73]. In 2009, few-layer graphene prepared on Ni in standard low-pressure reactors, i.e., close to atmospheric pressure, was transfered to a variety of supports using a process which had been developed decades ago [74], by dissolution of the metal supporting graphene, and its electronic and optical properties were studied [75]. A few months later, the same process was conducted with graphene prepared on Cu, onto which the growth is restricted to a single layer [76]. This stimulated considerable materials research effort worldwide, allowing to prepare meter-scale single layer graphene [77], millimiter-scale single-crystalline graphene [45], and ultra-high quality graphene having performances as good as those of exfoliated graphene [44].

To prevent the transfer step which inevitably induces defects in graphene, graphene may be directly prepared onto a variety of substrates by molecular beam epitaxy or CVD. Besides SiC, which is expensive especially in its non-doped form, mica [78], MgO [79, 80], h-BN [81, 82] substrates have been considered. The quality of graphene on these substrates is however thus far poorly characterized.

The lower-cost and higher-yield approach to the preparation of graphene is certainly a chemical route, consisting in the oxidation of graphite, for instance according to the Hummers method and derivatives, and sonication, followed by the reduction of the resulting graphene oxide [83, 84]. In graphite oxide, the presence of oxygen-containing functional groups on the graphene sheets makes them strongly hydrophilic, which eases their splitting and dispersion in water with the help of ultrasonic treatment [85, 86, 87]. The improvement of the reduction process, with the view of making it more efficient,i.e., leaving less functional groups in graphene) and more environmentally friendly is an important matter.

1.1.3 A partial overview on graphene's potential applications

Ten years only after its isolation graphene is being considered in numerous applications [figure 1.1.3] [88]. These would take benefit of the material's unique properties, to name only a few, the unprecedented mobility of its charge carriers at room temperature, its chemical inertness, its record mechanical strength and stretchability [89], its unrivaled heat conduction [90], its biocompatibility. Some of these potential applications are briefly discussed below.

conductive electrodes: Graphene has a 2.3% absorbance in the visible range [91] (which is considerable for a one-atom-thick material). Stacking of graphene layers with a number of layers such that the transmittance remains above 80% have an electrical resistance below that of

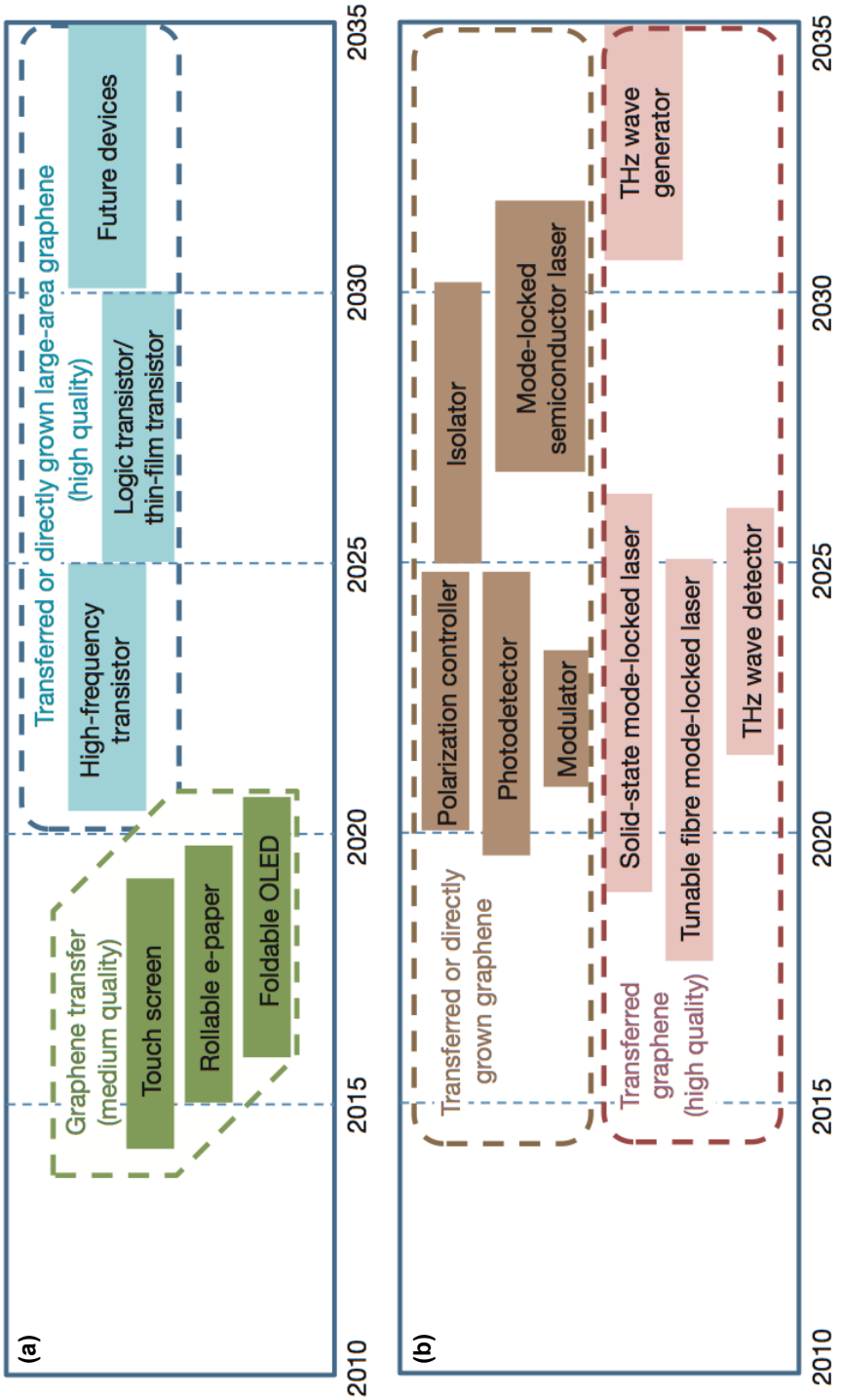

Figure 1.6: (a) Graphene-based display and electronic devices. Display applications are shown in green; electronic application are shown in blue. (b) Graphene-based photonics applications. Optical applications are shown in pink; optical interconnect applications are shown in brown. Possible application timeline, enabled by continued advances in graphene technologies, based on projections of products requiring advanced materials such as graphene. The figure gives an indication of when functional device prototype could be expected based on device roadmaps and the development schedules of industry leaders. [88]

indium tin oxide (ITO), the standard material in transparent conductive electrodes applications [92]. Being a good heat conductor is a decisive advantage of graphene in applications such as photovoltaics, in which heat must be efficiently evacuated. Moreover, as compared to ITO,

graphene has the potential of being much lower cost and much more environmentally friendly. It is also highly stretchable [93], which holds prospect for flexible devices. The issue of contacting graphene transparent conductive electrodes to metallic contacts is the main obstacle nowadays to the commercialization of graphene-based applications in this field.

Ultracapacitors: High performance energy storage systems must be able to store and relieve energy very quickly, to have a high capacity, and a long range life cycle. Highly porous and highly conductive materials are desirable for this purpose. Graphene prepared by chemical routes in principle offers such qualities. So far, the most performant graphene-based ultracapacitors use nitrogen-doped graphene prepared by a plasma process. They exhibit capacitances of 280 F/g and extremely high cycle life $> 2 \times 10^5$ [94]. Further improvements are expected as the surface area of graphene used in these applications will approach the limit value for purely single layer graphene, $2630 \mathrm{m}^2/\mathrm{g}$.

Radio frequency analog electronics: Graphene does not have an intrinsic band-gap in its electronic band structure which makes it unsuitable for logic electronics applications. A number of strategies is being considered for bypassing this limitation. The absence of a band-gap is not problematic for radio-frequency applications. Fast radio-frequency devices, such as needed for telecommunication purposes, operate in the 100 GHz to 1 THz regime. The cut-off frequency, which defines the accessible frequency range of a device, scales like the mobility of the conductive channel and inversely proportional to the width of the channel [95]. High performance graphene-based radio-frequency devices should then consist of high quality graphene shaped in the forms of thin channels. Few 100 GHz-cut-off frequency devices were accordingly prepared with few 1000 $\mathrm{cm}^2\mathrm{V}^{-1}\mathrm{s}^{-1}$ mobility (at room temperature) graphene (prepared on SiC or by CVD on metal) channels of ca. 100 nm width [96]. There is room for improvement: the best samples prepared by CVD have higher mobility and thinner devices could be prepared.

DNA translocation: One promising way to DNA translocation is the passage of DNA strands through nanopores and the measurement of electric signals associated to the interaction of every individual base with the nanopore edge. This requires (i) an impermeable membrane separating two differently charged solutions, the potential difference between the two solutions driving the passage of the charged DNA strand through the pore, (ii) nanopores having a diameter of the order of a DNA single strand "diamater" and a thickness at most equal to the distance between successive bases, (iii) a sufficient conductivity that the electric signal generated at the nanopore's edge can be collected with a remote electrode. Graphene in which nanopores have been engineered by ectron beam in principle offers all these qualities. Though the actual translocation of DNA with graphene was not yet proven, points (i) and (ii) were already addressed and confirm graphene's potential [97, 98].

1.2 Graphene and magnetism/spintronics

1.2.1 Spin transport in graphene

The spin-orbit interaction is a relativistic effect appearing when expressing the Dirac equation in the presence of the electron's spin [99]. It can be understood as the energy associated to the effect of a magnetic field, arising from the Lorentz transformation of the electric field generated by the nuclei (larger as the number of protons increases, i.e., for heavy atoms), in the rest-frame of the moving electron, on its magnetic spin. This energy thus scales like Z^4 and couples the spin and orbital moments of the electrons; due to the small Z of C, it is expected to be small in graphene. Using first principle calculations it was evaluated to be of the order of 0.01 K [100],

smaller than in carbon nanotubes in which the bending enhances spin-orbit effects, indeed a very small value four orders of magnitude smaller than in Si. Besides this relativistic effect, the spin of the electrons experiences the magnetic field induced by the moment held by the nuclei: this is the hyperfine interaction. Carbon being prominently composed of a zero-nuclei-moment isotope, C^{12}, this interaction only has a marginal role. Overall the electron spin in graphene experience little perturbations from the lattice and a spin-polarized current should travel long times (long spin life-time) before losing its polarization. Due to the high mobility of electrons in graphene, this should translate in large distances without loosing polarization, which is referred to as long spin-diffusion lengths. This property of graphene has stimulated large efforts in the view of efficient spin-transport devices, which could be easily build-up thanks to the 2D nature of graphene [figure 1.7], and which would have the potential of low-density, flexible, and biocompatible spintronics [101].

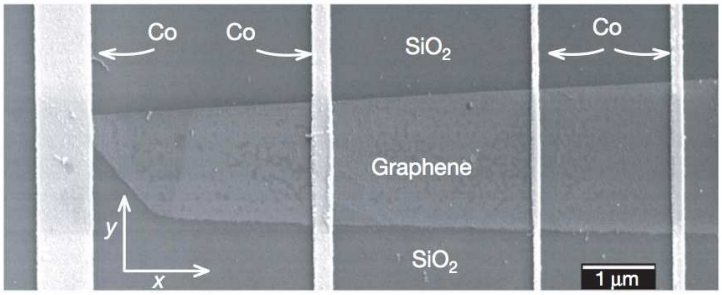

Figure 1.7: Scaning electron micrograph of a four-terminal single-layer graphene spin valve. Cobalt electrodes (Co) are evaporated across a Al_2O_3 (0.6 nm)/single-layer graphene stripe prepared on a SiO_2 surface. Al_2O_3 presents at a spin-dependent barrier which facilitates spin-injection between graphene and the electrodes [102]

.

In graphene contacted to two high resistance electrodes each composed of a Co deposit separated from graphene by an alumina high quality tunnel barrier, the measurement of the absolute magnetoresitance, which is the difference in resistance of the device, for Co electrodes with parallel and antiparallel magnetization, allows to determine the spin diffusion length [103] in the graphene channel. For graphene devices made of few-layer epitaxial graphene on $SiC(000\bar{1})$, values of the order of 100 μm were obtained at 2 K [104]. These are much larger than the values obtained previously in other graphene devices (see, e.g., [102]). Dlubak et al. suggest that the difference may be ascribed (i) to an overestimation of the quality of the alumina contacts in previous experiments, preventing a proper estimation of the spin diffusion length based on the resistance measurement, (ii) to the better isolation of graphene from sources of spin diffusion such as impurities and roughness in graphene flakes which are embedded in few layer graphene on SiC, as compared to graphene on SiO_2 [105].

1.2.2 Spin-filtering in graphene

The device discussed in the previous subsection is an example of a graphene-based spin-valve with a current-in-plane geometry. Spin information devices require a large absolute and relative magnetoresistance (the latter being normalized by the device resistance). While the first one is already ensured, the second one does not seem unrealistic with graphene. Indeed, with alumina

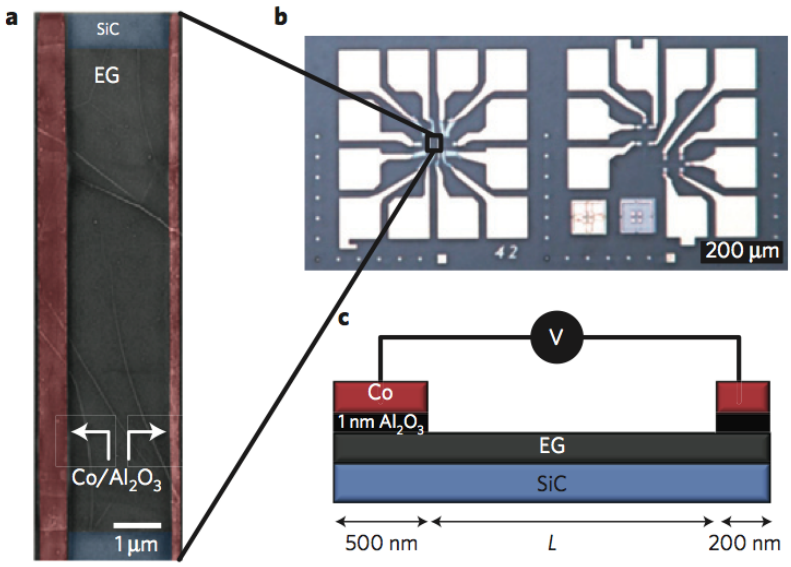

Figure 1.8: Devices patterned on epitaixal graphene: (a) Scanning electron micrograph of a two-terminal lateral spin valve with a distance $L = 2\mu$m between the Al_2O_3/Co electrnodes (coloured inred) deposited on the $w = 10$-μm-wide epitaxial graphene (EG) channel grown on the C face of the SiC substrate (coloured in blue). (b) Optical image of the set of two-terminal spintronics devices (left) and of a Hall bar device (right), both built on the same epitaxial graphene sheet. (c) Sketch representing the device geometry. [104]

barriers, close-to-10% values were obtained, already close to the optimal value [104]. Using MgO tunnel barriers instead of alumina could allow the realization of graphene-based spin-valves. For this to become possible, the issue of preparing high quality MgO barriers on graphene should be solved.

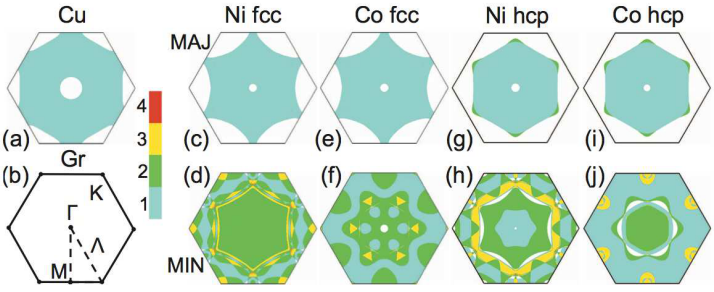

Figure 1.9: Fermi-surface projection onto close-packed planes for: (a) *fcc* Cu; (c) majority- and (d) minority-spin *fcc* Ni(111); (e) majority- and (f) minority-spin *fcc* Co(111); (g) majority- and (h) minority-spin *hcp* Ni(0001); (i) majority- and (j) minority-spin *hcp* Co(0001). For graphene and graphite, surfaces of constant energy are centered around the K point of the 2D interface Brillouin zone (b). The number of Fermi-surface sheets is given by the color bar. [106]

.

An alternative to spin-filtering with graphene is a current-perpendicular-to-the-plane geome-

try. Sandwiching graphene between two epitaxial pseudomorphic Ni(111) or Co(0001) electrodes was proposed for this purpose [107]. In such a device, the attractive property of graphene is not its long spin diffusion length, but the topology of its electronic band structure. The spin-polarization of the electron density of states in ferromagnetic Ni and Co translates into a two Fermi surfaces, one for the majority spin population, the other for the minority spin population, of which only the second one has some overlap with the Fermi surface of graphene [107] [figure 1.9]. Despite this only partial matching, tunneling through a single layer of graphene between the two ferromagnetic layers is expected, reducing the spin-filtering through the graphene barrier. Increasing the number of layers has been proposed as a way to suppress the tunnelling transport pathway. [figure 1.10]. An appealing property of such vertical spin-valves would be their low resistance-area ratio, allowing their miniaturisation and opening the way to high density magnetic storage [108].

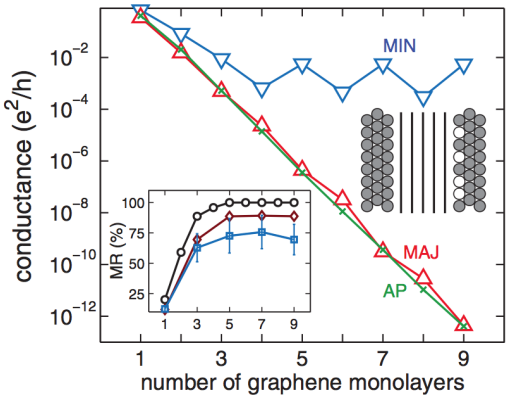

Figure 1.10: Conductances $G_{\mathrm{p}}^{\mathrm{min}}$ ($\bigtriangledown$), $G_{\mathrm{p}}^{\mathrm{maj}}$ ($\bigtriangleup$), and $G_{\mathrm{AP}}^{\sigma}(\times)$ of a Ni|graphene$_n$ |Ni junction as a function of the number of graphene layer n for ideal junctions. Inset: magnetoresistance as a function of n for: (circles) ideal junctions; (diamonds) Ni|graphene$_n$ |$Cu_{50}Ni_{50}$ |Ni junctions where the surface layer is a disordered alloy; (squares) Ni|graphene$_n$ |Ni junctions where the top layer sites occupied (sketch) [107].

$Ni_{0.9}Fe_{0.1}$ | graphene | Co stacks exhibiting 2% magnetoresistance were recently reported [109]. These devices are not however epitaxial and then do not take benefit of the above discussed effect. For realizing the initial proposal from Karpan et al., epitaxial growth seems the most relevant route. Graphene can be prepared in epitaxy on Ni(111) [110] and Co(0001 [111]. Growing flat ferromagnetic films on graphene is a more difficult task, due to the tendency of metals to form clusters on this material. Low temperature growth, or the use of deposition techniques like pulsed laser deposition which are known to favor the formation of flat films, are possible routes to avoid the clustering.

1.2.3 Spin-splitting in graphene

Above we have discussed the low intrinsic spin-orbit constant of graphene. A substantial spin-splitting may however be induced in graphene by extrinsic effect. Taking benefit of an electric field generated, rather than by the carbon atomic nuclei, by heavy atoms (Au) placed in the very vicinity of graphene, a strong Rashba effect was reported in graphene/Ni(111) with a Au single atomic layer intercalated between graphene and Ni(111)

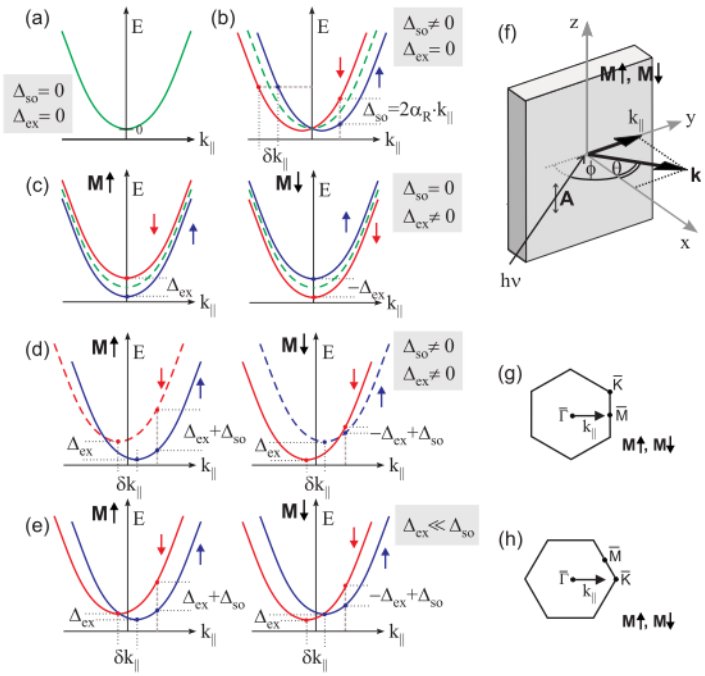

Figure 1.11: Behaviour of a (a) free-electron-like band with (b) Rashba effect, (c) ferromagnetic exchange, Rashba + exchange for (d) large and (e) small exchange splitting (where dashed band is absent in the case of 100% spin polarization). (f) Geometry of ARPES experimental setup and direction of $\mathbf{k}_\parallel$ within the Brillouin zone for (g) graphene/Ni(111) and (h) graphene/Co(0001). [8]

.

Stronger effects have been debated: a combination of an exchange interaction, associated to permanent magnetic moments in graphene [112], with the Rashba-extrinsic spin-orbit interaction was proposed as the origin for extremely large 5000 K spin-splitting reported in graphene/Ni(111) [110]. The two splittings should indeed sum up [113] [figure 1.11]:

$$\Delta_{\text{Rashba+exchange}} = \Delta_{\text{ex}} + \Delta_{\text{so}} = \Delta_{\text{ex}} + 2\alpha_{\text{R}} k_\parallel \tag{1.3}$$

, with k the electron's wave-vector and α_{R} the Rashba constant.

It was however latter argued that for such large splittings to be observed, significant Rashba effects should occur, at least much larger than those measurable in graphene/Ni(111) [8]. Thus far the question remains open why such strong effects could be observed.

1.2.4 Defect-induced magnetism in graphene

Like graphite, graphene is intrinsically diamagnetic [114], i.e., its atoms do no hold permanent magnetic moments. Imbalance in the number of atomic sites in a bipartite lattice such as graphene are known to yield zero-energy electronic states [115]. The mathematical demonstration of this effect is beyond the scope of this thesis. In undoped graphene, because of the electron-hole symmetry in this material, magnetic moments are expected in such states. It follows that permanent magnetic moments should be found for instance in graphene with atomic

defects such as single carbon atom vacancies [figure 1.12], or shaped in the forms of triangular nanoribbons. The magnetic moment can be estimated in a simple model assuming electron hoping between the different sites in graphene and an on-site potential (Hubbard model), using Lieb's theorem. According to this theorem the magnetic moment is half the imbalance in the number of atomic sites between the two sublattices. In the following, for the sake of briefness, we will only focus on the issue of single vacancy-induced magnetism, around which Lieb's theorem predicts a $\sim$1 μ_B magnetic moment.

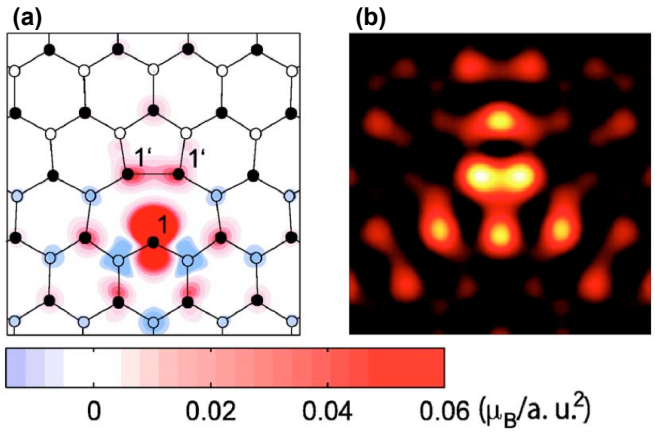

Figure 1.12: (a) Spin-density projection (in μ_B/a.u.^{2}) and (b) stimulated STM images on the graphene plane around the vacancy defect in the A sublattice. Carbon atoms corresponding to the A sublattice (○) and to the B sublattice (●) are distinguished. [116]

.

More advanced frameworks allow to refine the value of the single vacancy magnetic moment (see [117] for a partial review). At experimental level, vacancies are usually created in graphene and graphite by ion bombardment with $\sim$ 100 eV ions [118]. The electronic states of vacancies in graphene [119] and graphite [120, 121] have been studied with the help of scanning tunneling spectroscopy. It was found that these electronic states are sharp resonances located close to zero-energy (Fermi level). The study of the magnetic properties of graphene and graphene-like systems used to be much more controversial. Recently, graphene, available in sufficient quantity that it becomes suitable for SQUID measurements, and with such a purity that the presence of magnetic impurities can be rulled out, has become available. It is prepared by sonication of highly oriented pyrolitic graphite in various solvents. Clear evidence of paramagnetism as the vacancy density increases was found [122].

Beyond paramagnetism, ferromagnetism and antiferromagnetism have been scrutinized in graphene and graphene-like systems. As compared to paramagnetism, they require at least partial ordering of the magnetic moments around each defect. Such an ordering is to be mediated by the exchange interaction, also called Ruderman-Kittel-Kasuya-Yoshida (RKKY) interaction, which I will discuss in the subsection 1.2.5. A proper interaction between magnetic moments is not the only ingredient for observing ordered magnetic states at finite temperature. Indeed, the very weak spin-orbit interaction of carbon is not a priori compatible with the existence of a remanent state: a collective magnetic state in graphene and graphene-like systems should consist in a rapidly fluctuating global magnetization in the absence of external magnetic field. However, it has been argued that the presence of strains, of the interaction with a substrate, or of external

electric field, could stabilize a particular magnetization directions [123], and solutions are being proposed in order to enhance graphene's weak spin orbit interaction [124]. The prospect for magnetically ordered all-carbon systems is especially tantalizing with the view of spintronic and magnetic applications, e.g., low cost, light, and flexible ones, yet, the experimental observations remain extremely controversial. This is mainly due to the difficulty in ruling out magnetic impurities in the samples studied thus far. In this context, the reports for ferromagnetism in graphene systems, e.g., reduced graphene oxide [125, 126], graphene prepared by thermal exfoliation of graphene oxide [127], alteration of nanodiamond [128], arc discharge of graphite under hydrogen atmosphere [129], should be considered with caution and a critical perspective.

1.2.5 Ruderman-Kittel-Kasuya-Yoshida interaction on graphene

We turn to the discussion about the RKKY interaction in graphene. The unique electronic properties of graphene qualitatively modify the behavior known for this interaction in the case of metals. The RKKY interaction acts between two magnetic moments located on sites i and j, $\mathbf{S_i}$ and $\mathbf{S_j}$, through a coupling constant J_{ij}, which is proportional to the susceptibility: $\mathbf{S_i}$ polarizes the electronic bath between i and j, which itself interacts with $\mathbf{S_i}$, and vice versa. The form of the susceptibility depends on the nature of the i and j sites. As concerns the RKKY interaction, three kinds of sites are relevant: centers of hexagons (so-called plaquette position), carbon atoms of one sub-lattice, and carbon atoms of the other sub-lattice. The former case is relevant for magnetic atoms adsorbed on graphene, while the two others are typical binding sites for hydrogen atoms bond to graphene (also expected to be a source of magnetism in graphene) and the location of single atom vacancies.

The derivation of the susceptibility can be conducted in a tight binding framework by calculating a Fourier transform, thus implying the calculation of an integral over q, the momentum of the π electrons with respect to the Dirac point. Problematic is the fact that this integral gives strong weight to large q values, i.e., which do not correspond to the range in which electrons in graphene behave like chiral massless Dirac fermions anymore. Accordingly a cut-off must be imposed to the integral, but the use of a sharp one turns out problematic, yielding divergence and artificial oscillations of the susceptibility with q. Instead a smooth cut-off must be employed [130], which however is only partly satisfactory, the choice of the cut-off function being guided by mathematical rather than physical considerations. An alternative approach, based on Green's functions, allows to bypass these issues [131]. Using this latter approach it was found, for the Fermi energy at the location of the Dirac point, that:

- for $\mathbf{S_{i,j}}$ on the same carbon sub-lattice A,

$$J_{\mathrm{AA}} = -\frac{9\lambda\hbar^2}{257\pi t}\frac{1+\cos\left(\mathbf{K}-\mathbf{K}'\right)\cdot\mathbf{R}}{(R/a)^3} \tag{1.4}$$

- for $\mathbf{S_{i,j}}$ on different carbon sub-lattices A, B,

$$J_{\mathrm{BA}} = \frac{27\lambda\hbar^2}{257\pi t}\frac{1+\cos\left(\mathbf{K}-\mathbf{K}'\right)\cdot\mathbf{R}+\pi-\mathbf{2}\theta_{\mathbf{R}}}{(R/a)^3} \tag{1.5}$$

- for $\mathbf{S_{i,j}}$ on two plaquettes,

$$J_{\mathrm{plaq}} = \frac{324\lambda\hbar^2}{257\pi t}\frac{1}{(R/a)^3} \tag{1.6}$$

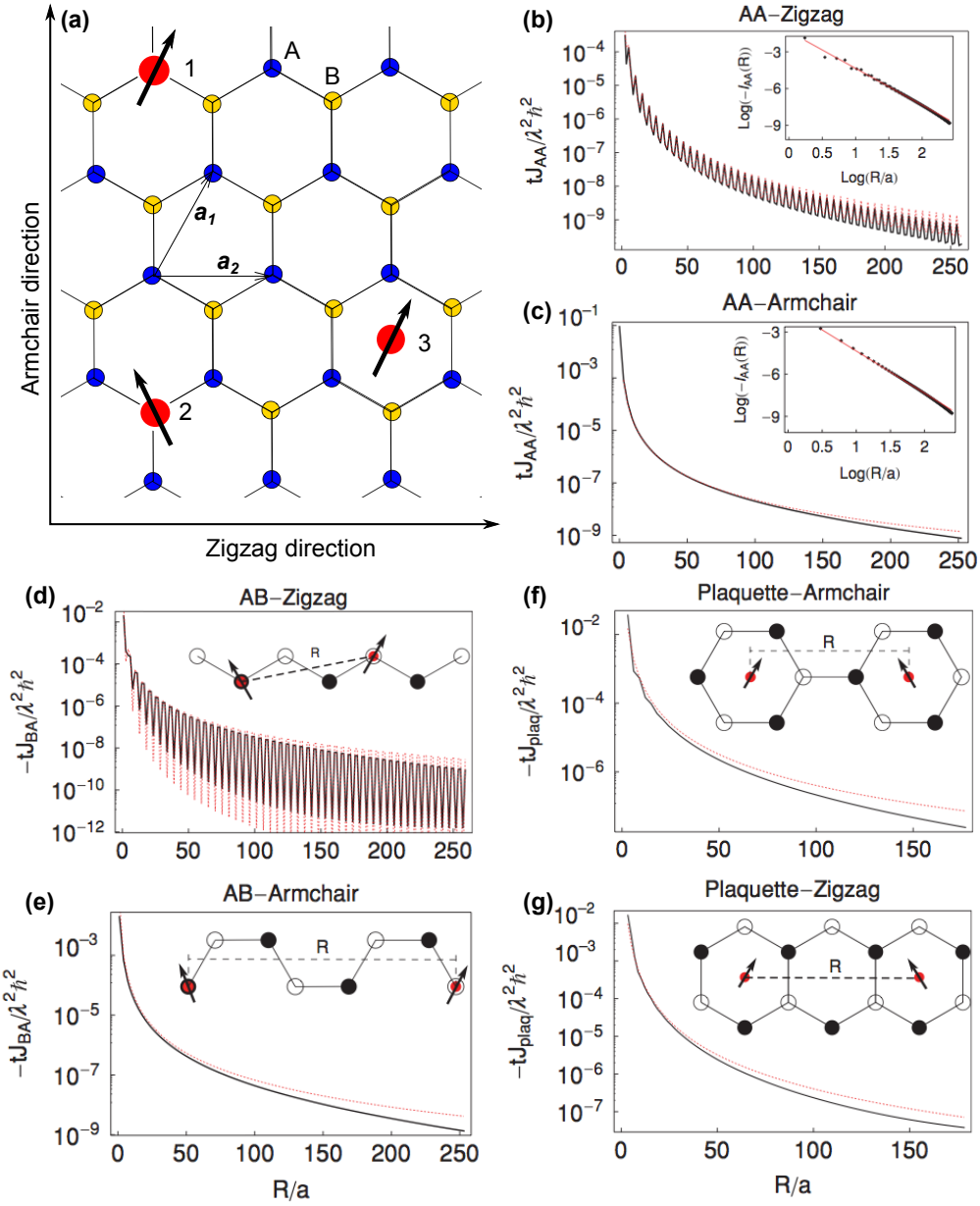

Figure 1.13: (a) A piece of graphene lattice displaying both zigzag and armchair directions with impurity spins located on sublattices A (1), sublattice B (2) and on plaquette sites (3). Plots of RKKY interaction between two impurities from the same sublattice J_{AA} (b,c), from different sublattice J_{BA} (d,e) and from the hexagonal plaquette (J_{plaq}) along zigzag and armchair directions. Black solid lines are the results with the full tight-binding band structure, and the red dashed lines indicate the long-distance behaviour as obtaine from (1.4), (1.5) and (1.6). The inset of (b,c) shows the log plot showing the long-distance R^{-3} behaviour, while there are noticeable differences for small R, especially visible in the inset. Note that since t is negative for graphene [131].

, where t is the nearest neighbour electron hoping, $\mathbf{K}$ and $\mathbf{K'}$ are the real space vectors marking the position of the K points of two inequivalent Dirac cones, and $\mathbf{R}$ is the real space vector between $\mathbf{S_i}$ and $\mathbf{S_j}$.

A first striking feature of the RKKY interaction in graphene is that it scales like $1/R^3$, unlike in conventional 2D electron gases for which the decay is slower, $1/R^2$-like. Noteworthy, recent calculations taking into account the dynamical character of the interaction predict is slower than $1/R^3$ [132], which is also the caser if electron-electron interactions, which are known to be very strong in graphene, are taken into account [133]. A second striking feature is that the interaction is antiferromagnetic between moments on different sub-lattices and ferromagnetic otherwise, which was already noticed in the seminal work of Saremi [130]. A third striking feature is that the interaction is oscillatory as a function of the separation between the moments in certain direction (zigzag) and not for others (armchair).

The calculation can also be performed for doped graphene, in which case the three above expression must be corrected with rather complex analytical factors [134]. For large distances their contribution can lead to an effective $1/R^2$ scaling law. In any case they account for an additional oscillatory behavior about zero, with Fermi-wavelength periodcity. This effect could be employed to tune the interaction between magnetic moments in graphene via a back-gate or dopants, with the view of controlling the magnetic ordering between these moments.

1.3 Low dimensional magnetism: ultrathin films and ordered nanomagnet arrays

1.3.1 Magnetic moments

In this subsection, I propose an overview of magnetic ultrathin films (2D) and clusters (0D). These exhibit properties modified in comparison with bulk forms or the atomic scale, while still very different from single atom properties.

The progress in nanomagnetic studies was made possible thanks to the progress in three respects. First, the preparation techniques in both deposition and patterning allow one to fabricate magnetic materials in the form of thin films or clusters down to the nanometer scale. Second, powerful characterization techniques were developed to characterize the magnetic properties of such nanostructures, in particular, x-ray magnetic circular dichroism and spin-polarized low energy electron microscopy that we have used in this study. Third, ever more powerful computing tools provides *ab initio* calculations allowing one to predict or support the experimental investigations. In reduced dimensions, nanostructures permit special phenomena to arise, such as: perpendicular magnetic anisotropy, giant magnetoresistance, tunnelling magnetoresistance, spin torques, superparamagnetism, remanence enhancement, exchange averaging of anisotropy. These effects have made possible the development of novel technology in the modern era, such as new magnetic recording media, spintronics, magnetic sensors.

While free atoms of most elements exhibit a magnetic moment based on Hund's rules, there are only Fe, Co, Ni and a few rare-earth showing a ferromagnetic behaviour in bulk and their alloys. Among these, Fe, Co, Ni are the only pure elements with a ferromagnetic ordering temperature significantly above room temperature. Nanostructures of these elements may display modified magnetic properties due to changes in their electronic structure when one-, two- or three-dimension(s) are reduced, corresponding to thin films, nanowires and clusters, respectively. Here, I describe in detail the case of Co which is investigated in our studies. A similar discussion for Fe may be found elsewhere [135].

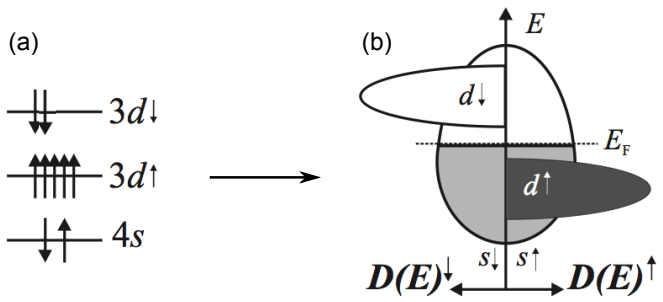

Figure 1.14: Schematic model showing the electronic structure of (a) single atom and (b) bulk of Co. [135]

Let us consider one atom of Co. It has nine electrons in total for the $3d$ and $4s$ levels. According to band filling and Hund's rule, two electrons fill the $4s$ orbital, the remaining seven electrons stay on the $3d$ orbitals comprising five for spin up and two for spin down. Therefore, the expected magnetic moment at ground state of a Co atom is 6 μ_B [figure 1.14(a)], half arising from spin and half from orbital angular momenta.

However, the atomic moment per atom measured in the bulk form is only 1.74 μ_B, i.e., it is first significantly reduced compared to an isolated atom, and amounts to a non-integer value. This can be explained by the underlying mechanism of Co as a metal. In a bulk metallic crystal, orbitals are delocalized to form a continuous band structure. Whereas the $4s$ band is largely delocalized, the $3d$ band is only partially delocalized with a width of a few eV only [figure 1.14(b)]. Hund's rules at the scale of a solid are replaced with the effect of exchange energy, resulting again from the combination of overlap of orbitals (giving rise to magnetostatic energy) and the exclusion principle, electrons being fermions. If exchange is strong enough (Stoner criterium) bands may be split at low enough temperature, the strength of the splitting determining the imbalance in spin moment. Notice that most electrons expected to occupy $4s$ states are transferred to $3d$ orbitals so Co is closer to filling 8.5 than 7 on this band. As Co is a strong ferromagnet (all the states of $3d$ band filled), an imbalance of 1.5 μ_B per atom is thus expected as concerns spin moment. Finally, let us add that crystal-field effects are dominant in $3d$ metals, selecting states with nearly zero orbital momentum as eigen states. Thus magnetization in $3d$ metals arises mostly from spin moment. All this is consistent with the experimental finding that bulk Co has thus a spin moment of 1.6 μ_B and a (parallel) orbital moment of 0.14 μ_B per atom.

In nanostructures, finite size effects or the occurrence of surface or interface atoms modify the electronic structure, i.e., the Fermi level or exchange interactions, thereby modifying the magnetic properties. Mostly two effects need to be discussed, with opposite trends: strengthening or weakening of magnetic order.

First, the reduced number of neighbours at an interface generally narrows the $3d$ band, increasing the density of states at the Fermi level. This makes the Stoner criteria easier to fulfil, increasing the splitting and therefore the spin imbalance and thus magnetization. Magnetic moments at interfaces have been extensively measured in the 80's and 90's and have indeed revealed the reality of this picture, with moments increased of up to a few tens of percent compared to their bulk value [136]. There are even a few cases of elements non-magnetic in the bulk form, displaying a moment in clusters where the Stoner criterium become satisfied, such as

for Rh and Ru [137].

An opposite effect arises: due to the reduced number of magnetic neighbours when surface/interface atoms are considered, the total effective exchange interaction is decreased, so that temperature effects are enhanced. A model case is thin films, due to the translational invariance. It is found experimentally and explained in a thickness-dependant mean-field theory that the decrease of Curie temperature with respect to bulk scales like:

$$\Delta T_{\mathrm{C}} \sim t^{-\lambda} \tag{1.7}$$

where t is the film thickness and λ depends on the nature of spin interaction. Experimentally, $\lambda = 1$ for ultrathin films [138].

1.3.2 Magnetic anisotropy energy in low dimensions

For relaxed bulk $3d$ materials, magnetic anisotropy energy (MAE) of microscopic origin is essentially the magnetocrystalline energy (E_{mc}). This energy originates from crystal field, i.e., the interaction between atomic orbitals with their local environment [139], and spin-orbit coupling, i.e., interaction between the residual orbital moment and the dominating spin moment. As a consequence, E_{mc} favours the alignment of magnetization along particular directions or planes, called easy axes or planes. The high energy direction or plane are hard axis or plane. For instance, in the *hcp* form of Co, the easy axis is the z direction and xy is hard plane. The anisotropy of magnetic energy may be expanded phenomenologically:

$$E_{\mathrm{mc}} = K_1 \sin^2\theta + K_2 \sin^4\theta + \ldots \tag{1.8}$$

. In Co we have $K_1 = 450$ kJ m^{-3} and $K_2 = 150$ kJ m^{-3}. In many systems and in textbook models of anisotropy and magnetization reversal, one often restricts the discussion to the case of uniaxial anisotropy of second order:

$$E_{\mathrm{mc}} = K_{\mathrm{u}} \sin^2\theta \tag{1.9}$$

with θ is the angle between the magnetization direction $\mathbf{M}$ and the z axis. K_{u} is a measure of the MAE.

In 1950's, s long time before the methods of thin film growth were experimentally suitably available, Néel predicted the modification of E_{mc} due to the breaking of symmetry of the atoms located at a surface, and introduced for the first time the concept of magnetic anisotropy at a surface [140].

$$E_{\mathrm{s}} = K_{\mathrm{s}} \sin^2\theta \tag{1.10}$$

where, K_s is the magnetic anisotropy coefficient of surface or interface. Although the Néel's model provided an estimated value of K_s which surprisingly agreed reasonably with the experimental measure around 0.1 mJ m^{-2}, latter, *ab initio* calculations were made possible and gave more accurate estimations. Bruno also proposed a tight binding model with a connection between the MAE and the anisotropy of orbital moment [141, 142]:

$$MAE = -\frac{G}{H}\frac{\xi}{4\mu_{\mathrm{B}}}(m_{\mathrm{L}}^{\perp} - m_{\mathrm{L}}^{\parallel}) \tag{1.11}$$

G/H, depends on the band structure, and ξ is the spin-orbit coupling coefficient. These are 0.2 and 0.05 for Co, respectively. In bulk materials, we have already pointed out that the wave

Table 1.2: Orbital momentum and magnetic anisotropy energy (MAE) of Co atoms on Pt as a function of coordination. [143, 144]

	bulk	1 ML	bi-atomic wire	mono-atomic wire	2 atoms	1 atom
Orbital momentum (μ_B/at)	0.14	0.31	0.37	0.68	0.78	1.13
MAE (meV/at)	0.04	0.14	0.34	2.0	3.4	9.2

function of electrons is nearly degenerate in rotation because of the crystal field interaction, therefore the orbital moment is very weak, in comparison with spin moments, explaining a moderate value for MAE. In contrast, in thin films and even more in nanostructures, crystal field becomes asymmetric at surfaces and interface. This gives rise to a significant increase of orbital moment and an extra MAE from E_s is accounted [141].

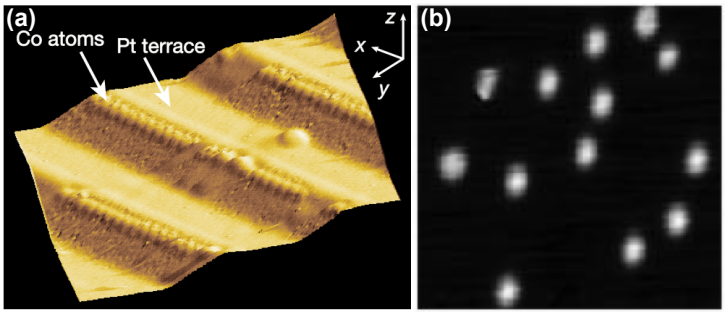

Figure 1.15: (a) Monoatomic Co wires decorating steps of Pt(997) [143]; (b) Single Co atoms on Pt(111) [144].

For structures smaller than a monolayer, the reduction of coordination is even more important. For instance, the case of an one-dimension interface[figure 1.15(a)] or the single-atoms on a surface [figure 1.15(b)] was experimentally realized. The magnetic studies exhibited a significantly variation of MAE. In particular, E_s increases remarkably from surfaces, down to steps, then to kinks or atoms. The anisotropy of orbital moment extracted from XMCD analysis displays a similar rise when reducing the size of systems, i.e., the same alternation with MAE consistent with Bruno's model (1.11). *Ab initio* calculations also confirm this tendency [145]. Table 1.2 lists the values for orbital moment and MAE in as function of dimensionality: bi-atomic island is closer with mono-atomic wire than single-atom, and bi-atomic wire is closer with monolayer than mono-atomic wire. For cluster of diameter ≈ 3 nm, surface effects are still dominant on the MAE [146].

Let us now focus on the impact of changes on MAE, and for this purpose focus again on the model case of thin films. The MAE of a thin film may be expressed as a function of film thickness [147]

$$MAE = K_{\text{eff}}(t)\sin^2\theta \tag{1.12}$$

where,

$$K_{\text{eff}} = K_{\text{bulk}} + 2\frac{K_s}{t} = K_{\text{mc}} + K_d + 2\frac{K_s}{t} \tag{1.13}$$

with $K_{\mathrm{d}} = 1/2\mu_0 M_{\mathrm{s}}^2$ is shape anisotropy. We have

$$MAE = E_{\perp} - E_{\parallel} \tag{1.14}$$

The competition of these terms determines the magnetization direction of thin films. Whereas in most cases $K_{\mathrm{mc}} + K_{\mathrm{d}}$ favours in-plane magnetization, K_{s} favours, in many cases, out-of-plane magnetization.

This is however a simplified picture. Indeed, there is a structural deformation of the magnetic film because of the lattice mismatch between substrate and thin film lattice parameters. This deformation of the lattice (the strain) also has and impact on the MAE through magnetoelastic energy.

$$E_{\mathrm{mel}} = \frac{1}{2} C\epsilon^2 + \frac{k}{t a_{\mathrm{f}}} |\eta + \epsilon - \epsilon^2| \tag{1.15}$$

Simple models for strain relaxation predicted that all deformations may be revealed as [148]:

$$E_{\mathrm{mel}} = B\epsilon \tag{1.16}$$

Then, we obtain:

$$K_{\mathrm{mel}} = \frac{kB}{a_{\mathrm{s}} C t} \tag{1.17}$$

where the initial lattice misfit is $\eta = (a_{\mathrm{f}} - a_{\mathrm{s}})/a_{\mathrm{s}}$ and strain $\epsilon = (a - a_{\mathrm{f}})/a_{\mathrm{f}}$ with a_{f}, a_{s} and a are film, and substrate lattice parameters in the relaxed form and actual lattice parameter of the film, respectively, and C is an elastic constant. From (1.17), this energy is inversely proportional to the thickness of the film, i.e., with the same scaling law as the contribution of E_{s} to the MAE. For this reason, E_{mel} is difficult to disentangle form E_{s} and is often considered as part of an effective surface energy term.

Let us discuss quantitatively K_{s}. In the 80's and 90's, it has been found that K_{s} is the highest for ferromagnetic thin film in contact with a non-magnetic metal of high spin-orbit interaction: Fe/Pd [149], Co/[150]Au , Co/Pd, Co/Pt [151]. Schematically, the dominating mechanism is the following: the non-magnetic metal becomes slightly spin-polarized in contact with the $3d$ ferromagnet, and although this polarization is small, the much larger spin-orbit coupling coefficient gives rise a large contribution in the MAE [152, 153]. A a result of this interaction, for small enough thickness, the magnetization easy axis turns from in-plane to out-of-plane; this is the spin reorientation transition (SRT). The SRT can occur within a range of a few monolayers or be abrupt within one monolayer as in Fe/W(110) [154] and Co/Ru(0001) [155]. Reasons of continuous SRT have long been debated, however resulting in no universal picture. The continuous SRT may result from either spatial distribution of properties, or terms of order four or higher in the MAE.

Ab initio calculations were performed taking into account the strain and modification of the electronic band structure of the film on contact with an environment such as substrate and capping layer, and showed a reasonable agreement with experimental observations [155]. Dorantes-Dávila et al. studied the effect of $3d/4d$ interfaces, using as theoretical model several Co monolayers on a Pd(111) substrate and capped by another monolayer of Pd, i.e., the system of $\mathrm{Pd}_1/\mathrm{Co}_m/\mathrm{Pd}(111)$ [156]. Both Pd/Co interfaces favour perpendicular magnetization, where as mentioned above Pd brings a larger contribution on the MAE than Co because it is a $4d$ element which remarkable polarization and significant spin-orbit interaction [157]. Gabary et

Table 1.3: Measured easy-axis of magnetization for the different Co-film/capping-layer combinations studied. [153]

Co	Capping material							
		Ag		Cu		Au		
thickness	Bare	1 ML	2 MLs	1 ML	2 MLs	1 ML	2 MLs	3 MLs
2 ML	PMA	PMA	PMA	PMA	PMA	PMA	PMA	PMA
3 ML	In-plane	PMA	In-plane	PMA	In-plane	PMA	PMA	PMA
4 ML	In-plane	In-plane	In-plane	PMA	In-plane	PMA	PMA	PMA
5 ML	In-plane	In-plane	In-plane	In-plane	In-plane	PMA	PMA	In-plane
4 ML	In-plane	In-plane	In-plane	In-plane	In-plane	PMA	PMA	In-plane

al. investigated the impact of capping layer of Ag, Cu or Au on few monolayer of Co on Ru substrate [153]. Using SPLEEM, they reported the dependence of SRT when capping with either of these noble metals. The results show that MAE depends on both ferromagnetic layer, and the element of capping (table 1.3). Besides, the experimentally MAE also depends on the deposition procedure of the thin films. For instance, the magnitude of K_{s} is only $\approx 50\%$ by PLD, in comparison with thermal deposition or electrodeposition. The reason is that the high energy atomic beam of PLD induces the intermixing at the interface with substrate, hence reduces the anisotropy at interface [158].

In recent years, an even stronger perpendicular magnetic anisotropy has been reported in systems with a ferromagnet and an oxide in contact. Among them, in 2009, Rodmacq et al. reported trilayer of Pt/Co/$\mathrm{AlO_x}$ with perpendicular magnetization beyond 3 nm of Co, a breaking record value. The PMA is increased thanks to the hybridization between $3d_{\mathrm{z}}$ orbitals in Co atoms and p_{z} orbitals of O atoms. In addition, the trilayer is thermally more stable than the system of Pt/Co/Pt due to the oxide layer [159]. In 2010, Ikeda et al. develope a magnetic tunnel junction of Ta/CoFeB(1.0 nm)/MgO(0.85 nm)/CoFeB(1.7 nm)/Ta with a high tunnel magnetoresistance (above 120%) and also perpendicular magnetic anisotropy thanks to the interface between CoFeB and MgO [160]. In this thesis another systems of ferromagnetic/non-magnetic, in particular, Co/graphene, are discussed (chapter 2 and 3—Part II).

1.3.3 Single domain and superparamagnetism

Extended ferromagnetic elements may be split in several domains, i.e., large regions where magnetization is essentially uniform. Domains are separated by domain walls, with a width between a few nanometers to a few hundreds of nanometers depending mostly on the strength of anisotropy. When the lateral dimensions of a magnetic material are reduced below some critical size, the coexistence of many domains together with domain walls and zero net moment costs more energy than the state of only one domain. Indeed, when the size decreases the energy of a domain wall decreases like d^2, whereas magnetostatic energy increases like d^3, where d is the size of the nanostructure. When putting in some numbers, this defines the so-called critical single domain size. For spherical clusters of some soft magnetic material, the single-domain diameter is estimated at about four times the dipolar exchange length $\sqrt{A/K_{\mathrm{d}}}$, which amount to fifteen to thirty nanometers depending on the $3d$ element or alloy [161]. Below this critical size, systems are essentially uniformly magnetized, and often called macrospins.

We now restrict the discussion to the macrospin regime. When applying a magnetic field on macrospins, their orientation of magnetization is determined by the competition between the ex-

ternal magnetic field and the internal MAE. At finite temperature, the macrospin moment can be reversed assisted by when thermal fluctuations exceeds the barrier height $\Delta E = KV$. Thermal activation is often described using the phenomenological Arrhenius-Néel-Brown approach the statistical time needed to overcome ΔE is

$$\tau_{\mathrm{m}} = \tau_0 \exp \frac{\Delta E}{k_{\mathrm{B}} T} \tag{1.18}$$

where, $\tau_0 \sim 10^{-9} - 10^{-10}$ seconds is the time scale characteristic of the material, and $1/\tau_0$ can be considered as an attempt frequency for the reversal. At a time scale shorter than τ_{m}, the macrospin is frozen, while at time scales much larger than τ_{m}, it fluctuates spontaneously. Equation (1.18) highlights an important parameter, the characteristic measuring time in an experiment τ_{m}. For probing the magnetic anisotropy of clusters, the require measure time must be less than relaxation time, but it is not always the case in practice. As a result, depending on the measure time of characterization technique, in particular XMCD, we can define a temperature called blocking temperature T_{B} below which the macrospin is frozen:

$$T_{\mathrm{B}} = \frac{\Delta E}{k_{\mathrm{B}} \ln(\frac{\tau_{\mathrm{m}}}{\tau_0})} \tag{1.19}$$

Above the blocking temperature, both hysteresis and remanence vanish. Let us first consider systems with a significant uniaxial MAE, as is the case of many self-organized systems with out-of-plane anisotropy. For $T \leq 5T_{\mathrm{B}}$, only rare events allow magnetization switching in the averaging time scale of the experiment, so that most of the time the macrospin remains is a state mostly either up or down. In that case the magnetization curve for a field applied along the easy axis of magnetization is expected to follow the law:

$$\langle M \rangle = M_{\mathrm{s}} \mathcal{B}_{\frac{1}{2}}(x) = M_{\mathrm{s}} \tanh(x) = M_{\mathrm{s}} \tanh\left(\frac{\mu_0 \mathcal{M} H}{k_{\mathrm{B}} T}\right) \tag{1.20}$$

where, M_{s} is the spontaneous magnetization and $\mathcal{M}$ is magnetic moment of the macrospin. Consequently, we can extract this moment from experimental data while assuming that other parameters of material such as magnetization and MAE are independent with the variation of temperature.

However, when $20T_{\mathrm{B}} \leq< T$, the magnetic anisotropy may be ignored and we recover the limit of an isotropic macrospin, described by the Langevin function.

$$M = M_{\mathrm{s}} \mathcal{L}(x) = M_{\mathrm{s}} \left(\tanh^{-1}(x) - x^{-1}\right) = M_{\mathrm{s}} \left(\tanh^{-1}\left(\frac{\mu_0 \mathcal{M} H}{k_{\mathrm{B}} T}\right) - \left(\frac{\mu_0 \mathcal{M} H}{k_{\mathrm{B}} T}\right)^{-1}\right) \tag{1.21}$$

The discussion above express models of superparamagnetic behaviour. Let us now consider its impacts on application. Depending on the particular application we have positive or negative impacts. Superparamagnetism limits the down-scaling of ferromagnetic grains used in magnetic hard disk devices, reducing the life time of storage. For overcoming this issue, one seeks to increase magnetic anisotropy by magnetoelastic or interfacial anisotropy, i.e., using special materials as substrates or capping layers. Moreover, the capping layer can not only avoid superparamagnetism but also prevent the oxidation of magnetic systems, suitable for applications. On the contrary, an advantage of superparamagnetism is preventing the segregation of ferromagnetic cluster on microfluidic or biomedicine [162]. This phenomenon is also helpful in

logic operations and information transmission at room temperature [163] or in picture painting without color but using photonic crystal fixed by magnetic field [164].

1.4 Epitaxial graphene on metals

Graphene (single- or few-layer) forms during high temperature treatments on many metals, presumably all transition metals. The reviews published on the topic [165, 166, 167, 168] keep track of the various substrates which have been considered, yet the fields remains quite active and new ones are addressed each year.

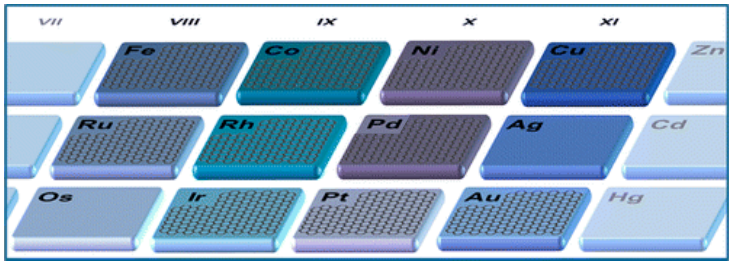

Figure 1.16: Transition metals support the growth of graphene by chemical vapour deposition. [168]

I first discuss the term "epitaxial" used to describe graphene/metal systems. Epitaxy of a material on top of a substrate (heteroepitaxy) implies either the prolongation of the atomic rows of the crystalline substrate by the material deposited on top or an alignment of the in-plane atomic rows of the material with those of the substrate. While the first case corresponds to the formation of actual chemical bonds, the second one is governed by van der Waals epitaxy and is known as van der Waals epitaxy [169]. A number of graphene/metal systems clearly belong to the first case, e.g., for Ni(111), Co(0001), Ru(0001) substrates; others presumably to the second case, for instance for Pt(111), Ir(111), and Cu(111), on which graphene can adopt a variety of crystalline orientation with respect to the substrate [170, 171, 172, 173].

Graphene growth on metals, so-called CVD, can occur following three processes, depending on the carbon solubility in the metal at high temperature (table 1.4) and on the stability of carbide phases:

Surface-confined growth: Carbon, either evaporated [208] or obtained by catalytic decomposition of hydrocarbons [210], on the hot surface of the metal, remain on the surface. Above a certain concentration of adatoms, graphene islands nucleate [171]. High temperatures allow to increase the mobility of carbon adatoms at the surface, thus to decrease the nucleation density, eventually leading to the formation of large single crystal graphene islands. The growth is thought to occur by the adjunction of few-carbon atom chains in pre-existing islands [171].. In the case of the growth with a hydrocarbon precursor, the growing graphene islands progressively cover the metal surfaces which allows to decompose the carbon-containing molecules. As a consequence growth slows down and asymptotically tends to a full coverage [207]. This mechanism makes the growth on metal surfaces like Ir(111), Pt(111) or Cu(111) self limited to a single layer of graphene, which is especially convenient. A derivative of this growth method consists in the room temperature adsorption of carbon precursors at the metal surface followed by an increase of the substrate temperature controlling the growth of graphene. This method, named

Table 1.4: Physical and chemical properties of transition metals (TM) with the ratio of lattice parameter with graphene (a_M/a_C) as support for graphene CVD and nature of the support (bulk single crystal, commercial foil, thin films). Carbon solubility is expressed in atomic % at 1300 K.

TM	(a_M/a_C)	Carbon solubility	Single crystal	Large-area foil	Thin film
Co	1.02	$\sim$ 1%[174]	[175]		[174, 176, 177]
Ni	1.01	$\sim$ 1%[174]	[178, 179]	[180, 181]	[182, 183, 75, 184]
Cu	1.04	$\sim$ 0.03%[174]	[185, 186]	[187, 188, 77, 189]	[190, 191, 192, 182]
Ru	1.10	$\sim$ 0.34%[193]	[194, 195]		[193]
Rh	1.09	[196]	[197]		
Pd	1.12	$\sim$ 2.5%[198]			[199]
Pt	1.14	$<$ 0.001%[200]	[201, 202, 203]		[204]
Re	1.12	$\sim$ 0.34%[205]	[206]		
Ir	1.10	$\sim$ 0.1%[205]	[207, 208, 209]		**our study**

temperature programmed growth (TPG) allows the preparation of graphene islands in reason of the low carbon density in a single layer of molecules adsorbed on the surface [207].

Growth by segregation: Carbon adatoms, either evaporated [211] or obtained by catalytic decomposition of hydrocarbons [212, 213] are dissolved inside the bulk of the metal, typically above 1100 K on Ni(111), Co(0001), and Ru(0001). Decreasing the temperatures leads to a drop in the carbon solubility and to a diffusion of the carbon atoms towards the surface of the metal. Close to the onset of carbon segregation towards the surface, carbon diffusion is faster than at lower temperature, but the bulk carbon concentration is closer to the surface concentration, i.e., the driving force for segregation is less important. The latter effect prevails upon the first one, so that growth is slower closer to the onset of segregation [213]. Hence as for surface-confined growth, it is advisable here to perform the growth at the highest possible temperature, in which case the growth is slow and carbon adatoms have larger surface mobility allowing them to nucleate in graphene islands with a low density, which will yield large single crystal islands. Note however that in case the carbon content in the bulk at high temperature exceeds the amount required for a single layer, performing the growth under these conditions will lead to the formation of multilayer graphene. In order to control (to some extent) the number of layers, adjusting the rate of the temperature decrease is necessary [214].

Carbide formation and transformation: Below carbon dissolution temperature, carbides can form onto metals strongly interacting with carbon, for instance on Ni(111), Co(0001), Rh(111), or Re(0001). The relative stability of the carbide and the graphene phases is not always in favor of the latter. However, even in such a case, one may exploit the different carbon saturation needed for forming graphene and the carbide to promote the formation of the other. On Ni(111) a favorable situation was encountered with a surface carbide forming at a few 100° under exposure to ethylene and progressively transforming into graphene [215].

Irrespective of the nature of the metal, various kinds of metal supports are employed for preparing graphene (table 1.4). Surface science studies, conducted for instance for unveiling the elementary processes during growth or for exploring the properties of graphene remaining on its support, require UHV conditions and ultra-clean samples with atomically smooth surfaces. In this view bulk single crystal are often used, but we have developed metal thin films of

Table 1.5: Process parameters (temperature, hydrocarbon pressure, flow rate, cooling rate and metal crystallinity) and their effect on graphene qualities (domain size, thickness uniformity and defect density) [216].

Parameter	Domain size	Thickness uniformity	Defect density
Temperature	Larger domain size with increased temperature		Lower defect density with increased temperature
Hydrocarbon pressure	Smaller domain size with pressure	Decreased uniformity with pressure	Higher defect density with pressure
Hydrocarbon flow rate	Smaller domain size with flow rate	Decreased uniformity with flow rate	High defect density with pressure
Cooling rate		Improved thickness uniformity with lower cooling rates	Lower defect density with lower cooling rates
Metal carbon solubility		Improve thickness uniformity with lower carbon solubility	
Metal crystallinity	Graphene domains can grow continously over grain boundaries, but graphene nucleates with an orientation related to that of the substrate	Improved thickness uniformity with single crystal substrates	

comparable quality. The initial works on graphene on metals from the 1960's were conducted using metal foils. The recent works as well. These provide a convenient and relatively low-cost sacrificial substrate, in the view of the transfer of graphene to other supports: in most applications nowadays CVD is considered a route to high quality large area graphene but a non conductive support is needed. For this purpose graphene on its metallic substrate is usually capped with a resin spin-coated layer before the metal is etched away by chemicals; then the graphene/resin is stamped to the desired support and the resin is dissolved, for instance with acetone [217]. The process has been upscaled to a roll-to-roll procedure allowing the production of very large area graphene [figure 1.17] [77].

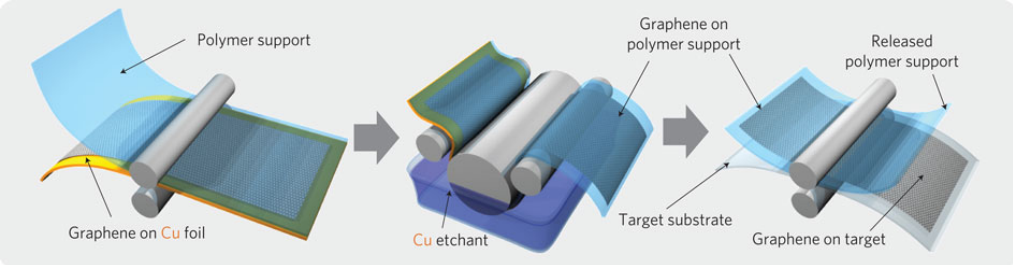

Figure 1.17: (Schematic of the roll-based production of graphene films grown on a copper foil. The process includes adhesion of polymer supports, copper etching (rinsing) and dry transfer-printing on a target substrate. A wet-chemical doping can be carried out using a setup similar to that used for etching. [77]

In the view of mass production of high quality graphene, bulk single crystal are prohibitively expensive and their chemical dissolution would be an economical nonsense. Commercial foils are less expensive but their dissolution in an industrial process would constitute a considerable waste of raw material (and, as one knows, the cost of raw metals is currently increasing) and an environmental issue. Moreover, the polycrystalline nature of these foils induces mosaicity in the graphene flakes grown on top and the metal grain boundaries generate regions where the number of graphene layers can be large and difficult to control [193]. In this context, high quality metal thin films appear a valuable alternative. Very encouraging results have been obtained, for instance with single-crystalline 400 nm-thick Cu(111) films deposited on sapphire as substrates for graphene [figure 1.18] [190]. During the same period, we have been working on a similar approach which will be detailled in a forthcoming chapter.

I now briefly discuss the structural properties of graphene on metals. Even for graphene /Ni(111) and graphene/Co(0001) which are a priori simple (1×1) commensurate structures in reason of the similar lattice parameter of graphene and of the surface of these metals, the structure is more complex than it seems. The general consensus from first-principle calculations is for instance, in graphene/Ni(111) a structure with one C sublattice on top of the Ni atoms of the top-most layer and the second C sublattice on top of the third layer of Ni atoms [218]. Experiments based on electron diffraction however point to a situation in which the second C sub-lattice is on top of the second layer of Ni atoms [165]. On other metal surfaces, whose in-plane lattice parameter is always substantially larger than that of graphene, moirés are found. These superstructure correspond to the (partial) local coincidence between the graphene and surface metal lattice [figure 1.19]. They have triangular symmetry if the metal surface lattice has the same symmetry as graphene, as is the case on (111) terminated face-centered cubic metals. They have a rectangular symmetry in case the metal surface lattice has rectangular symmetry,

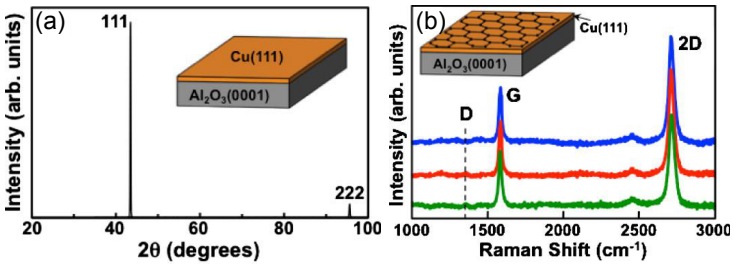

Figure 1.18: (a) XRD pattern of epitaxial Cu(111) on α-Al_2O_3(0001) substrate indicating only 111 and 222 reflections. (b) Raman spectra from three different regions of CVD graphene grown on epitaxial Cu(111)/α-Al_2O_3(0001) The 2D and G peaks are marked, and the dashed line marks the position of the defect D peak which is absent. [190]

like is the case on a (110) terminated face-centered cubic metal [219]. Their periodicity (a_m) is in the range of a few namometers, being defined by $a_\mathrm{m} = (a_\mathrm{C}^{-1} - a_\mathrm{metal}^{-1})^{-1}$, where a_C and a_metal are the lattice parameters of graphene and of the metal surface respectively, in the case of a triangular pattern [220]. For graphene/Ir(111), this is about 2.5 nm [221], and 6 nm for graphene/Cu(111) [186] in case the zigzag C rows align the high density atomic raws of the metal.

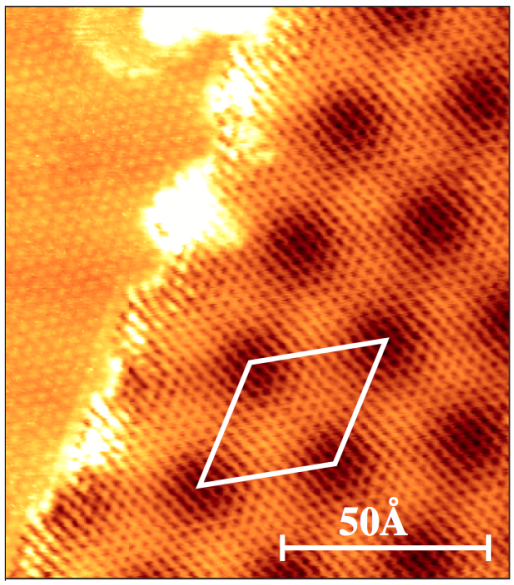

Figure 1.19: Atomic resolution STM topograph of graphene/Ir(111) exhibits the moiré superstructure and the hexagonal ring of C. White dot line follows the moiré lattice [220].

A number of defects have been studied in graphene on metals. Edge dislocations, which consist in a carbon heptagon-pentagon pair, allow for the accommodation of in-plane twins in graphene; they form grain boundaries around twinned domains [72]. Large-angle twins in graphene have received particular attention: on metals weakly interacting with graphene, like Pt(111) [201, 222], Ir(111) [208] and Cu(111) [173], several epitaxial relationships seem to have comparable energetic cost. Under certain conditions, it is possible to avoid the formation of these

epitaxial variants, for instance by taking benefit of the higher inertness of one of the variants, or by seeding the growth of graphene with well oriented graphene using a combination of the TPG method followed by CVD [172]. Accordingly a single crystallographic orientation can be obtained over the whole surface of a sample. Another common type of defect is the delamination of graphene along lines forming during the cooling down of the samples after their growth, due to the mismatch in thermal expansion coefficients between the metal and graphene [201, 223]. Less discussed in the literature are C vacancy islands trapped during growth, especially a moderate growth temperatures [207].

1.5 Objective of the present work: Ferromagnet - graphene interface

The present work, started in October 2009, aimed at the development of novel epitaxial systems combining the graphene and a ferromagnet, Co [figure 1.20], and at the understanding of the magnetic properties stemming from the graphene/ferromagnet interface. Both ultrathin films, on top of graphene and sandwiched between graphene and the metallic substrate, Ir(111), and small size, highly orderred nanoclusters, were explored.

First, we developed versatile thin Ir(111) films of high quality on sapphire substrates. Similar efforts have been undertaken by other groups worldwide at the same time, and within the years 2010 and 2011 the first reports, including ours, about graphene growth on high quality metal thin films, were published. The quality of the surface of these films was shown comparable to that of bulk single crystals, which provides a valuable alternative in the prospect of multi-technique characterizations and *ex situ* characterizations. We studied magnetic systems prepared on both thin Ir films and bulk single crystals.

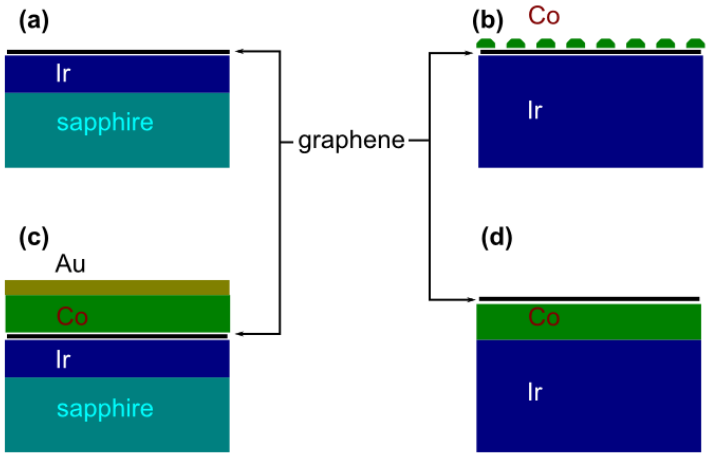

Figure 1.20: Epitaxial systems of the PhD works: (a) graphene/Ir thin film/sapphire, (b) Co clusters/graphene/Ir, (c) Au/Co thin film/graphene/Ir thin film/sapphire and (d) graphene/Co thin film/Ir.

We employed a unique technique for preparing thin Co films on graphene, pulsed laser deposition. Thus far our work is the only one reported using this technique, which allows to bypass the usual clustering of metal deposits on sp^2-hybridized carbon surfaces such as graphene.

We also made use of the process of intercalation prepare Co thin films capped with graphene. This method, which had been employed decades ago, has considerably grown in importance since 2008-2009, and has been applied to a variety of systems, including in graphene/ferromagnet systems by the Berlin group during the same period of time as our work [224]. For preparing nanoclusters we exploited a technique relying on the preferential nucleation of small clusters on graphene/metal moirés, which has been discovered in Köln in 2005 and started to be employed by other groups in 2009.

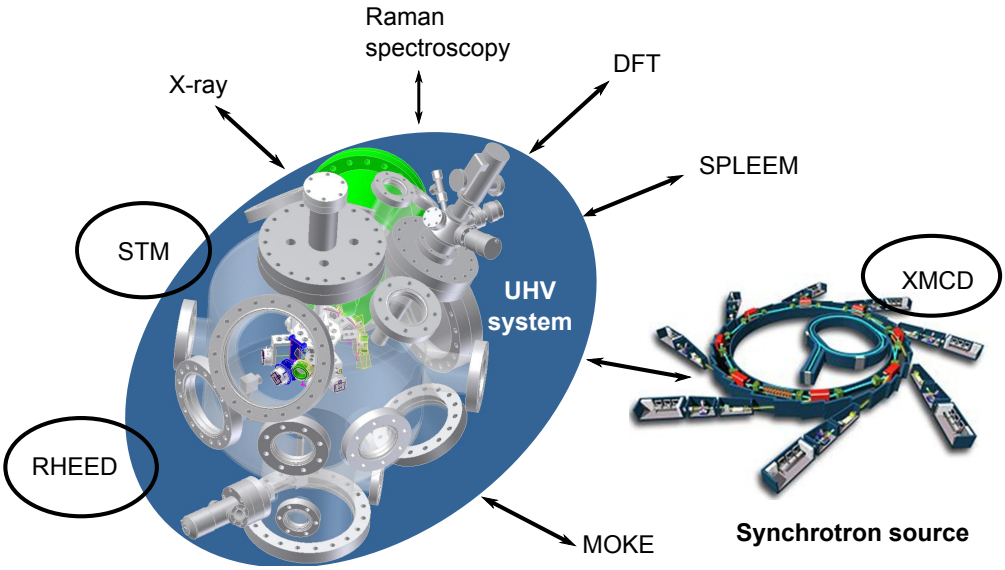

Figure 1.21: Technical supports of this PhD work: home ultrahigh vacuum chambers with *in situ* reflection high energy electron diffraction, scanning tunnelling microscopy, *ex situ* x-ray diffraction, Raman spectrosopy, magneto-optical Kerr effect. *in situ* spin-polarized low energy electron microscopy in collaboration, magnetic circular dichroism using synchrotron sources. First-principles density functional calculation was also performed.

We put special efforts in trying to correlate the structural, electronic and magnetic properties of the various systems which we have developed [figure 1.21]. For this purpose we have carried out various characterizations. Surface science techniques, some at synchrotron radiation sources, have been extensively used, including scanning tunneling microscopy, electron diffraction, low-energy electron microscopy with a spin-polarized electron source, and x-ray magnetic circular dichroism. We combined these characterizations with transmission electron microscopy, Raman spectroscopy, and MOKE magnetometry/microscopy, and confronted our results to spin-polarized density functional theory calculations.

The results presented in Part II of this manuscript also had a risk and ambitious objectives which have not yet been achieved and will be further discussed in the conclusion, but I still would like to mention here some of which for better highlighting the motivation of our work. In self-organized nanoclusters on graphene/metals, a long-term objective is the observation of collective magnetic states stemming from the interaction between clusters; in graphene/ferromagnetic thin film we expect induced magnetism in graphene due to the contact with the metal [112] and consider, beyond this thesis, addressing the magnetic domain structure in graphene as a function of the magnetization direction.

2

Experimental methods

Contents

The work presented in this manuscript is prominently surface science, regarding both the preparation of the new graphene-based systems and their fine characterization. Whenever possible it was conducted *in situ*. It has required a specific, simple, adaptation of an existing set of UHV systems at Institut Néel, allowing the preparation of graphene. A number of samples were investigated outside Institut Néel, at synchrotron sources (ESRF and SOLEIL) and with a specific electron microscope installed at NCEM, Berkeley. There either new preparation procedures were developed, and latter implemented in the lab, and the new samples were studied *in situ*, or samples prepared at the lab were studied (*ex situ* studies).

In this chapter I will first describe the experimental setups at the lab and outside the lab, then present the sample preparation techniques, then will pay special attention to two techniques, one upon which a large fraction of the results presented in the part II rely, x-ray magnetic circular dichroism (XMCD), and the other which is not standard, spin-polarized low-energy electron microscopy (SPLEEM). I will also briefly describe the conditions employed for performing more standard characterizations and shortly present the computational details chosen for the first-principle calculations.

2.1 Experimental setup at Institut Néel

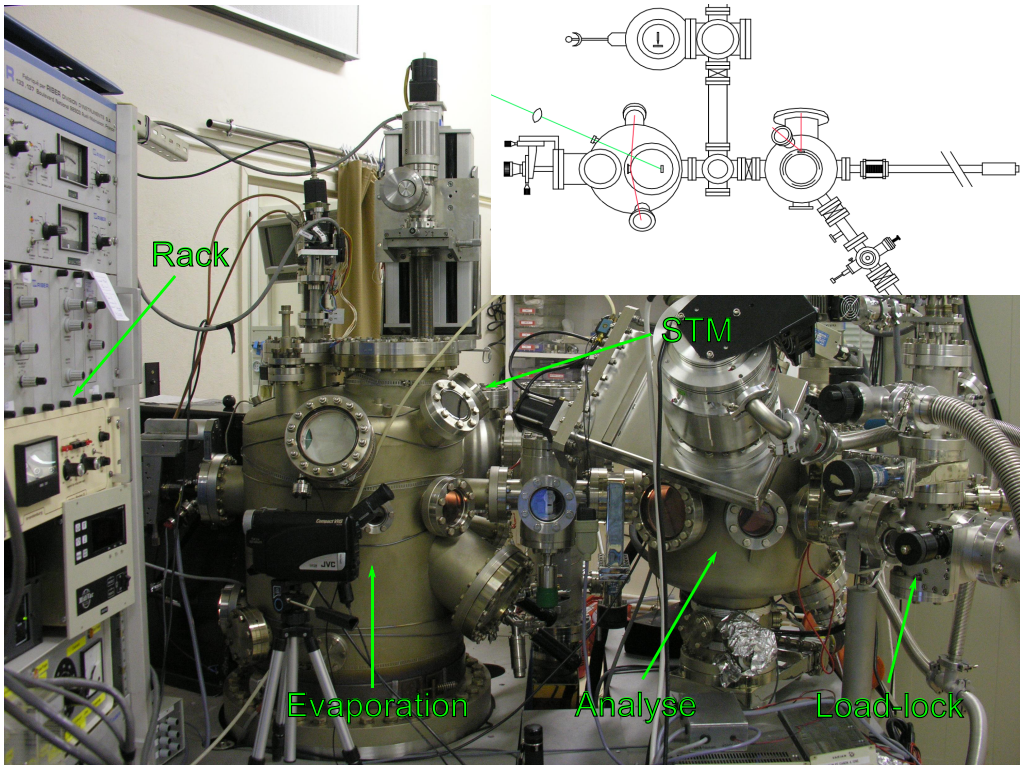

Figure 2.1: Experimental setup at the Néel Institute with three main interconnected UHV chambers: evaporation, analyse and STM. Inset is a top-view illustration of this T-shape-like systems

2.1.1 Overview of the UHV system

The setup consists of three UHV chambers interconnected under UHV via a T-shape tube [figure 2.1]. All chambers are equipped with on ion pump and a Ti sublimator. Except for the scanning tunneling microscope (STM) chamber under regular operation, in which mechanical vibration should be avoided, chambers also include one turbomolecular pump. In addition to these three chamber a smaller, connected to the "analyse" chamber is employed as a home-made load-lock allowing to introduce two samples at a time from outside the UHV system. Letting sufficient

time for the pressure to reach the 10^{-7} mbar regime in the load-lock before introducing the samples in the "analysis" chamber, degassing samples by high temperature (1100 K) annealing in this chamber before introducing them in the "evaporation" and STM chambers, allows to maintain base pressure in the low 10^{-10} mbar range in the "analysis" chamber and in the 10^{-11} mbar range in the "evaporation" and STM chambers.

Transfer between chambers are performed with transfer rods and rely on 1 inch molyblocks holding samples and holders with the same diameter hosting STM tips and metal targets. Samples are held on Omicron plaquettes compatible with the Omicron system.

The "analysis" chamber comprises an Auger electron spectrometer with a MACII analyser, a scanning ion gun (Thermo VX EX05), a caroussel-like garage capable of storing 12 samples or STM tips or metal targets, and having a home made electron bombardment (0.2 mm diameter Ta wire) heated sample holder. Samples temperatures are measured with a pyrometer. Gas can be introduced in low pressures through leak valves; one is connected to a tube bringing the carbon precursor (ethylene) at the surface of the heated sample (see discussion below) for chemical vapor deposition (CVD) of graphene.

The STM chamber includes a room-temperature Omicron STM-1 instrument (usually operated with W tips which can be thinned with ion bombardment in the "analysis" chamber), with a maximum field of view of 800 nm. The samples are taken out of their molyblock with the help of a wobble-stick and are either stored in a carousel garage or put under the STM. In the case of the non-conductive substrates (sapphire) used in this work, one of the springs holding the substrate to the Omicron plaquette must be moved with the help of the wobble-stick after preparation of the sample (usually, conductive deposits) in order to establish electrical contact and allow STM measurements. The STM tip can be moved at millimiter scale along the horizontal direction, which can be monitored with an optical video camera. This allows the study of samples with gradients of composition/thickness at their surface.

The "evaporation" chamber is equipped with a radiatively heated sample holder, rotatable in the azimuthal direction, with a high resolution 10–50 keV electron gun coupled to a fluorescent screen equipped with a 10 bit CCD camera for reflection high energy electron diffraction (RHEED) experiments, with a eight-slot metal target holder for pulsed laser deposition (PLD), with a quartz view ports letting in a pulsed laser for PLD, with a quartz microbalance for growth rate measurements, with a moveable mask for varying the composition/thickness of the deposits, and with two electron-beam evaporators (Tectra GmbH) for molecular beam epitaxy. All movements (mask, PLD target holder) are motorized and controlled through a computer that allows one to launch automatized commands.

2.1.2 Deposition techniques

Pulsed-laser deposition: The laser used for PLD in a frequency-doubled ($\lambda = 532$ nm) Quantel Nd–YAG. It has a pulse width of about 10 ns, a repeat frequency of 10 Hz and a maximum energy per shot of 150 mJ. The energy of the beam is adjusted by tuning the delay between the oscillator and the amplification stage of the laser while the pumping stays constant. The laser beam enters the chamber through a window and impinges on the target at an angles 27° away from the normal to the surface [figure 2.1(inset)]. A key parameter determining the evaporation rate is the fluence F, i.e., the energy entering the chamber per shot normalized by unit area of the spot size on the target. F can be adjusted with both the laser power and a convergent lens located outside the chamber on the beam path. the focal length of the lens is 500 mm. The focus is located ahead the target, at a distance 120–180 mm depending on

the element to evaporate. The resulting working value lies in the range 0.1–1 J m^{-2}, yielding a typical deposition rate of 0.05 nm min^{-1} at 10 Hz. The laser is swept on the target with the help of an *ex situ* mirror mounted on an electro-acoustic device. The substrate-to-target distance is 140 mm.

Molecular beam epitaxy: The molecular beam evaporators are located 20 cm away from the sample surface. A relatively high power is thus needed for achieving measurable growth rates, typically 0.06 nm min^{-1} for a Co rod heated by electron bombardment with 1500 V potential with respect to a filament heated to 1.7 A. The evaporators are equipped with mechanical shutters.

Chemical vapour evaporation of graphene: Ethylene is leaked through a valve onto the sample heated to high temperatures, between 1000 and 1500 K. The use of a tube bringing ethylene at the sample surface and locally increasing the pressure allows to perform CVD with 10^{-7} mbar pressures (and below) as measured with a remote Bayard-Alpert gauge. Careful dimensioning of the dosing tube has been done (see next subsection).

2.1.3 Dosing tube for graphene CVD

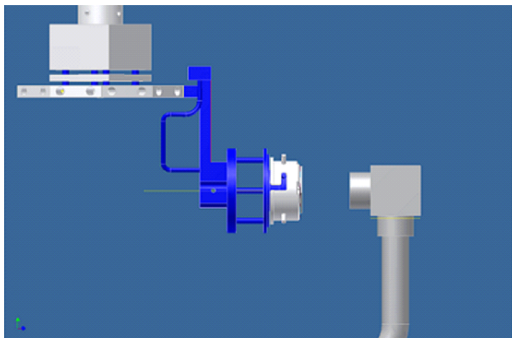

Figure 2.2: The position of the gas tube and the sample mounted on the oven during CVD process, the position of sample and oven can be changed.

The dimensioning of the geometry of the dosing tube used for CVD of graphene is guided by the following considerations: (i) the molecular flow at the sample surface should be as uniform as possible, (ii), the pressure increase at the sample surface should be the higher possible, and (iii) bringing the end of the tube to close to the hot sample surface might be mechanically delicate and could lead to pollution during growth due to the degassing of the tube. A good compromise was to use a 10 mm-diameter stainless-steel tube whose end is 10–20 mm from the sample surface (6.5 mm × 8.5 mm) [figure 2.2]. With this configuration, the factor between the local gas pressure at the sample surface and the global pressure is a few tens.

Below I present the derivation of the molecular beam profile, first from a point source, second from a cylinder tube. A tube is connected at one end to a gas reservoir where the pressure is high (typically in the range of 1 mbar), and at the other end to UHV. The pressure difference between both ends induces a gas flow inwards the chamber via the leak valve.

For a point source, the particle flux per solid angle I (s^{-1} Sr^{-1}) is

$$I(\theta) = I(0) \times f(\theta) \tag{2.1}$$

with the gas particle angular distribution function $f(\theta)$ (with $f(0) = 1$). $\dot{N}$ is the integral of the particle flux per second, namely

$$\dot{N} = \int_{2\pi} I(\theta) \mathrm{d}^2\Omega \tag{2.2}$$

The so-called peaking-factor [225], defined as

$$\kappa = \frac{\pi I(0)}{\dot{N}} \tag{2.3}$$

is the proportion of the gas beam in the forward direction. The π factor arises from normalization to one for a cosine tube emitter with $f(\theta) = \cos\theta$. This case is however too simple to account for our situation.

Introducing (2.3) on (2.2) yields

$$I(\theta) = \frac{\mathrm{d}^2\dot{N}}{\mathrm{d}\Omega^2} = \frac{\dot{N}}{\pi}\kappa f(\theta) \tag{2.4}$$

This is expressed per seconds and in units of solid angle. We are rather interested in the particle flux per unit sample area [226]. This is deducted from (2.1) by expressing the flux per unit area $\mathrm{d}S$ in the θ direction. For this we relate the unit solid angle $\mathrm{d}^2\Omega$ to the corresponding area defined by at a distance l:

$$\mathrm{d}^2\Omega = \frac{\mathrm{d}^2S}{l} = \frac{\mathrm{d}^2S}{\left(\frac{z}{\cos\theta}\right)^2} = \mathrm{d}^2S\frac{\cos^2\theta}{z^2} \tag{2.5}$$

, z being the distance between sample and tube. The projection of this area onto the sample surface yields another multiplication by $\cos\theta$. Then,

$$I(0) = \frac{\dot{N}}{\pi z^2}\kappa f(\theta)\cos^3\theta \tag{2.6}$$

this holds for a point source. For an extended source, such as the exit of a tube that we are interested in, the calculation is *a priori* much more complicated. However, it can be greatly simplified by assuming that the exit area of the tube is constituted by an infinite number of point sources. This is justified if the gas particle assembly at the exit of the tube has homogeneous speed, i.e., if the gas particles do not stick at the tube surface and if the tube aspect ratio is large. Then (2.6) can be re-written:

$$I(0) = \frac{\dot{N}}{\pi A z^2}\int_A \kappa f(\theta)\cos^3\theta \mathrm{d}A \tag{2.7}$$

For an angle θ comprised in $[0, \theta_\mathrm{c}$, where $\theta_\mathrm{c} = \arctan(2R/L)$ (R is the tube radius, L is its length), the following expression can be derived in the case of diffuse reflection of gas molecules at the tube walls [225]:

$$\kappa f(\theta) = \frac{2\cos\theta}{\pi W}\left((1-\frac{W}{2})T(p) + \frac{2}{3}(1-W)\frac{(1-\sqrt{(1-p^2)^3})}{p}\right) + \frac{1}{2}\cos\theta \tag{2.8}$$

Since $\theta_\mathrm{c} < 90°$, this does not describe the full range of possible θ emission directions for the half space at the exit of the tube. For θ comprised in $[\theta_\mathrm{c}, 90°]$ [225],

$$\kappa f(\theta) = \frac{\cos^2\theta}{\pi \sin\theta} \frac{8R}{3L} \frac{(1-W)}{W} + \frac{1}{2}\cos\theta \tag{2.9}$$

where W, the Clausing factor [227], writes $8R/(3L+8R)$ to a good approximation, $p = L\tan\theta/2R$ and $T(p) = \arccos p - p\sqrt{1-p^2}$. Note that from (2.8)

$$\kappa f(0) = \kappa = \frac{1}{W} \tag{2.10}$$

Rather than using the θ angular coordinate, we now express (2.8) as a function of the x coordinate along the sample surface (as the system has polar invariance, we do not introduce here the perpendicular coordinated, y). For this, we defined x' and y' the position on the tube exit surface, and simply express θ as a function of x', y', and x. This yields:

$$I(x) = \frac{\dot{N}}{\pi A z^2 W} \int_{-R}^{R} \int_{-\sqrt{R^2-x^2}}^{\sqrt{R^2-x^2}} f(\arctan(\sqrt{(x-x')^2 + \frac{y^2}{z}})) \cos^3(\arctan(\sqrt{(x-x')^2 + \frac{y^2}{z}}))\mathrm{d}x'\mathrm{d}y' \tag{2.11}$$

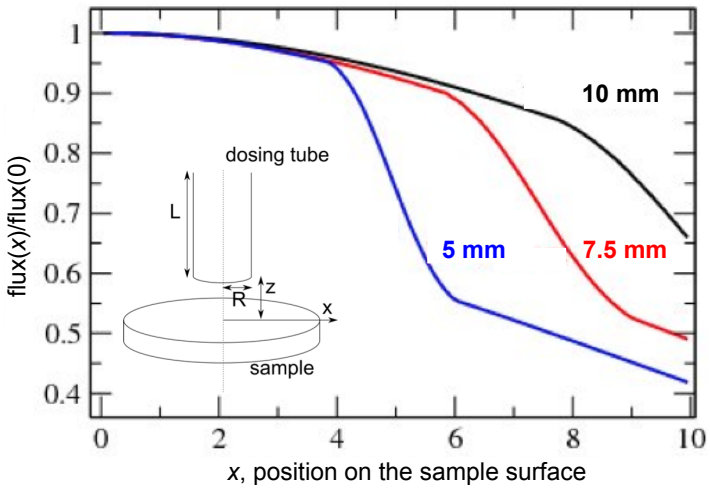

Figure 2.3: The gas profiles for the distance between tube-end and sample surface of 20 mm, with the tube diameter of 5 mm (blue), 7.5 mm (red) and 10 mm (black) for $z = 20$, $L = 185$ nm. Inset, schema of ethylene dosing configuration.

Figure (2.3) illustrate gas profiles in function of the diameter of the tube, for the 185-mm long tube, and tube-end positioned at 20 mm away form the sample surface. The geometry chosen in our experimental setup ensures 90% uniformity of the gas flux on the sample.

2.2 Experimental setups outside the home lab

2.2.1 The ID08 beamline at the ESRF

The ID08 beamline at the ESRF has an end-station [figure 2.4] combining a set of two interconnected UHV chambers, one used for sample preparation (ion bombardment, heated sample

which we strongly contributed to upgrade to electron-beam heating in order to reach 1500 K temperatures, electron-beam evaporators for MBE and leak valves which we used for graphene CVD), and the other hosting a variable temperature Omicron STM capable of imaging during MBE. The ensemble is connected via a long transfer tube to a load-lock module and to the cryomagnet chamber, which also is a UHV one, thanks to an initial turbomolecular pumping and latter cryogenic pumping. If needed, an electron-beam evaporator can be installed on the cryomagnet chamber. As a whole, the UHV end-station allows full sample-preparation and advanced structural and magnetic characterizations *in situ*.

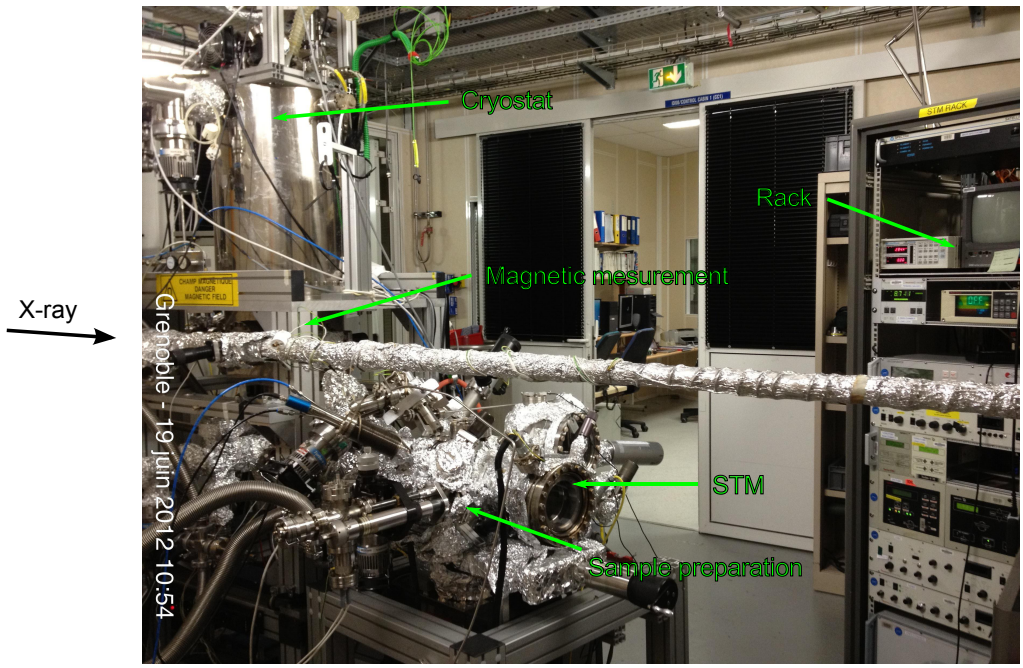

Figure 2.4: Dragon Beamline—ID08/ESRF, experimental set up with three interconnected UHV chambers: Sample preparation, STM, magnetic measurement. A superconducting magnet with ±5 T field, 7 K to 300 K sample temperatures, 10^{-8} Pa vacuum.

X-ray magnetic dichroism experiments are conducted on samples inside the cryomagnet chamber. The cryomagnet is a superconducting coil reaching 5 T; the sample temperature can be adjusted between 4 and 300 K. The ID08 beam-line is an Apple-type undulator producing 100% circularly polarized x-rays in a energy-range of 400–1500 eV (where one finds, e.g. the Co $L_{2,3}$ absorption edges). The absorption spectra were measured via the TEY (photocurrent of the sample) and were normalized to the photon flux probed by the photocurrent of a gold grid.

As of mid-2012, the upgrade of the beamline, especially of the cryomagnet and of the beamline optics, has started.

2.2.2 The DEIMOS beamline at SOLEIL

The end-station of the DEIMOS beamline at SOLEIL consists of two interconnected UHV chambers, one for sample preparation and the other for characterizations of the samples (e.g. STM) coupled to the cryomagnet chamber and to a load-lock module connected to a clean atmosphere glove box. Being among the first users of the beamline, the UHV preparation and

characterization chambers were not yet available at the time of our measurements. We thus performed *ex situ* x-ray magnetic dichroism measurements on samples prepared at the home lab and introduced in the cryomagnet chamber.

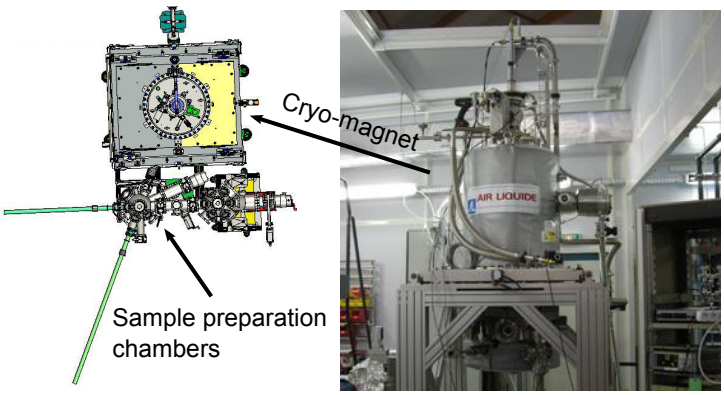

Figure 2.5: DEIMOS Beamline—SOLEIL Synchrotron, experimental set up with interconnected UHV chambers: Sample preparation and magnetic measurement. A Cryo-magnet with ±7 T field, 1.5 K to 370 K sample temperatures, 10^{-8} Pa vacuum.

The cryomagnet is a superconducting coil delivering a 7 T field parallel to the x-ray beam and 2 T perpendicular to it; the sample temperature can be varied between 1.5 and 350 K. The DEIMOS beamline is an Apple-II undulator producing variable polarizations (circular, continuous linear) in a 350–2500 eV energy range. The x-ray spot size is $80 \times 80 \mu m^2$. Absorption measurements are performed in TEY (fluorescence yield and transmission modes are also possible).

2.2.3 The SPLEEM microscope at NCEM

Three chambers are interconnected under UHV via a transfer rod. The first chamber has a fast-entry valve allowing to introduce samples and is equipped with a low-energy electron diffraction apparatus. A second chamber includes sample preparation facilities, with high temperature (2500 K) sample heating, ion bombardment, electron-beam evaporation, and comprises an Auger electron spectrometer. It is connected to the first one and to the first one where SPLEEM experiments can be performed. The sample holder in this third chamber is variable temperature from 35 to 2500 K. Electron beam evaporators and a leak valves allow MBE and graphene CVD in this chamber, during SPLEEM imaging.

For performing magnetic sensitive measurements, the electron source, a LaB_6 filament, is replaced by longitudinally spin-polarized electrons emitted by a GaAs photocathode under optical pumping conditions with the help of a laser [figure 3.9]. For easing the emission of spin-polarized electrons the work function of the GaAs surface is lowered by coadsorption of oxygen and cesium. A set of electrostatic and magnetic elements allow to adjust the direction of the spin-polarization with a 3° accuracy [228].

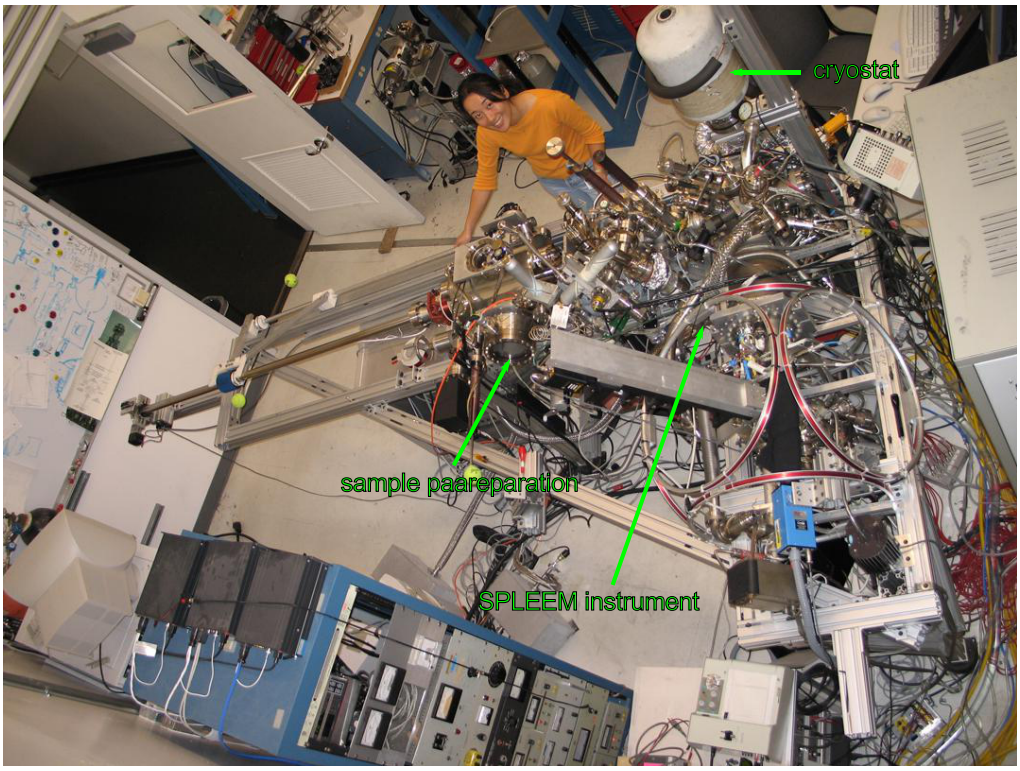

Figure 2.6: SPLEEM instrument. The sample chamber allows us to prepared the samples and then measured in SPLEEM chamber. Base pressure of 10^{-9} Pa, sample temperature in range of 130 K to 2500 K.

2.3 Substrate preparation

2.3.1 Sapphire substrates at Institut Néel

Samples prepared at Institut Néel were all grown on commercial two-inch C-plane sapphire wafers cut in 6.5 mm × 8.5 mm rectangles with the help of a Nd—YAG laser focused on the backside of the wafer, with a spherical lens with $f = 200$ mm [229]. Wafers from several suppliers have been used (Union Carbide, Bicon, Crystal GmbH, Roditi). The miscut was found to vary from wafer to wafer.

The wafers are then cleaned with deionized water, to remove the Al deposited at the back during the laser cutting. The rear of the wafer is then coated by sputtering with a 200–300 nm-thick layer of a refractory metal, usually W. The purpose of this layer is to absorb most of the heating radiation emitted by the filament on the deposition stage (in the case of radiation heating) and to evacuate electrons (in the case of electron bombardment heating). Without this layer a significant amount radiation is absorbed directly by the epitaxial film, resulting in high and uncontrollable temperatures.

The substrates sit on a 0.5 mm wedge onto Omicron-type plaquettes, they are held with two Mo springs and the plaquettes is placed on one-inch Riber molyblocks. The sample back-side directly "sees" the heating filament of the molyblock holders. Substrate temperatures up to 1500 K and 1100 K can be achieved with this setup with electron-beam heating and radiation heating

respectively, calibrated by an optical pyrometer and controlled routinely by a thermocouple in direct contract with the rear of the molyblock.

After introduction in the UHV system, the substrates are annealed to 1100 K twice during 45 min.

2.3.2 Single crystals

Single crystals polished with a (111) surface termination, with surface orientation better than 0.1°, purchased from Mateck and Crysteck, were prepared by repeated cycles of Ar^+ ion bombardment and flash annealing to 1500 K. Ion bombardment consisted of a first step with 1.5 keV ions and of a second step with 0.8 keV ions preventing deep ion implantation. In order to eliminate carbon contaminations from Ir bulk, prolonged 1100 K glowing under an oxygen back-pressure of 10^{-8} mbar was conducted.

2.4 X-ray magnetic circular dichroism

XMCD was first demonstrated in 1987 [230]. It consists of a varying x-ray absorption of a magnetic substance depending on the polarization of the x-rays. This difference can quantitatively analyzed in terms of orbital and spin moment contributions to the total magnetic moment of the substance. Being based on absorption measurements, the technique is chemically sensitive, allowing to discriminate the contribution of various magnetic species inside the same specimen. Being an absorption technique it exploits the broad energy range available at synchrotron sources, and thanks to the high brillance of the latter, it allows to probe very low amounts of magnetic matter, typically in the range of a percent of an atomic layer at third generation synchrotron sources (undulator beam-lines). The technique is thus currently applied to small size nano-structures and molecular magnets.

2.4.1 X-ray absorption

X-ray absorption occurs when a photon excites a core electron to an unoccupied valence state [figure 2.7], i.e. if its energy is above the difference in energy between the two electronic levels and if quantum mechanical selection rules are respected. The so-called corresponding absorption edges are called after the nature of the initial state of the core electron, K, L_1, L_2, L_3, M_1, if the initial state are $2s$, $2p_{1/2}$, $2p_{3/2}$, $3s_{1/2}$, respectively, for instance [231].

In a x-ray spectroscopy (XAS) measurement the energy of the x-rays is tuned across an absorption edge and the x-ray intensity transmitted through the sample, the fluorescence, or the current induced in the sample by the absorption of the photons (total electron yield, TEY), is measured. The TEY, which we measured in our experiments, probes all secondary electrons created in the sample, regardless of their kinetic energy. The number of these electrons is proportional to the number of excited atoms, thus proportional to the number of absorbe photons. The measured signal is usually more complex than a mere step function versus energy, which would be expected if only the core to unoccupied valence state transition would occur. Indeed it may for instance include contributions from dipolar transition, yielding resonant effects close to the edge, referred to as white lines.

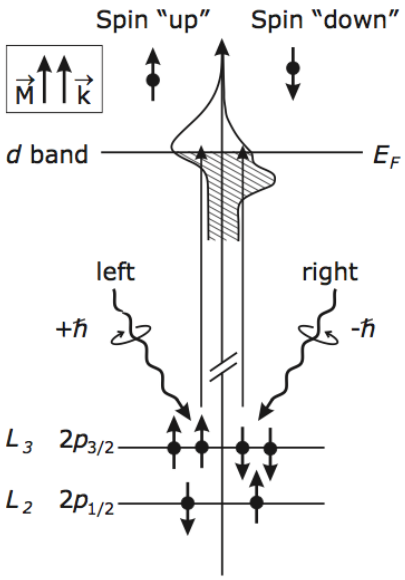

Figure 2.7: Illustration of the two step model for XMCD. In the first step spin-polarized photo electrons are generated. In the second step they are detected by the spin-split final states. [231]

2.4.2 X-ray magnetic circular dichroism

In a x-ray magnetic circular dichroism (XMCD) experiment, XAS is measured with x-rays having left and right circular polarization. The XMCD signal is obtained by (i) computing the difference of the XAS spectra (μ^+ and μ^-) obtained for the two polarizations and (ii) normalizing this difference to the isotropic XAS subtracted from the fraction of the absorption signal originating from the core to unoccupied valence state transition, which is a step-like function [232] of the Fermi-type, for the form

$$\mu_{\text{step}} = h\left(1 - \frac{2}{3}\frac{1}{(1+\exp^{(\frac{E-E_3-\epsilon}{\delta})}} - \frac{1}{3}\frac{1}{1+\exp{(\frac{E-E_2-\epsilon}{\delta})}}\right) \tag{2.12}$$

for the $L_{2,3}$ Co absorption edges (exhibiting maximum absorption at $E_{2,3}$), where ϵ is the position of the step with respect to $E_{2,3}$, δ is the step width and h the total step height. For the $3d$ ferromagnets, ϵ and δ are determined from a measured reference spectrum of a bulk-like film such that the application of the sum rules (see below) yields the value from literature for the magnetic moments. Eventually, the spectra are normalized to unity, to obtain the absorption and the magnetic information per atom.

The basic principle of XMCD is explained by a simple two-step model for the case of $3d$ transition metals [figure 2.7] [233]. In the first step, the interaction between x-ray and the metal yields a spin polarization of the excited electrons due to the strongly spin-orbit-split core level [234]. Left (right) circularly polarized x-rays excite more spin-up (spin-down) electrons from the $2p_{3/2}$ state to $3d$ state. The opposite occurs for the $2p_{1/2} \rightarrow 3d$ transition. In the second step, the final states determined by the selection rules act as a spin detector. The quantization axis of the detector is given by the magnetization direction.

The so-called sum rules analysis provides independently the ground-state expectation value

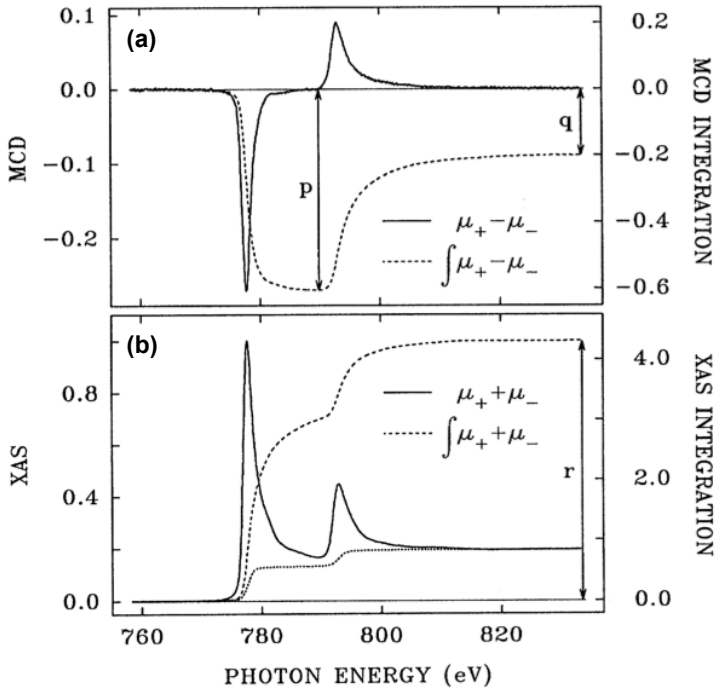

Figure 2.8: $L_{2,3}$ edge XAS and MCD spectra of cobalt: (a) the MCD and summed XAS spectra and their integrations. The dotted line shown in (b) is the two-step-like continuum function for edge-jump removal before the integration. The p and q shown in (a) and the r shown in (b) are the three integrals needed in the sum-rule analysis. [232]

of $\langle L_z \rangle$ [235] and $\langle S_z \rangle$ [236]:

$$\frac{L_z}{n_h} = \frac{4}{3}\frac{\int_{j_+ + j_-}(\mu_+ - \mu_-)\mathrm{d}E}{\int_{j_+ + j_-}(\mu_+ + \mu_-)\mathrm{d}E} \cdot \frac{l(l+1)}{c(c+1) - l(l+1) - 2} \tag{2.13}$$

$$\frac{2S_z}{n_h} = \frac{1}{3}\frac{\int_{j_+}(\mu_+ - \mu_-)\mathrm{d}E - \frac{c+1}{c}\int j_-(\mu_+ - \mu_-)\mathrm{d}E}{\int_{j_+ + j_-}(\mu_+ + \mu_-)\mathrm{d}E} \cdot \left(\frac{l(l+1) - 2 - c(c+1)}{6c} + \frac{l(l+1)l(l+1) + 2c(c+1) + 4 - 3(c-1)^2(c+2)^2}{12lc(l+1)}\frac{T_z}{S_z}\right)^{-1} \tag{2.14}$$

where $c = 1$ corresponds to the angular moment of the excited $2p$ state and $l = 2$ corresponds to the angular moment of the probed $L_{2,3}$ edges ($c = 2, l = 3$ for $M_{4,5}$ edges of the excited $3d$ states). The integral is over the energy range around the two spin-orbit-split states which are excited by the incoming photon, labelled with $j_\pm = c \pm 1/2$. $N_h = (4l + 2 - n)$ is the number of holes in the probed state with n the occupation number.

For Co, this gives:

$$\frac{m_L}{n_h} = -\frac{4}{3}\frac{\int_{L_3+L_2}(\mu_+ - \mu_-)\mathrm{d}E}{\int_{L_3+L_2}(\mu_+ + \mu_-)\mathrm{d}E} = -\frac{4}{3} \cdot \frac{q}{r} \tag{2.15}$$

$$\begin{aligned}\frac{m_{\mathrm{S}}}{n_{\mathrm{h}}} &= -\frac{3\int_{L_3}(\mu_+ - \mu_-)\mathrm{d}E - 2\int_{L_3+L_2}(\mu_+ - \mu_-)\mathrm{d}E}{\int_{L_3+L_2}(\mu_+ + \mu_-)\mathrm{d}E}\left(1 + \frac{7}{2}\frac{T_{\mathrm{z}}}{S_{\mathrm{z}}}\right)^{-1} \\ &= -\frac{6p - 4q}{r}\cdot\left(1 + \frac{7}{2}\frac{T_{\mathrm{z}}}{S_{\mathrm{z}}}\right)^{-1}\end{aligned} \tag{2.16}$$

where:

$$p = \int_{L_3}(\mu_+ - \mu_-)\mathrm{d}E \tag{2.17}$$

$$q = \int_{L_3+L_2}(\mu_+ - \mu_-)\mathrm{d}E \tag{2.18}$$

$$r = \int_{L_3+L_2}(\mu_+ + \mu_-)\mathrm{d}E \tag{2.19}$$

In the analysis presented in the second part of this manuscript, we assumed a value of 2.49 for $n_{\mathrm{h}} = 4l + 2 - n$, the number of holes in thin Co films [232]. We note that however, the ratio of orbital to spin moment; $m_{\mathrm{L}}/m_{\mathrm{S}}$, which we often present, does not depend on the values chosen for n_{h} (2.15 and 2.16).

2.5 Spin-polarized low-energy electron microscopy

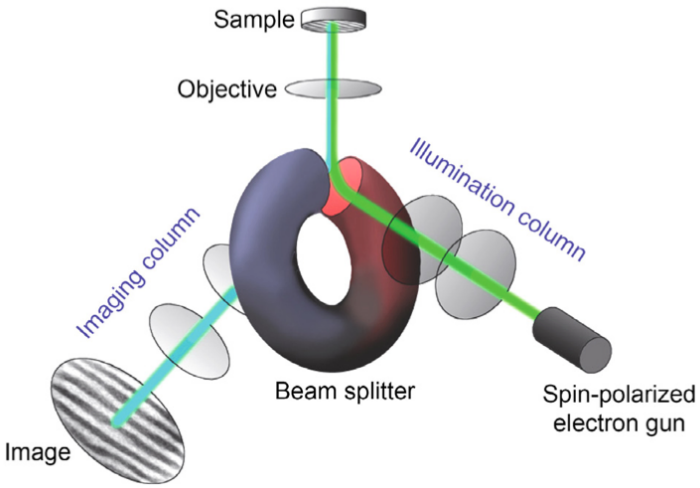

Figure 2.9: Schematics of a SPLEEM microscope. Spin-polarized electrons, photoemitted from a GaAs photocathode, are injected into a spin manipulator where azimuthal and polar orientation of the polarization is adjusted. Then, the electron beam passes through an illumination column, before being decelerated in the objective lens. Electrons finally hit the surface with normal incidence. Electrons that are backscattered elastically are collected in an imaging column and focused on a phosphorous screen, where a magnified image of the surface is obtained. The incoming and reflected electron beams are separated in a magnetic beam splitter using the Lorentz force [237].

In a low-energy electron microscope (LEEM) electrons with energy below 100 eV shine the surface of a sample, and the reflected electrons are employed to perform an image of the surface sample, with a ca. 10 nm lateral resolution, with the help of electromagnetic lenses [figure 3.9]. The electron reflectivity depends on both the structure and electronic band structure, and thus has a certain degree of chemical sensitivity. It can be probed as a function of the electrons' energy, providing a spectroscopic signature of the surface. Due to the low energy of the electrons the technique is highly surface sensitive, typically the few topmost atomic planes of a sample. By imaging rather the Fourier plane than the image plane it is possible to measure low-energy electron diffraction patterns.

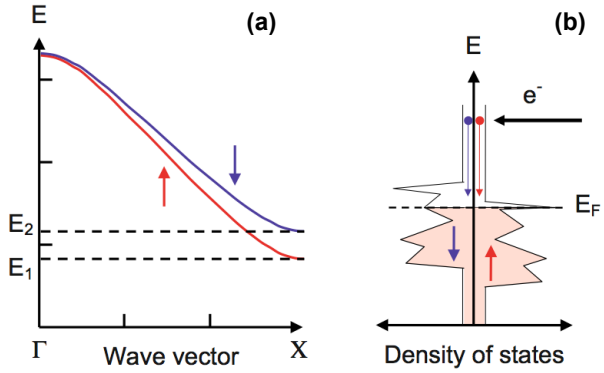

Figure 2.10: Two mechanisms leading to a different number of majority- and minority-spin electrons reflected from a ferromagnetic surface. (a) Sketch of the spin-split band structure in a ferromagnet along the (Γ) crystal direction. For an incident beam of energy ranging from E_1 to E_2, majority-spin electrons enter the crystal, while minority-spin electrons are effectively reflected due to the lack of available states. (b) Density of states in a ferromagnetic metal. Due to the differnt number of unoccupied electron states above Fermi energy for the two spin directions, the inelastic mean free path between electron-electron collisions is larger for majority spins than for minority spin. [237]

The origin of magnetic contrast in a spin-polarized LEEM is obviously much different from that discussed in other sections of this chapter. The electron reflectivity depends on the spin of the electrons due to the spin-orbit interaction in the material and due to the exchange interaction in the probed material, the latter being the prominent effect. Another effect, indirect, is due to electron-electron collisions: the inelastic mean free path of hot electrons depends on the spin of the electrons, since it depends on the number of s and d electronic states which are available for hot electrons above the Fermi level. Due to the higher number of such electronic states for minority than majority spin electrons in a ferromagnetic material [figure 2.10], the reflectivity of majority spin electrons is higher (less channels for de-excitations) [228].

In practice, measuring a SPLEEM image consists in measuring LEEM images with spin-polarization of the incoming electrons in two opposite directions, and normalizing by the average intensity. Each pixel of the image thus has the intensity

$$I_{\text{pixel}} = \frac{I_\uparrow - I_\downarrow}{I_\uparrow - I_\downarrow} \tag{2.20}$$

where, $I_\uparrow$ and $I_\downarrow$ are the pixel intensities for the two polarizations. As stated before, the

direction of the polarization can be chosen in any direction in space.

2.6 Standard characterizations

2.6.1 Raman spectroscopy

Raman spectroscopy and cartography was conducted *ex situ* with a Witec Alpha 500 spectrometer using a green laser (wavelength 532 nm) and 1 mW/μm^2 power. The signal is detected by a cooled-down CCD camera. The spectrometer is a 1800 lines/mm grating allowing spectral resolution of 0.01 cm^{-1} for 1O s acquisition time. Raman scattering was performed in a confocal mode using a $\times$100 objective (numerical aperture 0.9) yielding a spot-size fixed by the diffraction limit, of 320 nm, fixing the lateral resolution in Raman maps. For Raman mapping, the sample is placed on a x-y stage allowing displacements as small as 4 nm (i.e. well beyond the resolution imposed by the diffraction limit).

2.6.2 High resolution transmission electron microscopy

Cross-section high resolution transmission electron microscopy (HRTEM) was conducted *ex situ* using a JEOL 4000EX setup, at INAC/SP2M/LEMMA, CEA-Grenoble, with an acceleration voltage of 400 kV and a point resolution of 0.17 nm. Cross-section spicemens were obtained by mechanical grinding for thinning and ion milling using a precision ion polishing system.

2.6.3 X-ray diffraction with an anode

X-ray diffraction was conducted *ex situ* at the Néel Institute. In the scope of this thesis, we used x-ray pole figures to probe epitaxial orientation of multilayer stacking, yielding a stereographic projection of the scattered intensity, along the azimuthal (φ) and tilt (ψ) angles of samples. With the help of this technique the crystalline orientation and structure of the samples can be determined.

2.6.4 Magneto-optical Kerr effect characterizations

Magnetization revesal was probed by the mangeto-optical Kerr effect (MOKE). With a first setup, we gathered hysteresis loops, using a red laser (wavelength 633 nm) illuminating the surface over a few-μm wide spot. The incidence of the laser is 30° away form the surface normal, in which case MOKE is essentially sensitive to perpendicular magnetization (polar MOKE). the incident beam is linearly polarized. The reflected beam is split with a Wollaston prism to compute a difference signal, which is proportional to the magnetic moment of the sample perpendicular to the plane. The magnetic field was applied perpendicular to the surface. The hysteresis loops were averaged over hundreds to thousands of cycles performed at 11 Hz.

MOKE was also conducted in the view of performing magnetic microscopy, using a commercial microscope (Evico-magnetics). The images are recorded using a CCD camera. For all images presented in the second part of this manuscript, the initial image corresponding to saturatet magnetization was subtracted. Since polar Kerr effect reveal domains with a out-of-plane magnetization, it is suitable for imaging domain propagation for the thin films studied in the second part of this thesis, which have such a magnetization. The amount of mater in these samples was such that real time monitoring was possible.

2.6.5 Extraordinary Hall effect measurement

Extraordinary Hall effect (EHE) measurements were carried out at 300 K an up to 6T using the four-probe configuration. Mechanical as well as Ag-paint contacts were used on the non-patterned, i.e, as-grown, samples. EHE occurs when a magnetic filed applied perpendicular to the surface of a magnetic films.

2.7 First-principle calculation details

First-principles calculations were performed by M. Chshiev and H.-X. Yang at SPINTEC. They used the Vienna *ab initio* simulation package (VASP) [238, 239], with the generalized gradient approximation (Perdew-Burke-Ernzerhof) and projector augmented wave potentials [240].

The calculations were performed in two steps. First, out-of-plane structural relaxation was allowed and the Kohn-Sham equations solved with no spin-orbit interaction taken into account for determining the most favourable adsorption geometry of graphene on Co. Then the spin-orbit coupling was included and the total energy of the system was determined as a function of the orientation of the magnetic moments. The k-point mesh used in all calculations is $15 \times 15 \times 1$ sufficient to ensure good convergence in the total energy differences. The kinetic cutoff energy for the plan-wave basis set used to expand the Kohn-Sham orbitals was 520 eV. The Methfessel-Paxton method is used with a broadening of 0.2 eV for the partial occupancy smearing calculations. The atomic structures are relaxed until the Hellmann-Feynman forces acting on ions are smaller than 0.01 eV nm^{-1}. For the anisotropy calculations, the total energies are converged to 10^{-7} eV. A 2 nm vacuum slab was added on each side with periodic boundary conditions. The in-plane lattice constant was fixed to 0.2507 nm of *hcp* Co, and graphene was assumed to be pseudomorphic to Co. The vacuum thickness was chosen so as to avoid interactions between the two surfaces. Using these DFT calculations, we investigated the magnetic behaviour of Co/Interface and work function of Co surface with the graphene coverage [241].

Part II

RESULTS and DISCUSSION

1

Graphene on Ir(111) thin films on sapphire

Contents

In this chapter I present the UHV preparation of thin Ir films with a (111) surface termination prepared on sapphire substrates. Adjusting the growth conditions we were able to prepare single crystalline thin films of ca. 10 nm thickness, exhibiting atomically smooth terrace whose width is set by the width of the sapphire terraces. The structure of the thin films was carefully characterized with the help of complementary and *in situ* and *ex situ* techniques, STM, RHEED, HRTEM, XRD, and Raman spectroscopy. The growth method relies on pulsed laser deposition at low growth rates, performed at 700 K. 1100 K annealing allows to substantially improve the thin film quality. On these metal films, the growth of graphene occurs in a similar fashion as on bulk single crystals.

This work has been performed during 2009, and published at a moment when within a few-months period of time similar reports, using other substrates and/or other thin films were published as well.

1.1 Introduction—High quality metallic thin films as supports for graphene growth

Since 2004, there has been an increasing effort in developing efficient methods for preparing graphene, mostly motivated by the prospect of applications. By chemical vapor deposition (CVD) on transition metal surfaces large-area few-layer epitaxial graphene can be obtained and then in principle transferred to any support.

CVD of graphene has been long performed on bulk transition metal single crystals under ultrahigh vacuum (UHV) [166]. In 2008, more versatile methods for CVD were introduced, using polycrystalline Ni films on Si wafers or commercial foils as substrates. CVD was also operated

closer to atmospheric pressure [75, 242, 181]. However, due to the relatively high solubility of carbon in Ni. the precise control of the graphene layer thickness down to single layer turned out to be difficult [242]. This limitation was partly circumvented by employing Cu (films or foils), indeed, for which C solubility is much lower (Section 1.4). Yet, multilayer graphene could not be avoided at the location where Cu grain boundaries cross the surface [243]. Moreover polycrystalline metal films impose twinned domains in graphene, with length scale in the range of the distance between graphene nucleation centers (typically a few 10 μm). Intrinsic limitations to the quality of graphene are also imposed by substrate roughening at the high temperatures required for CVD. Above 1000 K under UHV, the sublimation of Cu occurs locally, in particular, on graphene-free region and induces roughness on the surface [244]. Since graphene's properties depend on the number of layers, and charge carrier scattering takes place at grain boundaries or substrate-induced rippling (both altering charge carrier's mobility), higher and better defined performances could be expected for higher quality metallic supports.

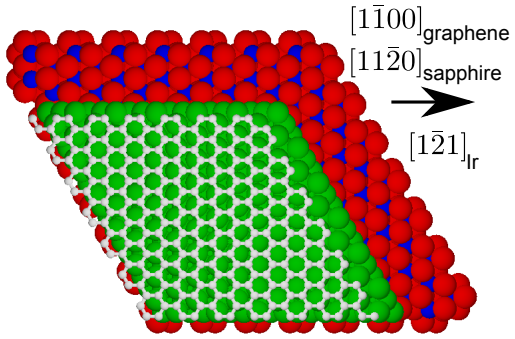

Figure 1.1: Ball-model of graphene/Ir/sapphire (white: graphene, green: Ir, blue and red: sapphire). Using the graphite index for graphene.

Using a single crystalline metal film onto which a continuous and transferable graphene sheet with single crystallographic orientation could be achieved is thus an attractive route. At the moment our work have been published a number of other reports appeared. Single crystalline Co films with a thickness of 200 nm were obtained by high temperature sputtering on Al_2O_3 (c-sapphire) substrates, and were employed for atmospheric CVD of graphene. Despite of the substantial high temperature carbon solubility of C on this metal, graphene was essentially single layer, as shown at millimeter scale by Raman spectroscopy measured on graphene transferred to SiO_2. This suggests that in the absence of grain boundaries in the metal multilayer region do not tend to form. Scanning electron microscopy however revealed the presence of multilayer patches on a 10 mm $\times$ 10 mm surface [174], possibly at the location of grain boundaries. Almost at the same time, epitaxial 50–100-nm-thick Ru films were obtained on c-sapphire by radio-frequency magnetron sputtering, yielding a highly crystalline surface. Besides STM which revealed the moiré between graphene and Ru(0001), micro-Raman analysis showed that the quality of graphene was still high for graphene resting on sapphire following chemical etching of Ru [245]. Still on c-sapphire, 400-nm-thick Cu films grown by thermal deposition allowed the growth of graphene. Large area and high quality graphene layer was confirmed by Raman spectroscopy after the transfer of graphene to SiO_2 [190]. On a MgO(111) substrate, 100 nm-thick Ni films were evaporated for the same purpose. Epitaxial graphene showed a quality as high as that of graphene grown on a bulk single crystal, as shown by LEED, ARUPS, and XPS characterizations. Transfer of graphene was also demonstrated in this system [246]. The

main interest for these crystalline thin films is the absence of grain boundaries which may be detrimental to the quality of graphene.

In the following sections, I report the preparation of single crystalline nanometers-thick Ir films on sapphire [figure 1.1], onto which graphene of high quality can be prepared. This stacking was developed to serve as a model system for multi-technique investigations of the properties of graphene contacted to a metal, including *ex situ* (which is no so convenient with bulk single crystals).

1.2 Structure of single crystal Ir(111) thin films on sapphire

Iridium was grown by PLD under UHV (base pressure 5 $\times 10^{-9}$ Pa) with a temperature-controlled process. C-plane sapphire (Al_2O_3) wafers was used as substrates. They were cut with either a focused laser or a diamond saw to fit in Omicron sample holder. Substrate cleaning followed the procedure described in Chapter 2—Part I and surface preparation of sapphire was completed by double outgassing at 1100 K under UHV during 45 min each one. The iridium layers were grown by PLD with 10 pulse per second, each pulse with a fluence in the range 0.1–1 J cm^{-2}, yielding an evaporation rate of the order of 0.05–0.1 nm min^{-1}. A computer-controlled mask could be move in front of the sample for producing wedge-shape layers, i.e., one sample with gradually increasing thickness in stead of numerous samples with different thickness, for reducing the cost and time in study. The optimized procedure in our investigation is the growth of 10 nm thickness film at 700 K and a following annealing step at 1100 K for 30 min.

We first characterize the surface quality of Ir(111). Streaky RHEED patterns [figure 1.2(b,d)] suggest that the Ir(111) surface is atomically smooth at the scale of a few 10 nm. Kikuchi lines are further evidences for the quality of the surface [figure 1.2(d)]. These patterns correspond to a crystalline surface of six-fold symmetry, consistent with the volume characterization (x-ray diffraction and TEM in the following). STM images reveal rough surface before annealing [figure 1.3(a)] but exhibit atomically smooth terraces after annealing separated by single atomic step edges [figure 1.2(a,c)]. The terrace width is of about 60 nm or 300 nm width directly related to the miscut of the wafer. In our studies, the miscut values of sapphire are 0.25° [figure 1.2(a)] and 0.03° [figure 1.2(c)], but we found no effect of the miscut angle to further investigation, for instance, the growth or magnetism. Comparably smooth and wide terraces are obtained on bulk single crystals only after ion bombardment and high temperature flash ($\simeq$ 1600 K for Ir) which however promotes the formation of metal step bunches, here absent. The very thin metal films do not dewet upon annealing consistent with the high melting temperature of Ir not enabling massive transport at 1100–1500 K.

The 5 nm film exhibit a much more structured surface. One observed numerous domains with typical sizes of a few 10 nm and with boundary preferentially along a set of direction with hexagonal symmetry, i.e., Ir$\langle 101 \rangle$ ones corresponding to well defined crystallographic directions [figure 1.3(b)]. Moreover, a marked large-scale superstructure develops on the surface. This superstructure has also hexagonal symmetry and rather well defined orientation with periodicity of 21 ± 5 nm [figure 1.3(b)]. The plausible reason of this pattern is expected for the strain fields generated up to the surface by a network of misfit dislocation buried at the surface between Ir and sapphire, assuring that Ir has its bulk lattice parameters, i.e., 1.3% between Ir and sapphire with the α-$Al_2O_3(0001)[11\bar{2}0] \| Ir(111)[11\bar{2}]$ epitaxial relationship [247]. Note that for the 10 nms-thick films, the observation of the buried dislocation network is much more difficult, consistent with the exponential decay of the amplitude of the surface strain field with the film thickness.

The influence of the annealing step is obvious when comparing figure 1.2(a) and 1.3(a). For

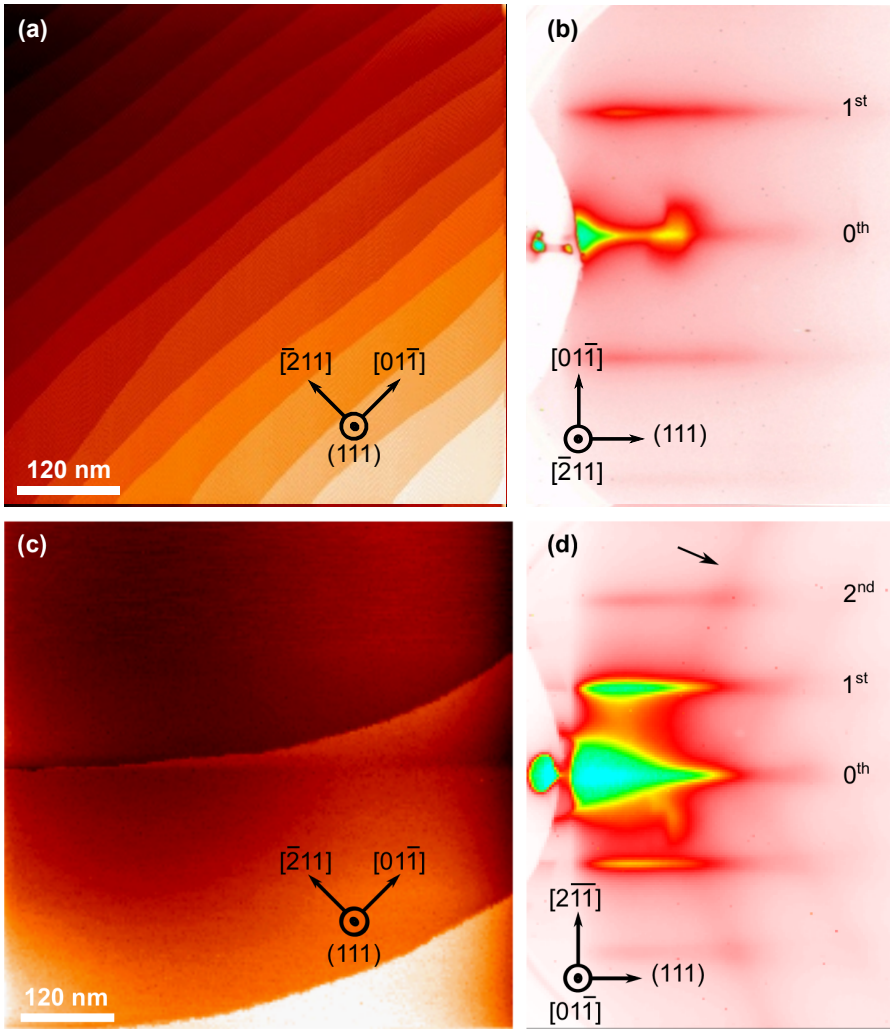

Figure 1.2: (a) STM topographs of 10 nm-thick Ir(111) films on sapphire after an annealing step at 1200 K, the contrast highlights atomic terraces whose width depending on sapphire miscut of (a) 0.25° ($\simeq$ 60 nm-wide terraces) and (c) 0.03° ($\simeq$ 300 nm-wide terraces). RHEED patterns (10 kV) at (b) $\langle 11\bar{2} \rangle$ and (d) $\langle 1\bar{1}0 \rangle$ azimuth showing the zeroth, first, and second order streaks of Ir(111) and Kikuchi lines (black arrow), revealing the single-crystalline quality of Ir. Crystallographic indexes refer to Ir.

mild annealing (900 K), the film surface exhibits curved features, which are atomic step edges, as well as lines which are 120° rotated one with respect to the other. We speculate that these are the surface traces of grain boundaries between 180° in-plane twins which are the only two domains for preserving the hexagonal symmetry of Ir/c-sapphire). These domains are also detected on the 5 nm-thick films with (200) x-ray ϕ-can [figure 1.5] and STM [figure 1.3(b)], i.e., with Ir(200) reflections in reciprocal space by azimuthal scan and with topograph in real space by near field measurement. In addition, the TEM images display the vertical grain boundaries observed near interface of the 10 nm films [figure 1.4(c)]. Iridium is fully relaxed to its bulk lattice parameter as evidenced by the formation of a network of misfit dislocations at the Ir/sapphire interface.

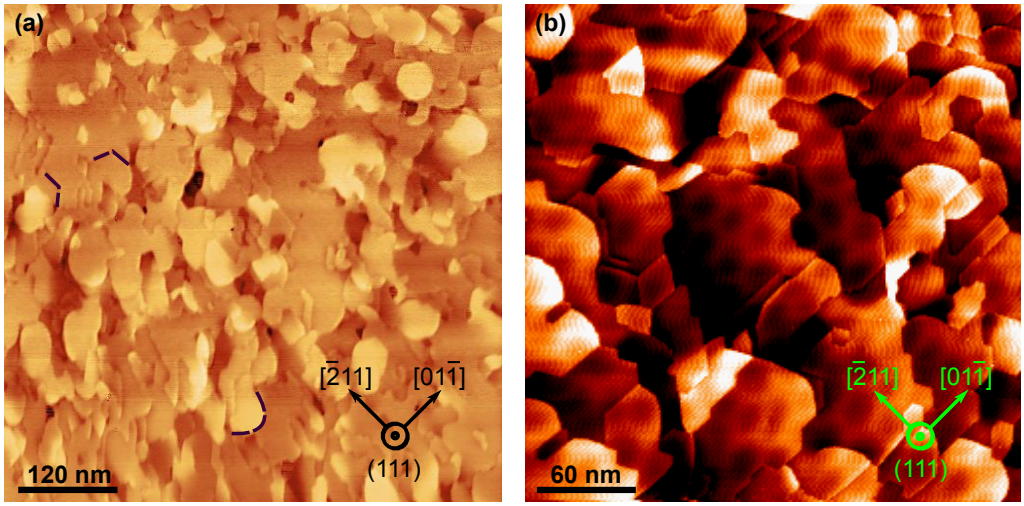

Figure 1.3: STM of (a) 10 nm-thick Ir(111) films annealed at 900 K and (b) of 5 nm-thick Ir(111) films annealed at 1200 K on sapphire. Dashed curves in (b) highlight two kinds of surface feature.

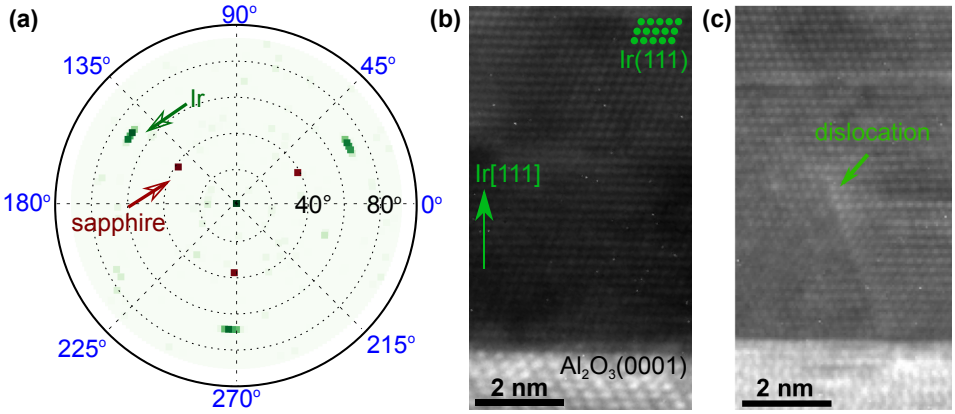

Figure 1.4: (a) X-ray pole figures (logarithm of the scattered intensity) for (10$\bar{1}$4) planes of sapphire (red) and a (111) planes of Ir (10 nm thick, grown at 700 K and annealed at 1100 K, green) on the same spherical coordinate system (azimuthal and scattering angles displayed in gray and black, respectively). The Ir Bragg peaks are broader than the sapphire ones, indicative of some spread in the epitaxial relationship. TEM cross sections of a 9 nm Ir film on sapphire, along the [1$\bar{1}$1] azimuth shows (c) crystalline region and twins near interface with sapphire. Green dots highlight the crystallographic structure of Ir. Crystallographic indexes refer to Ir.

We then address the crystalline structure of the Ir thin films. Figure 1.4(a) shows x-ray pole figures of sapphire and of the Ir thin film (10 nm). The threefold symmetry and Bragg diffraction angles prove that the Ir is (111)-textured and has a well-defined in-plane epitaxial relationship with sapphire, $\langle 11\bar{2}0\rangle_{\text{sapphire}} \| \langle 1\bar{2}1\rangle_{\text{Ir}}$ [figure 1.1], with a full-width at half maximum spread of 1° as derived from azimuthal angle scans. Before the 1100 K annealing step, x-ray φ-scan [figure 2.10], pole figures and STM evidence 180° twins along [111]. Consistently, TEM cross-sections [figure 1.4(b,c)] confirm that a single orientation is obtained on topmost atomic

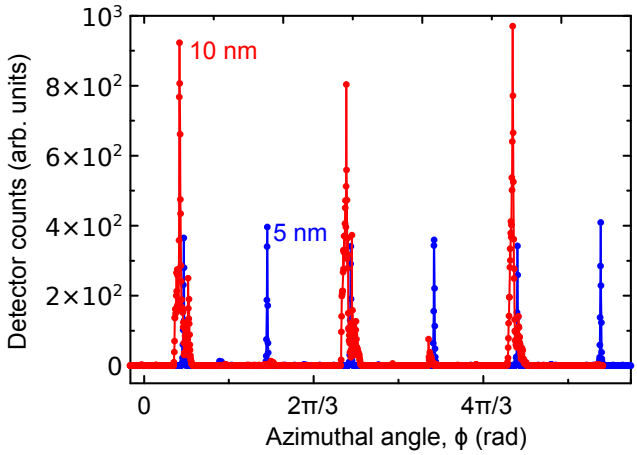

Figure 1.5: Scans of the azimuthal angle (ϕ) for first order (200) reflection for a 10 nm (red) and a 5 nm (blue) Ir thin films on c-sapphire.

layers following the annealing step, and that the Ir(111) films have a single-crystalline surface.

1.3 Structure of graphene on Ir(111) thin films

With a metallic surface of such high quality, graphene growth on the Ir(111) thin films proceeds like on bulk single crystals [207]. The ethylene (C_2H_4) gas was conducted in the vicinity of the sample surface by a dosing tube of 10 nm in diameter, ending 10 mm away from the sample surface. This setup ensured a local partial pressure higher than in the rest of the chamber, e.g., global pressure is in the range of 10^{-6} Pa during the CVD and in the range of 10^{-8} Pa as base pressure. The temperature of metallic surface set at 1200–1500 K, controlled by a thermal pyrometer, allows the catalytic decomposition of the hydrocarbon gas, for CVD graphene growth. After exposure under C_2H_4 flow in 20 min, the sample covered with single-layer graphene was cooled down by natural thermal radiation in UHV.

Small-angle twinned domains, having an extension between a few 10 to a few 100 nm, are found for growth performed at 1100 K, while a single crystallographic orientation, corresponding to the typical graphene/Ir(111) moiré [figure 1.6(b–d)], is found at 1400 K. The CVD growth proceeds graphene layer with full coverage ($< 100\%$ [figure 1.6(a, inset) and 1.8]. The uniform layer of graphene of high quality replicates the atomic smoothness of Ir(111) buffer layer by extending coherently across its atomic steps [figure 1.6(a) and 1.8].

The main orientation is $\langle 1\bar{1}00\rangle_C \| \langle 1\bar{2}1\rangle_{Ir}$, as shown by RHEED. Graphene rods are only found along the $\langle 1\bar{1}0\rangle$ azimuth of Ir(111) [figure 1.7(b)]. In this orientation, also superstructure rods from the moiré are observed [figure 1.7(a,b)]. The distances from the Ir, graphene, and moiré streaks to the central one allows to estimate the in-plane lattice parameters of graphene and the moiré, 0.246 ± 0.001 nm and 2.634 ± 0.014 nm, respectively, which is similar to the situation on bulk single crystals [220].

STM topographs display the typical wrinkles [242] and Ir step edge reshaping [207] [back and white arrow in figure 1.8]. One solution to minimize the density ripples is employing the TPG procedure at high temperature and then CVD at 1200 K, required temperature for the growth of high quality graphene. Neither STM nor RHEED detected any evidence of multilayer

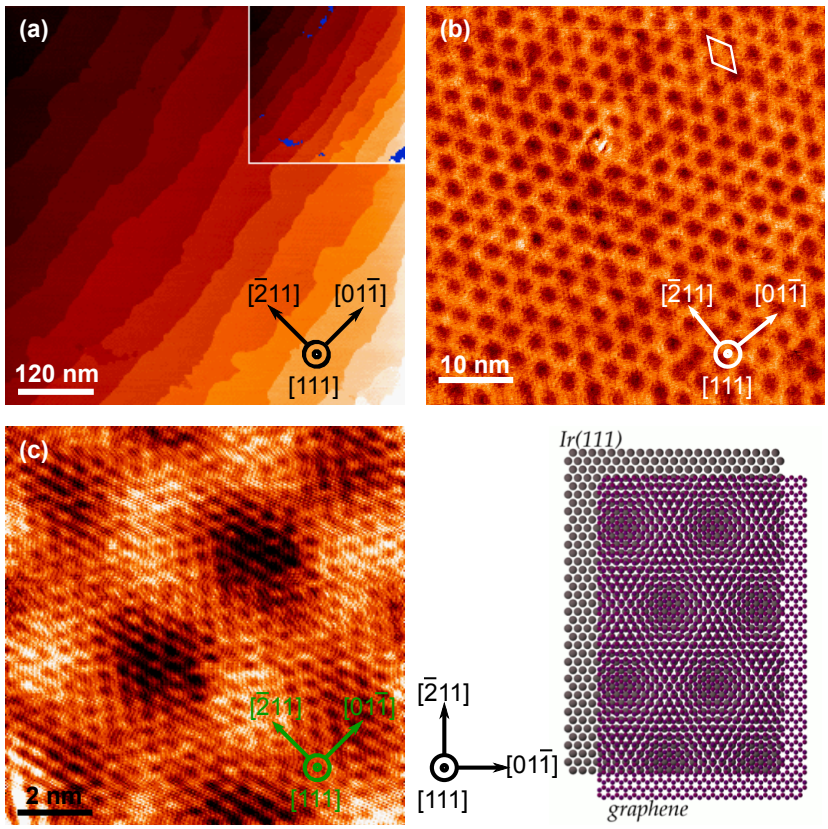

Figure 1.6: Single graphene layer grown at 1400 K on the Ir (111) film, in real space: STM topographs (a) of epitaxial graphene on Ir(111), (inset) the few remaining areas not covered by graphene are highlighted in blue, (b) evidencing the moiré (white rhombus) and (c) revealing the six-atom-carbon rings at atomic resolution. (d) Hexagonal atomic structures of Ir(111) surface (below, gray) and graphene (above, violet) [248]. Crystallographic indexes refer to Ir.

graphene as they well characterized single layer of graphene on the Ir surface.

The Raman spectra presented in figure 1.9(a) is averaged over a 20 μm $\times$ 20μm region. It shows the characteristic features for single-layer graphene, i.e., the G and 2D peaks, whose frequency shifts are 1594 cm^{-1} (FWHM: 7 cm^{-1}) and 2688 cm^{-1} (FWMH: 17 cm^{-1}), respectively. The I_{2D}/I_G ratio$>$ 1 and the shape of the 2D peak are strong evidence of single-layer graphene [249]. As compared to graphene on others supports (epitaxially grown or exfoliated), G and 2D band positions are both shifted to higher frequency and their FWHM are extremely sharp, most prominently for the G band. These observations indicate a charge transfer between graphene and its Ir support [249], the sign of the shift suggesting p-doping of graphene, which agrees with photoemission spectroscopy [250]. The absence of a D band implies that graphene is quasi-defect-free, consistent with the STM data. One could expect the wrinkles rising the D peak like in Raman spectra of CNT [251], but the wrinkles/graphene area ratio is negligible to induce observable D peak. The narrow width of the G band rules out the presence of amorphous carbon. The strong background observed for all spectra is due to Ir luminescence. Previous attempts in measuring Raman spectra for graphene on Ir bulk single-crystals remained unsuccessful. But Starodub et al. claimed that hybridization of the π band is responsible for the

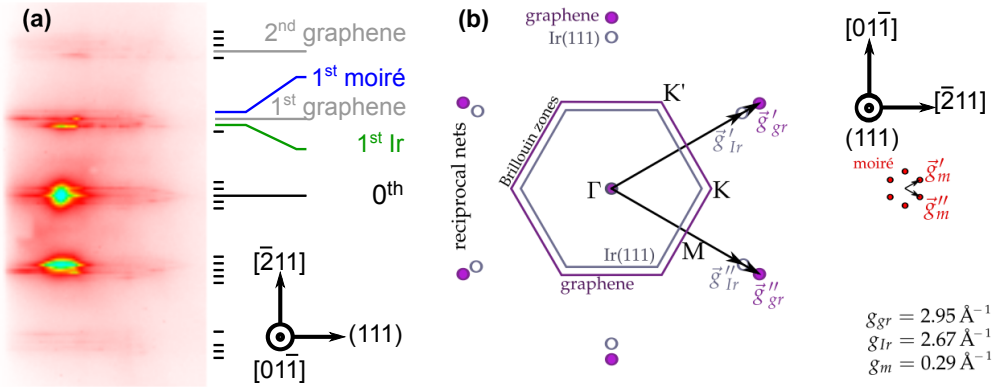

Figure 1.7: Single graphene layer on the Ir (111) film in epitaxial relationship $\langle 11\bar{2}0\rangle_{\text{sapphire}} \| \langle 1\bar{2}1\rangle_{\text{Ir}}$ in reciprocal space: (a) RHEED pattern of graphene/Ir(111) (10keV, $\langle 1\bar{1}0\rangle$) azimuth). First order Ir, graphene, moiré streaks are highlighted as well as the zeroth order streak and one second order moiré streak. (b) Brillouin zones of Ir(111) and graphene together with the moiré superstructure [248]. Crystallographic indexes refer to Ir.

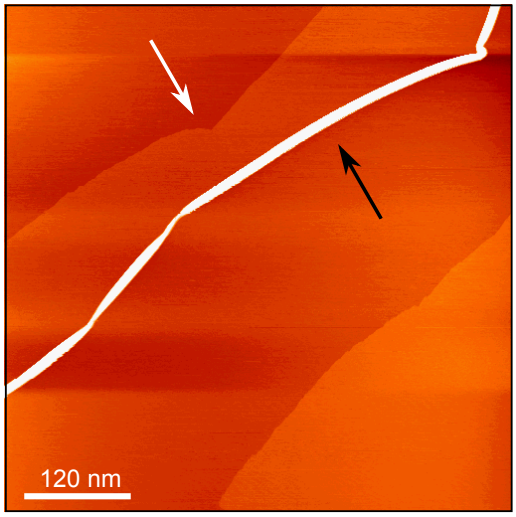

Figure 1.8: STM topographs showing graphene wrinkles (black arrow) as well as reshaping of underneath Ir step edges of graphene/Ir(111) (grown at 1400 K).

loss of the Raman signal of the main graphene domain [252]. In this case, our Raman observation could be obtained from rotational domains which coexist with the main domain grown by CVD on Ir(111) [208]. Figure 1.9(b-d) shows a large-are spatial maps of the Raman G band intensity, 2D density and 2D position. These maps are remarkably homogeneous on graphene-covered regions while the black areas are graphene-free regions. The observed fluctuations are artifacts originating from low signal-to-noise ratio due to the strong Ir backgound. We propose that the presence of holes on graphene allows for the intercalation of species between graphene and Ir substrate upon exposure to the air. This might strongly decouple graphene (including the main domain) on Ir and could also explain the discrepancy of Raman spectra between our observation in air and that of Starodub et al. [252].

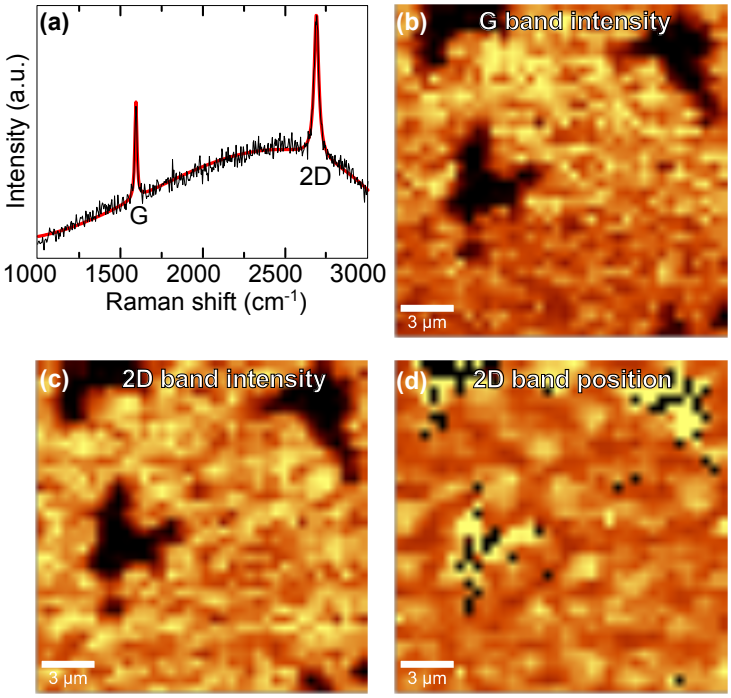

Figure 1.9: (a) Raman spectrum showing G and 2D peaks and $30 \times 30\mu$m maps of the (b) G density, (c) 2D density and (d) 2D position. (laser wavelength: 532 nm, power: 1.7 m W μm^{-2}).

1.4 Conclusion and perspectives

I have shown that extremely high quality, large area, single layer graphene can be prepared by UHV CVD on 10 nm-thick single crystalline Ir(111) films grown on sapphire wafers. These new samples are especially suited for multi-technique characterizations as we have shown and we will further show in this manuscript. Moreover they open a route towards high quality graphene production. The transfer of graphene to arbitrary supports whose choice will be governed by the triggered application, is the next step. Preliminary works in this direction, with electrochemical etching of Ir, indicate that transfer to sapphire is possible.

I mention that soon after we optimized the graphene/Ir/sapphire system, Zeller et al. developed a related system, consisting of 150 nm-thick Ir thin films deposited on an yttria-stabilized zirconia buffer layer (40–150 nm) on Si(111) [253]. This system also appears suitable for the growth of high quality graphene. The mosaic spread of the Ir thin films in this system, below 0.2°, is better than in the case of our system (1°) while our preparation procedure seems more straightforward.

2

Thin epitaxial cobalt films on graphene on Ir(111)

Contents

In this Chapter, I present the preparation, structure, and magnetic properties of the first ferromagnet/graphene hybrid system which we have developed. We have used the graphene/Ir/sapphire system whose preparation has been described in the previous chapter, and prepared Co ultra-thin films on top by PLD. Thanks to this technique we were able to prepare flat Co films, whose structure was improved by a mild annealing. Before *ex situ* analysis the samples were capped with a Au layer. STM, RHEED, HRTEM, performed *in situ* allowed to unveil the structure of the system. *Ex situ* focussed Kerr magnetometry and microscopy, EHE measurements, and UHV XMCD allowed to address the magnetic properties of the Au-capped systems. The results were compared to spin-polarized DFT calculations.

We found that the thin films display perpendicular magnetic anisotropy in the thickness range between 0.65 and 1.30 nm, in agreement with first-principles calculations. The domain propagation follows a thermal creep-like regime with domain size larger than 1 μm, and a magnetic field as low as 3.5 mT reversing magnetization in 1-nm-thick Co film. Comparing these results with those obtained for Co films of the same thickness, but not annealed, and with Co films directly on Ir (i.e. without graphene) reveals that the annealing step favors perpendicular magnetic anisotropy and that graphene enhances this tendency, presumably thanks to the hybridization between C and Co atoms. Non-metallic contributions observed in absorption experiments support this latter point. The sum rules calculations from XMCD signals also hint at covalent bonding between Co and C atoms, and display a decrease of the Co magnetic moment, in comparison with bulk Co.

2.1 Introduction—Graphene/ferromagnet hybrid systems

The promising potential of graphene in spintronics, exceeding that of other carbon materials, has been highlighted in a wealth of theoretical predictions over the last few years. Similarly to carbon nanotubes, efficient spin transport and injection have been proposed, making use of the low spin-orbit and hyperfine interactions in carbon, combined with a high conductivity. The superiority of graphene is to bring this in two dimensions, which allows complex networks to be designed by lithography, and promises a better control of the interfaces with other materials to build hybrid architectures. Large spin transport over few 100 μm has already reported [104].

Not only spin transport but also spin polarization in graphene is a topic of intense interest. For this, the two-dimensional (2D) nature of graphene is again appealing, either for shaping nanoribbons whose edges may intrinsically carry spin-polarized currents [254] or because extended contact to a suitable support is needed, including Rashba spin splitting of the conduction bands [9, 8, 255]. Graphene may also be inserted between two planar ferromagnets to build giant magnetoresistance junctions operated in a current perpendicular to the plane configuration, with neither too low (like for giant magnetoresistance) nor too high (like for tunnel magnetoresistance) resistance-area product, and with extremely thin spacers (see more in 1.2) [107, 10].

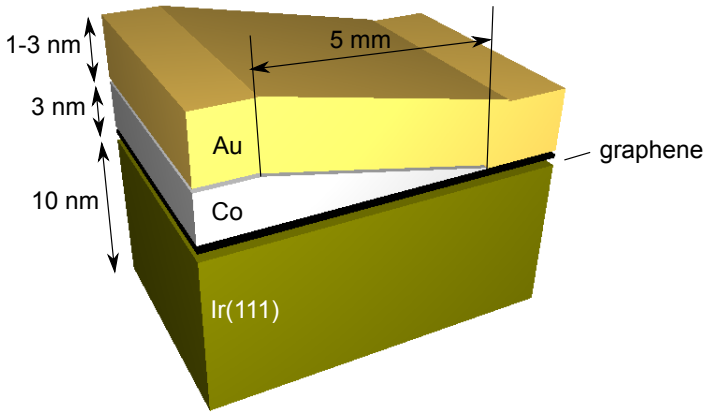

Figure 2.1: Schematics of a Co wedge deposit on graphene/Ir(111), capped by a Au layer. Typical thickness for the various layers are displayed.

The magnetoresistive effect oulined in the latter proposal calls for the availability of epitaxial ferromagnetic/graphene/ferromagetic trilayers, due to the importance of band matching with graphene [256]. This requires that epitaxial graphene be prepared on ferromagnetic supports, which was demonstrated years ago [257], and also requires the development of epitaxial 2D ferromagnetic layers on top of graphene. We foresee that such layers may serve as building blocks in a number of spintronics setups beyond the scope in an ultrathin 2D metallic ferromagnetic layer sandwiched between graphene and another metal layer of a heavy element such as gold. A strong out-of-plane electron potential gradient results from the structural inversion asymmetry imposed by the two distinct interfaces. This fields may exceed that in Pt/Co/alumina trilayers where a strong s-d-mediated Rashba field was recently proposed [258]. Also, contrary to relatively thick ferromagnetic substrates employed so far [8, 259], ultrathin films offer the opportunity to tune

the spontaneous magnetization direction as a function of the film thickness, from in-plane to perpendicular. Thus crossed spin-polarizers could be achieved.

To the best of our knowledge, there exists no report about trully 2D films of transition metals having a thickness ranging from one to a few atomic layers on either graphite or graphene. Molecular beam epitaxy (MBE) in ultrahigh vacuum yields 3D clusters even when the deposition is carried out down at temperature down to a few tens of Kelvins [260]. Superstructures such as moiré on graphite [261] or graphene (Figure 4), or on the reconstructed graphitic layer of SiC [262, 263], may provide 2D lattices of nucleation sites for the clusters. The growth mode of 2D (wetting) or 3D (dewetting) is determined by the minimum total energy of obtaining surfaces and interfaces. In the absence of superstructures, cluster nucleation is sparse and proceeds at defect sites or at random when the clusters are large enough to become immobile. Large adatom and cluster diffusion lengths on graphene and graphite were calculated by first principles [264, 265, 266], consistent with sparse nucleation.

Here, instead of MBE, we used PLD, which proved suitable to prepare ultrathin 2D thin films on graphene/Ir(111)/Al_2O_3(0001) [figure 2.1]. Iridium is a suitable supporting surface for this study thanks to self-limitation of a single graphene growth and a weak perturbation (rehybridization of C atoms) on the electronic properties of graphene (Section 1.4). Thus, the features of overgrowth Co and its magnetic properties are expected to be largely applicable to the case of isolated graphene.

2.2 Growth of two-dimensional ultrathin cobalt films on graphene

Graphene of high quality is grown by CVD on PLD Ir(111) thin film on c-sapphire, as exhibited in Chapter 1. For this system, the metallic films (Co and Au) were grown by PLD at room temperature. The magnetic film requires an annealing step at 750 K before deposition of capping layer.

At room temperature, PLD Co growth on graphene/Ir(111) nearly follows a layer-by-layer mode up to about 1.5 nm [figure 2.2]. Only monolayer-high islands and/or trenches are found, arising from the unavoidable non-integer mean number of atomic layers found at an arbitrary stage of deposition. This growth mode is noticeably different from that with MBE, which leads to metal clusters at the same temperature and in this range of thickness. We believe that the much higher instantaneous deposition rate of PLD leads to higher nucleation density of smaller clusters at the initial stages and during the growth. As a result, the pulsed metal plume tends to force layer-by-layer mode [267, 158]. However, we can not exclude that a few high energetic ions may create defects in graphene, also providing nucleation sites. This latter process was evidenced, e.g., for Co/Au [268, 158], and is demonstrated for our case in the next section. While the high bonding energy with graphene should go against this, the light weight of C atoms against impinging Co ions may allow for the creation of defects. At later stages mounds set in and roughness progressively increases, probably due to the progressive increase of mean island size.

For both regimes, the annealing of the deposit at 750 K yields a flat and crystalline Co film, with a mean terrace width again only limited by the miscut angle of the wafer [figure 2.2, 2.3]. Cobalt was finally capped at room temperature with 1.5–3 nm Au to protect the films from air oxidation for *ex situ* characterizations.

HR-TEM [figure 2.4(a)] confirms the smoothness and uniformity of the Co layer. The Co layer contains stacking faults [figure 2.4(b)] and can therefore be viewed as a mixture of hexagonal compact (*hcp*) Co (its stable structure in the bulk form at room temperature) [figure 2.6]

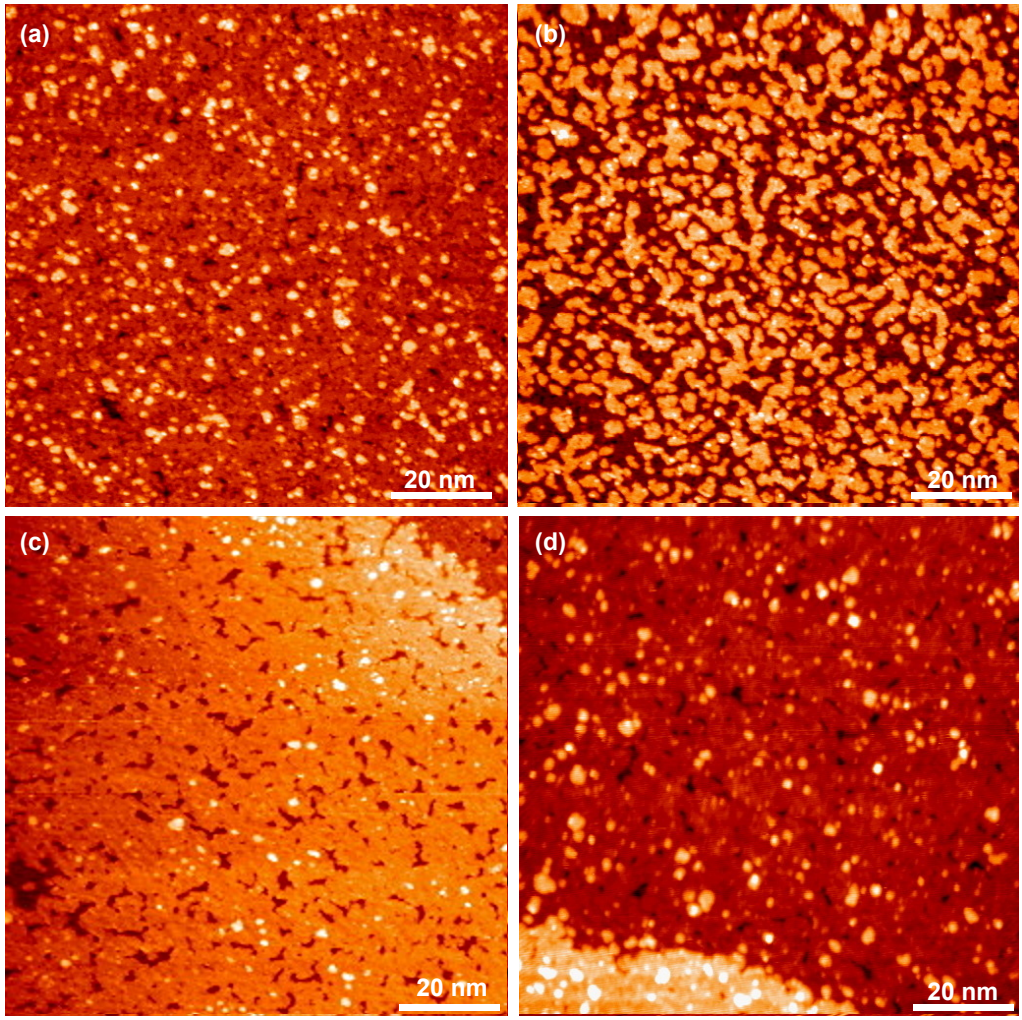

Figure 2.2: 100×100 nm^2 STM topographs (2.4 V, 0.8 nA) of Co PLD deposited at room temperature on graphene/Ir(111). The sequence illustrates a close to perfect layer-by-layer growth for Co, illustrate here for 3 (a), 3.4 (b), 4 (c) and 5 (d) atomic layers.

and face-centered cubic (*fcc*) Co (stable above 700 K in the bulk, but often stabilized in nanostructures). The graphene sheet can not be clearly identified on these images, probably due to the graphene—Co spacing being similar to that of Co [256].

2.3 Magnetic properties

Magnetic properties of as-grown and annealed films were probed in-the-lab with the MOKE magnetometry and microscopy and at synchrotron SOLEIL with XMCD, which are described in Chapter 2—Part I

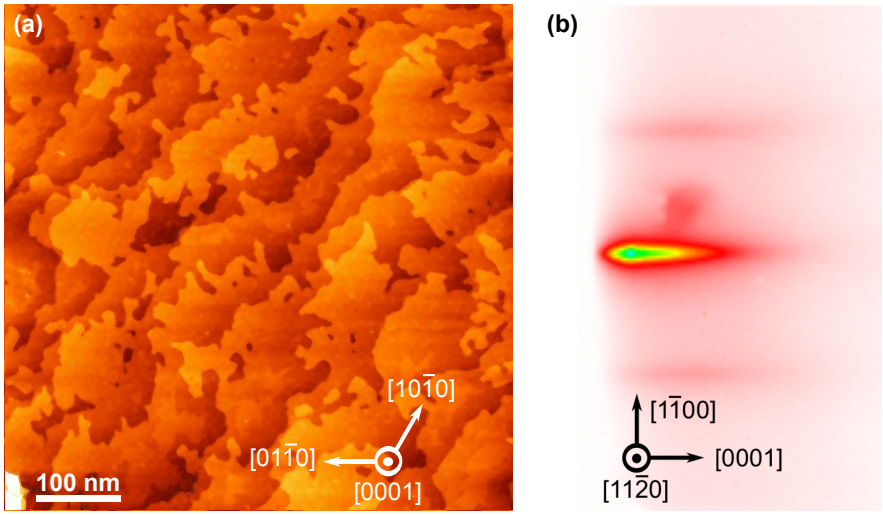

Figure 2.3: (a) 600×600 nm^2 STM topographs of Co film of thickness 1.7 nm ($\simeq$9 atomic layers) annealed at 450°C. (b) RHEED pattern (10 kV) at $\langle 11\bar{2}0$ azimuth showing the crystalline surface of Co. Crystallographic indexes refer to *hcp* Co.

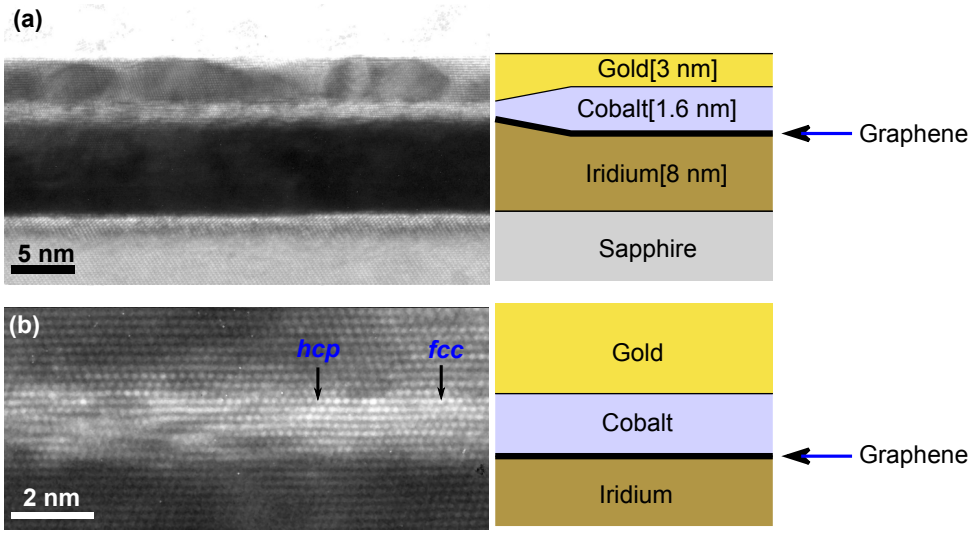

Figure 2.4: (a) Large and (b) close-up cross-sectional HR-TEM images of a 1.6 nm Co film capped with Au on graphene/Ir(111). In (b), stacking faults are observed in the Co atomic lattice and a mixture of *fcc* and *hcp* regions is seen.

2.3.1 Magnetic moments

Here, the XMCD results are discussed to study in detail the magnetic state of cobalt on graphene and are systematically compared with other known systems such as cobalt on iridium without graphene or with graphene but no annealing. Figures 2.5(a) and 2.5(b) display TEY absorption spectra of annealed and not annealed films of Co deposited on graphene, 0.8 nm-thick, and capped by Au. These were measured at 10 K and under an applied field of 5 T. Notice the

underlying multipeak structure of the L_3 edge, especially for the annealed sample. $3d$ oxides display such peaks, so the first explanation could be oxidation of the samples. However, samples grown under identical UHV conditions directly on Ir do not show these features. Generally speaking, such sub-peaks hint at the existence of well-defined energy levels, such a result from chemical bounds. These arise in oxides, however also in nitrides or carbides. Preliminary results of *ab initio* simulation of XAS (Y. Joly, Néel Institute, private communication) indeed display such peaks for Co films on graphene. It is therefore likely that these structures are intrinsic to the system, and do not come from oxides or other defects.

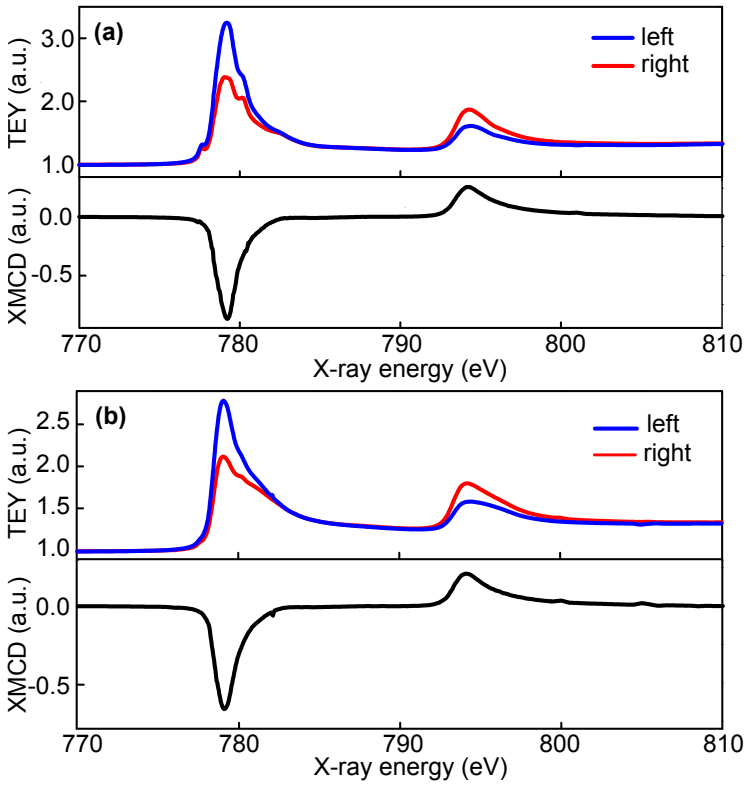

Figure 2.5: TEY and XMCD signals from (a) annealed and (b) non-annealed 0.8 nm-thick films of Co on graphene across the $L_{2,3}$ Co absorption edges, for left and right circularly polarized x-ray in perpendicular incidence at 10 K under magnetic filed of 5 T. TEY signal display multi-peak for annealed sample.

Let us now extract the magnetic information. The charge transfer from Co to graphene can be estimated by inspecting the electronic band structure of graphene on Co(0001), as revealed by ARPES measurements [8]. It is ca. E=2.5 eV shifted to lower energies, which can be translated in terms of a charge density equal to $E^2/(\pi(\hbar v_F)^2) = 4.6\times10^{14}$ cm^{-2}, i.e., 0.26 holes per Co atom. This charge transfer is too weak, we thus consider that Co atoms have the same electron occupation number as in bulk (7.51). Applying the sum rules on XMCD signals [figure 2.5], we deduce the orbital and spin moment per cobalt atom, 0.18 μ_B/atom and 1.29 μ_B/atom for non-annealed samples, and 0.19 μ_B/atom and 1.22 μ_B/atom for annealed ones, respectively (table 2.1).

While the spin moments negligibly change for annealed and non-annealed layers, they are

Table 2.1: spin moment, orbital moment, anisotropy of spin density and orbital moment of annealing and non-annealing Au/Co/graphene/Ir systems. $m_{\mathrm{T}}^{\gamma} = \langle T_{\gamma} \rangle \mu_{\mathrm{B}}/\hbar$ reflects the anisotropy of electron spin density within the Wigner-Seitz cell [233].

Sample	$m_{\mathrm{S}}(\mu_{\mathrm{B}})$	$m_{\mathrm{L}}(\mu_{\mathrm{B}})$	$m_{\mathrm{L}}/m_{\mathrm{S}}$	$m_{\mathrm{T}}^{\parallel} - m_{\mathrm{T}}^{\perp}(\mu_{\mathrm{B}})$	$m_{\mathrm{L}}^{\parallel} - m_{\mathrm{L}}^{\perp}(\mu_{\mathrm{B}})$
Au/Co(0.8 nm)/graphene/Ir non-annealing	1.29	0.18	0.143	0.084	0.222
Au/Co(0.8 nm)/graphene/Ir annealing (750 K)	1.22	0.19	0.155	0.030	-0.041
Au/Co(0.8 nm)/Au annealing (450 K) [142]	1.68	0.22	0.13	0.048	-0.12

both 20% smaller than the bulk value of 1.62 μ_{B}/atom (table 2.1). A reduction of magnetic moment can be explained by the interaction with the graphene layer as experimentally observed [112] and predicted by first-principle calculations [218] for graphene/Ni(111). It is also consistent with our calculations in graphene/Co(0001) (see Section 2.7—Part I). The reduction can be understood as result of carbidization of the Co atoms or a high density of Co-C bonds. However, notice that for the case of Co-Pt clusters covered by amorphous carbon and annealed even at higher temperature (950 K) [269], this kind of multi-peak is absent. Therefore, a different chemical bonding, or smaller ratio of surface atoms (of thin film as compared with clusters), is suspected in our case. Moreover, the multipeak is observed with both in-plane and out-of-plane incidences, whereas grazing incidence (with a component of polarization perpendicular to the plane) would be able to probe only perpendicular Co-C bonds. This means that not only Co-C bonds perpendicular to the interface are relevant, but also Co-C bonds with an in-plane component. A plausible reason is that the atomic PLD Co flux comprises ions whose energy is high enough (typically, > 17 eV) to substantially remove C atoms from graphene. As a result, there are small regions around these defects with the interface between Co and the damaged graphene. Then, the annealing step may contribute to the formation of a carbide from these defects. Notice that there are only four atomic layers of Co on one graphene layer (with two sublattices), the total ratio of C atoms/Co atoms is about 1/2. This mean that the component of Co carbide defects after annealing could be considerable to contribute on the large multi-peak feature.

The orbital moments in both kinds of layers (table 2.1) are also much higher than the bulk value. Notice that the high value of the orbital moment in the annealed layer may be associated with the shoulder and sub-peaks at the Co L_3 edge. The comparation with the sandwiched Au/Co/Au system [142] with a magnetic layer having the same thickness (table 2.1), points out the role of the graphene/ferromagnetic interface increases the orbital moment.

All these finding are consistent with first-principles calculations, performed in collaboration with H.-X. Yang and M. Chshiev [270, 241]. Using the model shown on figure 2.6, they predicted a significant hybridization of graphene π orbitals with Co 3d ones, consistent with earlier calculations [256]. In that case, while the total magnetic moment of Co in the middle layer (1.633 μ_{B}) is close to the bulk one, the moment at the interface with graphene is reduced by 0.1 μB. In contrast, we find an increase of 0.1 μ_B at the free surface of Co, which is consistent with the usual situation where magnetic moments are enhanced at interfaces with vacuum, for most transition metals or oxides, and explained on the basis of the narrowing of the 3d band of

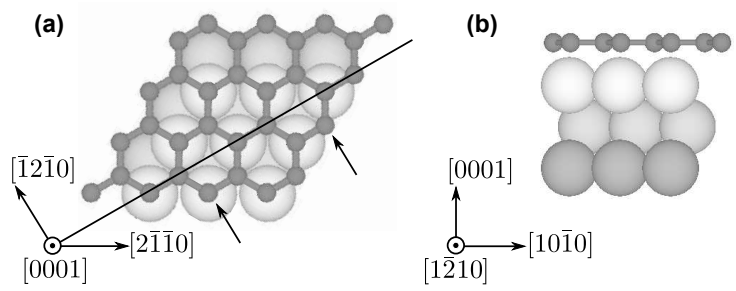

Figure 2.6: Geometry of the vertically-relaxed Co/graphene slab derived from the first principles calculations. (a) Top view and (b) cross-sectional view in the plane defined by [0001] and [$10\bar{1}0$, as depicted with a line and arrows in (a). Co(*hcp*) and carbon appear in light and dark gray. Crystallographic indexes refer to the Co lattice.

the ferromagnet [271, 272].

2.3.2 Magnetic anisotropy

We now discuss the role of graphene in the magnetic anisotropy of the present Co thin films. Various measurements were performed on the wedge-shape samples of Co deposited on Ir(111)/ sapphire(0001), with and without graphene, and capped with Au. Some samples were annealed before the Au capping (the hysteresis loops are shown in Appendix A).

For the annealed Co system, we obtain out-of-plan magnetization [figure 2.7(b)]. Before quantifying these data, let us notice magnetic energy given by the Stoner-Wohlfarth model:

$$E = K_{\text{eff}} \sin^2\theta - \mu_0 M_{\text{s}} \cos(\theta - \theta_H) \tag{2.1}$$

where θ is the angle between the magnetization M and the easy axis z, θ_{H} is the angle between the applied field H and the easy axis. When the system is magnetically saturated ($dE/d = 0$), we derive the following function:

$$H = \frac{2K_{\text{eff}}}{\mu_0 M_{\text{s}}} \frac{\cos\theta \sin\theta}{\sin(\theta - \theta_{\text{H}})} = H_{\text{a}} \frac{\cos\theta \sin\theta}{\sin(\theta - \theta_{\text{H}})} \tag{2.2}$$

with the magnetization is $M = \cos(\theta - \theta_{\text{H}})$ and saturation magnetization is $M_{\text{s}} = 1.18 \times 10^6$ (A m^{-1}), determined from XMCD analysis, we have $H_{\text{a}} = 1.6$ T. By fitting our data with (2.2), we have $K_{\text{eff}} = 1.9 \times 10^6$ J m^{-3}. With $K_{\text{d}} = 1/2\mu_0 M_{\text{s}}^2 = 8.7 \times 10^5$ J m^{-3}, we find a magnetocrysalline anisotropy constant $K_{\text{mc}} = 10^6$ J m^{-3}.

The magnetic field needed to saturate the magnetization of a system along a hard axis direction is a measure of the strength of its MAE. In the simple case of uniaxial second-order anisotropy, which we assume here, the field required is the so-called anisotropy field $H_{\text{a}} = 2K/\mu_0 M_{\text{s}}$. We have used the extraordinary Hall effect (EHE) to estimate this anisotropy field, at 300 K and for a film Au/Co[0.9 nm]/graphene/Ir. The field has been applied in the plane of the stacking. Due to experimental misalignement in the cryostat, a small out-of-plane angle of the order of a few degrees exists between the magnetic field and the sample surface. This misalignment is large enough to break the out-of-plane symmetry and induces a non-zero net perpendicular remanence, i.e., nonzero EHE at zero applied field. A saturation field is clearly evidenced [figure 2.8], from whose fit an anisotropy field of 0.37±0.05 T is deduced, corresponding

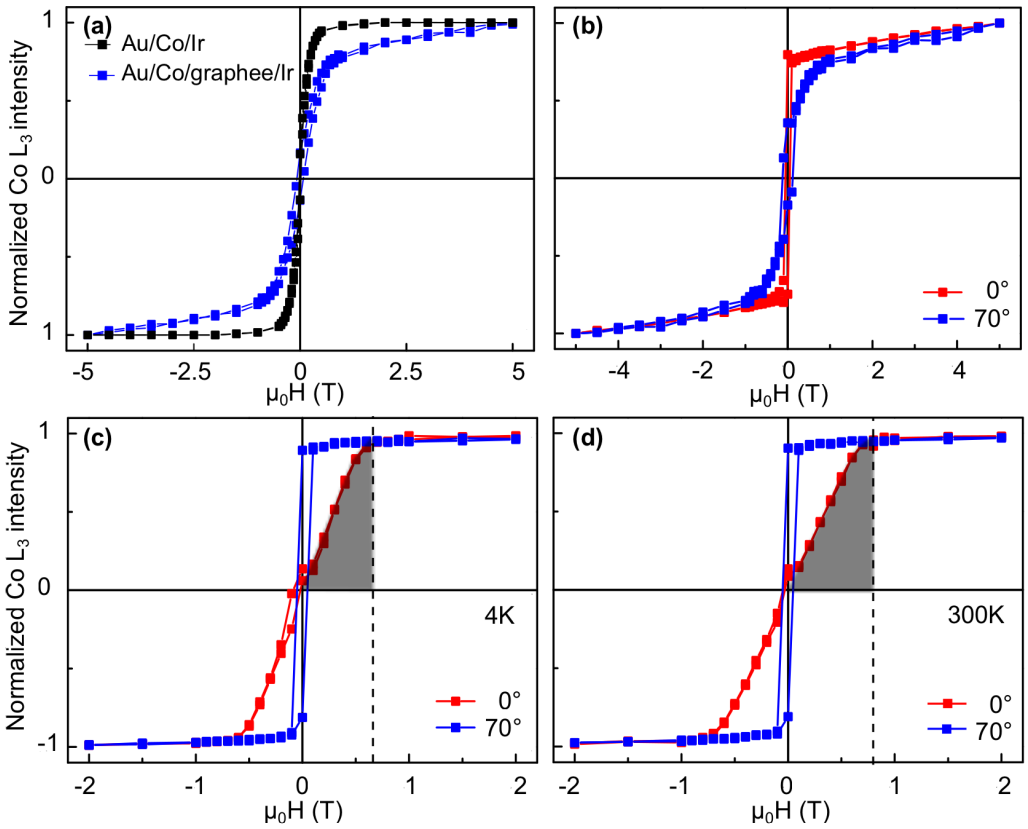

Figure 2.7: Normalized M-H loops obtained by subtracting the TEY signals at the Co L_3 edge and pre-edge value: (a) Au-capped annealed cobalt (0.8 nm) on (a) graphene/Ir(111) (blue) and on Ir(111) (black) measured at 4K for 0° incidence. (b) Annealed Au-capped cobalt (0.8 nm) on graphene/Ir(111) at 4K. Au-capped non-annealed cobalt (0.8 nm) on graphene/Ir(111) at (c) 4K and (d) 300K. The loops in (b-d) are measured for 0° (red) and 70° (blue) incidence.

to an MAE of $264\pm36\ \times10^{3}$J m^{-3}, i.e., $0.237\pm0.032\ \times10^{-3}$J m^{-2} for the 0.9 nm-thick Co layer. The 80 ± 10 mT coercive field [figure 2.8] is consistent with the already measured out-of-plane 3 mT coercive field reported before, assuming a misalignment angle of 2°. The magnitude of the experimental EHE is 1.4 mΩ. Note that this value is low due to the fact that most the current flows in the metallics bottom and capping layers (Appendix A).

In both cases of stacking with and without graphene, the out-of-plane to in-plane transition for the magnetization occurred at a thickness of about 2.5 nm at low temperature (see Appendix A). Comparing with symmetric Au/Co/Au films with our Au/Co/graphene system, it is clear, from the lower values that we obtained for both the anisotropy field and the critical thickness for perpendicular anisotropy, that the major effect for sustaining perpendicular anisotropy should arises from the (upper) Au/Co interface. In the following I quantitatively discuss all anisotropies as densities normalized to the thickness of the film considered here, 0.9 nm, so that they read as J m^{-2}.

In a crude approach for estimating the Co/graphene interface anisotropy, we assume that the MAE of the Co layer can be separated into contributions from Co/Au and Co/graphene interfaces, magnetocrystalline and shape anisotropies for Co. For the latter two, with the stak-

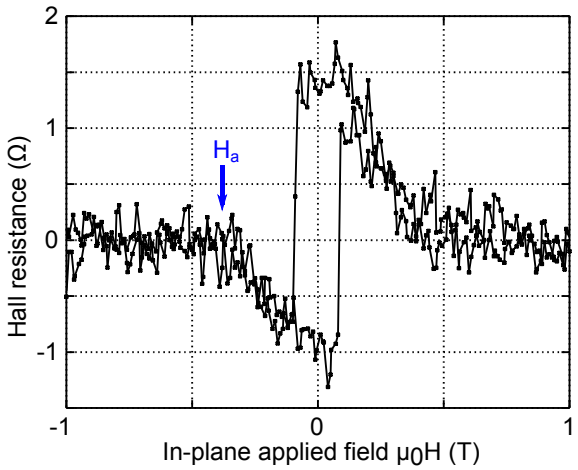

Figure 2.8: Hall resistance of as a function of the applied field, at 300 K, measured for Au/annealed Co (0.8 nm)/graphene/Ir. The direction of the applied field is almost in the plane of the sample, within an uncertainty of a few degrees.

ing faults of *hcp* and *fcc* might further enhance the MAE, we consider the bulk values for *hcp* Co at room temperature for simplifying the model [273]. This neglects effects of finite temperature, which are enhanced in low dimensions, as I will mention later. The bulk magnetocrystalline anisotropy equals 0.36 mJ m^{-2} for 0.9 nm thickness. The volume density for the shape anisotropy, $-\mu_0 M_s^2/2$, corresponds to -0.82 mJ m^{-2} for 0.9 nm thickness assuming bulk magnetization. Based on the expected Co/Au interface anisotropy of 0.5 mJ m^{-2} [274], the value of 0.15 mJ m^{-2} is then derived for the Co/graphene interface to reach the overall value of 0.237 mJ m^{-2} derived from EHE. The corresponding magnetocrystalline anisotropy constant is $K_{\mathrm{mc}} = 1.12 \times 10^6$ J m^{-3} close to the above fitting analysis in this Subsection. Interestingly, assuming the usual $1/t$ variation of MAE would yield 1.33 nm thickness for the vanishing of PMA, in good agreement with the MOKE measurement at room temperature (1.3 nm). At this stage, we conclude that a Co/graphene interface seems to favour perpendicular anisotropy, although to a lesser extent than a Au/Co interface.

We used first-principles calculations to try to understand the role of the Co/graphene interface in PMA. As MAE depends subtly on strain and local environment, the structural details of the Co slab and its interfaces should be taken into account accurately for a quantitative discussion. However, whereas Co and graphene have very similar lattice parameters, a large in-plane lattice mismatch exists between bulk Au and Co ($\simeq$ 14%); and Ir and Co/graphene ($\simeq$ 7%), one with another. Co/graphene, Au and Ir lattices are therefore *a priori* not commensurate and could only be approximated with a unit cell of at least 10 nm lateral size, which is out of the reach of first-principles calculations. We therefore selected two simple cases that we compared: two slabs with a thickness of three atomic layers of Co, either free standing or in contact with a commensurate graphene sheet on one side [figure 2.6]. Hexagonal compact Co, observed in (at least) a noticeable fraction of the films by TEM, was considered. A 2 nm vacuum slab was added on each side with periodic boundary conditions. Note that experimentally the graphene/Ir(111) interface is expected to have little influence since the interaction (charge transfer and orbital hybridization) between graphene and Ir(111) is limited [250]. As the most stable structural arrangement for graphene on Co(0001) (0.2507 nm in-plane lattice parameter) we found that

half the carbon atoms sit right atop the Co atoms of the uppermost layer, and the other half of the carbon atoms sit in an *fcc* site [figure 2.6], consistent with recent theoretical results [10]. The interface distance is 0.211 nm after out-of-plane relaxation.

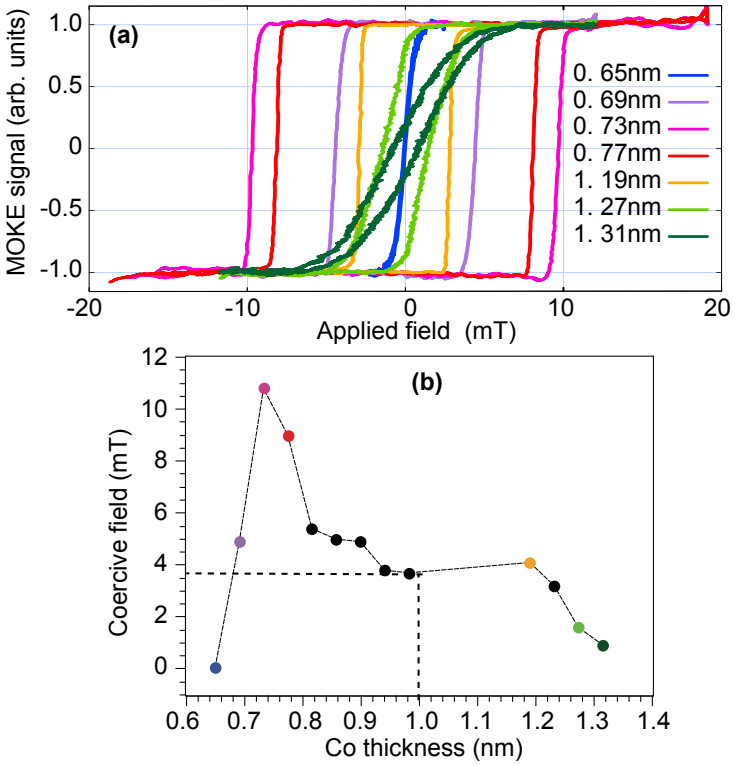

Figure 2.9: (a) Room temperature focused MOKE hysteresis loops of annealed Co (capped with 3 nm Au, on graphene/Ir(111)) with various thickness in the range of PMA. The loops have been cycled and averaged at 11 Hz. (b) Coercive field (H_C) as a function of the thickness of the Co layer, as derived from loops in (a) (and others which are not displayed for clarity in (a)). The peak of coercivity at low thickness may be related either to the expected variation of anisotropy, roughly inversely proportional to the thickness, or to the relative influence of thickness fluctuations.

We present two findings that are of particular relevance in view of the observed PMA. A significant hybridization of graphene π orbitals with Co 3d ones was predicted by first-principles calculations [256]. Looking at the significant effect of graphene on the magnetism of Co, it is clear that the MAE should be affected. The MAE of the slabs was computed as the difference in total energy values for in-plane and out-of-plane magnetic moments. The threee-atomic-layer-thick Co slabs, with and without a graphene overlayer, both exhibit PMA, with magnitude 1.0133 and 1.2274 mJ m^{-2}, respectively, excluding the magnetostatic energy. This means that, again based on the sole discussion of the contribution of interfaces, both the Co/vacuum and Co/graphene interfaces promote PMA, the former of 0.8 mJ m^{-2}, however, slightly more than the latter 0.6 mJ m^{-2}. This agrees with the EHE measurements. With an expected anisotropy energy of 0.5 mJ m^{-2} for the Co/Au interface and a negligible bulk anisotropy constant, the magnetocrystalline anisotropy constant K_{mc} is found equal to 1.8×10^6 J m^{-3}, about two times higher than the value evaluated value from EHE measurement.

Let us compare our theoretical findings with existing works. Our calculations suggest that Co/vacuum favors perpendicular magnetization. This is consistent with the recent first-principles calculations [153], but is in contradiction with earlier reports based on tight binding [141], *ab initio* [156] calculations and experimental studies [275, 276]. These contradictions probably stem from the oversimplifed model separating MAE in contributions for the bulk and interfaces, the latter with a universal well-defined value depending solely on the interfacial elements. Layer-resolved first-principles calculations point to complex variations of MAE as a function of the thickness of the magnetic film [156, 277] and capping layers [153]. El Gabaly *et al.* highlight that anisotropy at interfaces indeed arises not only from the capping layer but also from the surface and sub-surface magnetic atomic layers [153]. These authors stress that below four atomic layers the concept of interface anisotropy should fail, much beyond the approximation made above about the value of magnetization in layers of finite thickness (combined thermal and low-dimensional effects). Differences with all-metal interfaces are also expected due to the large magneto-elastic contribution to the MAE [153] arising from the large misfit with elements such as Au and Pt, which does not occur with graphene. Further experiments with varying interfaces and thickness in a systematic way are required for shedding light on these issues.

In addition, whereas the hysteresis loops are totally saturated in the Co/Ir system at 2 T, the saturation is not reached in Co/graphene/Ir samples even at 5 T [figure 2.7(a)]. The additional slope in the loops suggests that the graphene interface induces exchange interaction on Co film which favors antiparallel magnetization or non-collinear magnetization arrangements. This non-collinearity may arise from the atomic arrangement at the interface or from the neighboring magnetic domains.

We finally discuss the temperature dependence of anisotropy. For Au/annealed Co/graphene/Ir, the transition thickness is 1.3 nm obtained in MOKE measurements at room temperature [figure 2.9(a)] and is 2.5 nm obtained in XMCD measurements at 4 K. This means that the value is doubled in XMCD measurements at low temperature.

For the non-annealed sample measured by XMCD on [figure 2.7(c, d)] which show in-plan magnetization, both the magnetostatic energy and uniaxial anisotropy contribute to the magnetic anisotropy energy and we have:

$$MAE = K_{\mathrm{mc}} \sin^2\theta + K_{\mathrm{d}} \sin^2\theta = K_{\mathrm{eff}} \sin^2\theta \tag{2.3}$$

At a given temperature, $K_{\mathrm{mc}} = 1/2\mu_0 H_{\mathrm{a}} M_{\mathrm{s}}$ and $K_{\mathrm{d}} = 1/2\mu_0 M_{\mathrm{s}}^2$, then $K_{\mathrm{mc}} = K_{\mathrm{eff}} - K_{\mathrm{d}}$ (J m^{-3}). From sum rules analysis yielding atomic moments, magnetization may be calculated. Calculation for the XMCD spectra at 4 K and 300 K, the magnetic moments per atom $m = m_{\mathrm{S}} + m_{\mathrm{L}}$ are 1.47 μ_{B}, and 1.51 μ_{B}, respectively. With the lattice parameters of bulk *hcp* Co, $(a, c) = (0.25\mathrm{nm}, 0.41\mathrm{nm})$, we derive the saturation magnetization $M_{\mathrm{s}} = m/V$, where V is volume occupied by a Co atom. Then, K_{eff} (J m^{-3}) is determined by gray areas from the $M - H$ loops in figure 2.7(c, d). As a result for the analysis at 4 K and 300 K, we have $(K_{\mathrm{eff}},\ K_{\mathrm{d}},\ K_{\mathrm{mc}}) = (3.5 \times 10^5,\ 9.5 \times 10^5,\ -6.0 \times 10^5)$ and $(4.2 \times 10^5, 8.0 \times 10^5,\ -3.8 \times 10^5)$, respectively. Notice that the temperature variation of anisotropy is larger than the temperature variation of magnetization:

$$\left|\frac{\Delta K_{\mathrm{mc}}}{K_{\mathrm{mc}}}\right| = 3.7 \times 10^{-1} > \left|\frac{\Delta M_{\mathrm{s}}}{M_{\mathrm{s}}}\right| = \left|\frac{\Delta m}{m}\right| = 2.7 \times 10^{-2} \tag{2.4}$$

This feature is found in most systems, that can be understood in "oversimplified" model such as local magnetism [278]. As consequence, H_{a} increases from 0.60 T to 0.77 T when increasing

the measurement temperature from 4 K to room temperature.

2.3.3 Coercivity

In this section, we discus magnetization reversal features of annealed Co/graphene films with perpendicular anisotropy.

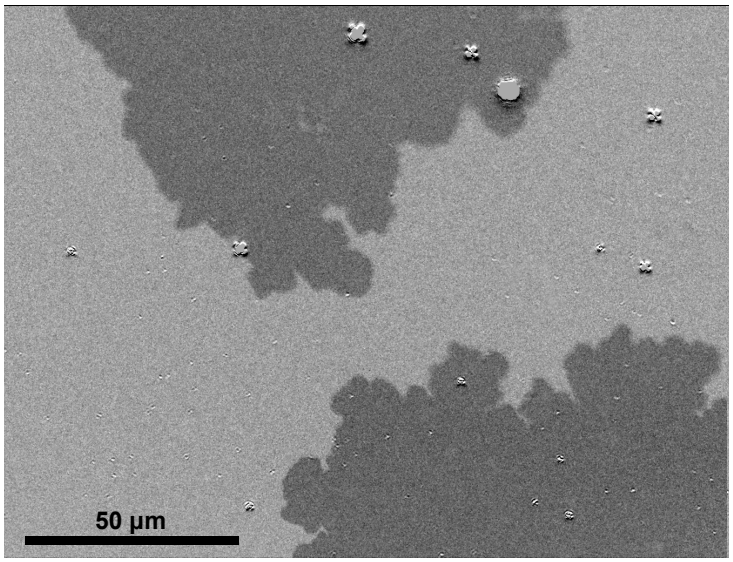

Figure 2.10: 170×130 μm^2 MOKE microscopy image of a 1 nm Co film (capped with 3 nm Au, on graphene/Ir(111) following partial magnetization reversal with a field of 3.5 mT applied perpendicular to the plane of the film, opposite to the initial magnetization direction. The initial domain appears bright, while the reversed domains appear dark. The latter nucleated outside the field of view, and inflated through thermally activated domain wall propagation, a so-called creep regime.

Measurement were performed at room temperature in the laboratory, based on the magneto-optical Kerr effect. The coercive field $\mu_0 H_C$ is of the order of a few mT [figure 2.9]. This value is several orders of magnitude lower than the anisotropy field (0.37 T). This suggests that magnetization reversal proceeds by the nucleation of a few reversed domains at defects of the extended film (sample edges, scratches, etc.) [279], followed by an easy propogation of domain walls through the remaining part of the film. This picture of weak pinning is further suggested by the abruptness of magnetization reversal around H_C. A confirmation of this fact is gained by monitoring magnetic domains during magnetization reversal, using Kerr microscopy. Under quasi-static conditions, the average size of the domains is indeed larger than 100 μm [figure 2.10], and magnetization reversal proceeds solely through the propagation of domain walls. The domain wall propagation is stochastic occurs in sudden jumps; it is thermally activated. This is the so-called creep regime, characteristic of weak pinning [280]. Low coercivity is difficult to achieve in PMA materials because their MAE is large by nature. Thus all local variations and defects are liable to induce energy barriers and energy wells proportional to this MAE and thus of large magnitude. Similar weak pinning and low coercivity have been demonstrated in a couple of selected metal-on-metal systems, in the very special cases where magnetism is weakened by either selecting extremely low thickness [281] or by weakening anisotropy and magnetism by

ion irradiation [282]. For Co/graphene low coercivity is maintained through the entire range of thickness for PMA, which points to the intrinsic quality of the layer microstructure.

2.4 Conclusion

In the view of spintronics setups, we developed the first ferromagnet/graphene system. It is based on thin films only, thus suitable (unlike a system which would be obtained on bulk single crystal) for standard lithography techniques allowing to prepare devices and for magneto-transport measurements (unlike with a bulk single crystal which would shunt most of the electrical currents). Experiments and good uniformity of the layers is confirmed by the very low coercivity of a few milliteslas over the entire PMA range, suitable for the reliable control of magnetization via magnetic or electric fields.

The Co films were the first atomically smooth one on graphene. PLD was crucial in this respect, for its ability to favor layer-by-layer growth. We found a decrease in spin moments but an increase in orbital moments from annealed to non-annealed systems. X-ray absorption showed a triple peak at the Co L_3 edges in samples for which Co was annealed, whose origin can be traced back to the extended formation of C-Co bonds, including some involving defects in graphene, which could be generated during PLD of Co.

Based on the measurement of PMA, first-principles calculations and comparison with the literature, PMA was mainly ascribed to the Au/Co interface, with a weaker contribution from the Co/graphene interface. The annealed Co films capped with Au and exhibit PMA in the thickness range of 0.65–1.3 nm. At low temperature, the Au/annealed Co/graphene/Ir and Au/annealed Co/Ir (without graphene) exhibit the same transition thickness of about 2.5 nm for out-of-plane to in-plane magnetization. This indicate that the Au/Co interface have more effect on PMA than graphene/Co one. In the other hand, we found also strong evidences that the hybridization at the Co/graphene interface promotes PMA, with a contribution of the same order magnitude as that of the Co/Au interface. A tighter Co-graphene contact following annealing may explain the in-plane and out-of-plane easy directions of magnetization in Co observed by XMCD in annealed and non-annealed samples respectively.

For the annealed sample, we observed the PMA with low coercivity. In addition, the average size of domains exceeds 100 μm. The domain wall propagation occurs like creep regime in thermal activation with weak pinning.

The results in this chapter will be discussed in the view of the results obtained for another system, discussed in the next chapter, in the last chapter (5 of this part).

3

Thin epitaxial cobalt films intercalated between graphene and Ir(111)

Contents

In this chapter, I present a second ferromagnet-graphene hybrid, consisting of a Co film sandwiched between graphene and an Ir(111) substrate. Unlike the system addressed in the previous chapter, the ferromagnetic thin films is protected from air by graphene layer of high quality, thus no further capping layer is needed. The Co film preparation follows a two-step procedure, first room temperature deposition onto graphene, second intercalation between graphene and its substrate by annealing. We establish a procedure which allows a mild annealing intercalation unlike in most systems studied thus far in the literature. This is especially desirable for achieving a smooth interface between Co and the substrate. For easing intercalation, we purposely made use of graphene with a substantial density of defects through which Co atoms can intercalate. LEEM, Auger spectroscopy, and DFT calculations provide converging and clear evidence of the effectiveness of the intercalation procedure.

The magnetic properties were investigated with SPLEEM as a function of the Co film thickness, which revealed PMA until thicknesses as high as 2.5 nm, and a gradual transition from out-of-plane to in-plane magnetization expending across a wide range of 0.8 nm. We compared the new system to Co film without a topmost graphene interface, deposited and annealed directly on the Ir substrate. The much smaller critical thickness for PMA in this system, 1.2 nm, clearly established the strong role of the graphene/Co interface. More precisely, the Co/graphene interface anisotropy was found to be about three time larger than the one at the vacuum/Co interface.

3.1 Introduction

As discussed in the previous chapter, metal deposition onto sp^2-hybridized forms of C like graphene usually leads to metal clusters. For bypassing this effect, we showed in the previous chapter that, instead of MBE, PLD can be employed. Another option is the intercalation between graphene and its substrate. Works on graphite intercalation compounds [283] inspired works on graphene/metal systems as early as in the 1980's [284]. In seminal works on the intercalation of Pt between graphene and Ir(111), one of the main issue associated to intercalation was highlighted: an intermixing between the intercalant and the substrate is liable to occur depending on the temperature employed for achieving intercalation. No detailled investigation of this effect was however performed at this time. Since then, in the blooming piece of work devoted to intercalation of various species between graphene and its (various) substrates, this issue as been overlooked. So has been the nature of the actual pathways allowing intercalation: first-principle calculations find very large energy barriers to the diffusion of atomic species through carbon rings or defects such as heptagon-pentagon pairs, consistent with the strongly impermeable nature of graphene even with respect to such small atoms as He [285]. Intercalation is believed to occur through defects, though the kind of defects which are relevant is unknown.

Thus far mainly single atomic layers have been intercalated (see, for instance [212, 9, 286, 6, 201]). It is expected that the interaction between graphene and the intercalated atomic layer stabilizes the latter and hinders intermixing. In this sense the intercalated single layer is certainly a simpler system than a thicker intercalated layer. In the view of probing the effects of interfaces on the ferromagnetic properties of a (Co) thin film, the ability to vary the thickness of the intercalated film is however crucial.

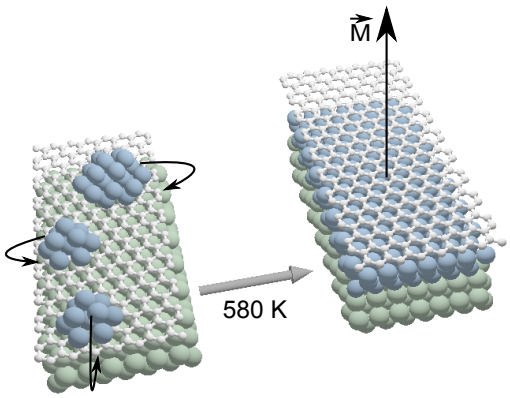

Figure 3.1: A clustered Co deposited on graphene/Ir(111) intercalated between graphene and Ir(111) following mild annealing. The magnetization in the intercalated Co film remains perpendicular to the surface for thicknesses up to 2.5 nm.

With the help of STM, Auger electron spectroscopy (AES), Raman spectroscopy, and LEEM, we developed high-quality large-area nanometer-thick Co films having a topmost interface with graphene and no substantial intermixing with their substrate. Spin-polarized LEEM (SPLEEM) shows that this interface protects Co against air oxidation, whereas it promotes perpendicular magnetization in Co, with a remarkable strength, about two times as much as interfaces with other materials. The preparation relies on UHV CVD combined to intercalation of Co between graphene and its substrate, Ir(111), made effective at mild temperature [figure 3.1].

The investigation was performed at the National Center for Electron Microscopy, Lawrence Berkeley National Laboratory, California, USA, in collaboration with A. K. Schmid and A. T. N'Diaye.

3.2 Intercalated Co film between graphene and Ir(111)

Experiments were conducted in two separate UHV sytems (base pressure in the low 10^{-10} mbar or below): one using the CVD graphene on single crystal for SPLEEM and AES, the other using graphene on thin film for STM measurements. Co was deposited at room temperature by electron-beam deposition at a rate of ≈3ML/min, which was determined by measuring electron-reflectivity oscillations with the LEEM as a function of Co deposition time. Graphene was prepared by CVD with 10^{-8} to 10^{-7} mbar ethylene partial pressures. For SPLEEM, an Ir(111) single crystal was used and cleaned with repeated cycles of Ar^+ sputtering and high-temperature flash (1500 K) under oxygen (10^{-8} mbar at 1100 K), whereas a freshy grown Ir((111) thin film prepared on sapphire (described in Chapter 1) was used for STM and Raman measurements.

3.2.1 Preparing graphene suitable for intercalation

Single-layer graphene growth on Ir(111) at 1400 K proceeds with a low nucleation density, typically a few single-crystal nuclei in a 50 μm field-of-view region [compare figure 3.2(a,b)]. As a result, grain boundaries are found with a low density, as shown in chapter 1. They form as domains with different crystallographic orientation with respect to the substrate, upon coalescence of the growing graphene islands having different orientations [208]. Intercalation of a Co film overgrown on such full-layer graphene requires temperatures exceeding 1000 K, presumably to promote large-enough surface diffusion that Co adatoms can reach the grain boundaries. Using such high temperature poses the problem of alloying between Co and Ir [287].

Intercalation was made effective at lower temperatures by using graphene having a higher density of defects [figure 3.2]. On this image, the contrast is uniform not because coverage is full, however because the island size can not be resoluble with LEEM.

Figure 3.3 shows an STM topograph of graphene grown at a lower temperature of 900 K with 10 min of 10^{-6} Pa (chamber pressure) C_2H_4 dosing on Ir(111). The typical moiré pattern arising from the lattice mismatch between graphene and Ir(111), having triangular symmetry with about 2.5 nm periodicity [72], shows domains having an extension of the order of 10 nm and whose orientation varies over long distances, which reflects the ill-defined crystallographic orientation of graphene on Ir(111) for this growth temperature. A variety of defects is observed, noticeably, heptagon-pentagon pairs formed at the boundary between misoriented graphene domains and appearing as bright protrusions and nanometer-sized vacancies appearing as holes in graphene (the depth of these holes does not depend on tunneling bias, confirming their topographic rather than electronic nature). There are found in 10^{15} and 10^{16} m^{-2} densities, respectively. Such high densities are due to the higher mosaic spread and high nucleation density, prominently at substrate step edges and to a low mobility of vacancies, which are trapped in the graphene lattice [207].

Raman spectroscopy of defected graphene reveals a G band overlapping with a D' band, a very small 2D band, and a strong D band, which are found at 1609 ± 5 cm^{-1}, 1634 ± 5 cm^{-1}, 2700 ± 8 cm^{-1}, and 1359 ± 4 cm^{-1}, respectively [figure 3.4]. As compared with high-quality graphene (prepared at 1400 K), whose signal stems from graphene domains having zigzag C

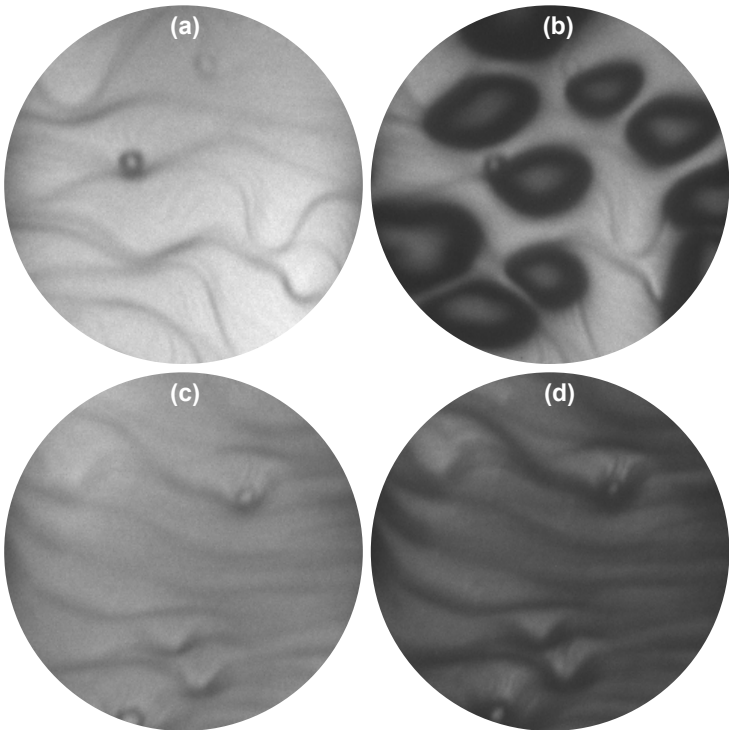

Figure 3.2: LEEM images (50 μm field of view, electron energy 4.5 eV) (a,c) of bare Ir(111) and Ir(111) partially covered with graphene grown at 1400 K (b) and 900 K (d). Graphene-covered regions appear in dark. Graphene island edges in panel (b) appear blurry due to electron deflection by the abrupt change in electric potential at the step edge. Graphene island size in panel (d) is too small for LEEM resolution so that we can not distinguish the whether graphene or Ir.

rows misaligned with respect to the Ir(111) dense-packed rows [288], the G band is broad and blue-shifted. These are not due to stress because the decreased stress in graphene prepared at lower temperature [223] would result in a red shift. The strong decrease in the 2D to G bands intensity ratio points to C-metal hybridization [289]. Assuming a donation of one tenth of an electron from a metal to a C atom at a defect (a lower estimate corresponding to graphene strongly interacting with a metal [290]), the extent of the G-band blue shift would correspond to a defect density of $\approx 5 \times 10^{15}$ m^{-2} [291], which agrees with the STM analysis. The strong D band intensity is attributed to the contribution of off-zone center phonons at defects, activating the otherwise forbidden double-resonance Raman scattering process [292]. The D' is ascribed to zone-edge and midzone phonons at defects [293].

3.2.2 Intercalation of Co

For high-quality graphene (grown at 1400 K), a high intercalation temperature of 1000 K is needed [294]. Such as temperature causes dewetting of Co and Co/Ir intermixing, which sets in above $\approx$ 600 K, as observed by SPLEEM in the form of a decrease in the magnetic contrast and by X-ray photoemission spectroscopy as a decrease in the area below Co peaks and an increase in the area below Ir peaks for fewer than 10 monolayers of Co deposited. In the following,

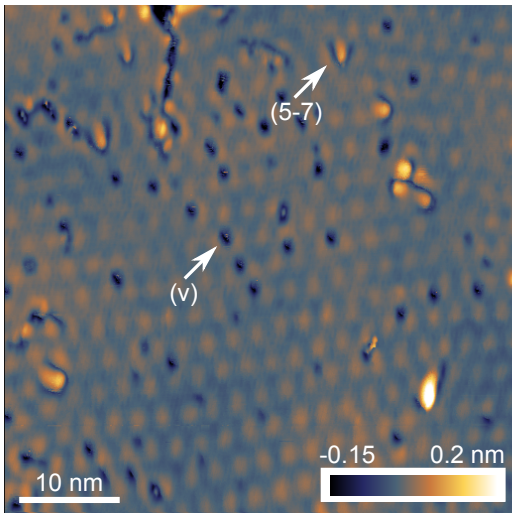

Figure 3.3: STM topograph (50×50 nm^2) of graphene grown on Ir(111) at 900 K. One vacancy (v) and one heptagon-pentagon pair (5-7) are highlighted as interpreted in [72].

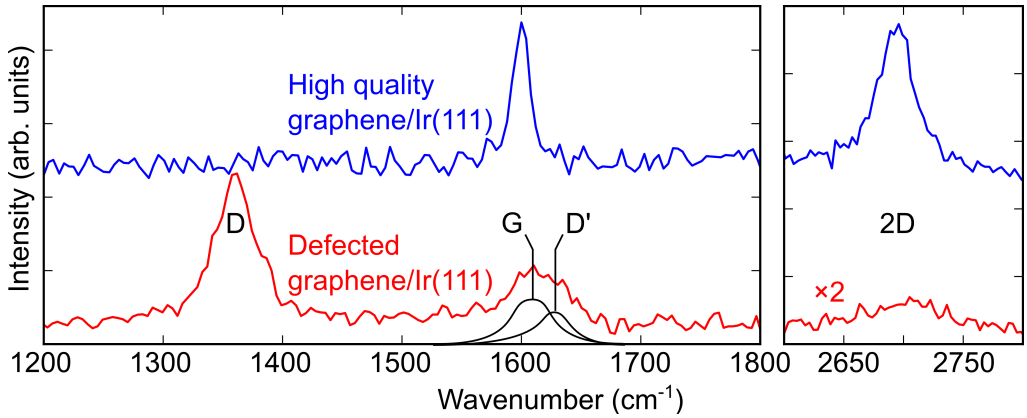

Figure 3.4: Background-subtrated Raman spectra around the D, G, D', and 2D bands of graphene for graphene/Ir(111) prepared at 1400 K (blue) and at 900 K(red).

we focus on Co deposits on defective graphene (grown at 900 K), for which a lower annealing temperature, 530 K, is sufficient for the appearance of a magnetic contrast. This lower annealing temperatures allows us to stabilize Co films of thickness down to a single atomic layer and to prevent intermixing at the Co/Ir interface [figure 3.6. Low-energy electron diffraction conducted in a separate UHV chamber for 5 MLs of Co sandwiched between graphene and Ir(111), reveals an epitaxial relationship between Co and Ir, with the surface dense-packed rows of Co-aligning Ir ones.

The intercalation scenario is confirmed by AES before and after annealing [figure 3.5]. Figure 3.6 summaries element specific peak heights from Auger-electron spectra collected during the preparation of a graphene/Co(2ML)/Ir(111) sample. A single-layer graphene covering clean Ir(111) substrate produces a 272 eV carbon peak at the level marked by a circles and reduced the magnitude of the 39 eV iridium peak to the level mark by squares. Subsequent room

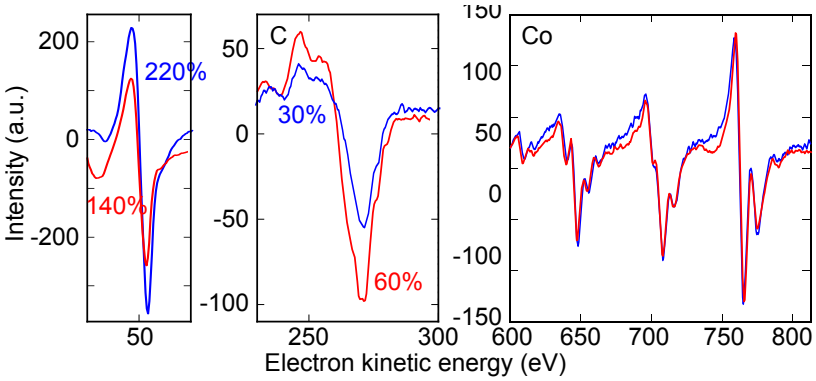

Figure 3.5: Auger electron spectra of 8 MLs Co as a function of kinetic energy, around the Ir NOO, C KVV, and Co LMM transition, before (blue) and after (red) annealing. Percentages indicate the intensity of the Ir and C Auger peaks normalized to the intensity of the Co peak.

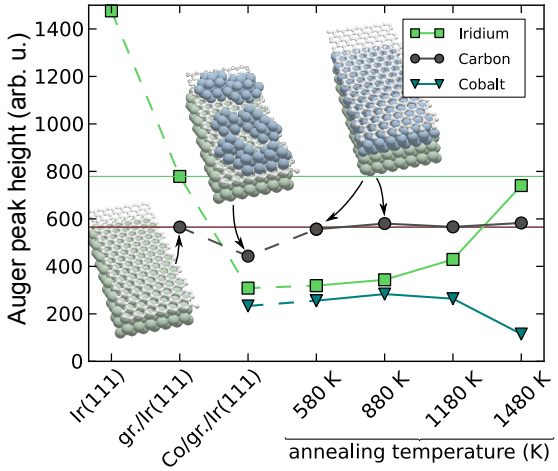

Figure 3.6: Intercalating Co grown on graphene/Ir(111). Tracking elemental Auger peak intensities during graphene and Co deposition, Co intercalation (annealing in the range of 580–880 K) and loss of Co during over-annealing above 880 K.

temperature deposition of a dose of cobalt equivalent to 2 MLs thickness reduces the C and Ir peaks [figure 3.6]. However, even moderate annealing, holding 580 ± 20 K for 5 min, already brings the carbon signal back to the level which corresponds to bare graphene at the top of the sample [black circles on figure 3.6]. After subsequent annealing steps up to 880 K (always holding target temperatures within ± 20 K for 5 min) the Auger peak heights remain constant until, for higher annealing temperature, the gradual increase of the Ir signal in conjunction with reduction of the Co signal indicates that integrity of the cobalt layer is lost [blue triangles on figure 3.6]. Co—Ir is an isomorphic binary alloy system and Co might be dissolving into the Ir crystal (and/or might be lost due to sublimation) [295]. This observation explains the need to use defected graphene to promote intercalation at mild temperature. However, stability of the three elemental Auger peaks within a wide range of annealing temperature between about 550—880 K indicates that Co/Ir(111) interfaces are kinetically quite stable. Note that in this

experiment, a thin Co deposit was use (equivalent to about 2 ML) so that all three elemental Auger electron peaks can be tracked in all phases of the sample preparation. In thicke Co deposits, for instance of 10 MLs or thicker, the 39 eV iridium peak and the 272 eV carbon peak from buried graphene are essentially suppressed.

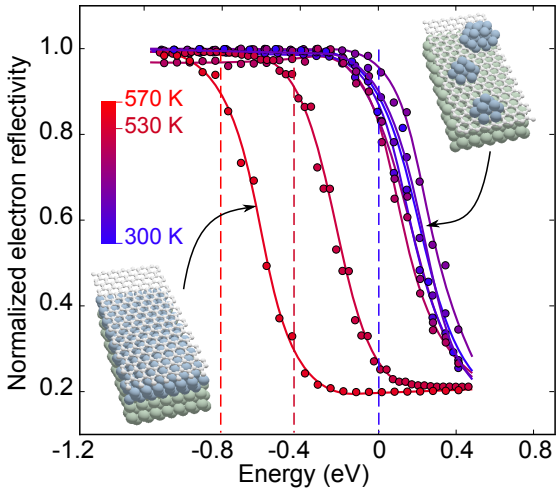

Figure 3.7: Intercalating Co grown on graphene/Ir(111). Tracking normalized electron reflectivity by SPLEEM, as a function of the incident energy of the electron beam for different annealing temperatures. Before annealing, a graphene/Ir(111) film was buried under a Co film, which has a high work function. During annealing in the temperature range above 530 K progressive reduction of the surface, as the Co layer intercalates between the graphene and the Ir(111) substrate.

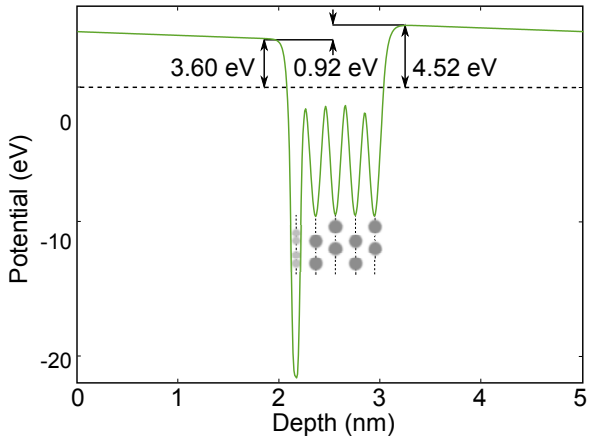

Figure 3.8: Electrostatic potential energy of a graphene/Co slab (sketched on a side-view with gray balls) relative to the Fermi level. decreasing by 0.92 eV from 4.52 on the vacuum side to 3.60 eV on the graphene side.

To track the intercalation process in case of larger Co deposits, we used *in situ* LEEM observation, where the presence of graphene at the sample surface is clearly identified. Low-energy

electron microscopes are very sensitive tools to resolve the value of the surface work function with high spatial and energy resolution [296]. Graphene can be identified as it has a characteristically low work function compared to metal surfaces [284, 208]. When the energy of the incident beam is lower than the surface work function, the reflectivity of the surface is essentially 100%, while reflectivity decreases by a subsantial factor when electrons have enough kinetic energy to enter the crystal. As shown in figure 3.7, after annealing at 530 K, a strong reduction of reflectivity threshold is observed by 0.8 eV. This means that the work function uniformly across the sample surface. This is typical of the work function reduction from graphene-free to graphene-capped transition metals such as Ni [257] and points to a graphene termination of the surface. Qualitatively supporting this scenario, density functional theory calculations for a Co slab with vacuum and graphene interfaces predict a reduction of 0.9 eV of the electrostatic potential for one side of the slab to the other [figure 3.8]. This gives an estimate for the work function difference between graphene-capped and graphene-uncapped Co.

We conclude that the entire Co film, 8 MLs thick in the case of figure 3.5 and 3.9 has been intercalated at the graphene/Ir(111) interface and has wet the substrate surface. No sign of intermixing at the Co/Ir interface was found in photoemission measurements. After annealing at higher temperature (900 K), full intermixing of Co–Ir can be observed by STM through the moiré with parameter larger than one of graphene on Iridium. Otherwise, because of the similar lattice parameters of Co and graphene (Table 1.5), the moiré of graphene on Co is not straightforward to observe in epitaxial multilayer.

The driving force for the intercalation is presumably an increase in the number of bounds, either strong or weak ones, which the Co film can form with graphene and Ir once intercalated. Indeed, the calculated surface energies of graphene is only 0.05 J m^{-2} [297] , negligible as compared with the value of Co as 3.2 J m^{-2} [298]. In addition, calculated binding energies of graphene with Co and Ir are -0.033 eV per C atom and -0.432 eV per C atom [299], i.e., the Ir/graphene is physisorption interface while Co/graphene is Chemisorption interface. As a evidence, the intercalation mechanism of Co between graphene is energetically favourable. We intercalated several MLs of Co at once at moderate temperature, whereas only single atomic layers or atom-by-atom intercalation was investigated to date [10, 294].

3.3 Magnetic properties of graphene on Co on Ir system

We now turn to the comparison of the magnetic properties of graphene-capped and -uncapped Co films, which reveals quantitative differences and points to dominant interface effects due to a strong interaction between graphene and Co. In SPLEEM, the contrast is defined as the normalized difference between images probed by spin up and spin down. It reaches 3% for electrons having an energy below 4.5 eV, against 1.5% for bare Co yields SPLEEM contrast reaching for electrons above this energy. These contrast values are typical of Co films of good quality [237], consistent with the good electron diffraction (LEED) on these surfaces.

SPLEEM images of Co intercalated between graphene and Ir(111) recorded at room temperature after annealing [figure 3.9(a,b)], contrast with those recorded for Co films of the same thickness directly grown on Ir(111) and annealed once for all [figure 3.9(c,d)]. Eight MLs Co films intercalated at the graphene/Ir(111) interface is prominently out-of-plane magnetized. Careful inspection reveals a marginal in-plane component of the magnetization for the latter. The much stronger interface anisotropy on the graphene/Co side than on the Co/Ir side could yield nonuniform magnetization configuration originating form inhomogeneities in Co thickness, that is, configurations that minimize dipolar (shape) and interface energies [300, 301]. For Co/Ir(111),

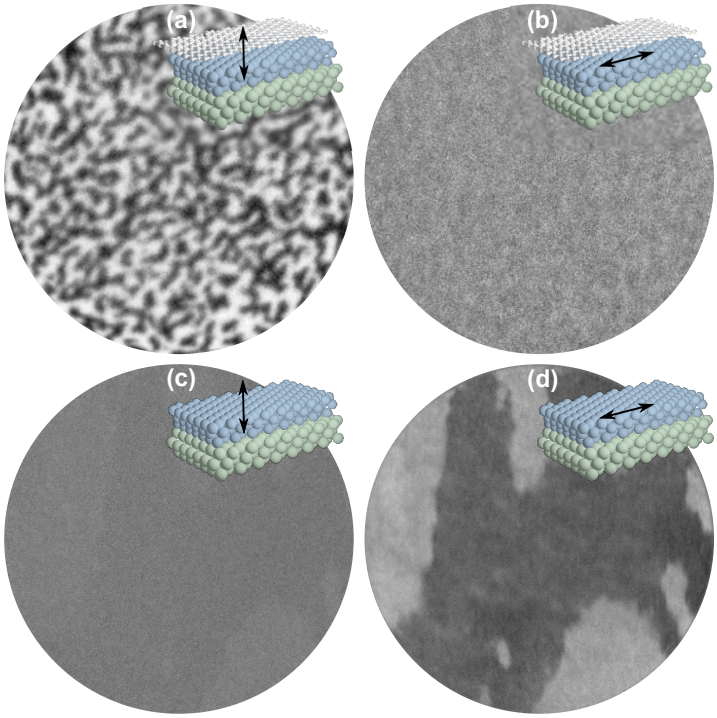

Figure 3.9: SPLEEM (20 μm field of view), electron energy 3.5 eV for (a,b) and 5.5 eV for (c,d)] image of 8 MLs Co films, constructed by subtracting two images acquired with opposite polarization of the spin of the incident electrons and normalizing by the average of the two images. Panels (a) and (b) are measured for intercalated graphene/Co/Ir(111), with electron polarization perpendicular to and in the sample surface, respectively. Panels (c) and (d) are measured for vacuum/Co/Ir(111), with perpendicular and in-plane polarization, respectively. The Co layers are prepared by the same procedure for both systems.

the transition between in-plane and out-of-plane magnetization occurs abruptly, within 1 ML, at $\approx$ 6 MLs of Co. For graphene/Co/Ir(111), the transition extends up to $\approx$ 13 MLs ($\approx$ 2.6 nm) within 3 to 4 MLs. This shows that the graphene/Co interface allows fine control of the magnetization direction and strongly favors perpendicular magnetization in the Co films underneath, beyond most cases of Co/metal interfaces displaying perpendicular magnetic anisotropy (PMA). As already discussed in Chapter 2, the origin of the contribution of the graphene/Co interface lies in the chemical bonding between the two stacks. In that sense, we identify a similarity with the case recently uncovered interface of Co with oxides such as Al_2O_3 and MgO [302, 160], giving rise to giant interface anisotropy.

To estimate the contribution of the graphene/Co interface to the PMA, we start by assuming that the MAE is uniaxial with second order. The energy of magnetic layers can then be written $E = -K\sin^2(\theta)$, where θ is the angle between the magnetization and the normal to the film and the total magnetic anisotropy. K includes shapes anisotropy $K_\mathrm{s} = -(1/2)\mu_0 M_\mathrm{s}^2$ and magnetocrystalline anisotropy K_mc. The latter may be split in a volume contribution K_V and surface/interface contributions:

$$K_{\mathrm{mc},1} = K_{\mathrm{v}} + (K_{\mathrm{Co/Ir}} + K_{\mathrm{vacuum/Co}})/t \tag{3.1}$$

$$K_{\mathrm{mc},2} = K_{\mathrm{v}} + (K_{\mathrm{Co/Ir}} + K_{\mathrm{Gr/Co}})/t \tag{3.2}$$

for case (1) of bare Co/Ir(111) films and for case (2) of graphene covered films, respectively, with t the film thickness. Critical thickness of bare graphene covered films, t_1 and t_2, correspond to the condition $K_{\mathrm{mc}} = -K_{\mathrm{s}}$. In our case the shape anisotropy is constant from (3.1) we can write

$$K_{\mathrm{v}} + (K_{\mathrm{Co/Ir}} + K_{\mathrm{vacuum/Co}})/t_1 = K_{\mathrm{v}} + (K_{\mathrm{Co/Ir}} + K_{\mathrm{Gr/Co}})/t_2 \tag{3.3}$$

which permits us to estimate the contribution of the graphene/Co interface to PMA, with rough hypothesis of equal volume contribution K_{v} in both systems with and without graphene:

$$K_{\mathrm{Gr/Co}} = (t_2/t_1 - 1)K_{\mathrm{Co/Ir}} + (t_2/t_1)K_{\mathrm{vacuum/Co}} \tag{3.4}$$

The interface energy $K_{\mathrm{Co/Ir}}$ was reported to be 0.8 mJ/m^2 [303]. While experiments [276] showed that the value of $K_{\mathrm{vacuum/Co}}$ is close to zero in the case of Co films strained to match the 0.277 nm lattice contant of Pt(111), strain-dependent *ab initio* calculations [155] showed that the value of the surface anisotropy increases to approximately 0.3 mJ/m^2 when the in-plane lattice constant is reduced to the value of bulk Co, 0.251 nm. We observed the critical thickness to increase by the factor of 13/6 when the Co films are intercalated under graphene. Assuming that this increase is driven by the difference of interface anisotropy between Co—vacuum and Co—graphene interfaces alone, it follows that the value of $K_{\mathrm{Gr/Co}}$ is approximately 1.6 mJ/m^2, as already mentioned. This value is relatively large compared to values unusually reported for Co/metal interfaces, confirming that additional mechanisms are working in our system, such as chemical bonding. We can also not exclude that the intercalation process and surfactant role of graphene layer affects the wetting of the Co film on the Ir(111) surface and its structural properties. These effects may induce strain in the FM and induce changes in the crystallography (bulk lattice parameters of Co and Ir are 0.27 nm and 0.25 nm, respectively), thus modifying the magnetic anisotropy (Section 1.3). Finally, in supposition a negligible value of K_{V} in comparison with $\sum K_{\mathrm{interfaces}}/t$, we have the unaxial anisotropy constant $K_{\mathrm{mc}} \approx 9.2 \times 10^5$ J m^{-3}. We take this value to compare with that of other systems in chapter 5.

3.4 Conclusion

In summary, we have shown that Co films, protected by a graphene overlayer and having an abrupt interface with their substrate, can be conveniently prepared via UHV CVD, followed by intercalation at mild temperatures. Intercalation is a colander-like effect, through graphene defects. The graphene/Co interface has a surprisingly strong interface magnetic anisotropy, which promotes perpendicular magnetization in films as thick as 13 MLs and induces a very extended reorientation of the magnetization direction, allowing us to control the magnetization direction across as much as 4 MLs.

In a recent study, Decker et al. investigated the intercalation and magnetic properties of a single layer of Co between graphene and Ir(111), and found PMA as we do. They observed a graphene/Co moiré revealing that the Co is pseudomorphic to Ir(111), and revealed a varying

spin-polarization in Co/graphene along the moiré, which according to spin-polarized DFT calculation should lead to large spin moments locally induced in graphene [304]. The analysis of the effects of strains, through the analysis of the moiré for instance, as a function of the thickness of Co, is an important one for further understanding the magnetic properties.

4

Magnetism of self-organized nanoclusters on graphene/Ir(111)

Contents

In Chapters 2 and 3, I reported the growth and magnetic properties of ultrathin ferromagnetic films in contact with graphene. In the present chapter, I discuss the investigation of graphene-ferromagnetic systems different in nature, including, instead of ferromagnetic thin films, self-organized magnetic clusters. Nanoclusters composed of various transition metals were shown to self-organized on the moire between graphene and Ir(111).

Fe and Co clusters, comprising 26–2700 atoms were deposited by molecular beam epitaxy. For achieving self-organization the clusters were seeded with the help of small Ir or Pt clusters nicely organized onto the moire. The structure and magnetic properties were studied *in situ* with the help of STM and XMCD, respectively. The sum rules calculation indicate a substantial decrease of the orbital moments but similar spin moment, in comparison with bulk values. At the lowest temperature allowed in our measurements, ca. 10 K, the few 10 atoms-clusters are superparamagnetic. Surprisingly they exhibit no magnetic anisotropy, suggesting a a very weak effect of the cluster/graphene interface. We observe difficult saturation of the magnetization of the clusters and a temperature-dependent susceptibility which could be interpreted as the manifestation of magnetic domains exceeding the cluster size in a simple Langevin description of the system, i.e., to magnetic interactions between the clusters. We also observed metal cluster damage under soft x-ray exposure, which we ascribe to the decomposition of graphene by the clusters.

4.1 Introduction—Magnetic nanoclusters on epitaxial graphene

A noticeable effort is focused at theory level on understanding the magnetic properties of graphene in the presence of transition metals like Fe, Co, or Ni. For example, the graphene-

mediated exchange interaction between adatoms or impurities each holding a net magnetic moment has been explored and unconventional scaling with distance has been anticipated [11]. Also, magnetic anisotropies as high as required for room-temperature magnetic storage have been predicted for Co dimers [12]. So far, experimentalists investigated simpler systems, most prominently the interface between a ferromagnetic layer and graphene. They are indispensable for basic information on proximity-induced magnetic moments in carbon [7] or the graphene/Co magnetic anisotropy Chapter 2, 3. The 2D array of Co nano-clusters of about 2 nm-scale is obtained on BN/Rh(111) by the mean of buffer layer assisted growth (BLAG) thank to the corrugated template surface [135]. Capping with non-magnetic materials (Pt, Au, Al_2O_3) and magnetic material (MnPt), this systems exhibit no remanence but are suitable to study basic physical phenomena of nanomagnetism such as exchange bias effect.

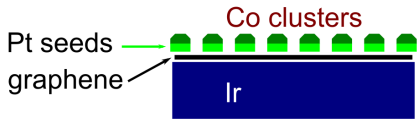

Figure 4.1: A simple illustration of self-organization of magnetic clusters (Co, Fe) with the help of self-organized seed (Ir, Pt) on graphene/Ir(111).

A step towards low-dimensional systems is the assembly of equally sized Fe, Co, or Ni clusters comprising 10–10^3 atoms [figure 4.1, which are well adapted to the study of the size-dependant magnetic properties. Such clusters can be prepared on epitaxial graphene, e.g., on Ir(111) [305], Rh(111) [306], or Ru(0001) [307], using graphene moirés as templates. The experiment was conducted *in situ* at the ID08 (Dragon) Beamline, European Synchrotron Radiation Facility (ESRF).

4.2 Structural properties of Co and Fe nanoclusters on graphene on Ir(111)

Sample preparation and STM were performed in two interconnected ultra-high vacuum chamber; high resolution STM was performed using the same sample preparation in another system. Ir(111) was cleaned by cycles of Ar^+ sputtering and flash annealing to 1500 K. Graphene on Ir(111) was prepared by CVD of ethene following a two step procedure yielding a closed and perfectly oriented monolayer [172]. Co, Ir, and Pt evaporation was performed close to room temperature. The deposited amount θ is specified in ML, 1 ML being the surface atomic density of Ir(111).

In these systems, the strong interaction between graphene and metallic clusters forms thank to local sp^2 to sp^3 hybridization within particular regions of moiré pattern, i.e., self organization. While the clusters lattices can be grown on graphene on Ir(111) for Ir, Pt, W and Re [308], the self-organized mechanism does not work with the magnetic clusters such as Ni, Fe and Co. This mechanism is based of the bonding of every second carbon atom in graphene alternatively with the metallic atoms of clusters and substrate. One might consider the criterion of the effective self-organization combining from three factor: large cohesive strength of the metal, rehybridization of C atom of graphene in contact with cluster and match between nearest atoms with every second C atom [308]. Due to the perfect self-organization of Ir clusters, the optimal nearest distance of metal atoms is considered around 0.27 nm, beyond the nearest neighbour distance of

the magnetic metal (around 0.25 nm). In our investigation, we study the magnetism of clusters as a function on their size, therefore we deposited beforehand a small amount of self-organized cluster as seed superlattice, using the small-size clusters effective self-organization like Ir or Pt to define the cluster lattice and further grow of magnetic metal. This allows us to control growth and the size of magnetic magnetic clusters afterwards [305].

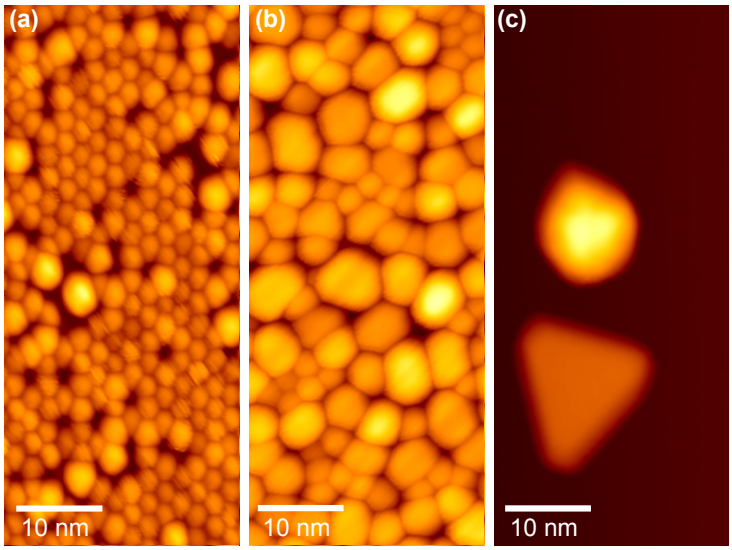

Figure 4.2: STM topographs of metal clusters on graphene on Ir(111): (a) Co_{26} seeded by Pt_{13}, (b) Co_{500} seeded by Ir_{50}, and (c) pure Co_{2700}. Numbers are in averages and determined by the amount of metal deposition with density of clusters.

Through seeding with Pt and Ir, for small $\theta < 1$ ML, arrays of Co clusters with the moiré pitch of 2.5 nm are formed. The majority of clusters is rather uniform in size, while a fraction of about 15% of the cluster is coalesced form two (or three) clusters each of which is formed in a moiré unit cell [305]. For $\theta > 1$ ML, still dense arrays are obtained, but each cluster spans several moiré cells and is anchored by several seeds [305]. Deposition of Co without seeds leads to sparse, disordered cluster assemblies. Here, I report results on five samples (Table 4.1): triangular lattices of Co_{26} (26 atoms in average) seeded by Pt_{13} [figure 4.2(a)], similar to $Ir_{13}Co_{26}$ and $Pt_{16}Fe_{26}$), Co_{500} seeded by three to four Ir_{15}, Ir_{50} hereafter, [figure 4.2(b)], and pure Co_{2700} [figure 4.2(c)]. The cluster size are determined by the amount in monolayer, i.e., number of total atoms, of deposited metal according to the area density of clusters. For example, the amount of $\phi = 0.13$ ML of Pt or Ir put into practice for the self-organized of seeds offers the highest occupied sites on the moiré pattern, i.e. highest cluster density, yielding the size of 13 atoms with the height of 1 atomic layer [305].

4.3 Magnetic properties of Co and Fe nanoclusters

We observed similar magnetic behavior for Fe and Co clusters of the same size. In the following, we focus on the case of Co clusters.

XMCD was conducted at the ID08 beamline of the European Synchrotron Radiation Facility, monitored in the total electron yield (TEY) mode using $(99 \pm 1\%)$ circularly polarized light and

Table 4.1: Orbital (m_L), spin (m_S) magnetic moments and their ratio (m_L/m_S) measured at 5 T, 10 K with the x-ray beam perpendicular to the samples, which were prepared with different deposited amount of seeding and magnetic material (ϕ), and the average cluster distance (d) for each sample (except for $Pt_{13}Co_{26}$, $Ir_{13}Co_{26}$ and $Pt_{16}Fe_{26}$, where d is the moiré pitch).

Sample	ϕ(ML)	d(nm)	$m_S(\mu_B)$	$m_L(\mu_B)$	m_L/m_S
$Pt_{16}Fe_{26}$	0.13/0.25	2.5	2.0 ± 0.2	0.09 ± 0.02	0.13 ± 0.04
Fe_{bulk} [232]			1.98	0.085	0.043
$Pt_{13}Co_{26}$	0.13/0.25	2.5	1.5 ± 0.2	0.22 ± 0.02	0.15 ± 0.04
$Ir_{13}Co_{26}$	0.13/0.25	2.5	1.0 ± 0.2	0.20 ± 0.02	0.20 ± 0.04
$Ir_{50}Co_{500}$	0.17/1.70	4.8	1.7 ± 0.2	0.20 ± 0.02	0.12 ± 0.03
Co_{2700}	0.25	30	1.7 ± 0.2	0.18 ± 0.02	0.11 ± 0.03
Co_{bulk} [232]			1.62	0.15	0.095

up to ±5 T magnetic fields.To test x-ray beam damage effects, also small Co_8 clusters seeded by Ir_4 were also probed.

The TEY was measured at 10 K and ±5 T across the Co $L_{2,3}$ absorption edges for left- and right circular polarizations of an x-ray beam entering the sample under varying incidence from normal to grazing (70°). Subtracting the TEY measured for ±5 T or opposite polarizations yields the XMCD signal (see Chapter 2—Part I). Figure 4.3(a) shows the TEY of $Pt_{13}Co_{26}$ at 5 T in normal incidence for both circular polarizations, while figure 4.3(b) shows the XMCD signal for normal and grazing incidence. No sign of Co oxidation is seen. Magnetization versus filed (M-H) loops were obtained by subtracting the TEY measured at the Co L_3 edge (779 eV) by the pre-edge value at 774 eV and then normalizing to the pre-edge value.

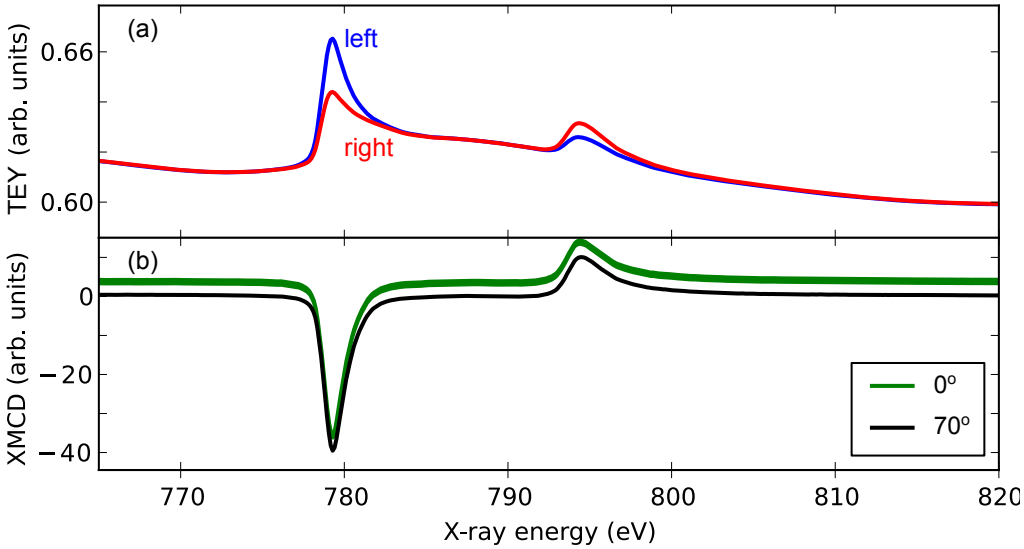

Figure 4.3: (a) TEY from $Pt_{13}Co_{26}$ clusters across the $L_{2,3}$ Co absorption edges, for left and right circularly polarized x-rays in perpendicular (⊥) incidence, at 5 T and 10 K. (b) XMCD signals for ⊥ and 70° incidence (vertically shifted for clarity).

We used sum rules [236] with the number of holes value for bulk and followed the procedure described by Ohresser *et. al.* [309] for deriving the orbital (m_L) and effective spin (m_S, including a dipolar term) magnetic moments at 5 T, where the M-H loops are close to saturation [figure 4.4(b)]. for Co, we find $m_S = 1.5 \pm 0.2\ \mu_B$, comparable to the bulk value of 1.62 μ_B. On the contrary, m_L/m_S is larger than the 0.095 bulk value [310]. Increasing the cluster size ($Ir_{50}Co_{500}$ and Co_{2700}) does not substantially modify m_S but results in a decrease of m_L/m_S towards the bulk value. The same tendency is also noticed for Fe cluster (table 4.1). The good agreement of the experimentally measured m_S with the bulk value indicates that a possible charge transfer between Co, Pt, and graphene does not significantly affect the Co magnetism. The enhancement of m_L/m_S for small clusters compared to the bulk is typical of small-size objects and arises from the local loss of symmetry (lower coordination or strain).

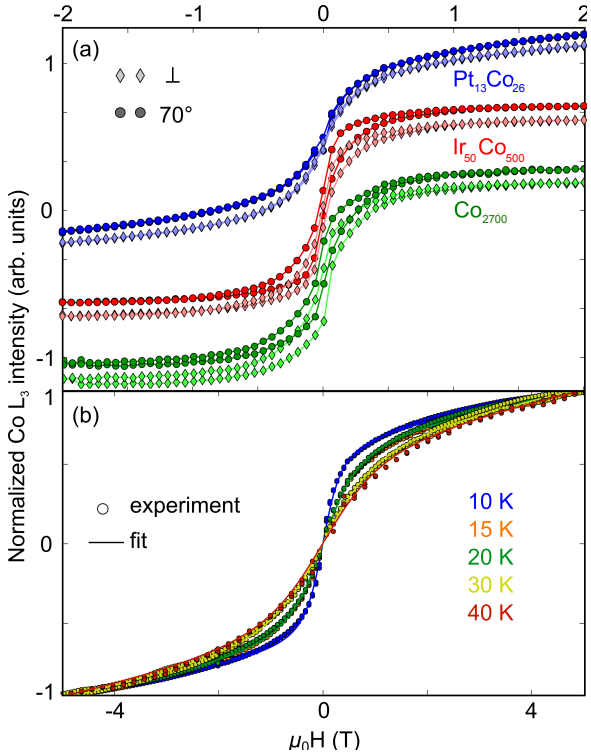

Figure 4.4: (a) Normalized M-H loops at 10 K for $Pt_{13}Co_{26}$, $Ir_{50}Co_{500}$, and Co_{2700} for in-plane (70°) and perpendicular (⊥) incidence. (b) Temperature M-H loops and Langevin fits for $Pt_{13}Co_{26}$ at ⊥ incidence. Curves are vertically shifted.

M-H loops display very weak anisotropies for all cluster sizes [figure 4.4(a)]. For $Pt_{13}Co_{26}$ clusters, they do not seem to reach saturation and show no hysteresis down to 10 K [figure 4.4(b)]. A decrease of the zero-field susceptibility is observed as temperature increases [figure 4.4(b)]. Larger clusters have non-zero coercivity, which vanishes at 40 ± 5 K.

The anisotropy of m_L is here negligible. Within the Bruno model linking the magnetic anisotropy energy (MAE) with the anisotropy of m_L (arising from crystal structure, strain, and interface hybridization) [141], this is consistent with the nearly isotropic hysteresis loops. We do not consider dipolar anisotropy here, as the arrangement of the magnetic atoms in the seeded clusters is unknown and the difference between Co and Pt lattice parameters is high

(about 11%). The observation of weak MAE whatever the environment (Pt or Ir seeding) and cluster size is similar to the capped Co clusters on BN/Ru(111) [135] and contrasts with other low-dimensional magnetic systems on metal surfaces [309, 144, 311].

The absence of coercivity and the decrease of the zero-field susceptibility with increasing temperature are strong indications that the $Pt_{13}Co_{26}$ clusters are superparamagnetic, as often is the case for such small nanoclusters at these temperatures. Given the close-to-isotropic magnetic properties of teh clusters, the M-H loops were fitted with a Langevin function (1.21), i.e., assuming no magnetic anisotropy. An additional slope χ_{add} was included in the fits, as discussed latter:

$$M(H) = M_{\mathrm{s}} \left(\tanh^{-1} \left(\frac{\mu_0 \mathcal{M} H}{k_{\mathrm{B}} T} \right) - \left(\frac{\mu_0 \mathcal{M} H}{k_{\mathrm{B}} T} \right)^{-1} \right) + \chi_{\mathrm{add}} H, \tag{4.1}$$

The resulting magnetic moment $m = 107 \pm 19\ \mu_{\mathrm{B}}$ was found mostly independent of temperature, confirming the relevance of the fitting function. Dividing m by the average number of Co atoms per cluster gives $4.1\mu_{\mathrm{B}}$ per atom. This value is unphysical for metallic Co even in low coordination [144] and largely exceeds that derived from sum rules (applied at 5 T, i.e., beyond the $[-1, +1]$ T field region where most variations of the Langevin function occur). The inhomogeneity in cluster sizes as visible in figure 4.2(a) cannot account for the high value of m as only 15% of the islands are coalesced ones with a double or triple size. Even if there are magnetic moments induced in the all atoms of Ir or Pt seeds, the value of total moment per atom ($\sim 2.74\ \mu_{\mathrm{B}}$) is still unreal. The large m value hence points to correlated spin blocks significantly larger than a single cluster. Notice that the cluster size is about 1 nm and the nearest cluster distance is 2.5 nm, the nearest clusters are not in contact one to other. The spin blocks might be given by magnetic coupling between Co atoms from neighbouring clusters or indirect through graphene (RKKY interaction) depending which of these two effects prevails at this speculative stage.

Let me now address the linear susceptibility (linear slope in figure 4.4(b) or linear term in equation 4.1), dominating M-H loops above ± 2 T, which was taken into account in the fitting as an addtional slope. The slope does not vary with temperature, hinting at an origin different from superparamagnetism. Such linearity up to fields much higher than the expected spontaneous magnetization cannot be ascribed to dipolar energy. Instead, tt might indicate exchange interactions favoring antiparalled or non-collinear magnetization arrangements. Whether this non-collinearity arises within each cluster in a hedge-hog fashion [312] or from a block of neighboring clusters remains speculative with the present data.

For larger clusters ($Ir_{50}Co_{500}$ and Co_{2700}), the vanishing of coercivity (40 ± 5 K) is presumably dominated by the blocking temperature of the largest clusters, around 10 nm in diameter and 3 nm in the height for Co_{2700} assemblies.

Finally, I discuss the degradation of the cluster upon exposure to x-rays. As documented by figure 4.5, the XMCD signal as well as XAS spectra decreases through 8 hours exposure by 40%, as derived from the sum rules. Surfaces measured after the same waiting time, but not exposed to the beam, did not show any reduction of moment. Therefore, surface contamination may be excluded. Consequently, the beam induces damage to the sample. Such a degradation is common for fragile magnetic species [313, 314] but is usually not observed for metal clusters. We surmise that the x-ray beam promotes the decomposition of graphene by the clusters, similar to what happens at elevated temperature [315]. Then, carbon enrichment of the clusters might be liable for the reduction of the Co XMCD signal.

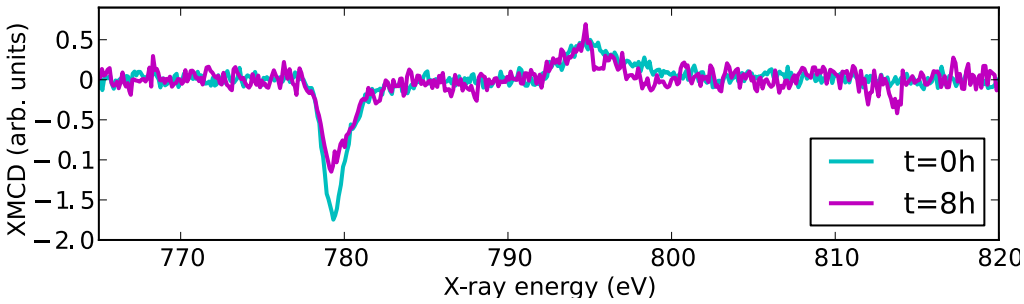

Figure 4.5: (a) XMCD signal normalized to absorption for Ir_4Co_8, at the beginning and after 8 h irradiation.

4.4 Conclusion

Using XMCD, we explored the magnetism of Co and Fe clusters on graphene/Ir(111), which we related to the custer size and distribution by (STM). Surprisingly, we found extremely weak magnetic anisotropies, although orbital moments are found to be slightly enhanced compared to bulk values, as it is expected due to the contribution of weakly coordinated atoms. From a simple analysis we derive macrospin values too large to correspond to a single cluster. This suggests magnetic interactions between clusters, for instance through the substrate, though the model which we employed is probably too simple to allow definitive conclusions to be drawn on this fact. We also identify degradation of the clusters upon exposure to the x-ray beam.

Further experiments are needed in a temperature range in which the cluster will become ferromagnetic. This would allow us to probe magnetic configuration induced by magnetic interactions between the clusters, such as parallel alignment of the magnetic moment of each clusters. Varying the distance between the clusters, by using graphene-metal moires having different periodicities, may allow to explore ferromagnetic or antiferromagnetic exchange interactions.

5

Summarizing the distinctive magnetic proporties in the three hybrid systems

In this chapter, I summarize the main magnetic properties of the three systems which have been studied, Au/Co/graphene/Ir, graphene/Co/Ir, and nanoclusters/graphene/Ir.

The magnetic moments (spin and orbital components) are systematically smaller for thin films than for clusters (table 5.1). One would expect the oposite if the effect of the low-coordination of atoms in these low-dimensional systems would prevail. Here we are led to the conclusion that the strength of the interaction between graphene and the magnetic element, stronger for thin films, modifies the chemical nature of this magnetic element, in turn reducing its magnetic moments. This effect is not only expected at the ferromagnet/graphene interface, but also at the interface between the ferromagnet and either the capping layer (Au, in the first kind of systems) or the substrate (Ir, in the second kind of systems). In all cases (thin films and clusters) the orbital moments are smaller than in the bulk, which is expected.

I now discuss the magnetic anisotropy of the thin Co films. At 4 K the annealed Au/Co/graphene/Ir systems has PMA until 2.5 nm; at room temperature it has PMA between 0.65 nm and 1.3 nm, and in-plane magnetization beyond this range. In contrast, non annealed Au/Co/graphene/Ir displays in-plane magnetization already for a 0.8 nm thickness. At room temperature, graphene/Co/Ir systems has PMA until 2.5 nm. The magnetocrystalline anisotropy constants are negative for non-annealed Au/Co/graphene/Ir and positive for annealed Au/Co/graphene/Ir and graphene/Co/Ir with comparable values for the two latter systems (table 5.1). The fact that Co/Ir and Co/Au are known to have different magnetic anisotropy energy contributions [316, 142] suggests different Co/graphene contributions from one system to the other. At this point we may only surmise that the contact between graphene and Co is different in the two systems, presumably better in the intercalated system.

A possible important difference between the two systems, besides the perfection of interfaces, might be the strain in the films, which has strong effect on the magnetocrystalline anisotropy. Growth on graphene, like is the case in Au/Co/graphene/Ir, is not expected to be associated with substantial epitaxial strain in view of the small graphene-Co lattice mismatch. On the contrary, the intercalation of Co between graphene and Ir, exploited for the formation of the graphene/Co/Ir system, is know to be accompanied by a large strain. The first intercalated Co layer was indeed shown to be pseudomorphic to Ir [304]. This corresponds to a high tensile strain in Co, given the 10% lattice mismatch between bulk Co and bulk Ir. The extent to which this strain will be "transmitted" to the Co layers beyond the first intercalated one remains

Table 5.1: Magneticrystalline anisotropy constants of investigated systems with their thickness t (nm), thickness of a Co atomic ML is ≈ 0.2 nm. Thickness of cluster is in average. atomic magnetic moment m (μ per Co atom). K_{mc} (J m^{-3}) calculated specific thicness of Co layer at 300 K.

Sample	Ir/Gr/Co/Au	Ir/Gr/Co/Au	Ir/Co/Gr	Gr/Co/Au	$Pt_{13}Co_{26}$/Gr
Growth	PLD as growth	PLD annealing	MBE intercalation	VASP	MBE self-organization
t	0.8	0.8	2.6	0.6	0.08
Method	MOKE, XMCD	MOKE, XMCD	SPLEEM	DFT	XMCD
m	1.47	1.41		1.70	1.72
K_{mc}	-3.8×10^5	10^6, 1.12×10^6	9.2×10^5	1.8×10^6	

unknown and deserves dedicated experiments. Note that tensile strain in Co might have a side-effect further increasing the interface magnetic anisotropy at the Co/graphene interface: tensile strains cause a decrease of the electronic density and are liable to induce higher reactivity [317], thus stronger C-Co bonds.

Conclusion and perspectives

1 General conclusion

Among numerous interests in research, graphene is potentially tought as a new material which may play an important role in the development in electronic and spintronic applications. In this PhD, we study the use of graphene as a template to modify the magnetic properties of ferromagnetic materials via the effect of interface with graphene, or provide organized arrays with high degree of spatial order. The thesis covers two parts from the background and methods to the result and discussion.

In the first Part, I give an overview in the history of graphene from the initial observation to its proposal application based on its extraordinary properties:

First, there are many preparation methods of graphene and graphene-based materials which may be used in applications, for instance with the examples of conductive electrodes, ultracapacitors, RF analog electronics, DNA translocation, ... These are found with corresponding unique performances in Section 1.1. Among them, epitaxial CVD graphene growth on metal surfaces, including the use of epitaxial thin film and single crystal which are the methods used in our study, are described in Section 1.4. Next, in Section 1.2, we focused on the unique magnetic behaviour of graphene and its hybrids such as defect-induced magnetism, RKKY effect, spin transport, spin-filtering and spin-splitting. These properties rise from the lightness of carbon, as well as from linear-dispersion electronic structure of this two-dimensional materials.

The magnetism of reduced dimension structures such as thin film and nanocluster are discussed in Section 1.3. In general, at nano-scale, materials exhibit properties different from the bulk, including electronic and magnetic properties. For instance, the magnetic anisotropy energy and single domains of nanostructure revealed numerous applications, especially in spintronics and data storage.

Finally, hybrid structures, i.e., the combination of two-dimensional graphene and these low-dimensional magnetic structures, are presented in Section 1.5 as one objective of our study put in the current context. Finally, in Chapter 2, I report the realization and characterization of these structure thank to the available experimental supports. In there, single-layer graphene is developed by CVD process, while metallic structure are deposited by PLD and MBE. Then, the samples are characterized *in situ* and *ex situ* by STM, RHEED, HRTEM for structural properties and SPLEEM, XMCD using synchrotron sources for magnetic properties.

In the second Part, Co ultrathin films or cluster have been investigated as ferromaget for hybrid structures:

Chapter 1 provides a new process to growth the graphene of high quality using an on-wafer Ir surface. On sapphire (0001), we optimized the growth of an ultrathin film of Ir(111), typically in the thickness range of [8–11] nm. These are enough for obtaining a crystaline surface of Ir(111) as the thinnest films used for CVD graphene growth in our best knowledge. These films are *fcc*

single-crystalline and display atomically-smooth terraces at their surface, whose regular width directly reflects the miscut of sapphire substrate. This thin film procedure allows one to cut down the research expenditures either of time and finances, in comparison with the single crystal. In addition, these thin films are experimentally demonstrated for growing graphene as high quality and suitable for numerous *ex situ* characterizations, for instance Raman spectroscopy, ARPES in the laboratory or through collaborations.

One of the main topics of thesis work is use the graphene of high quality on thin film as substrate to grow and to study the magnetic properties of epitaxial Co thin films, as seen in Chapter 2. The magnetic films are deposited by PLD which forces to form an ultrathin film of a few monolayer via layer-by-layer growth mode illustrated by STM images. Then, the Co layers are, directly or after an annealing step, capped by ultrathin gold layer to avoid the oxidation in *ex situ* investigations. The crystalline structure of the cobalt layer, a mixture of *fcc* and *hcp*, was characterized with HRTEM. Magnetic properties are characterized by many techniques: EHE measurement, MOKE focus and imagery at atmosphere and XMCD under UHV. *Ab initio* calculation were provided under a collaboration to support the results for the non-annealing film, an in-plane magnetization is found for all thickness. On the contrary, the annealing step at mild temperature tunes the in-plane to out-of-plane magnetization which the important role of Co/graphene interface. This interface are experimentally shown to favour PMA in the thickness range of [0.65–1.50] nm, consistent with the *ab inito* first-principles calculation. Besides, we observed multiple peaks on the XAS measurement at Co L_3 which is probably the feature of the partial carbidization of annealing Co thin films. The plausible reason is that graphene may be damaged under the PLD of Co. This would induce because there might be extra Co-C bonds in the system compared to the sole Co/graphene. Finally, magnetic domains of area exceeding 100 μm-scale were obtained, the domain wall propagation proceeds in the thermal creep regime, with weak pinning. An open question remains, as whether graphene still separates the Ir and Co surfaces, as the PLD and annealing step could damage and split graphene off Ir surface like intercalation (described in Chapter 3).

The third topic in the thesis is using graphene with intentionally induced defects on both single crystal and thin film to promoted the intercalation of ferromagnetic thin film, given in Chapter 3. The intercalation process is activated by a mild annealing. We studied the intercalation process and the structural properties of the system with the help of work function analysis, Auger electron spectroscopy, electron diffraction, STM, Raman spectroscopy and low-energy electron microscopy. Thanks to spin-polarized (SPLEEM), we find that the Co films, which are intrinsically air-protected, exhibit room temperature ferromagnetism with a magnetization perpendicular to the surface in the range between one and 13 monolayers. This rather unusual large range points to a very strong magnitude of the interface graphene-Co magnetic anisotropy energy, as compared to other systems. Comparing graphene/Co/Ir and Co/Ir stackings, we show that the magnetic anisotropy is several times larger for the graphene/Co interface than for the free Co surface, presumably due to a significant hybridization between cobalt d and carbon p_z states, which appears stronger in this system than in the related system which we studied, PLD Co/graphene/Ir. Intercalation opens the route for the elaboration at mild temperature of graphene/ferromagnetic ultrathin films for spintronics.

In Chapter 4, using in situ scanning tunnelling microscopy and in situ X-ray magnetic circular dichroism, we investigate cobalt-rich nanoclusters which are self-organized or randomly distributed on graphene on Ir(111). Surprisingly, we find almost no magnetic anisotropy for the smallest clusters ($Pt_{13}Co_{26}$), contrary to most observations in other systems which are self-organized at surfaces with higher magnetic moment per atom [311]. Increasing the cluster size

($Ir_{50}Co_{500}$ and Co_{2700}) does not substantially modify m_S, but results in a decrease of m_L/m_S towards the bulk value. The enhancement of m_L/m_S for small clusters compared to the bulk is typical of small-size objects and arises from the local breaking of symmetry, i.e., lower coordination or strain. The modelling of the temperature-dependant hysteresis loops of $Pt_{13}Co_{26}$ clusters in the superparamagnetic state points to a spin-block size exceeding that of the clusters, which could be an indication of magnetic coupling between the clusters. Finally, we observe a reduction of the x-ray magnetic circular dichroism signal versus time due to soft x-ray exposure, which we ascribe to damages induces in the graphene upon strong illumination.

2 Perspectives and open questions:

CVD graphene on metallic thin film:

Iridium is a highly corrosion-resistant material, with strong electrochemical potentials on aggressive chemical etchant, we met an obstacle to remove totally the ultrathin metallic film without damaging graphene layer in transferring steps. A further step could be to investigate the growth of an ultrathin film of an etchable and metal with also how-carbon solubility such as Cu. The PLD growth of ultrathin films might be applied other transition metals or alloy with varying composition in order to tuning the moiré parameters, i.e., changing the lattice parameters and distribution [318] of self-organized clusters.

PMA of ferromagnetic/graphene hybrid systems:

The PMA systems ensure that a high magnetic remanence, low magnetostatic interactions with the surrounding due to the ultrathin aspect ratio of the layers and high thermal stability can be achieved, even for nanostrutures down to a very small lateral size, which is promising for sustaining high-remanence nanomagnets in devices down to very small lateral dimensions. PMA also opens the door to the easy realization of graphene-based devices with cross-magnetized electrodes such as those needed for efficient spin-transfer torque magnetization precession. Other graphene-relevant interfacial effects expected in such asymmetric layers pertain to novel ways of controlling magnetization, such as Rashba fileds [258] and electric fields [319].

Instead of graphene/Ir(111), other graphene supports may be employed. Exfoliated graphene, graphene/SiC and graphene prepared on metals and transferred to insulating supports [75, 242] would *a priori* be well suited to lateral transport devices.

Graphene/Co thin film hybrid systems are promising in a number of respects in the view of spintronics applications. We foresee that the systems is well-suited for the easy control of magnetization by means of either laser illumination through the transparent graphene electrode, external electric field appled through a gate dielectric layer deposited on top of the graphene protective barrier, or electric current passed through current lines designed by lithography on graphene/Co thin films. We anticipate further magnetic engineering of the interface between Co and sp^2 materials by controlling the number/nature of defects in the sp^2 materials and the composition of this material and by replacing the bottom (metal) contact with another graphene contact. The preparation method that we developed holds generality for other high-quality graphene-metal and low-dimensional lamelllar materials/metal hybrids systems.

Magnetism of self-organized cluster on graphene moiré:

Basing on our result so far, with a view to access unquestionably the intrinsic magnetic (moment and anisotropy) and coupling properties of arrays of magnetic clusters on graphene, we have repeated and extended experiments. The data is under analyse in the time of this thesis editing. For solving the issue of cluster onset of coalescence; we proceeded to Ir_{20} seeding which past experiments showed to provide more robustness against future coalescence. The analysis

is under way and the first intention exhibits no difference to the reported result, at least, for the magnetic isotropy. It would also be valuable to access to lower temperatures (1.5 K) to see blocked states, and gain information on the magnetic anisotropy. Monitoring and avoiding beam damage; could be done thanks to the defocusing of the x-ray beam specifically implemented at the DEIMOS beamline, SOLEIL synchrotron.

While the structure of mixed cluster on graphene is still unclear, the characterization of symmetry of the systems may allow to understand more about the observed behaviour such as the arrangement of magnetic moments inside the cluster and the mediated role of graphene interface. The systematic investigation of clusters size may be necessary to draw trends of exchange interaction at such low dimensions. Finally, the optimization of an inert capping layer is under optimization for the further *ex situ* characterizations and also for the possible applications. While metals often wet however modify the cluster lattice, insulators such as Al_2O_3 or amorphous carbon are considered as possible capping layers.

It could be interesting to explore other kinds of systems on graphene/metal moiré. For instance, Rhodium clusters on graphene/Ir(111) or on graphene/Ru(0001) [320]. As an element near the Stoner's criterion, Rh clusters comprising 12–32 atoms are magnetic and hold magnetic moments per atom exceeding the value of bulk Ni [321, 322]. Furthermore, Rh cluster array can be used as seeding for the growth of CoRh and FeRh systems which might show a magnetic polarization of 4*d* Rh states [323]. Indeed, the self-organized clusters of Rh on graphene have recently been investigated and their data are under evaluation. In early consideration, the system exhibits no magnetic behaviour.

Other perspectives

The intercalation of Eu between graphene and Iridium, which could give almost free-standing graphene, x-ray standing wave experiments (XWS, not yet published) and spin-polarized band structure in graphene (DFT calculations), as well as interersting magnetic phase transitions between different Eu magnetic phases.

The issue of inducing magnetism in graphene through the contact with Co is under investigation. This could lead to the study of magnetism in 2D carbon. Imaging magnetic domains, with x-ray photoemissionelectron microscopy (XPEEM) at the carbon edge in graphene, is a tantalizing proposal, for instance.

Finally, combining graphene with strong spin-orbit supports, e.g., Au, Ir, and magnetic clusters could induce some magnetic moments in graphene. The system is an interesting approach to induce strong spin-polarizatoin in graphene. This could be adressed with spin-polarized ARPES

List of Figures

List of Tables

Glossary

Acronyms and Abbreviations

a.u.: arbitrary units.
AAS: atomic absorption spectrometry
AES: Auger electron spectroscopy
ARPES: angle-resolved photoemission spectroscopy
ARUPS: angle-resolved ultraviolet photoelectron spectroscopy
BN: boron nitride
CCD cts.: charge-coupled device counts
C_2H_4: ethylene
CNT: carbon nanotube
CVD: chemical vapour deposition
0D: zero-dimensional
1D: one-dimensional
2DEG: two-dimensional electron gas
3D: three-dimensional
DFT: density functional theory
DNA: deoxyribonucleic acid
DOS: density of states
T_C: Curie temperature
EG: epitaxial graphene
EHE: extraordinary Hall effect
EPR: election paramagnetic resonance
ESRF: European Synchrotron Radiation Facility
FET: field effect transistor
FM: ferromagnet
GO: graphene oxide
Gr: graphene
h-BN: hexagonal boron nitride
HOPG: highly ordered pyrolytic graphite
HRTEM: high resolution transmission electron microscopy
FWHM: full width at half maximum
IMFP: inelastic mean free path
IQHE: integer quantum Hall effect
IQHS: integer quantum Hall state
LEED: low-energy electron diffraction
LEEM: low-energy electron microscopy
MAE: magnetic anisotropy energy
MOKE: magneto-optical Kerr effect
ML: monolayer
NCEM: National Center for Electron Microscopy, Berkeley
PEEM: photoemission electron microscopy
PLD: pulsed laser deposition
PMA: perpendicular magnetic anisotropy
QHE: quantum Hall effect
RF: radio frequency
RGO: reduced graphene oxide
RKKY: Ruderman-Kittel-Kasuya-Yoshida
SEMPA: scanning electron microscopy with polarization analysis
SiC: silicon carbide
SPLEEM: spin-polarized low-energy electron microscopy
SRT: spin reorientation transition
SQUID: superconducting quantum interference device
STM: scanning tunnelling microscopy
SW: Stone-Wales
TEY: total electron yield
TMR: magnetoresistances
UHV: ultrahigh vacuum
VSM: vibrating sample magnetometer
XMCD: x-ray magnetic circular dichroism
XMLD: x-ray magnetic linear dichroism
XPS: x-ray photoelectron spectroscopy
XRD: x-ray diffraction

A

Hysteresis loops of Au-capped cobalt films on graphene/Ir and on Ir(111)

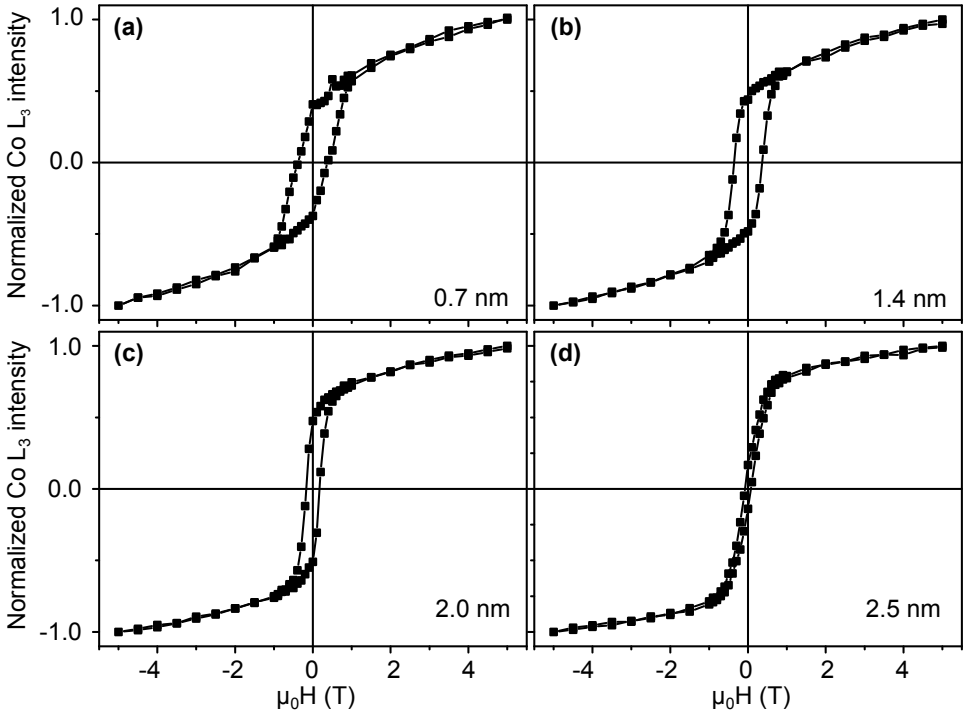

Figure A.1: Normalized M-H loops at 4K for 0° incidence for annealing Au-capped cobalt on graphene/Ir(111) in function of thickness: (a) 0.7 nm, (b) 1.4 nm, (c) 2.0 nm and (c) 2.5 nm

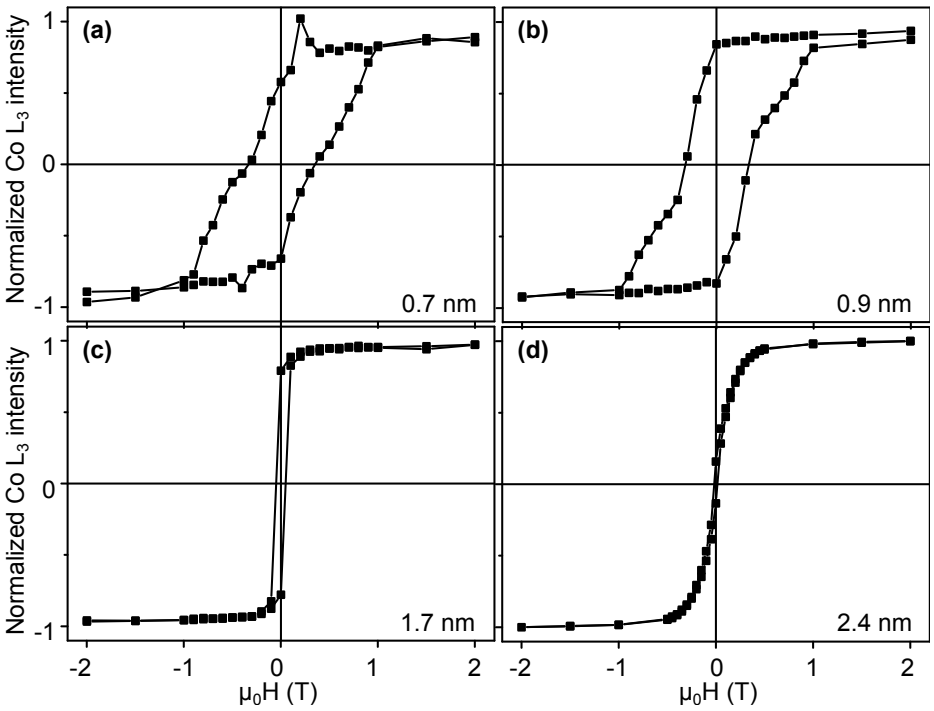

Figure A.2: Normalized M-H loops at 4K for 0° incidence for annealing Au-capped cobalt on Ir(111) in function of thickness: (a) 0.7 nm, (b) 0.9 nm, (c) 1.7 nm and (c) 2.4 nm

A

Extraordinary Hall resistances in Au/Co/graphene/Ir stacking

Due to the metallic character of the bottom layer (Ir+graphene) and capping layer (Au), most of the in-plane current does not flow through the Co layer. The magnitude of the experimental EHE is 1.4 mΩ at 300 K. Note that this value is low compared with other Co films with perpendicular such as Pt/Co/Pt (125 mmΩ, [324]). The square resistance of a 9-nm-thick Ir layer is 5.9 Ω sq^{-1} [figure A.1] with a residual resistivity ratio of 8.8. Assuming 80 and 10 Ω sq^{-1} specific resistances for the Co and Au regions, respectively, and that the specific resistance of graphene should drop by at least one order of magnitude as compared to undoped graphene (1000 Ω sq^{-1}) due to charge transfer from Ir and Co, less than 10% of the current should flow through Co if the heterostructure behaves as resistors in parallel, i.e., neglecting interface contributions and the finite-thickness effect. The literature values for Co EHE (0.24 $\times 10^{-10} \Omega$ m T^{-1}) and magnetization (1.43 10^6 A m^{-1}) yield an EHE resistances of 62 m Ω for 0.9 nm thickness. The measured EHE of 1.4 mΩ corresponds to 2.4% of the current flowing through Co, indeed less than 10%. Other effects may contribute forward further decreasing the EHE (100% out-of-plane remanence, partial short circuit of the transverse EHE electric field by the metallic layers).

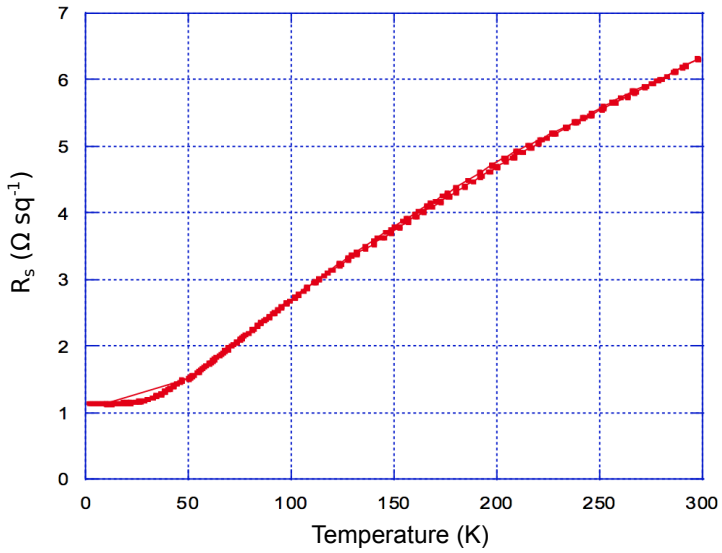

Figure A.1: Specific resistance decrease from 6.35 Ω sq^{-1} at 300 K down to 1.14 Ω sq^{-1} at 2K. Because Ir is single crystal thin film, its resistivity goes to very low value when cooling down. The short-circuit effect is more efficient at low temperature.

Bibliography

[1] Peter G Bruce, Bruno Scrosati, and Jean-Marie Tarascon. Nanomaterials for Rechargeable Lithium Batteries. *Angewandte Chemie International Edition*, 47(16):2930–2946, April 2008.

[2] Donghai Wang, Daiwon Choi, Juan Li, Zhenguo Yang, Zimin Nie, Rong Kou, Dehong Hu, Chongmin Wang, Laxmikant V Saraf, Jiguang Zhang, Ilhan A Aksay, and Jun Liu. Self-Assembled TiO 2–Graphene Hybrid Nanostructures for Enhanced Li-Ion Insertion. *ACS Nano*, 3(4):907–914, April 2009.

[3] P V Kamat. Graphene-Based Nanoarchitectures. Anchoring Semiconductor and Metal Nanoparticles on a Two-Dimensional Carbon Support. *The Journal of Physical Chemistry Letters*, 2009.

[4] Adrien Allain, Zheng Han, and Vincent Bouchiat. Electrical control of the superconducting-to-insulating transition in graphene–metal hybrids. *Nature Materials*, 11(7):590–594, May 2012.

[5] Elena Bekyarova, Mikhail E Itkis, Palanisamy Ramesh, Claire Berger, Michael Sprinkle, Walt A de Heer, and Robert C Haddon. Chemical Modification of Epitaxial Graphene: Spontaneous Grafting of Aryl Groups. *Journal of the American Chemical Society*, 131(4):1336–1337, February 2009.

[6] M Weser, E N Voloshina, K Horn, and Yu S Dedkov. Electronic structure and magnetic properties of the graphene/Fe/Ni(111) intercalation-like system. *arXiv.org*, cond-mat.mtrl-sci(16):7534–7536, January 2011.

[7] M Weser, Y Rehder, K Horn, M Sicot, M Fonin, A B Preobrajenski, E N Voloshina, E Goering, and Yu S Dedkov. Induced magnetism of carbon atoms at the graphene/Ni(111) interface. *Applied Physics Letters*, 96(1):012504–4, 2010.

[8] O Rader, A Varykhalov, J Sánchez-Barriga, D Marchenko, A Rybkin, and A Shikin. Is There a Rashba Effect in Graphene on 3d Ferromagnets? *Physical Review Letters*, 102(5):057602, February 2009.

[9] A Varykhalov, J Sánchez-Barriga, A Shikin, C Biswas, E Vescovo, A Rybkin, D Marchenko, and O Rader. Electronic and Magnetic Properties of Quasifreestanding Graphene on Ni. *Physical Review Letters*, 101(15):157601–157604, October 2008.

[10] Oleg Yazyev and Alfredo Pasquarello. Magnetoresistive junctions based on epitaxial graphene and hexagonal boron nitride. *Physical Review B*, 80(3):035408, July 2009.

[11] Vadim Cheianov and Vladimir Fal'ko. Friedel Oscillations, Impurity Scattering, and Temperature Dependence of Resistivity in Graphene. *Physical Review Letters*, 97(22):226801, November 2006.

[12] Ruijuan Xiao, Daniel Fritsch, Michael Kuz'min, Klaus Koepernik, Helmut Eschrig, Manuel Richter, Knut Vietze, and Gotthard Seifert. Co Dimers on Hexagonal Carbon Rings Proposed as Subnanometer Magnetic Storage Bits. *Physical Review Letters*, 103(18):187201, October 2009.

[13] Stephen J Blanksby and G Barney Ellison. Bond Dissociation Energies of Organic Molecules. *The Journal of Physical Chemistry Letters*, 36(4):255–263, April 2003.

[14] Joerg R Jinschek, Emrah Yucelen, Hector A Calderon, and Bert Freitag. Quantitative atomic 3-D imaging of single/double sheet graphene structure. *Carbon*, 49(2):556–562, February 2011.

[15] A K Geim and K S Novoselov. The rise of graphene. *Nature Materials*, 6(3):183–191, March 2007.

[16] J Boardman, I E S Edwards, N G L Hammond, and E Sollberger. *The Cambridge Ancient History*. Cambridge University Press, February 2008.

[17] H W Kroto, J R Heath, S C O'Brien, R F Curl, and R E Smalley. C60: Buckminsterfullerene. *Nature*, 318(6042):162–163, November 1985.

[18] S Iijima. Helical microtubules of graphitic carbon. *Nature*, 354(6348):56–58, November 1991.

[19] LV Radushkevich and VM Lukyanovich. About the structure of carbon formed by thermal decomposition of carbon monoxide on iron substrate. *J. Phys. Chem.(Moscow)*, 26:88–95, 1952.

[20] K S Novoselov. Electric Field Effect in Atomically Thin Carbon Films. *Science*, 306(5696):666–669, October 2004.

[21] HP Boehm and U. Hofmann. Surface properties of extremely thin graphite lamellae. In *Proc. 5th Conf. on Carbon*, 1962.

[22] A H Castro Neto, N M R Peres, K S Novoselov, and A K Geim. The electronic properties of graphene. *Reviews of Modern Physics*, 81(1):109–162, January 2009.

[23] Kin Mak, Changgu Lee, James Hone, Jie Shan, and Tony Heinz. Atomically Thin MoS_2: A New Direct-Gap Semiconductor. *Physical Review Letters*, 105(13):136805, September 2010.

[24] K S Novoselov. Two-dimensional atomic crystals. *Proceedings of the National Academy of Sciences*, 102(30):10451–10453, July 2005.

[25] Desalegne Teweldebrhan, Vivek Goyal, and Alexander A Balandin. Exfoliation and Characterization of Bismuth Telluride Atomic Quintuples and Quasi-Two-Dimensional Crystals. *Nano Letters*, 10(4):1209–1218, April 2010.

[26] Boubekeur Lalmi, Hamid Oughaddou, Hanna Enriquez, Abdelkader Kara, Sébastien Vizzini, Bénidicte Ealet, and Bernard Aufray. Epitaxial growth of a silicene sheet. *Applied Physics Letters*, 97(22):223109–223109–2, 2010.

[27] Patrick Vogt, Paola De Padova, Claudio Quaresima, Jose Avila, Emmanouil Frantzeskakis, Maria Asensio, Andrea Resta, Bénédicte Ealet, and Guy Le Lay. Silicene: Compelling Experimental Evidence for Graphenelike Two-Dimensional Silicon. *Physical Review Letters*, 108(15):155501, April 2012.

[28] P R Wallace. The Band Theory of Graphite. *Physical Review*, 71:622–633, May 1947.

[29] J Slonczewski and P Weiss. Band Structure of Graphite. *Physical Review*, 109(2):272–279, January 1958.

[30] Gordon Semenoff. Condensed-Matter Simulation of a Three-Dimensional Anomaly. *Physical Review Letters*, 53(26):2449–2452, December 1984.

[31] F D M Haldane. Model for a Quantum Hall Effect without Landau Levels: Condensed-Matter Realization of the "Parity Anomaly". *Physical Review Letters*, 61(18):2015–2018, October 1988.

[32] M I Katsnelson, K S Novoselov, and A K Geim. Chiral tunnelling and the Klein paradox in graphene. *Nature Physics*, 2(9):620–625, August 2006.

[33] Andrea F Young and Philip Kim. Quantum interference and Klein tunnelling in graphene heterojunctions. *Nature Physics*, 5(3):222–226, February 2009.

[34] N Stander, B Huard, and D Goldhaber-Gordon. Evidence for Klein Tunneling in Graphene p-n Junctions. *Physical Review Letters*, 102(2):026807, January 2009.

[35] De-en Jiang, Bobby G Sumpter, and Sheng Dai. First principles study of magnetism in nanographenes. *The Journal of Chemical Physics*, 127(12):124703, 2007.

[36] K S Novoselov, A K Geim, S V Morozov, D Jiang, M I Katsnelson, I V Grigorieva, S V Dubonos, and A A Firsov. Two-dimensional gas of massless Dirac fermions in graphene. *Nature*, 438(7065):197–200, November 2005.

[37] Yuanbo Zhang, Yan-Wen Tan, Horst L Stormer, and Philip Kim. Experimental observation of the quantum Hall effect and Berry's phase in graphene. *Nature*, 438(7065):201–204, November 2005.

[38] C Berger. Electronic Confinement and Coherence in Patterned Epitaxial Graphene. *Science*, 312(5777):1191–1196, May 2006.

[39] M O Goerbig. *Ultracold Gases and Quantum Information: Lecture Notes of the Les Houches Summer School in Singapore*, volume 91. ukcatalogue.oup.com, May 2011.

[40] Yisong Zheng and Tsuneya Ando. Hall conductivity of a two-dimensional graphite system. *Physical Review B*, 65(24):245420, June 2002.

[41] Alexander S Mayorov, Daniel C Elias, Ivan S Mukhin, Sergey V Morozov, Leonid A Ponomarenko, Kostya S Novoselov, A K Geim, and Roman V Gorbachev. How Close Can One Approach the Dirac Point in Graphene Experimentally? *Nano Letters*, 12(9):4629–4634, September 2012.

[42] P Neugebauer, M Orlita, C Faugeras, A L Barra, and M Potemski. How Perfect Can Graphene Be? *Physical Review Letters*, 103(13):136403, September 2009.

[43] Alexander Tzalenchuk, Samuel Lara-Avila, Alexei Kalaboukhov, Sara Paolillo, Mikael Syväjärvi, Rositza Yakimova, Olga Kazakova, T J B M Janssen, Vladimir Fal'ko, and Sergey Kubatkin. Towards a quantum resistance standard based on epitaxial graphene. *Nature Nanotechnology*, 5(3):186–189, January 2010.

[44] Nicholas Petrone, Cory R Dean, Inanc Meric, Arend M van der Zande, Pinshane Y Huang, Lei Wang, David Muller, Kenneth L Shepard, and James Hone. Chemical Vapor Deposition-Derived Graphene with Electrical Performance of Exfoliated Graphene. *Nano Letters*, 12(6):2751–2756, June 2012.

[45] Zheng Yan, Jian Lin, Zhiwei Peng, Zhengzong Sun, Yu Zhu, Lei Li, Changsheng Xiang, E Loïc Samuel, Carter Kittrell, and James M Tour. Toward the Synthesis of Wafer-Scale Single-Crystal Graphene on Copper Foils. *ACS Nano*, 6(10):9110–9117, October 2012.

[46] Seung Yol Jeong, Sung Hun Kim, Joong Tark Han, Hee Jin Jeong, Soo Yeon Jeong, and Geon-Woong Lee. Highly Concentrated and Conductive Reduced Graphene Oxide Nanosheets by Monovalent Cation- Interaction: Toward Printed Electronics. *physica status solidi (a)*, 22(15):3307–3314, April 2012.

[47] L Sun and B Fugetsu. Massive production of graphene oxide from expanded graphite. pages 1–12, January 2013.

[48] Xuekun Lu, Minfeng Yu, Hui Huang, and Rodney S Ruoff. Tailoring graphite with the goal of achieving single sheets. *Europhysics Letters (EPL)*, 10(3):269, August 1999.

[49] G Zhang. Tubular Graphite Cones. *Science*, 300(5618):472–474, April 2003.

[50] Du Xu, Ivan Skachko, Fabian Duerr, Adina Luican, and Eva Y Andrei. Fractional quantum Hall effect and insulating phase of Dirac electrons in graphene. *Nature*, 462(7270):192–195, October 2009.

[51] K I Bolotin, K J Sikes, Z Jiang, M Klima, G Fudenberg, J Hone, P Kim, and H L Stormer. Ultrahigh electron mobility in suspended graphene. *Solid State Communications*, 146(9-10):351–355, June 2008.

[52] C R Dean, A F Young, I Meric, C Lee, L Wang, S Sorgenfrei, K Watanabe, T Taniguchi, P Kim, K L Shepard, and J Hone. Boron nitride substrates for high-quality graphene electronics. *Nature Nanotechnology*, 5(10):722–726, August 2010.

[53] D V BADAMI. Graphitization of -Silicon Carbide. *Nature*, 193(4815):569–570, February 1962.

[54] A J Van Bommel, J E Crombeen, and A Van Tooren. LEED and Auger electron observations of the SiC(0001) surface. *Surface Science*, 48(2):463–472, March 1975.

[55] Claire Berger, Zhimin Song, Tianbo Li, Xuebin Li, Asmerom Y Ogbazghi, Rui Feng, Zhenting Dai, Alexei N Marchenkov, Edward H Conrad, Phillip N First, and Walt A de Heer. Ultrathin Epitaxial Graphite: 2D Electron Gas Properties and a Route toward Graphene-based Nanoelectronics. *The Journal of Physical Chemistry B*, 108(52):19912–19916, December 2004.

[56] I Forbeaux, J M Themlin, and J M Debever. Heteroepitaxial graphite on 6H-SiC(0001):Interface formation through conduction-band electronic structure. *Physical Review B*, 58(24):16396–16406, December 1998.

[57] K V Emtsev, F Speck, Th Seyller, and L Ley. Interaction, growth, and ordering of epitaxial graphene on SiC0001 surfaces: A comparative photoelectron spectroscopy study. *Physical Review B*, 77(15):155303–10, April 2008.

[58] C Virojanadara, M Syväjarvi, R Yakimova, L Johansson, A Zakharov, and T Balasubramanian. Homogeneous large-area graphene layer growth on 6H-SiC(0001). *Physical Review B*, 78(24):245403, December 2008.

[59] Nicolas Camara, Jean-Roch Huntzinger, Gemma Rius, Antoine Tiberj, Narcis Mestres, Francesc Pérez-Murano, Philippe Godignon, and Jean Camassel. Anisotropic growth of long isolated graphene ribbons on the C face of graphite-capped 6H-SiC. *Physical Review B*, 80(12):125410, September 2009.

[60] Konstantin V Emtsev, Aaron Bostwick, Karsten Horn, Johannes Jobst, Gary L Kellogg, Lothar Ley, Jessica L McChesney, Taisuke Ohta, Sergey A Reshanov, Jonas Röhrl, Eli Rotenberg, Andreas K Schmid, Daniel Waldmann, Heiko B Weber, and Thomas Seyller. Towards wafer-size graphene layers by atmospheric pressure graphitization of silicon carbide. *Nature Materials*, 8(3):203–207, February 2009.

[61] Walt A de Heer, Claire Berger, Xiaosong Wu, Mike Sprinkle, Yike Hu, Ming Ruan, Joseph A Stroscio, Phillip N First, Robert Haddon, Benjamin Piot, Clément Faugeras, Marek Potemski, and Jeong-Sun Moon. Epitaxial graphene electronic structure and transport. *Journal of Physics D: Applied Physics*, 43(37):374007, September 2010.

[62] Luxmi, N Srivastava, Guowei He, R Feenstra, and P Fisher. Comparison of graphene formation on C-face and Si-face SiC 0001 surfaces. *Physical Review B*, 82(23):235406, December 2010.

[63] Victor Yu Aristov, Grzegorz Urbanik, Kurt Kummer, Denis V Vyalikh, Olga V Molodtsova, Alexei B Preobrajenski, Alexei A Zakharov, Christian Hess, Torben Hänke, Bernd Büchner, Ivana Vobornik, Jun Fujii, Giancarlo Panaccione, Yuri A Ossipyan, and Martin Knupfer. Graphene Synthesis on Cubic SiC/Si Wafers. Perspectives for Mass Production of Graphene-Based Electronic Devices. *Nano Letters*, 10(3):992–995, March 2010.

[64] A Ouerghi, A Kahouli, D Lucot, M Portail, L Travers, J Gierak, J Penuelas, P Jegou, A Shukla, T Chassagne, and M Zielinski. Epitaxial graphene on cubic SiC(111)/Si(111) substrate. *Applied Physics Letters*, 96(19):191910, 2010.

[65] Alexander Tzalenchuk. QHE in SiC graphene. pages 1–7, July 2009.

[66] T Shen, J J Gu, M Xu, Y Q Wu, M L Bolen, M A Capano, L W Engel, and P D Ye. Observation of quantum-Hall effect in gated epitaxial graphene grown on SiC (0001). *Applied Physics Letters*, 95(17):172105, 2009.

[67] J Hass, F Varchon, J Millán-Otoya, M Sprinkle, N Sharma, W de Heer, C Berger, P First, L Magaud, and E Conrad. Why Multilayer Graphene on 4H-SiC(0001^{-}) Behaves Like a Single Sheet of Graphene. *Physical Review Letters*, 100(12), March 2008.

[68] F Hiebel, P Mallet, F Varchon, L Magaud, and J-Y Veuillen. Graphene-substrate interaction on 6H-SiC(0001[over ¯]) : A scanning tunneling microscopy study. *Physical Review B*, 78(15):153412, October 2008.

[69] Xiaosong Wu, Yike Hu, Ming Ruan, Nerasoa K Madiomanana, John Hankinson, Mike Sprinkle, Claire Berger, and Walt A de Heer. Half integer quantum Hall effect in high mobility single layer epitaxial graphene. *Applied Physics Letters*, 95(22):223108–223108–3, 2009.

[70] B C BANERJEE, T J HIRT, and P L WALKER. Pyrolytic Carbon Formation from Carbon Suboxide. *Nature*, 192(4801):450–451, November 1961.

[71] Alexander E Karu. Pyrolytic Formation of Highly Crystalline Graphite Films. *Journal of Applied Physics*, 37(5):2179–2181, 1966.

[72] Johann Coraux, Alpha T N'Diaye, Carsten Busse, and Thomas Michely. Structural Coherency of Graphene on Ir(111). *Nano Letters*, 8(2):565–570, February 2008.

[73] Peter W Sutter, Jan-Ingo Flege, and Eli A Sutter. Epitaxial graphene on ruthenium. *Nature Materials*, 7(5):406–411, April 2008.

[74] S M Irving and P L Walker, Jr. Interaction of evaporated carbon with heated metal substrates. *Carbon*, 5(4):399–402, September 1967.

[75] Alfonso Reina, Xiaoting Jia, John Ho, Daniel Nezich, Hyungbin Son, Vladimir Bulovic, Mildred S Dresselhaus, and Jing Kong. Large Area, Few-Layer Graphene Films on Arbitrary Substrates by Chemical Vapor Deposition. *Nano Letters*, 9(1):30–35, January 2009.

[76] X Li, W Cai, J An, S Kim, J Nah, D Yang, R Piner, A Velamakanni, I Jung, E Tutuc, S K Banerjee, L Colombo, and R S Ruoff. Large-Area Synthesis of High-Quality and Uniform Graphene Films on Copper Foils. *Science*, 324(5932):1312–1314, June 2009.

[77] Sukang Bae, Hyeongkeun Kim, Youngbin Lee, Xiangfan Xu, Jae-Sung Park, Yi Zheng, Jayakumar Balakrishnan, Tian Lei, Hye Ri Kim, Young Il Song, Young-Jin Kim, Kwang S Kim, Barbaros Özyilmaz, Jong-Hyun Ahn, Byung Hee Hong, and Sumio Iijima. Roll-to-roll production of 30-inch graphene films for transparent electrodes. *Nature Nanotechnology*, 5(8):574–578, July 2010.

[78] Gunther Lippert, Jarek Dabrowski, Max Lemme, Charles Marcus, Olaf Seifarth, and Grzegorz Lupina. Direct graphene growth on insulator. *physica status solidi (a)*, 248(11):2619–2622, August 2011.

[79] Mark H Rümmeli, Alicja Bachmatiuk, Andrew Scott, Felix Börrnert, Jamie H Warner, Volker Hoffmann, Jarrn-Horng Lin, Gianaurelio Cuniberti, and Bernd Büchner. Direct Low Temperature Nano-Graphene Synthesis over a Dielectric Insulator. March 2011.

[80] Sneha Gaddam, Cameron Bjelkevig, Siping Ge, Keisuke Fukutani, Peter A Dowben, and Jeffry A Kelber. Direct graphene growth on MgO: origin of the band gap. *Journal of Physics: Condensed Matter*, 23(7):072204, February 2011.

[81] Xuli Ding, Guqiao Ding, Xiaoming Xie, Fuqiang Huang, and Mianheng Jiang. Direct growth of few layer graphene on hexagonal boron nitride by chemical vapor deposition. *Carbon*, 49(7):2522–2525, June 2011.

[82] C Oshima, A Itoh, E Rokuta, T Tanaka, K Yamashita, and T Sakurai. A hetero-epitaxial-double-atomic-layer system of monolayer graphene/monolayer h-BN on Ni(111). *Solid State Communications*, 116(1):37–40, August 2000.

[83] Rod Ruoff. Graphene: Calling all chemists. *Nature Nanotechnology*, 3(1):10–11, January 2008.

[84] Sungjin Park, Jinho An, Inhwa Jung, Richard D Piner, Sung Jin An, Xuesong Li, Aruna Velamakanni, and Rodney S Ruoff. Colloidal Suspensions of Highly Reduced Graphene Oxide in a Wide Variety of Organic Solvents. *Nano Letters*, 9(4):1593–1597, April 2009.

[85] Masukazu Hirata, Takuya Gotou, Shigeo Horiuchi, Masahiro Fujiwara, and Michio Ohba. Thin-film particles of graphite oxide 1:. *Carbon*, 42(14):2929–2937, January 2004.

[86] Masukazu Hirata, Takuya Gotou, and Michio Ohba. Thin-film particles of graphite oxide. 2: Preliminary studies for internal micro fabrication of single particle and carbonaceous electronic circuits. *Carbon*, 43(3):503–510, January 2005.

[87] Tamás Szabó, Anna Szeri, and Imre Dékány. Composite graphitic nanolayers prepared by self-assembly between finely dispersed graphite oxide and a cationic polymer. *Carbon*, 43(1):87–94, January 2005.

[88] K S Novoselov, V I Fal ko, L Colombo, P R Gellert, M G Schwab, and K Kim. A roadmap for graphene. *Nature*, 490(7419):192–200, October 2012.

[89] C Lee, X Wei, J W Kysar, and J Hone. Measurement of the Elastic Properties and Intrinsic Strength of Monolayer Graphene. *Science*, 321(5887):385–388, July 2008.

[90] Alexander A Balandin, Suchismita Ghosh, Wenzhong Bao, Irene Calizo, Desalegne Teweldebrhan, Feng Miao, and Chun Ning Lau. Superior Thermal Conductivity of Single-Layer Graphene. *Nano Letters*, 8(3):1–6, February 2008.

[91] R R Nair, P Blake, A N Grigorenko, K S Novoselov, T J Booth, T Stauber, N M R Peres, and A K Geim. Fine Structure Constant Defines Visual Transparency of Graphene. *Science*, 320(5881):1308–1308, June 2008.

[92] F Bonaccorso, Z Sun, T Hasan, and A C Ferrari. Graphene photonics and optoelectronics. *Nature Photonics*, 4(9):611–622, August 2010.

[93] Xuesong Li, Yanwu Zhu, Weiwei Cai, Mark Borysiak, Boyang Han, David Chen, Richard D Piner, Luigi Colombo, and Rodney S Ruoff. Transfer of Large-Area Graphene Films for High-Performance Transparent Conductive Electrodes. *Nano Letters*, 9(12):4359–4363, December 2009.

[94] Hyung Mo Jeong, Jung Woo Lee, Weon Ho Shin, Yoon Jeong Choi, Hyun Joon Shin, Jeung Ku Kang, and Jang Wook Choi. Nitrogen-Doped Graphene for High-Performance Ultracapacitors and the Importance of Nitrogen-Doped Sites at Basal Planes. *Nano Letters*, 11(6):2472–2477, June 2011.

[95] Frank Schwierz. Graphene transistors. *Nature Nanotechnology*, 5(7):487–496, May 2010.

[96] Yanqing Wu, Keith A Jenkins, Alberto Valdes-Garcia, Damon B Farmer, Yu Zhu, Ageeth A Bol, Christos Dimitrakopoulos, Wenjuan Zhu, Fengnian Xia, Phaedon Avouris, and Yu-ming Lin. State-of-the-Art Graphene High-Frequency Electronics. *Nano Letters*, 12(6):3062–3067, June 2012.

[97] S Garaj, W Hubbard, A Reina, J Kong, D Branton, and J A Golovchenko. Graphene as a subnanometre trans-electrode membrane. *Nature*, 467(7312):190–193, August 2010.

[98] Christopher A Merchant, Ken Healy, Meni Wanunu, Vishva Ray, Neil Peterman, John Bartel, Michael D Fischbein, Kimberly Venta, Zhengtang Luo, A T Charlie Johnson, and Marija Drndić. DNA Translocation through Graphene Nanopores. *Nano Letters*, 10(8):3163–3167, August 2010.

[99] J J Sakurai. *Neutral currents and gauge theories–past, present, and future*, volume 48. AIP, December 1978.

[100] Hongki Min, J E Hill, N A Sinitsyn, B R Sahu, Leonard Kleinman, and A H MacDonald. Intrinsic and Rashba spin-orbit interactions in graphene sheets. *Physical Review B*, 74(16), October 2006.

[101] Tatiana L Makarova. Ferromagnetic Carbon Nanostructures. In *link.springer.com*, pages 467–476. Springer Berlin Heidelberg, Berlin, Heidelberg, 2008.

[102] Nikolaos Tombros, Csaba Jozsa, Mihaita Popinciuc, Harry T Jonkman, and Bart J van Wees. Electronic spin transport and spin precession in single graphene layers at room temperature. *Nature*, 448(7153):571–574, July 2007.

[103] H Jaffrès, J M George, and A Fert. Spin transport in multiterminal devices: Large spin signals in devices with confined geometry. *Physical Review B*, 82(14):140408, October 2010.

[104] Bruno Dlubak, Marie-Blandine Martin, Cyrile Deranlot, Bernard Servet, Stéphane Xavier, Richard Mattana, Mike Sprinkle, Claire Berger, Walt A de Heer, Frédéric Petroff, Abdelmadjid Anane, Pierre Seneor, and Albert Fert. Highly efficient spin transport in epitaxial graphene on SiC. *Nature Physics*, 8(7):557–561, June 2012.

[105] H Ochoa, A Castro Neto, and F Guinea. Elliot-Yafet Mechanism in Graphene. *Physical Review Letters*, 108(20):206808, May 2012.

[106] V M Karpan, P A Khomyakov, A A Starikov, G Giovannetti, M Zwierzycki, M Talanana, G Brocks, J van den Brink, and P J Kelly. Theoretical prediction of perfect spin filtering at interfaces between close-packed surfaces of Ni or Co and graphite or graphene. *Physical Review B*, 78(19):195419, November 2008.

[107] V Karpan, G Giovannetti, P Khomyakov, M Talanana, A Starikov, M Zwierzycki, J van den Brink, G Brocks, and P Kelly. Graphite and Graphene as Perfect Spin Filters. *Physical Review Letters*, 99(17):176602, October 2007.

[108] P Khomyakov, A Starikov, G Brocks, and P Kelly. Nonlinear screening of charges induced in graphene by metal contacts. *Physical Review B*, 82(11):115437, September 2010.

[109] Enrique Cobas, Adam L Friedman, Olaf M J van't Erve, Jeremy T Robinson, and Berend T Jonker. Graphene As a Tunnel Barrier: Graphene-Based Magnetic Tunnel Junctions. *Nano Letters*, 12(6):3000–3004, June 2012.

[110] Yu Dedkov, M Fonin, U Rüdiger, and C Laubschat. Rashba Effect in the Graphene/Ni(111) System. *Physical Review Letters*, 100(10):107602, March 2008.

[111] A Varykhalov and O Rader. Graphene grown on Co(0001) films and islands: Electronic structure and its precise magnetization dependence. *Physical Review B*, 80(3):035437, July 2009.

[112] Yu S Dedkov, M Fonin, and C Laubschat. A possible source of spin-polarized electrons: The inert graphene/Ni(111) system. *Applied Physics Letters*, 92(5):052506, 2008.

[113] O Krupin, G Bihlmayer, K Starke, S Gorovikov, J Prieto, K Döbrich, S Blügel, and G Kaindl. Rashba effect at magnetic metal surfaces. *Physical Review B*, 71(20):201403, May 2005.

[114] J McClure. Band Structure of Graphite and de Haas-van Alphen Effect. *Physical Review*, 108(3):612–618, November 1957.

[115] M Inui, S Trugman, and Elihu Abrahams. Unusual properties of midband states in systems with off-diagonal disorder. *Physical Review B*, 49(5):3190–3196, February 1994.

[116] Oleg Yazyev and Lothar Helm. Defect-induced magnetism in graphene. *Physical Review B*, 75(12):125408, March 2007.

[117] Oleg V Yazyev. Emergence of magnetism in graphene materials and nanostructures. *Reports on Progress in Physics*, 73(5):056501, April 2010.

[118] J Hahn and H Kang. Vacancy and interstitial defects at graphite surfaces:Scanning tunneling microscopic study of the structure, electronic property, and yield for ion-induced defect creation. *Physical Review B*, 60(8):6007–6017, August 1999.

[119] M Ugeda, D Fernández-Torre, I Brihuega, P Pou, A Martínez-Galera, Rubén Pérez, and J Gómez-Rodríguez. Point Defects on Graphene on Metals. *Physical Review Letters*, 107(11):116803, September 2011.

[120] M M Ugeda, I Brihuega, F Guinea, and J M Gómez-Rodríguez. Missing Atom as a Source of Carbon Magnetism. *Physical Review Letters*, 104(9):096804, March 2010.

[121] Takahiro Kondo, Yujiro Honma, Junepyo Oh, Takahiro Machida, and Junji Nakamura. Edge states propagating from a defect of graphite: Scanning tunneling spectroscopy measurements. *Physical Review B*, 82(15):153414, October 2010.

[122] R R Nair, M Sepioni, I-Ling Tsai, O Lehtinen, J Keinonen, A V Krasheninnikov, T Thomson, A K Geim, and I V Grigorieva. Spin-half paramagnetism in graphene induced by point defects. *Nature Physics*, 8(3):199–202, January 2012.

[123] Oleg Yazyev. Magnetism in Disordered Graphene and Irradiated Graphite. *Physical Review Letters*, 101(3):037203–4, July 2008.

[124] Conan Weeks, Jun Hu, Jason Alicea, Marcel Franz, and Ruqian Wu. Engineering a Robust Quantum Spin Hall State in Graphene via Adatom Deposition. *Physical Review X*, 1(2):021001, October 2011.

[125] Yan Wang, Yi Huang, You Song, Xiaoyan Zhang, Yanfeng Ma, Jiajie Liang, and Yongsheng Chen. Room-Temperature Ferromagnetism of Graphene. *Nano Letters*, 9(1):220–224, January 2009.

[126] H S S Ramakrishna Matte, K S Subrahmanyam, and C N R Rao. Novel Magnetic Properties of Graphene: Presence of Both Ferromagnetic and Antiferromagnetic Features and Other Aspects. *Journal of Physical Chemistry C*, 113(23):9982–9985, June 2009.

[127] K S Subrahmanyam, S R C Vivekchand, A Govindaraj, and C N R Rao. A study of graphenes prepared by different methods: characterization, properties and solubilization. *Journal of Materials Chemistry*, 18(13):1517, 2008.

[128] Odd Andersson, B Prasad, Hirohiko Sato, Toshiaki Enoki, Yoshihiro Hishiyama, Yutaka Kaburagi, Masanori Yoshikawa, and Shunji Bandow. Structure and electronic properties of graphite nanoparticles. *Physical Review B*, 58(24):16387–16395, December 1998.

[129] K S Subrahmanyam, L S Panchakarla, A Govindaraj, and C N R Rao. Simple Method of Preparing Graphene Flakes by an Arc-Discharge Method. *Journal of Physical Chemistry C*, 113(11):4257–4259, March 2009.

[130] Saeed Saremi. RKKY in half-filled bipartite lattices: Graphene as an example. *Physical Review B*, 76(18):184430, November 2007.

[131] M Sherafati and S Satpathy. RKKY interaction in graphene from the lattice Green's function. *Physical Review B*, 83(16):165425, April 2011.

[132] S R Power, F S Guimarães, A Costa, R Muniz, and M Ferreira. Dynamic RKKY interaction in graphene. *Physical Review B*, 85(19):195411, May 2012.

[133] Annica Black-Schaffer. Importance of electron-electron interactions in the RKKY coupling in graphene. *Physical Review B*, 82(7):073409–4, August 2010.

[134] M Sherafati and S Satpathy. Analytical expression for the RKKY interaction in doped graphene. *Physical Review B*, 84(12):125416–5, September 2011.

[135] V Sessi. Coordination dependent magnetic properties of 3d and 4d metal nano-structures. pages 1–141, April 2010.

[136] U Gradmann. Magnetism in ultrathin transition metal films. pages 1–49.

[137] E C Stoner. Collective Electron Specific Heat and Spin Paramagnetism in Metals. *Proceedings of the Royal Society A: Mathematical, Physical and Engineering Sciences*, 154(883):656–678, May 1936.

[138] P JENSEN and K BENNEMANN. Magnetic structure of films: Dependence on anisotropy and atomic morphology. *Surface Science Reports*, 61(3):129–199, May 2006.

[139] D Sander. The magnetic anisotropy and spin reorientation of nanostructures and nanoscale films. *Journal of Physics: Condensed Matter*, 16(20):R603–R636, May 2004.

[140] Louis Néel. Anisotropie magnétique superficielle et surstructures d'orientation. *Journal de Physique et le Radium*, 15(4):225–239, 1954.

[141] P Bruno. Tight-binding approach to the orbital magnetic moment and magnetocrystalline anisotropy of transition-metal monolayers. 39:1–4, January 1989.

[142] D Weller, J Stöhr, R Nakajima, A Carl, M Samant, C Chappert, R Mégy, P Beauvillain, P Veillet, and G Held. Microscopic Origin of Magnetic Anisotropy in Au/Co/Au Probed with X-Ray Magnetic Circular Dichroism. *Physical Review Letters*, 75(20):3752–3755, November 1995.

[143] P Gambardella, A Dallmeyer, K Maiti, M C Malagoli, W Eberhardt, K Kern, and C Carbone. Ferromagnetism in one-dimensional monatomic metal chains. *Nature*, 416(6878):301–304, March 2002.

[144] P Gambardella. Giant Magnetic Anisotropy of Single Cobalt Atoms and Nanoparticles. *Science*, 300(5622):1130–1133, May 2003.

[145] R Guirado-López, J Dorantes-Dávila, and G Pastor. Orbital Magnetism in Transition-Metal Clusters: From Hund's Rules to Bulk Quenching. *Physical Review Letters*, 90(22):226402, June 2003.

[146] Olivier Fruchart and André Thiaville. Magnetism in reduced dimensions. *Comptes Rendus Physique*, 6(9):921–933, November 2005.

[147] U Gradmann and J Müller. Flat Ferromagnetic, Epitaxial 48Ni/52Fe(111) Films of few Atomic Layers. *physica status solidi (a)*, 27(1):313–324, 1968.

[148] W A Jesser and D Kuhlmann-Wilsdorf. The Geometry and Energy of a Twist Boundary between Crystals with Unequal Lattice Parameters. *physica status solidi (a)*, 21(2):533–544, 1967.

[149] W Weber, D Wesner, G Güntherodt, and U Linke. Direct observation of spin-split electronic states of Pd at the Pd(111)/Fe(110) interface. *Physical Review Letters*, 66(7):942–945, February 1991.

[150] M Speckmann, H Oepen, and H Ibach. Magnetic Domain Structures in Ultrathin Co/Au(111): On the Influence of Film Morphology. *Physical Review Letters*, 75(10):2035–2038, September 1995.

[151] Jeong-Won Lee, Jong-Ryul Jeong, Sung-Chul Shin, Jonggeol Kim, and Sang-Koog Kim. Spin-reorientation transitions in ultrathin Co films on Pt(111) and Pd(111) single-crystal substrates. *Physical Review B*, 66(17):172409, November 2002.

[152] Jan Vogel, Alain Fontaine, Vincent Cros, Frédéric Petroff, Jean-Paul Kappler, Gérard Krill, Andrei Rogalev, and José Goulon. Structure and magnetism of Pd in Pd/Fe multilayers studied by x-ray magnetic circular dichroism at the Pd L2,3sedges. *Physical Review B*, 55(6):3663–3669, February 1997.

[153] Farid El Gabaly, Kevin F McCarty, Andreas K Schmid, Juan de la Figuera, M Carmen Muñoz, Laszlo Szunyogh, Peter Weinberger, and Silvia Gallego. Noble metal capping effects on the spin-reorientation transitions of Co/Ru(0001). *New Journal of Physics*, 10(7):073024, July 2008.

[154] Iron nanostructures studied by spin-polarised scanning tunneling microscopy. pages 1–97, June 2004.

[155] Farid El Gabaly, Silvia Gallego, Carmen Muñoz, Laszlo Szunyogh, Peter Weinberger, Christof Klein, Andreas Schmid, Kevin McCarty, and Juan de la Figuera. Imaging Spin-Reorientation Transitions in Consecutive Atomic Co Layers on Ru(0001). *Physical Review Letters*, 96(14):147202, April 2006.

[156] J Dorantes-Dávila, H Dreyssé, and G Pastor. Magnetic Anisotropy of Transition-Metal Interfaces from a Local Perspective: Reorientation Transitions and Spin-Canted Phases in Pd Capped Co Films on Pd(111). *Physical Review Letters*, 91(19):197206, November 2003.

[157] J Dorantes-Dávila and G Pastor. Magnetic Anisotropy of One-Dimensional Nanostructures of Transition Metals. *Physical Review Letters*, 81(1):208–211, July 1998.

[158] C Clavero, A Cebollada, G Armelles, and O Fruchart. Growth mode, magnetic and magneto-optical properties of pulsed-laser-deposited Au/Co/Au(111) trilayers. *Journal of Magnetism and Magnetic Materials*, 322(6):647–652, April 2009.

[159] B Rodmacq, A Manchon, C Ducruet, S Auffret, and B Dieny. Influence of thermal annealing on the perpendicular magnetic anisotropy of Pt/Co/AlOx trilayers. *Physical Review B*, 79(2):024423, January 2009.

[160] S Ikeda, K Miura, H Yamamoto, K Mizunuma, H D Gan, M Endo, S Kanai, J Hayakawa, F Matsukura, and H Ohno. A perpendicular-anisotropy CoFeB–MgO magnetic tunnel junction. *Nature Materials*, 9(9):721–724, July 2010.

[161] Stephen Blundell. *Magnetism in Condensed Matter*. Oxford University Press, October 2001.

[162] Q A Pankhurst, J Connolly, S K Jones, and J Dobson. Applications of magnetic nanoparticles in biomedicine. *Journal of Physics D: Applied Physics*, 36(13):R167–R181, June 2003.

[163] R P Cowburn. Room Temperature Magnetic Quantum Cellular Automata. *Science*, 287(5457):1466–1468, February 2000.

[164] Hyoki Kim, Jianping Ge, Junhoi Kim, Sung-eun Choi, Hosuk Lee, Howon Lee, Wook Park, Yadong Yin, and Sunghoon Kwon. Structural colour printing using a magnetically tunable and lithographically fixable photonic crystal. *Nature Photonics*, 3(9):534–540, August 2009.

[165] Y Gamo, A Nagashima, M Wakabayashi, M Terai, and C Oshima. Atomic structure of monolayer graphite formed on Ni(111). *Surface Science*, 374(1-3):61–64, March 1997.

[166] J Wintterlin and M L Bocquet. Graphene on metal surfaces. *Surface Science*, 603(10-12):1841–1852, June 2009.

[167] Matthias Batzill. The surface science of graphene: Metal interfaces, CVD synthesis, nanoribbons, chemical modifications, and defects. *Surface Science Reports*, 67(3-4):83–115, March 2012.

[168] Rebecca S Edwards and Karl S Coleman. Graphene Film Growth on Polycrystalline Metals. *The Journal of Physical Chemistry Letters*, page 120815080732008, August 2012.

[169] Atsushi Koma. Van der Waals epitaxy—a new epitaxial growth method for a highly lattice-mismatched system. *Thin Solid Films*, 216(1):72–76, August 1992.

[170] T A Land, T Michely, R J Behm, J C Hemminger, and G Comsa. STM investigation of single layer graphite structures produced on Pt(111) by hydrocarbon decomposition. *Surface Science*, 264(3):261–270, March 1992.

[171] Elena Loginova, N C Bartelt, P J Feibelman, and K F McCarty. Factors influencing graphene growth on metal surfaces. *New Journal of Physics*, 11(6):063046, June 2009.

[172] R van Gastel, Alpha T N'Diaye, D Wall, Johann Coraux, C Busse, N M Buckanie, F J Meyer zu Heringdorf, M Horn von Hoegen, T Michely, and B Poelsema. Selecting a single orientation for millimeter sized graphene sheets. *Applied Physics Letters*, 95(12):121901–121901–3, 2009.

[173] Shu Nie, Joseph Wofford, Norman Bartelt, Oscar Dubon, and Kevin McCarty. Origin of the mosaicity in graphene grown on Cu(111). *Physical Review B*, 84(15):155425, October 2011.

[174] Hiroki Ago, Yoshito Ito, Noriaki Mizuta, Kazuma Yoshida, Baoshan Hu, Carlo M Orofeo, Masaharu Tsuji, Ken-ichi Ikeda, and Seigi Mizuno. Epitaxial Chemical Vapor Deposition Growth of Single-Layer Graphene over Cobalt Film Crystallized on Sapphire. *ACS Nano*, 4(12):7407–7414, December 2010.

[175] Daejin Eom, Deborah Prezzi, Kwang Taeg Rim, Hui Zhou, Michael Lefenfeld, Shengxiong Xiao, Colin Nuckolls, Mark S Hybertsen, Tony F Heinz, and George W Flynn. Structure and Electronic Properties of Graphene Nanoislands on Co(0001). *Nano Letters*, 9(8):2844–2848, August 2009.

[176] Eunho Kim, Hyosub An, Hyunchul Jang, Won-Ju Cho, Naesung Lee, Wan-Gyu Lee, and Jongwan Jung. Growth of Few-Layer Graphene on a Thin Cobalt Film on a Si/SiO2 Substrate. *Chemical Vapor Deposition*, 17(1-3):9–14, February 2011.

[177] Xianbao Wang, Haijun You, Fangming Liu, Mingjian Li, Li Wan, Shaoqing Li, Qin Li, Yang Xu, Rong Tian, Ziyong Yu, Dong Xiang, and Jing Cheng. Large-Scale Synthesis of Few-Layered Graphene using CVD. *Chemical Vapor Deposition*, 15(1-3):53–56, March 2009.

[178] D Usachov, A Dobrotvorskii, A Varykhalov, O Rader, W Gudat, A Shikin, and V Adamchuk. Experimental and theoretical study of the morphology of commensurate and incommensurate graphene layers on Ni single-crystal surfaces. *Physical Review B*, 78(8):085403, August 2008.

[179] Yi Zhang, Lewis Gomez, Fumiaki N Ishikawa, Anuj Madaria, Koungmin Ryu, Chuan Wang, Alexander Badmaev, and Chongwu Zhou. Comparison of Graphene Growth on Single-Crystalline and Polycrystalline Ni by Chemical Vapor Deposition. *The Journal of Physical Chemistry Letters*, 1(20):3101–3107, October 2010.

[180] G Nandamuri, S Roumimov, and R Solanki. Chemical vapor deposition of graphene films. *Nanotechnology*, 21(14):145604, March 2010.

[181] Large-scale graphitic thin films synthesized on Ni and transferred to insulators: Structural and electronic properties. *Journal of Applied Physics*, 107(4):044310, 2010.

[182] Youngbin Lee, Sukang Bae, Houk Jang, Sukjae Jang, Shou-En Zhu, Sung Hyun Sim, Young Il Song, Byung Hee Hong, and Jong-Hyun Ahn. Wafer-Scale Synthesis and Transfer of Graphene Films. *Nano Letters*, 10(2):490–493, February 2010.

[183] Xuesong Li, Weiwei Cai, Luigi Colombo, and Rodney S Ruoff. Evolution of Graphene Growth on Ni and Cu by Carbon Isotope Labeling. *Nano Letters*, 9(12):4268–4272, December 2009.

[184] Hye Jin Park, Jannik Meyer, Siegmar Roth, and Viera Skakalova. Growth and properties of few-layer graphene prepared by chemical vapor deposition. *Carbon*, 48(4):1088–1094, April 2010.

[185] L Zhao, K T Rim, H Zhou, R He, T F Heinz, A Pinczuk, G W Flynn, and A N Pasupathy. The Atomic-scale Growth of Large-Area Monolayer Graphene on Single-Crystal Copper Substrates. *arXiv.org*, cond-mat.mes-hall, August 2010.

[186] Li Gao, Jeffrey R Guest, and Nathan P Guisinger. Epitaxial Graphene on Cu(111). *Nano Letters*, 10(9):3512–3516, September 2010.

[187] Qingkai Yu, Luis A Jauregui, Wei Wu, Robert Colby, Jifa Tian, Zhihua Su, Helin Cao, Zhihong Liu, Deepak Pandey, Dongguang Wei, Ting Fung Chung, Peng Peng, Nathan P Guisinger, Eric A Stach, Jiming Bao, Shin-Shem Pei, and Yong P Chen. Control and characterization of individual grains and grain boundaries in graphene grown by chemical vapour deposition. *Nature Materials*, 10(6):443–449, May 2011.

[188] Xuesong Li, Carl W Magnuson, Archana Venugopal, Rudolf M Tromp, James B Hannon, Eric M Vogel, Luigi Colombo, and Rodney S Ruoff. Large-Area Graphene Single Crystals Grown by Low-Pressure Chemical Vapor Deposition of Methane on Copper. *Journal of the American Chemical Society*, 133(9):2816–2819, March 2011.

[189] Zheng Han, Amina Kimouche, Adrien Allain, Hadi Arjmandi-Tash, Antoine Reserbat-Plantey, Sébastien Pairis, Valérie Reita, Nedjma Bendiab, Johann Coraux, and Vincent Bouchiat. Suppression of Multilayer Graphene Patches during CVD Graphene growth on Copper. May 2012.

[190] Kongara M Reddy, Andrew D Gledhill, Chun-Hu Chen, Julie M Drexler, and Nitin P Padture. High quality, transferrable graphene grown on single crystal Cu(111) thin films on basal-plane sapphire. *Applied Physics Letters*, 98(11):113117–113117–3, 2011.

[191] Baoshan Hu, Hiroki Ago, Yoshito Ito, Kenji Kawahara, Masaharu Tsuji, Eisuke Magome, Kazushi Sumitani, Noriaki Mizuta, Ken-ichi Ikeda, and Seigi Mizuno. Epitaxial growth of large-area single-layer graphene over Cu(111)/sapphire by atmospheric pressure CVD. *Carbon*, 50(1):57–65, January 2012.

[192] Yui Ogawa, Baoshan Hu, Carlo M Orofeo, Masaharu Tsuji, Ken-ichi Ikeda, Seigi Mizuno, Hiroki Hibino, and Hiroki Ago. Domain Structure and Boundary in Single-Layer Graphene Grown on Cu(111) and Cu(100) Films. *The Journal of Physical Chemistry Letters*, 3(2):219–226, January 2012.

[193] Shigeo Yoshii, Katsuya Nozawa, Kenji Toyoda, Nozomu Matsukawa, Akihiro Odagawa, and Ayumu Tsujimura. Suppression of Inhomogeneous Segregation in Graphene Growth on Epitaxial Metal Films. *Nano Letters*, 11(7):2628–2633, July 2011.

[194] P Sutter, M S Hybertsen, J T Sadowski, and E Sutter. Electronic Structure of Few-Layer Epitaxial Graphene on Ru(0001). *Nano Letters*, 9(7):2654–2660, July 2009.

[195] Yi Pan, Haigang Zhang, Dongxia Shi, Jiatao Sun, Shixuan Du, Feng Liu, and Hong-jun Gao. Highly Ordered, Millimeter-Scale, Continuous, Single-Crystalline Graphene Monolayer Formed on Ru (0001). *Advanced Materials*, 21(27):2777–2780, December 2008.

[196] W J Arnoult and R B McLellan. SOLUBILITY OF CARBON IN RHODIUM, RUTHENIUM, IRIDIUM, AND RHENIUM. *Am. Mineral.; (United States)*, January 1972.

[197] Silvan Roth, Jürg Osterwalder, and Thomas Greber. Synthesis of epitaxial graphene on rhodium from 3-pentanone. *Surface Science*, 605(9-10):L17–L19, May 2011.

[198] H Yokoyama, H Numakura, and M Koiwa. The solubility and diffusion of carbon in palladium. *Acta Materialia*, 46(8):2823–2830, May 1998.

[199] Soon-Yong Kwon, Cristian V Ciobanu, Vania Petrova, Vivek B Shenoy, Javier Bareño, Vincent Gambin, Ivan Petrov, and Suneel Kodambaka. Growth of Semiconducting Graphene on Palladium. *Nano Letters*, 9(12):3985–3990, December 2009.

[200] E B Watson. Diffusion and solubility of C in Pt. *Am. Mineral.; (United States)*, 72:5-6.

[201] Peter Sutter, Jerzy T Sadowski, and Eli Sutter. Graphene on Pt(111): Growth and substrate interaction. *Physical Review B*, 80(24):245411, December 2009.

[202] T A Land, T Michely, R J Behm, J C Hemminger, and G Comsa. STM investigation of the adsorption and temperature dependent reactions of ethylene on Pt(111). *Applied Physics A*, 53(5):414–417, November 1991.

[203] M Gao, Y Pan, L Huang, H Hu, L Z Zhang, H M Guo, S X Du, and H J Gao. Epitaxial growth and structural property of graphene on Pt(111). *Applied Physics Letters*, 98(3):033101–033103, 2011.

[204] Byung Jin Kang, Jeong Hun Mun, Chan Yong Hwang, and Byung Jin Cho. Monolayer graphene growth on sputtered thin film platinum. *Journal of Applied Physics*, 106(10):104309–104309–6, 2009.

[205] E K Ohriner. Rhenium and iridium. pages 1–17, March 2008.

[206] E Miniussi, M Pozzo, A Baraldi, E Vesselli, R Zhan, G Comelli, T Menteş, M Niño, A Locatelli, S Lizzit, and D Alfè. Thermal Stability of Corrugated Epitaxial Graphene Grown on Re(0001). *Physical Review Letters*, 106(21):216101, May 2011.

[207] Johann Coraux, Alpha T N'Diaye, Martin Engler, Carsten Busse, Dirk Wall, Niemma Buckanie, Frank-J Meyer zu Heringdorf, Raoul van Gastel, Bene Poelsema, and Thomas Michely. Growth of graphene on Ir(111). *New Journal of Physics*, 11(2):023006, February 2009.

[208] Elena Loginova, Shu Nie, Konrad Thürmer, Norman Bartelt, and Kevin McCarty. Defects of graphene on Ir (111): Rotational domains and ridges. *Physical Review B*, 80(8):085430–8, August 2009.

[209] R Brako, D Šokčević, P Lazić, and N Atodiresei. Graphene on the Ir(111) surface: from van der Waals to strong bonding. *New Journal of Physics*, 12(11):113016, November 2010.

[210] N R Gall, E V Rutkov, and A Ya Tontegode. Intercalation of nickel atoms under two-dimensional graphene film on (111)Ir. *Carbon*, 38(5):663–667, January 2000.

[211] Elena Loginova, Norman C Bartelt, Peter J Feibelman, and Kevin F McCarty. Evidence for graphene growth by C cluster attachment. *New Journal of Physics*, 10(9):093026, September 2008.

[212] Y S Dedkov, A Shikin, V Adamchuk, S Molodtsov, C Laubschat, A Bauer, and G Kaindl. Intercalation of copper underneath a monolayer of graphite on Ni(111). *Physical Review B*, 64(3), June 2001.

[213] Kevin F McCarty, Peter J Feibelman, Elena Loginova, and Norman C Bartelt. Kinetics and thermodynamics of carbon segregation and graphene growth on Ru(0001). *Carbon*, 47(7):1806–1813, June 2009.

[214] Qingkai Yu, Jie Lian, Sujitra Siriponglert, Hao Li, Yong P Chen, and Shin-Shem Pei. Graphene segregated on Ni surfaces and transferred to insulators. *Applied Physics Letters*, 93(11):113103, 2008.

[215] Jayeeta Lahiri, Travis S Miller, Andrew J Ross, Lyudmyla Adamska, Ivan I Oleynik, and Matthias Batzill. Graphene growth and stability at nickel surfaces. *New Journal of Physics*, 13(2):025001, February 2011.

[216] R Murali. *Graphene Nanoelectronics*. springer.com.

[217] Hassan Raza. *Graphene Nanoelectronics*. Metrology, Synthesis, Properties and Applications. Springer, March 2012.

[218] Giovanni Bertoni, Lionel Calmels, Anne Altibelli, and Virginie Serin. First-principles calculation of the electronic structure and EELS spectra at the graphene/Ni(111) interface. *Physical Review B*, 71(7):075402, February 2005.

[219] N Vinogradov, A Zakharov, V Kocevski, J Rusz, K Simonov, O Eriksson, A Mikkelsen, E Lundgren, A Vinogradov, N Mårtensson, and A Preobrajenski. Formation and Structure of Graphene Waves on Fe(110). *Physical Review Letters*, 109(2):026101, July 2012.

[220] Alpha T N'Diaye, Johann Coraux, Tim N Plasa, Carsten Busse, and Thomas Michely. Structure of epitaxial graphene on Ir(111). *New Journal of Physics*, 10(4):043033, April 2008.

[221] Alpha T N'Diaye, Sebastian Bleikamp, Peter Feibelman, and Thomas Michely. Two-Dimensional Ir Cluster Lattice on a Graphene Moiré on Ir(111). *Physical Review Letters*, 97(21):215501, November 2006.

[222] Pablo Merino, Martin Švec, Anna L Pinardi, Gonzalo Otero, and José A Martín-Gago. Strain-Driven Moiré Superstructures of Epitaxial Graphene on Transition Metal Surfaces. *ACS Nano*, 5(7):5627–5634, July 2011.

[223] Alpha T N'Diaye, Raoul van Gastel, Antonio J Martínez-Galera, Johann Coraux, Hichem Hattab, Dirk Wall, Frank-J Meyer zu Heringdorf, Michael Horn-von Hoegen, José M Gómez-Rodríguez, Bene Poelsema, Carsten Busse, and Thomas Michely. In situ observation of stress relaxation in epitaxial graphene. *arXiv.org*, cond-mat.mes-hall(11):113056, June 2009.

[224] Yu S Dedkov and M Fonin. Electronic and magnetic properties of the graphene–ferromagnet interface. *New Journal of Physics*, 12(12):125004, December 2010.

[225] H C W Beijerinck and N F Verster. Velocity distribution and angular distribution of molecular beams from multichannel arrays. *Journal of Applied Physics*, 46(5):2083–2091, 1975.

[226] Andrew M Glines, Robert N Carter, and A Brad Anton. An alternative for gas dosing in ultrahigh vacuum adsorption studies. *Review of Scientific Instruments*, 63(2):1826, 1992.

[227] P. Clausing. Steady flow of highly rarefied gases. *Physica*, 9:65–80, 1929.

[228] N Rougemaille, Alpha T N'Diaye, Johann Coraux, C Võ-Văn, O Fruchart, and A K Schmid. Perpendicular magnetic anisotropy of cobalt films intercalated under graphene. *Applied Physics Letters*, 101(14):142403–142403–3, October 2012.

[229] O Fruchart, P O Jubert, M Eleoui, F Cheynis, B Borca, P David, V Santonacci, A Liénard, M Hasegawa, and C Meyer. Growth modes of Fe(110) revisited: a contribution of self-assembly to magnetic materials. *Journal of Physics: Condensed Matter*, 19(5):053001, January 2007.

[230] G Schütz, W Wagner, W Wilhelm, P Kienle, R Zeller, R Frahm, and G Materlik. Absorption of circularly polarized x rays in iron. *Physical Review Letters*, 58(7):737–740, February 1987.

[231] Claudia Sorg. Magnetic Properties of 3d and 4f Ferromagnets Studied by X-ray Absorption Spectroscopy. pages 1–155, February 2006.

[232] C T Chen, Y U Idzerda, H J Lin, N V Smith, G Meigs, E Chaban, Ho G H, E Pellegrin, and F Sette. Experimental Confirmation of the X-ray Magnetic Circular Dichroism Sum Rules for Iron and Cobalt. *Physical Revew Letters*, pages 1–4, July 1995.

[233] J Stöhr. X-ray magnetic circular dichroism spectroscopy of transition metal thin films. *Journal of Magnetism and Magnetic Materials*, 75:253–272, December 1995.

[234] U Fano. Spin Orientation of Photoelectrons Ejected by Circularly Polarized Light. *Physical Review*, 178(1):131–136, February 1969.

[235] B Thole, P Carra, F Sette, and G van der Laan. X-ray circular dichroism as a probe of orbital magnetization. *Physical Review Letters*, 68(12):1943–1946, March 1992.

[236] Paolo Carra, B T Thole, Massimo Altarelli, and Xindong Wang. X-ray circular dichroism and local magnetic fields. *Physical Review Letters*, 70(5):694–697, February 1993.

[237] N Rougemaille and A K Schmid. Magnetic imaging with spin-polarized low-energy electron microscopy. *The European Physical Journal Applied Physics*, 50(2):20101–, April 2010.

[238] G Kresse and J Hafner. Ab initio molecular dynamics for liquid metals. *Physical Review B*, 47(1):558–561, January 1993.

[239] G Kresse. Efficient iterative schemes for ab initio total-energy calculations using a plane-wave basis set. *Physical Review B*, 54(16):11169–11186, October 1996.

[240] P E Blöchl. Projector augmented-wave method. *Physical Review B*, 50(24):17953–17979, December 1994.

[241] Hongxin Yang. First-principles study of spintronic phenomena in magnetic tunnel junctions and graphene. pages 1–117, May 2012.

[242] Keun Soo Kim, Yue Zhao, Houk Jang, Sang Yoon Lee, Jong Min Kim, Kwang S Kim, Jong-Hyun Ahn, Philip Kim, Jae-Young Choi, and Byung Hee Hong. Large-scale pattern growth of graphene films for stretchable transparent electrodes. *Nature*, 457(7230):706–710, January 2009.

[243] Cecilia Mattevi, Hokwon Kim, and Manish Chhowalla. A review of chemical vapour deposition of graphene on copper. *Journal of Materials Chemistry*, 21(10):3324, 2011.

[244] Joseph M Wofford, Shu Nie, Kevin F McCarty, Norman C Bartelt, and Oscar D Dubon. Graphene Islands on Cu Foils: The Interplay between Shape, Orientation, and Defects. *Nano Letters*, 10(12):4890–4896, December 2010.

[245] P W Sutter, P M Albrecht, and E A Sutter. Graphene growth on epitaxial Ru thin films on sapphire. *Applied Physics Letters*, 97(21):213101–213101–3, 2010.

[246] Takayuki Iwasaki, Hye Jin Park, Mitsuharu Konuma, Dong Su Lee, Jurgen H Smet, and Ulrich Starke. Long-Range Ordered Single-Crystal Graphene on High-Quality Heteroepitaxial Ni Thin Films Grown on MgO(111). *Nano Letters*, 11(1):79–84, January 2011.

[247] J Eymery, D Buttard, F Fournel, H Moriceau, G Baumbach, and D Lübbert. Dislocation strain field in ultrathin bonded silicon wafers studied by grazing incidence x-ray diffraction. *Physical Review B*, 65(16):165337, April 2002.

[248] Ivo Pletikosić. Electronic states of epitaxial graphene on iridium for almost neutral to highly doped graphene. *PhD Thesis*, pages 1–98, December 2012.

[249] Andrea C Ferrari. Raman spectroscopy of graphene and graphite: Disorder, electron–phonon coupling, doping and nonadiabatic effects. *Solid State Communications*, 143(1-2):47–57, July 2007.

[250] I Pletikosić, M Kralj, P Pervan, R Brako, Johann Coraux, Alpha T N'Diaye, C Busse, and T Michely. Dirac Cones and Minigaps for Graphene on Ir(111). *Physical Review Letters*, 102(5):056808, February 2009.

[251] A Jorio, M A Pimenta, A G Souza Filho, R Saito, G Dresselhaus, and M S Dresselhaus. Characterizing carbon nanotube samples with resonance Raman scattering. *New Journal of Physics*, 5:139–139, January 2003.

[252] Elena Starodub, Aaron Bostwick, Luca Moreschini, Shu Nie, Farid Gabaly, Kevin McCarty, and Eli Rotenberg. In-plane orientation effects on the electronic structure, stability, and Raman scattering of monolayer graphene on Ir(111). *Physical Review B*, 83(12):125428, March 2011.

[253] Patrick Zeller, Sebastian Dänhardt, Stefan Gsell, Matthias Schreck, and Joost Wintterlin. Scalable synthesis of graphene on single crystal Ir(111) films. *Surface Science*, 606(19-20):1475–1480, October 2012.

[254] Young-Woo Son, Marvin L Cohen, and Steven G Louie. Half-metallic graphene nanoribbons. *Nature*, 444(7117):347–349, November 2006.

[255] Spin and angular resolved photoemission experiments on epitaxial graphene. April 2010.

[256] G Giovannetti, P Khomyakov, G Brocks, V Karpan, J van den Brink, and P Kelly. Doping Graphene with Metal Contacts. *Physical Review Letters*, 101(2):026803, July 2008.

[257] Chuhei Oshima and Ayato Nagashima. Ultra-thin epitaxial films of graphite and hexagonal boron nitride on solid surfaces. *Journal of Physics: Condensed Matter*, 9(1):1–20, January 1999.

[258] Ioan Mihai Miron, Gilles Gaudin, Stéphane Auffret, Bernard Rodmacq, Alain Schuhl, Stefania Pizzini, Jan Vogel, and Pietro Gambardella. Current-driven spin torque induced by the Rashba effect in a ferromagnetic metal layer. *Nature Materials*, January 2010.

[259] M Weser, Y Rehder, K Horn, M Sicot, M Fonin, A B Preobrajenski, E N Voloshina, E Goering, and Yu S Dedkov. Induced magnetism of carbon atoms at the graphene/Ni(111) interface. *Applied Physics Letters*, 96(1):012504, 2010.

[260] C Binns, S H Baker, C Demangeat, and J C Parlebas. Growth, electronic, magnetic and spectroscopic properties of transition metals on graphite. *Surface Science Reports*, 34(4-5):107–170, January 1999.

[261] J Xhie, K Sattler, M Ge, and N Venkateswaran. Giant and supergiant lattices on graphite. *Physical Review B*, 47(23):15835–15841, June 1993.

[262] Wei Chen, Kian Ping Loh, Hai Xu, and A T S Wee. Growth of monodispersed cobalt nanoparticles on 6H–SiC(0001) honeycomb template. *Applied Physics Letters*, 84(2):281, 2004.

[263] Siew Wai Poon, Wei Chen, Eng Soon Tok, and Andrew T S Wee. Probing epitaxial growth of graphene on silicon carbide by metal decoration. *Applied Physics Letters*, 92(10):104102, 2008.

[264] Pablo Jensen, X Blase, and Pablo Ordejón. First principles study of gold adsorption and diffusion on graphite. *Surface Science*, 564(1-3):173–178, August 2004.

[265] P Lehtinen, A Foster, A Ayuela, A Krasheninnikov, K Nordlund, and R Nieminen. Magnetic Properties and Diffusion of Adatoms on a Graphene Sheet. *Physical Review Letters*, 91(1):017202, June 2003.

[266] Kevin T Chan, J B Neaton, and Marvin L Cohen. First-principles study of metal adatom adsorption on graphene. *Physical Review B*, 77(23):235430, June 2008.

[267] J Shen, Zheng Gai, and J Kirschner. Growth and magnetism of metallic thin films and multilayers by pulsed-laser deposition. *Surface Science Reports*, 52(5-6):163–218, February 2004.

[268] O Fruchart, G Renaud, J P Deville, A Barbier, F Scheurer, M Klaua, J Barthel, M Noblet, O Ulrich, J Mané-Mané, and J Kirschner. Self-organized growth of nanosized flat dots and vertical magnetic Co pillars on Au(111). *Journal of Crystal Growth*, 237-239:2035–2040, April 2002.

[269] Florent Tournus, Alexandre Tamion, Nils Blanc, Abdelkrim Hannour, Laurent Bardotti, Brigitte Prével, Philippe Ohresser, Edgar Bonet, Thierry Epicier, and Véronique Dupuis. Evidence of L10 chemical order in CoPt nanoclusters: Direct observation and magnetic signature. *Physical Review B*, 77(14):144411–11, April 2008.

[270] Hong-Xin Yang, Mairbek Chshiev, Danil Boukhvalov, Xavier Waintal, and Stephan Roche. Inducing and optimizing magnetism in graphene nanomeshes. *Physical Review B*, 84(21):214404, December 2011.

[271] A J Freeman and Ru-quian Wu. Electronic structure theory of surface, interface and thin-film magnetism. *Journal of Magnetism and Magnetic Materials*, 100(1-3):497–514, November 1991.

[272] G Chiarotti. *Physics of Solid Surfaces: Electronic and Vibrational Properties*, volume 24b of *Landolt-Börnstein - Group III Condensed Matter*. Springer-Verlag, Berlin/Heidelberg, 1994.

[273] E. P. Wohlfarth. *Handbook of Magnetic Materials*. North Holland, August 1986.

[274] P Beauvillain, A Bounouh, C Chappert, R Mégy, S Ould-Mahfoud, J P Renard, P Veillet, D Weller, and J Corno. Effect of submonolayer coverage on magnetic anisotropy of ultrathin cobalt films M/Co/Au(111) with M=Au, Cu, Pd. *Journal of Applied Physics*, 76(10):6078–6080, 1994.

[275] M T Johnson, P J H Bloemen, F J A den Broeder, and J J de Vries. Magnetic anisotropy in metallic multilayers. *Reports on Progress in Physics*, 59(11):1409–1458, January 1999.

[276] S Rusponi, T Cren, N Weiss, M Epple, P Buluschek, L Claude, and H Brune. The remarkable difference between surface and step atoms in the magnetic anisotropy of two-dimensional nanostructures. *Nature*, 2(8):546–551, July 2003.

[277] H X Yang, M Chshiev, B Dieny, J H Lee, A Manchon, and K H Shin. First-principles investigation of the very large perpendicular magnetic anisotropy at Fe|MgO and Co|MgO interfaces. *Physical Review B*, 84(5):054401, August 2011.

[278] Earl Callen and Herbert Callen. Magnetostriction, Forced Magnetostriction, and Anomalous Thermal Expansion in Ferromagnets. *Physical Review*, 139(2A):A455–A471, July 1965.

[279] Dominique Givord, Michel Rossignol, and Vitoria M T S Barthem. The physics of coercivity. *Journal of Magnetism and Magnetic Materials*, 258-259:1–5, March 2003.

[280] Burkard Hillebrands and Kamel Ounadjela, editors. *Spin Dynamics in Confined Magnetic Structures I*, volume 83 of *Topics in Applied Physics*. Springer Berlin Heidelberg, Berlin, Heidelberg, September 2001.

[281] Jae-Chul Lee, Kab-Jin Kim, Jisu Ryu, Kyoung-Woong Moon, Sang-Jun Yun, Gi-Hong Gim, Kang-Soo Lee, Kyung-Ho Shin, Hyun-Woo Lee, and Sug-Bong Choe. Universality Classes of Magnetic Domain Wall Motion. *Physical Review Letters*, 107(6):067201, August 2011.

[282] C Chappert. Planar Patterned Magnetic Media Obtained by Ion Irradiation. *Science*, 280(5371):1919–1922, June 1998.

[283] M S Dresselhaus and G Dresselhaus. Intercalation compounds of graphite. *Advances in Physics*, 30(2):139–326, April 1981.

[284] A Ya Tontegode. Carbon on transition metal surfaces. *Progress in Surface Science*, 38(3-4):201–429, January 1991.

[285] J Scott Bunch, Scott S Verbridge, Jonathan S Alden, Arend M van der Zande, Jeevak M Parpia, Harold G Craighead, and Paul L McEuen. Impermeable Atomic Membranes from Graphene Sheets. *arXiv.org*, cond-mat.mtrl-sci, May 2008.

[286] C Riedl, C Coletti, T Iwasaki, A A Zakharov, and U Starke. Quasi-Free-Standing Epitaxial Graphene on SiC Obtained by Hydrogen Intercalation. *Physical Review Letters*, 103(24):246804–4, December 2009.

[287] J Sato. Cobalt-Base High-Temperature Alloys. *Science*, 312(5770):90–91, April 2006.

[288] Elena Starodub, Aaron Bostwick, Luca Moreschini, Shu Nie, Farid El Gabaly, Kevin F McCarty, and Eli Rotenberg. In-plane orientation effects on the electronic structure, stability and Raman scattering of monolayer graphene on Ir(111). *arXiv.org*, cond-mat.mtrl-sci:1–28, December 2010.

[289] Adrien Allard and Ludger Wirtz. Graphene on Metallic Substrates: Suppression of the Kohn Anomalies in the Phonon Dispersion. *Nano Letters*, 10(11):4335–4340, November 2010.

[290] P A Khomyakov, G Giovannetti, P C Rusu, G Brocks, J van den Brink, and P J Kelly. First-principles study of the interaction and charge transfer between graphene and metals. *Physical Review B*, 79(19):195425, May 2009.

[291] A Das, S Pisana, S Piscanec, B Chakraborty, S K Saha, U V Waghmare, R Yiang, H R Krishnamurhthy, A K Geim, A C Ferrari, and A K Sood. Electrochemically Top Gated Graphene: Monitoring Dopants by Raman Scattering. *arXiv.org*, cond-mat.mtrl-sci, September 2007.

[292] M S Dresselhaus, G Dresselhaus, A Jorio, A G Souza Filho, and R Saito. Raman spectroscopy on isolated single wall carbon nanotubes. *Carbon*, 40(12):2043–2061, January 2002.

[293] T Chieu, M Dresselhaus, and M Endo. Raman studies of benzene-derived graphite fibers. *Physical Review B*, 26(10):5867–5877, November 1982.

[294] A Ya Tontegode. Carbon on transition metal surfaces, 1991.

[295] Byron G Johnson, Paul J Berlowitz, D Wayne Goodman, and Calvin H Bartholomew. The structural and chemisorptive properties of ultrathin cobalt overlayers on W(110) and W(100). *Surface Science*, 217(1-2):13–37, July 1989.

[296] Barış Ünal, Yu Sato, K F McCarty, N C Bartelt, T Duden, C J Jenks, A K Schmid, and P A Thiel. Work function of a quasicrystal surface: Icosahedral Al–Pd–Mn. *Journal of Vacuum Science & Technology A: Vacuum, Surfaces, and Films*, 27(5):1249, 2009.

[297] Shiren Wang, Yue Zhang, Noureddine Abidi, and Luis Cabrales. Wettability and Surface Free Energy of Graphene Films. *Langmuir*, 25(18):11078–11081, September 2009.

[298] H Skriver and N Rosengaard. Surface energy and work function of elemental metals. *Physical Review B*, 46(11):7157–7168, September 1992.

[299] Cheng Gong, Geunsik Lee, Bin Shan, Eric M Vogel, Robert M Wallace, and Kyeongjae Cho. First-principles study of metal–graphene interfaces. *Journal of Applied Physics*, 108(12):123711–123711–8, 2010.

[300] A Thiaville and A Fert. Twisted spin configurations in thin magnetic layers with interface anisotropy. *Journal of Magnetism and Magnetic Materials*, 113(1-3):161–172, July 1992.

[301] A Rettori, L Trallori, P Politi, M G Pini, and M Macciò. Surface magnetic reconstruction. *Journal of Magnetism and Magnetic Materials*, 140-144:639–642, February 1995.

[302] Lavania Elena Nistor. Magnetic tunnel junctions with perpendicular magnetization: anisotropy, magnetoresistance, magnetic coupling and spin transfer torque switching. pages 1–218, December 2011.

[303] F J A den Broeder, W Hoving, and P J H Bloemen. Magnetic anisotropy of multilayers. *Journal of Magnetism and Magnetic Materials*, 93:562–570, February 1991.

[304] Régis Decker, Jens Brede, Nicolae Atodiresei, Vasile Caciuc, Stefan Blügel, and Roland Wiesendanger. Atomic-scale magnetism of cobalt-intercalated graphene. *Physical Review B*, 87(4):041403, January 2013.

[305] Alpha T N'Diaye, Timm Gerber, Carsten Busse, Josef Mysliveček, Johann Coraux, and Thomas Michely. A versatile fabrication method for cluster superlattices. *New Journal of Physics*, 11(10):103045, October 2009.

[306] M Sicot, S Bouvron, O Zander, U Rüdiger, Yu S Dedkov, and M Fonin. Nucleation and growth of nickel nanoclusters on graphene Moiré on Rh(111). *Applied Physics Letters*, 96(9):093115–093115–3, 2010.

[307] Q Liao, H J Zhang, K Wu, H Y Li, S N Bao, and P He. Nucleation and growth of monodispersed cobalt nanoclusters on graphene moiré on Ru(0001). *Nanotechnology*, 22(12):125303, February 2011.

[308] Alpha T N'Diaye. Epitaxial graphene and cluster lattices on Iridium(111). pages 1–225, February 2010.

[309] Philippe Ohresser, N Brookes, S Padovani, F Scheurer, and H Bulou. Magnetism of small Fe clusters on Au(111) studied by x-ray magnetic circular dichroism. *Physical Review B*, 64(10), August 2001.

[310] C Chen, Y Idzerda, H J Lin, N Smith, G Meigs, E Chaban, G Ho, E Pellegrin, and F Sette. Experimental Confirmation of the X-Ray Magnetic Circular Dichroism Sum Rules for Iron and Cobalt. *Physical Review Letters*, 75(1):152–155, July 1995.

[311] N Weiss, T Cren, M Epple, S Rusponi, G Baudot, S Rohart, A Tejeda, V Repain, S Rousset, Philippe Ohresser, F Scheurer, P Bencok, and H Brune. Uniform Magnetic Properties for an Ultrahigh-Density Lattice of Noninteracting Co Nanostructures. *Physical Review Letters*, 95(15):157204, October 2005.

[312] M Respaud. Magnetization process of noninteracting ferromagnetic cobalt nanoparticles in the superparamagnetic regime: Deviation from Langevin law. *Journal of Applied Physics*, 86(1):556, 1999.

[313] P Ghigna, A Campana, A Lascialfari, A Caneschi, D Gatteschi, A Tagliaferri, and F Borgatti. X-ray magnetic-circular-dichroism spectra on the superparamagnetic transition-metal ion clusters Mn12 and Fe8. *Physical Review B*, 64(13):132413, September 2001.

[314] A Lehnert, S Rusponi, M Etzkorn, S Ouazi, P Thakur, and H Brune. Magnetic anisotropy of Fe and Co adatoms and Fe clusters magnetically decoupled from Ni_3Al(111) by an alumina bilayer. *Physical Review B*, 81(10):104430, March 2010.

[315] Sujit S Datta, Douglas R Strachan, Samuel M Khamis, and A T Charlie Johnson. Crystallographic Etching of Few-Layer Graphene. *Nano Letters*, 8(7):1912–1915, July 2008.

[316] Hidetake Itoh, H Yanagihara, Katsutoshi Suzuki, and Eiji Kita. Coexistence of the uniaxial anisotropy and the antiferromagnetic coupling in Co/Ir(111) superlattices. *Journal of Magnetism and Magnetic Materials*, 257(2-3):184–189, February 2003.

[317] M Mavrikakis, B Hammer, and J Nørskov. Effect of Strain on the Reactivity of Metal Surfaces. *Physical Review Letters*, 81(13):2819–2822, September 1998.

[318] O Fruchart, A Rousseau, D Schmaus, A L'Hoir, R Haettel, and L Ortega. Epitaxial refractory-metal buffer layers with a chemical gradient for adjustable lattice parameter and controlled chemical interface. *Applied Physics Letters*, 98(13):131906–131906–3, 2011.

[319] M Weisheit, S Fahler, A Marty, Y Souche, C Poinsignon, and D Givord. Electric Field-Induced Modification of Magnetism in Thin-Film Ferromagnets. *Science*, 315(5810):349–351, January 2007.

[320] Zihao Zhou, Feng Gao, and D Wayne Goodman. Deposition of metal clusters on single-layer graphene/Ru(0001): Factors that govern cluster growth. *Surface Science*, 604(13-14):L31–L38, July 2010.

[321] A Cox, J Louderback, and L Bloomfield. Experimental observation of magnetism in rhodium clusters. *Physical Review Letters*, 71(6):923–926, August 1993.

[322] A J Cox, J G Louderback, S E Apsel, and L A Bloomfield. Magnetism in 4d-transition metal clusters. pages 1–4, November 2012.

[323] A Smekhova, N Atamena, D Ciuculescu, P Lecante, F Wilhelm, C Amiens, and A Rogalev. XANES and XMCD studies of FeRh and CoRh nanoparticles. *Journal of Physics: Conference Series*, 200(7):072091, February 2010.

[324] N Siadou, M Androutsopoulos, I Panagiotopoulos, L Stoleriu, A Stancu, T Bakas, and V Alexandrakis. Magnetization reversal in [Ni/Pt]6/Pt(x)/[Co/Pt]6 multilayers. *Journal of Magnetism and Magnetic Materials*, 323(12):1671–1677, June 2011.

VÕ VĂN Chi
Email: tvovanchi@yahoo.com

(Jun. 2013)

"If you want to go fast, go alone.
If you want to go far, go together."
(old African proverb)

EXPERIENCE	
Jul. 2013 -	Science and Technology Policy Analyst at Đà Nẵng High-Tech Park, Việt Nam
Oct. 2009 - Mar. 2013	Research on **hybrid systems of magnetic structures in contact with graphene**, Néel Institute/CNRS-Grenoble: - Growth and characterization of ultrathin films/graphene and clusters/graphene Eleven beamtimes at **the ESRF and the SOLEIL synchrotron**: - X-ray magnetic circular dichroism: ID08, DEIMOS - X-ray standing wave and X-ray photoemission: ID32 - Grazing incidence small angle X-ray scattering: BM32 Employee of the **Nanosciences Foundation**
Feb. 2009- Jul. 2009	Undergraduate internship, Néel Institute: - Growth of epitaxial graphene on graphene under **ultra-high vacuum**
EDUCATION	
Oct. 2009 - Mar. 2013	PhD, Université Joseph Fourier/Université de Grenoble, France: - Speciality: **NanoPhysics** - PhD thesis: Epitaxial graphene on metal for new magnetic nanometric systems
Sep. 2004 - Jul. 2009	BE, Hồ Chí Minh City University of Technology, Việt Nam: - Speciality: **Advanced Materials Engineering** **- Training program of engineers of excellence in Việt Nam** - Graduation rank: **01st/13 students** Equivalent diploma in Engineering of Ecole Central Paris, France
COMPETENCE	
Experimental skills: scanning tunneling microscopy, reflection high energy electron diffraction, ultra-high vacuum, pulsed-laser deposition, molecular beam epitaxy, Raman spectroscopy Languages: English, French, Vietnamese Informatics: Unix, iOS, Python	
AWARD	
Gold Medal for BE graduation, Hồ Chí Minh University of Technology, Việt Nam, 2009 **Second class prize**, national excellent student competition on **Chemistry**, Việt Nam, 2004 **Third class prize**, national excellent student competition on **Chemistry**, Việt Nam, 2003	
OTHER	
Vice-President of the Association of Vietnamese students in Grenoble, 400 members, 2012	

PUBLICATIONS

1. Chi Võ Văn, Stefan Schumacher, Johann Coraux, Violetta Sessi, Olivier Fruchart, Nick B. Brookes, Philippe Ohresser, Thomas Michely. "Magnetism of cobalt nanoclusters on graphene", *Applied Physics Letters* **99**, 142504 (2011).
2. Chi Võ Văn, Amina Kimouche, Antoine Reserbat-Plantey, Olivier Fruchart, Pascale Bayle-Guillemaud, Nedjma Bendiab, Johann Coraux. "Epitaxial graphene prepared by chemical vapor deposition on single crystal thin films on sapphire", *Applied Physics Letters* **98**, 181903 (2011).
3. Chi Võ Văn, Zoukaa Kassir-Bodon, Hong-Xin Yang, Johann Coraux, Jan Vogel, Stefania Pizzini, Pascale Bayle-Guillemaud, Mairbek Chshiev, Laurent Ranno, Valérie Guisset, Philippe David, Violaine Salvador, Olivier Fruchart. "Ultra-thin epitaxial cobalt films on graphene for spintronic investigations and applications", *New Journal of Physics* **12**, 103040 (2010).
4. Timm Gerber, Marin Petrović, Elin Grånäs, Stefan Schumacher, Fabian Craes, Daniel F. Förster, Ulrike A. Schöder, Johann Coraux, Chi Võ Văn, Jörg Zegenhagen, Petar Pervan, Jesper N. Andersen, Carten Busse, Marko Kralj, Jan Knudsen and Thomas Michely. "Understanding core level shifts of graphen", *submitted*.
5. Nils Blanc, Johann Coraux, Chi Võ Văn, Alpha T. N'Diaye, Olivier Geaymond, Gilles Renaud. "Local deformations and incommensurability of high-quality epitaxial graphene on a weakly interacting transition metal", *Physical Review B* **86**, 235439 (2012).
6. Johann Coraux, Alpha T. N'Diaye, Nicolas Rougemaille, Chi Võ Văn, Amina Kimouche, Nedjma Bendiab, Olivier Fruchart, Andrea K. Schmid. "Air-Pritected epitaxial graphene/ferromagnet hybrids prepared by chemical vapor deposition and intercalation", *The Journal of Physical Chemistry Letters* **3 (15)**, 2059-2063 (2012).
7. Nicolas Rougemaille, Alpha T. N'Diaye, Johann Coraux, Chi Võ Văn, Olivier Fruchart, Adreas K. Schmid. "Perpendicular magnetic anisotropy of cobalt films in contact with graphene", *Applied Physcis Letters* **101**, 142403 (2012).

CONFERENCES and WORKSHOPS:

1. "Graphene-ferromagnet hybrid systems", **contribution**, *International conference on nanosciences + Technology (ICNT2012)*, Paris, France (07/2012)
2. "Magnetism of cobalt nanoclusters on grahene on iridium", **contribution**, *International conference on magentism (INTERMAG2012)*, Vancouver, Cananda (05/2012)
3. "Ultrathin cobalt films contacted to graphene", *International conference on magnetism (INTERMAG 2012)*, contribution, Vancouver, Canada (05/2012)
4. "Graphene-ferromagnet hybrid system", *annual meeting of the GDR-I GNT: "Graphene and Nanotubes" Science and Applications*, **contribution,** Ecully, France (01/2012).
5. "Ultra-thin epitaxial cobalt films on graphene: perpendicular magnetic anisotropy", *XIIIth Louis Néel colloquium*, **contribution**, Albé, France (03/2010).
6. "Self-organized magnetic cluster on moiré patterns", **best poster prize**, *European workshop on self-organized nanomagnets*, Aussois, France (03/2009).
7. Other conferences and workshops:

- European workshop on epitaxial graphene (EWEG2013), Aussois, France (01/2013),
- Users' metting and associated workshops-ESRF, Grenoble, France (02/2012)
- Internatonal workshop on carbon-based spintronics (CSPIN2011), Dresden, Germany (10/2011)
- XIVth Louis Néel colloquium, Brest, France (09/2011).

SCHOOLS

1. European school on magnetic: "Time-dependence phenomena on magnetism", Târgoviște, Romania (2011).
2. Graphene international school, Cargèse, France (2010).

REFEREES:

- Oliver Fruchart, Institut Néel/CNRS, Grenoble, France. Olivier.Fruchart@grenoble.cnrs.fr
- Johann Coraux, Institut Néel/CNRS, Grenoble, France. Johann.Coraux@grenoble.cnrs.fr

Résumé

Graphène est un candidat pour la préparation de dispositifs spintroniques de nouvelle génération tirant partie de sa grande longueur de diffusion de spin et de la grande mobilité de ses porteurs de charge. En interagissant avec matériau ferromagnétique, il pourrait en outre devenir un élément actif, comme le suggèrent des études récentes par physique des surfaces, qui mettent en évidence un moment magnétique de quelques fractions de magnéton de Bohr dans le graphène en contact avec du fer, et une séparation en spin des bandes électroniques du graphène, d'environ 10 meV, par un effet Rashba au contact d'un élément de grand numéro atomique (l'or). La façon dont le graphène peut influencer les propriétés, par exemple magnétiques, des matériaux qui y sont contactés, reste peu étudiée. Les systèmes hybrides de haute qualité, constitués de graphène en contact avec des couches minces magnétiques ou des plots de taille nanométrique, sont des terrains de jeu pour explorer les deux aspects, la manipulation des propriétés du graphène par son interaction avec d'autres espèces, et vice versa. Dans le graphène contacté à des couches magnétiques ultra-minces par exemple, de forts effets d'interface pourraient être exploités pour contrôler l'aimantation du matériau magnétique. L'auto-organisation quasi-parfaite récemment découverte pour des plots nanométriques sur graphène, pourrait permettre d'explorer les interactions magnétiques, potentiellement transmises par le graphène, entre plots.

Trois systèmes hybrides de haute qualité, intégrant du graphène préparé par dépôt chimique en phase vapeur sur le surface (111) de l'iridium, ont été développés sous ultra-haut vide (UHV) : des films ultra-minces de cobalt déposés sur graphène, et intercalés à température modérée entre graphène et son substrat, ainsi que des plots nanométriques riches-Co et -Fe, organisés avec une période de 2.5 nm sur le moiré entre graphène et Ir(111). Auparavant, des films de 10 nm d'Ir(111), monocristallins, déposés sur saphir, ont été développés. Ces films ont été par la suite utilisés comme substrats en remplacement de monocristaux massifs d'Ir(111). Ces nouveaux substrats ont ouvert la voie à des caractérisations multi-techniques ex situ, peu utilisées jusqu'alors pour étudier les systèmes graphène/métaux préparés sous UHV.

Au moyen d'une combinaison de techniques de surface in situ et de sondes ex situ, les propriétés structurales, vibrationnelles, électroniques et magnétiques des trois nouveaux systèmes hybrides ont été caractérisées et confrontées à des calculs ab initio. Un certain nombre de propriétés remarquables ont été mises en évidence. L'interface entre graphene et cobalt implique de fortes interactions C-Co qui conduisent à une forte anisotropie magnétique d'interface, capable de pousser l'aimantation hors de la surface d'un film ultra-mince en dépit de la forte anisotropie de forme dans ces films. Cet effet est optimum dans les systèmes obtenus par intercalation entre graphène et iridium, qui sont par ailleurs naturellement protégés des pollutions de l'air. Les plots nanométriques, au contraire, semblent peu interagit avec le graphène. Des plots comprenant environ 30 atomes restent superparamagnétiques à 10 K, n'ont pas d'anisotropie magnétique, et leur aimantation est difficile à saturer, même sous 5 T. D'autre part, la taille des domaines magnétiques semble dépasser celle d'un plot unique, ce qui pourrait être le signe d'interactions magnétiques entre plots.

Summary

Graphene is a candidate for next generation spintronics devices exploiting its long spin transport length and high carrier mobility. Besides, when put in interaction with a ferromagnet, it may become an active building block, as suggested by recent surface science studies revealing few tenth of a Bohr magneton magnetic moments held by carbon atoms in graphene on iron, and a Rashba spin-orbit splitting reaching about 10 meV in graphene on a high atomic number element such as gold. The extent to which graphene may influence the properties, e.g. magnetic ones, of the materials contacted to it was barely addressed thus far. High quality hybrid systems composed of graphene in contact with magnetic thin layers or nanoclusters are playgrounds for exploring both aspects, the manipulation of the properties of graphene by interaction with other species, and vice versa. In graphene contacted to ultra-thin ferromagnetic layers for instance, strong graphene/ferromagnet interface effects could be employed in the view of manipulating the magnetization in the ferromagnet. The recently discovered close-to-perfect self-organization of nanoclusters on graphene, provides a way to probe magnetic interaction between clusters, possibly mediated by graphene.

Three high quality hybrid systems relying on graphene prepared by chemical vapor deposition on the (111) surface of iridium have been developed under ultra-high vacuum (UHV): cobalt ultra-thin and flat films deposited on top of graphene, and intercalated at moderate temperature between graphene and its substrate, and self-organized cobalt- and iron-rich nanoclusters on the 2.5 nm-periodicity moiré between graphene and Ir(111). Prior to these systems, 10 nm-thick Ir(111) single-crystal thin films on sapphire were developed: they were latter employed as a substrate replacing bulk Ir(111) single-crystals usually employed. This new substrate opens the route to multi-technique characterizations, especially ex situ ones which were little employed thus far for studying graphene/metal systems prepared under UHV.

Using a combination of in situ surface science techniques (scanning tunneling microscopy, x-ray magnetic circular dichroism, spin-polarized low-energy electron microscopy, auger electron spectroscopy, reflection high-energy electron diffraction) and ex situ probes (x-ray diffraction, transmission electron microscopy, Raman spectroscopy, MOKE magnetometry) the structural, vibrational, electronic, and magnetic properties of the three new graphene hybrid systems were characterized and confronted to first-principle calculations. Several striking features were unveiled. The interface between graphene and cobalt involves strong C-Co interactions which are responsible for a large interface magnetic anisotropy, capable of driving the magnetization out-of-the plane of the surface of an ultra-thin film in spite of the strong shape anisotropy in such films. The effect is maximized in the system obtained by intercalation between graphene and iridium, which comes naturally air-protected. Nanoclusters, on the contrary, seem to weakly interact with graphene. Small ones, comprising ca. 30 atoms each, remain super paramagnetic at 10 K, have no magnetic anisotropy, and it turns out difficult, even with 5 T fields to saturate their magnetization. Besides, the magnetic domains size seem to exceed the size of a single cluster, possibly pointing to magnetic interactions between clusters.